Analysis And Design Of Morphological Filter In The Fractional Domain And Under Alpha Stable Distribution Environment For Signal Processing Applications

Thesis Submitted

in fulfillment of the requirements for the award of degree

of

DOCTOR OF PHILOSOPHY

by

Aditi Bajaj

Reg. No. 901706001

Under the Supervision of

Dr. Sanjay Kumar

Associate Professor

ECED

THAPAR INSTITUTE
OF ENGINEERING & TECHNOLOGY
(Deemed to be University)

Department of Electronics and Communication Engineering

Thapar Institute of Engineering and Technology

Patiala -147004

March 2024

DECLARATION

I hereby declare that the work which is being presented in thesis entitled **"Analysis and Design of Morphological Filter in the Fractional Domain and under Alpha Stable Distribution Environment for Signal Processing Applications,"** in the fulfillment of the requirements for the award of the Degree of **Doctor of Philosophy** submitted in the *Department of Electronics and Communication Engineering of the Thapar Institute of Engineering and Technology, Patiala* is an authentic record of my own research work carried out during a period of July, 2017 to March, 2024 under the supervision of Dr. Sanjay Kumar, Associate Professor, Department of Electronics and Communication Engineering, Thapar Institute of Engineering and Technology, Patiala. The matter presented in the thesis has not been submitted in part or full to any other University or Institute for the award of any degree in India or abroad.

Dated: 07/March/2024

Aditi Bajaj

Aditi Bajaj
(901706001)

It is certified that the above statement made by the candidate is correct to the best of my knowledge and belief.

Dated: 07/March/2024.

(Dr. Sanjay Kumar).

Dr. Sanjay Kumar
(Supervisor)

CERTIFICATE

It is hereby certified that the thesis entitled **"Analysis and Design of Morphological Filter in the Fractional Domain and under Alpha Stable Distribution Environment for Signal Processing Applications,"** submitted by Ms. Aditi Bajaj, a research scholar in the *Department of Electronics and Communication Engineering, Thapar Institute of Engineering and Technology, Patiala*, for the award of the degree of **Doctor of Philosophy**, is a record of bonafide research work carried out by her under my supervision and guidance. She has fulfilled the requirements for the submission of this thesis which has reached the requisite standard. The results embodied in this thesis have not been submitted to any other University or Institute for the award of any degree or diploma.

Dated: 07/March/2024.

(Dr. Sanjay Kumar)

Dr. Sanjay Kumar
Associate Professor, ECED
Thapar Institute of Engineering and Technology
Patiala, Punjab-147004
India.

Dedication

Matr devo bhava
Pitr devo bhava
Acharya devo bhava

Look upon your mother as your God
Look upon your father as your God
Look upon your teacher as your God

- from the sacred Vedic hymns of the *Taittireeya Upanishad* of India.

ACKNOWLEDGEMENTS

I am beyond grateful to have reached the stage where, with blessings of God, I am wrapping my seven years' worth of research work and I have the honour to express my sincere gratitude to everyone who has been part of my incredible Ph.D. journey.

First and foremost, I am grateful to be supervised by Dr. Sanjay Kumar, who has introduced me to the world of research. Despite being new to research, I believe I was able to jump-start my Ph.D. path with the help of his imparted knowledge and skills during the early years of my journey. He created a supportive research environment and has always encouraged the idea of teamwork. The periodic sharing of his collection of research papers, research discussions on the problems where we get stuck and his invaluable guidance have been instrumental in shaping this thesis. He not only supervised the technical aspects, but he also been a great role model for me over the years, nurturing me with his honest research attitude, passion for learning, disciplined way of life, and spiritual conversations. One of his major teachings was that we can achieve anything with dedication, and his similar perspectives on life lessons inspired me to embark on my Ph.D. quest. Finally, I will always be indebted to him for trusting my abilities, having confidence in me, letting me explore and find my own ways of doing research and continuing to be a guiding force in my efforts to stay focused and on track with my work.

I would also like to express my regards to the present Head of DECE, Dr. Kulbir Singh and Dr. Alpana Agarwal (former Head DECE) for providing the facilities for research work. Additionally, I would like to sincerely thank my doctoral committee Dr. Harish Garg, Dr. Vinay Kumar, Dr. Ashutosh Singh and late Dr. Urvinder Singh, for providing their supportive feedback and encouragement in due course of my Ph.D. Also, I am thankful to my ECED faculty members, Dr. Geetika Dua, Dr. Mayank Agarwal, Dr. Pravindra Kumar, Dr. Dinesh Bhardwaj and Dr. Mohit Agarwal with whom I had the privilege to have research talks during my teaching associateship hours. I would also like to express thankfulness to Dr. Navneet Sharma, Dr. Amit Kumar Kohli, Dr. Sudhanshu Tyagi, Dr. Amit Mishra, Dr. Rana Pratap Yadav and Dr. Gagandeep Kaur for being constant well-wishers. Also, I am extremely thankful to Ph.D. coordinator Dr. Mayank Kumar Rai for his help in streamlining the submission process. I am incredibly grateful of Dr. Ravinder Agarwal (DEIE) for providing consistent exposure to multiple conferences.

I would also like to thank Mr. S.N. Ram, Mr. B.P. Singh, Mr. Arun Kumar, Mr. Amanpreet Singh, Mr. Karanjeet Singh, Mr. Sunil Singh, Mr. Hardeep Singh, Mr. Hitesh Gupta, Mr. Gundeep Singh, Mr. Manohar and Ms. Madhu for their help during the lab hours of teaching associateship, which has helped me in enhancing practical knowledge of the electronics subjects. I also want to extend my thankfulness to Mr. Vinod Bhatt, Ms. Ramanjeet Kaur and Mr. Vijay for supporting and helping with all the paperwork and clerical formalities during the course of Ph.D. I am deeply grateful to Dr. Shri Ram and Ms Archana Nanda for helping me access research articles and books, which greatly helped me complete my research work.

The whole credit for motivating me to start this incredible Ph.D. journey goes to Dr. Sanjay Kumar and my father, Mr. Ashwani, who have encouraged and supported my learning zeal and gave it the shape of this doctoral degree. I will always be indebted to my mother, Ms. Asha, whose love and encouragement have been my anchor during this challenging but rewarding journey. I am grateful to share my love for science with my younger brother Achitya, who has helped me to grow as a critical thinker. I would also like to thank my maternal and paternal family for always being a constant source of joy and motivation. All in all, with the blessings of my late grandparents (maternal and paternal) and the unwavering support and love of my family, I feel immensely blessed for their presence in my life.

I would also like to extend my heartfelt gratitude to my in-law's family for their unconditional love, support, and genuine care and concern. I am beyond grateful for their overwhelming gestures from providing a studious space when needed to cooked meals even during late-night study sessions. Also, I have learned so much from the wisdom of my younger brother-in-law Shivam. His presence has always made me feel respected and cherished. I am truly blessed to have married into such a wonderful family.

As I reflect on my journey as a Ph.D. student, I am filled with immense gratitude to have been surrounded by Dr. Amandeep Kaur, Dr. Anmol Gupta, Ms. Deepika Singh, Ms. Sweta Sinha, Ms. Manpreet Kaur and Dr. Abhinav Jain for sparing their valuable time in having general research talk as well as the social conversations over a cup of tea. I am grateful to my BioSAIL's research mates Dr. Anmol Gupta and Dr. Amandeep Kaur, for their relentless support, encouraging words that kept me going, constant listening, and presence at times of triumph, disappointment, and every other milestone. Discussion sessions with Dr.

Amandeep Kaur have helped me realign my research goals from time to time and Dr. Anmol Gupta has helped me improve my writing and technical skills. Overall, their presence has helped me sail through the journey of my Ph.D. I would also like to thank Dr. Ishan Chawla for sharing his research approach, which has helped me structure my literature work and re-trace my referred research papers.

I am deeply grateful to Ms Anjana Bhatia (maternal aunt) and Dr. R.K. Bahl for showering me with love and wisdom and being my second home in Patiala. I would also like to give a special acknowledgment to my friends, Mr. Abhinav Kapila and Ms. Priyanka Srivastava, for always fuelling my determination to pursue my journey and to Dr. Kanwarpreet Kaur, whose words of wisdom have helped in my research progress.

My acknowledgment would be incomplete without thanking Deepti ma'am for being a constant supporter and encouraging me to cherish this journey and every phase of life with a positive mindset. Her warmth and comforting conversation have always acted as a catalyst in lifting my spirits.

Lastly, I am deeply grateful to my best friend, soulmate and my "better best-half," Mr. Ayuk Mahajan, for being a constant pillar of strength. My research work completion results from his unwavering belief in me, constant nudging to achieve goals, unconditional love and endless sacrifices. From accompanying me with late-night studies to providing insightful research discussions, from being my biggest critic to being my biggest cheerleader, his support in every aspect of life has given me the biggest boost in confidence. When nobody believes, you have to believe in yourself, but he was the one who believed in me more than I have. His approach towards the work-life balance has transformed my approach to dealing with chaotic events and panic situations. This Ph.D. finish line would not have been achieved without his rock support.

With all those sleep-deprived nights, days of achievements and days of gaining experience, I learned one thing: just keep on doing the work; the Ph.D. journey is nothing but a string of these fleeting moments. Finally, this research journey would never have been possible if Dr. Sanjay Kumar had not introduced me to the intricate world of time-frequency tools, which instilled in me the curiosity to explore different research avenues.

Aditi Bajaj

ABSTRACT

Non-stationary signal analysis is a widely researched field in signal processing since we come across various non-stationary kind of signals such as human speech, music, bio-medical signals etc., in our day-to-day lives. Within the dynamic domain of signal processing, non-stationary signals challenge conventional analysis with their ever-changing characteristics. With the inefficiency of Fourier transform (FT) in analyzing such time-varying signals, the concept of time-frequency (TF) tools was formulated, revolutionizing non-stationary signal analysis by providing time-dependent power spectrum and simultaneous localization in both time and frequency domains. Impressed by the realm of TF tools, this research is focused on improving the analysis of very important non-stationary signal existing in nature—an electrocardiogram (ECG) signal, which is quasiperiodic and known to encompass a non-stationary nature. Therefore, research work in the thesis is centered around improving the performance of ECG analyzing system with a primary focus on its noise analysis model, denoising and QRS complex detection.

ECG is considered a health biomarker and its one cardiac cycle comprises P, QRS and T waves. These components contain important clinical information that can be interpreted in different ways such as any change in their morphological pattern is an indication of cardiac arrhythmia, wave interval timings of QRS complex provide information about heart rate variability (HRV) and other features extracted from these beats can help in identifying various heart disorders. However during signal acquisition, ECG signal is distorted by various types of noise such as powerline interference, baseline drift and muscular artifacts, which have spectral characteristics that coincide with those of ECG signals. The variability in the physiology of QRS complex influences the morphology of ECG signal, alongside its susceptibility to noise. Thus, noise removal is an essential part of ECG processing, along with accurately delineating the QRS complex in designing computer-aided diagnosis tools to assist physicians and doctors in providing suitable medical interventions.

Furthermore, several research methods employing time and frequency domain approaches have been *proposed* in the literature, but non-stationary characteristics of ECG signals hinder their effectiveness. Since TF tools have the virtue of dealing with non-stationarity, various TF tool-based methods have been documented in the literature for ECG denoising and detecting QRS complexes. However, getting a high reconstruction rate and better retaining of significant information is still an open problem. The work in this thesis utilizes

the benefits of fractional Fourier transform (FrFT) to expand conventional time-frequency (TF) tools to time-fractional frequency domain with fractional order parameter a, thus addressing the challenges and ambiguities of time-varying morphology of ECG signal faced by existing state-of-the-art methods.

Moreover taking a step backward, susceptibility to various noises and artifacts for an ECG signal is very high. Yet, established denoising methods always employ the additive white Gaussian noise model to compensate for such undesirable additions and use this noise assumption to validate their efficacy for reliable performance. Although, justification for using this Gaussian distribution is backed by the Central Limit Theorem (CLT), defined for random variables with finite variance. But *what if variables possess infinite variance and thus do not have a Gaussian nature?* Therefore, an improvement window exists for analyzing the noise analysis model, which brings us to our next research aim of investigating the nature of noises that corrupt an ECG signal.

This investigation study for the noise model is segregated into three parts. The first part employs statistical tools to prove that the noises corrupting ECG signals deviate from Gaussianity. Second part focuses on proving the resemblance of ECG noises with non-Gaussian α-stable distribution model. Finally, negative impact on the performance of conventional methods (employing the implicit assumption of noises following Gaussian distribution) for R-peak detection and classification is illustrated by considering their functioning in real-time scenarios modelled by α-stable distribution model.

After establishing the non-Gaussian nature of ECG noises, further research aims to design methods based on alternative noise analysis model. The study delves into the domain of morphological signal processing to thoroughly examine design techniques for morphological filters (MFs). However, it is observed that less attention is paid to the design of structuring elements (SE) while working towards designing MF in the literature. Thus, a design of novel SE is put forward by merging the concept of cross-convolution with FrFT. In the context of preprocessing ECG signals, it is imperative to ensure that noise suppression techniques do not result in losing vital information. Hence, utilization of *proposed* SE in conjunction with *proposed* morphological operation (MO) enables adaptation to the non-stationary changes in ECG signals and ensures the suppression of noises along with facilitating the preservation of distinctive attributes of ECG signals.

Furthermore, as a major contribution to research work, a fractional lower-order fractional Stockwell transform (FLO-FrST) based on fractional lower-order statistics (FLOS) is *proposed*, which aims to resolve the shortcomings of existing TF tools by providing better 3Rs', namely resolution, reconstruction and robustness. This tool provides four degrees of freedom, leading to superior performance, particularly in terms of 3Rs' compared to its counterpart TF tools.

Additionally, study includes an electroencephalogram (EEG) as another biomedical signal to demonstrate the effectiveness of *proposed* FLO-FrST in classifying epileptic activity. The scope of presented work is broadened by including these non-stationary EEG signals for analysis. The performance of *proposed* FLO-FrST system is validated through the utilization of various convolutional neural network (CNN) models, showcasing its ability to excel in diverse modeling scenarios and providing good performance.

In a broader sense, presented study has *proposed* solutions for non-stationary signals under non-Gaussian environment. This study has enabled a new perspective to adopt noise model analysis, ranging from impulsive to Gaussian noise environments. Additionally, *proposed* study amalgamates the concepts from multidisciplinary signal processing domains and comes up with robust tools and methods to analyse non-stationary signals in non-Gaussian environment. For instance, with an amalgamation of FrFT with ST, flexibility in terms of degrees of freedom has been added over traditional methods in processing ECG signals, putting together design methods of SE with cross-convolution window concept and FrFT has provided shape adaptability to classical morphological filtering, and by bringing together concepts of FrFT and ST with FLOS has provided fractional frequency domain support to existing fractional lower-order time-frequency (FLO-TF) approaches by improving over resolution, reconstruction and robustness for noise environments ranging from impulsive to Gaussian. Finally, this opens up new horizons and calls for more focus on research, opting for alternate noise analysis models to overcome performance shortcomings in conventional methods and exploring the applications of *proposed* tools in other applications of signal processing as well.

List of Publications

International Journals

1. **A. Bajaj** and S. Kumar, "QRS Complex Detection Using Fractional Stockwell Transform and Fractional Stockwell Shannon Energy," *Biomedical Signal Processing and Control*, vol. 54, p. 101628, 2019. https://doi.org/10.1016/j.bspc.2019.101628. (**SCI Journal**, **Impact Factor: 5.1, Publisher: ELSEVIER**)
2. **A. Bajaj** and S. Kumar, "A Robust Approach to Denoise ECG Signals Based on Fractional Stockwell Transform," *Biomedical Signal Processing and Control*, vol. 62, p. 102090, 2020. https://doi.org/10.1016/j.bspc.2020.102090. (**SCI Journal**, **Impact Factor: 5.1, Publisher: ELSEVIER**)
3. **A. Bajaj** and S. Kumar, "Design of ECG Denoising Digital Filter Under α-Stable Noise Environment Based on Morphological Signal Processing," *Circuits, Systems, and Signal Processing*, 2024. https://doi.org/10.1007/s00034-024-02602-8. (**SCI Journal**, **Impact Factor: 2.3, Publisher: SPRINGER**)
4. **A. Bajaj** and S. Kumar, "Design of Novel Time–Frequency Tool for Non-stationary α-Stable Environment and its Application in EEG Epileptic Classification,"*Arabian Journal for Science and Engineering*, 2024. https://doi.org/10.1007/s13369-023-08634-7. (**SCI Journal**, **Impact Factor: 2.9, Publisher: SPRINGER**)
5. **A. Bajaj** and S. Kumar, "The Investigation and Validation of the α-Stable Distribution Characteristics for Noises that Corrupt ECG Signals," *Arabian Journal for Science and Engineering*. (**SCI Journal**, **Impact Factor: 2.9, Publisher: SPRINGER**)

Conference Papers

1. **A. Bajaj** and Sanjay Kumar, "ECG Analysis Using Fractional Stockwell Transform: A Novel Approach", presented at *13th Western Pacific Conference on Acoustics (WESPAC)*, CSIR-NPL, New Delhi, India, November 11-15, 2018.

2. **A. Bajaj** and Sanjay Kumar, "ECG Processing in α-Stable Distribution Noise Environment using Fractional Lower-Order Fractional Stockwell Transform", presented at *9th National Conference on Advances in Metrology (AdMet-2024)*, Gurugram University, Gurugram, India; March 08-09, 2024.

List of Abbreviations

AAMI	Association for Advancement of Medical Instrumentation
ANSI	American National Standards Institute
ARR	Arrhythmia
AWGN	Additive white Gaussian noise
CAD	Computer-Aided Diagnosis
CC	Cross Correlation
CDF	Cumulative Distribution Function
CHF	Congestive Heart Failure
CLT	Central Limit Theorem
CNN	Convolutional Neural Network
CVDs	Cardiovascular Disorders
CWT	Continuous Wavelet transform
DFrFT	Discrete Fractional Fourier Transform
DFT	Discrete Fourier Transform
DL	Deep Learning
eCDF	Empirical Cumulative Distribution Function
ECF	Empirical Characteristic function
ECG	Electrocardiogram
EEG	Electroencephalogram
EMD	Empirical Mode Decomposition
EMG	Electromyogram
EVD	Eigenvalue Decomposition
FC	Fractional Calculus
FFT	Fast Fourier Transform
FIR	Finite Impulse Response
FLOM	Fractional Lower-Order Moments

FLO-FrST	Fractional Lower-Order Fractional Stockwell Transform
FLO-PWVD	Fractional Lower-Order Polynomial Wigner-Ville Distribution
FLO-ST	Fractional Lower-Order Stockwell Transform
FLO-STFT	Fractional Lower-Order Short-Time Fourier Transform
FLO-TF	Fractional Lower-Order Time-Frequency
FLO-TFD	Fractional Lower-Order Time-Frequency Distribution
FLO-TFR	Fractional Lower-Order Time-Frequency Representation
FLO-WVD	Fractional Lower-Order Wigner-Ville Distribution
FLOS	Fractional Lower-Order Statistics
FN	False Negative
FoSP	Fractional-Order Signal Processing
FP	False Positive
FrFT	Fractional Fourier Transform
FrSE	Fractional Structuring Element
FrSShnE	Fractional Stockwell Shannon Energy Envelope
FrST	Fractional Stockwell transform
FrWT	Fractional Wavelet Transform
FT	Fourier Transform
GCLT	Generalized Central Limit Theorem
GGD	Generalized Gaussian distribution
GMD	Gaussian Mixture Distribution
GSL	Great Salt Lake
GSNR	Generalized Signal-to-Noise-Ratio
HRV	Heart Rate Variability
IDFrFT	Inverse Discrete Fractional Fourier Transform
JP	Jones-Parks
JTFA	Joint Time-Frequency Analysis
KS	Kolmogorov-Smirnov
LCT	Linear Chirplet Transform
LRD	Long-Range Dependence
MCO	Morphological Convolution Operator

MF	Morphological Filter
MIT-BIH	Massachusetts Institute of Technology-Beth Israel Hospital
ML	Machine Learning
MLW	Main-Lobe Width
MM	Mathematical Morphology
MMF	Mathematical Morphological Filter
MO	Morphological Operation
MSP	Morphological Signal Processing
NLM	Non-Local Mean
NSR	Normal Sinus Rhythm
PCG	Phonocardiogram
PDF	Probability Density Function
PLI	Powerline Interference
PMP	Performance Metric Parameters
PRD	Percent Root Mean Square Difference
PVC	Premature Ventricular Contraction
RMSE	Root-Mean-Square-Error
SDR	Signal-to-Distortion Ratio
SE	Structuring Element
ShnE	Shannon energy
SShnE	Stockwell Shannon Energy
SLL	Side Lobe Level
ST	Stockwell Transform
STFrFT	Short-Time Fractional Fourier Transform
STFT	Short-Time Fourier Transform
SVPB	Supraventricular Premature Beat
TBP	Time-Bandwidth Product
TF	Time-Frequency
TFD	Time-Frequency Distribution
TFR	Time-Frequency Representation
TFSAP	Time-Frequency Signal Analysis and Processing

tLSD	t Location-Scale Distribution
TMF	Time-Varying Morphological Filtering
TP	True Positive
VAG	Vibroarthrogram
VMG	Vibromyogram
WD	Wigner Distribution
WT	Wavelet transform
WVD	Wigner-Ville Distribution

List of Symbols

$\boldsymbol{a}$	Fractional Order Parameter
$\boldsymbol{\varphi}$	Fractional Rotation Parameter
$\boldsymbol{\Gamma}$	Gamma Function
$\boldsymbol{\alpha}$	Characteristic Exponent of α-Stable Distribution
$\boldsymbol{\beta}$	Symmetry Parameter of α-Stable Distribution
$\boldsymbol{\gamma}$	Scale Parameter of α-Stable Distribution
$\boldsymbol{\delta}$	Location Parameter of α-Stable Distribution
$\boldsymbol{u_{\varphi}}$	Fractional Fourier frequency
$\boldsymbol{r}$	Ripple Ratio of Dolph-Chebyshev Window.
$\ominus$	Erosion Morphological Operation
$\circ$	Opening Morphological Operation
$\oplus$	Dilation Morphological Operation
$\blacksquare$	Closing Morphological Operation
$\boldsymbol{\mathcal{F}_{\mathcal{F}}^{\varphi}}(.)$	Fractional Fourier Transform Operator
$\boldsymbol{\lambda}$	QRS Complex Detection Threshold
$\boldsymbol{\rho}$	Fractional Lower-Order Parameter
$(.)^{<\rho>}$	Fractional Lower-Order Operator
$\boldsymbol{p}$	First Window Adjustment Parameter of Fractional Stockwell Transform
$\mathbb{F}$	Integer Order Operator
$\boldsymbol{q}$	Second Window Adjustment Parameter of Fractional Stockwell Transform
$\boldsymbol{\sigma(n)}$	Gaussian distribution noise
$\boldsymbol{\alpha_s}$	α-Stable Distribution-based Noise Model
$\boldsymbol{\theta(t)}$	Characteristic function of α-stable distribution

List of Figures

List of Tables

Table of Contents

Chapter 1

Introduction

1.1 General

Signal processing is the heart of technological advancements encompassing the theories and algorithms for analyzing and processing signals. It is a boon to the medical field and for other non-medical applications like security, home automation, etc. With extensive applications in diverse disciplines of research and engineering [1, 2], the primary goals of signal processing are often categorized into four main areas:

(i) *Signal Generation*: This includes mechanisms to acquire and synthesize signals for describing underlying information. It includes fields like sensing, synthesis, and acquisition.

(ii) *Signal Representation*: This includes the use of mathematical models to characterize signals. It deals with the field of applied mathematics and information theory and includes tools like the Fourier transform for suitable analysis of signals [1].

(iii) *Signal Manipulation*: This field circumscribes the processing techniques for separating/attenuating the desired component of an observed signal from noise or enhancing certain components to extract useful information.

(iv) *Signal Interpretation*: After acquiring and processing signal, various techniques like segmentation are applied to extract useful information. This branch of signal processing includes fields like classification and pattern recognition.

Recently, the focus of research in the field of signal processing has been shifting towards developing solutions for more complex and demanding situations that are *non-stationary* and *non-Gaussian* in nature. However, depending solely on a single branch of signal processing is inadequate to tackle these issues, thereby requiring the investigation of many

interdisciplinary domains within signal processing. The research encapsulated in the presented work is motivated by our desire to address the challenges that arise while working with *non-stationary* signals in a *non-Gaussian* environment. This chapter presents a comprehensive overview of the key areas that motivate our research. It includes a basic introduction to *morphological signal processing*, *fractional-order signal processing*, *time-frequency signal analysis and processing*, as well as their applications.

1.2 Concept of Morphological Signal Processing (MSP)

MSP, a non-linear signal processing branch, originated from mathematical morphology (MM), originally from the mathematical framework for set theory and lattice algebra. The pioneering work in MM was done by French researchers Matheron [3] and Serra [4] in 1960s, to study geometric structures of image objects as sets in Euclidean space. Since then, MM concept has been successfully applied to various areas of image processing like filtering, segmentation, character recognition, edge detection, etc., and have applications in areas like medical imaging and oil spills detection [5, 6, 7].

Utilizing the concepts of MM, Maragos and Schafer [8, 9] later introduced the unified theory for the representation of classical linear and non-linear filters in terms of morphological correlations/transformations [10]. This unified theory assisted in analyzing geometric structures of binary signals (classified as set), multi-level signals (classified as functions) and filters (set-processing and function-processing). Filters employing such MM concept, used for filtering signals based on sets and functions, were referred to as mathematical morphological filter or simply morphological filters (MFs). These MFs locally modify the geometric features of signals using non-linear signal transformations.

As the name "morphology" implies shape or form, MSP is the study for analyzing and quantifying the shape, size and other geometric aspects of the signal. The analysis and processing are performed using – morphological transformations, referred to as morphological operators (MOs) and another signal, referred to as structuring element (SE). As stated by Matheron [3]: "*knowledge about an object depends on how we observe it.*" In reference to MFs, this implies that the choice of SE with appropriate MO influences the information one can extract. The simplicity of using morphology-based processing lies in the concept that applying or fitting SE using MOs are determined by the kind of information we desire. Hence, conforming to their efficient algorithms and easy implementations, MFs

are widely used in 1-D and 2-D applications, including but not limited to biomedical signal processing [11, 12, 13], mechanical fault diagnosis [14] and seismic signal processing [15].

Furthermore, literature has presented the approximations of various linear and non-linear filters like median filter and order statistics [16]. Also, morphological wavelet theory has been reported in which these MOs are utilized in non-linear multi-resolution signal decomposition schemes [17, 18].

However, the majority of research conducted focuses on designing various MFs by integrating combinations of MOs, with less attention placed on designing SE. Hence, this thesis aims to introduce a new SE design based on the principles of MSP for effectively filtering non-stationary signals in both Gaussian and non-Gaussian environments.

1.3 Concept of Fractional-Order Signal Processing (FoSP)

"Fractional-order" is an intriguing concept and has attracted the attention of scientists and engineers for a long time. From the time of understanding the beauty of fractions by recognizing the *golden ratio: 1.618:1*, *natural exponential: e=2.71828* and π*=3.14159*, the approach of "*fractional thinking*" was incorporated, which resulted in amalgamating various concepts with *fractional* terminology. For instance, between integers *fractional* numbers were introduced; in between integer-order calculus, there is *fractional-order* calculus; in between integer-order moments, there are non-integer order moments, i.e., *fractional-order* moments; and in between time and frequency domain, *fractional* Fourier transform was formulated.

Recalling the very first evidence of long-range dependence (LRD), Hurst reported this phenomenon by analyzing data collected from the Nile River in Egypt [19]. Another, historical example of Great Salt Lake (GSL), where variation of its elevation has been an issue since 1875 [20]. Among several methods employed to estimate its elevation from time to time, their insufficient performance led to the evidence of heavy-tailed data [21].

Owing to these characteristics of data, many research studies pointed out that the α-stable process was better at handling LRD and heavy-tailed data. Delving deeper, the link between fractional calculus (FC) and the LRD process was found, as LRD processes could be generated using fractional-order differential systems [22, 23]. Similarly, α-stable process was found as the result of fractional-order diffusion equations [23]. With this, it is

imperative to say that FC holds significant importance in describing many natural and man-made phenomena.

Furthermore, to glance at FC [24], which encompasses fractional-order differentiation and fractional-order integration, is an extended concept of conventional Newtonian calculus. As derived from the field of pure mathematics, it has been successfully applied in various fields of science and engineering [25, 26, 27].

Apart from this, another important tool that captures the essence of "fractionalization" and offers a solution for analyzing LRD processes is the fractional Fourier transform (FrFT) [28]. It generalizes the definition of classical Fourier transform, allowing for fractional values of transform order [29].

Lastly, in order to put this *fractionalization* in proper context from the viewpoint of signal processing, the cumulative knowledge of three major components– fractional calculus, α-stable distribution, and fractional Fourier transform forms the backbone of fractional-order signal processing (FoSP). Therefore, with the demand for analyzing and understanding these fractional processes, the methods for fractional-order signal processing have become an active research area.

For this reason, this thesis aims to explore the applicability of FoSP tools in processing signals. Since real-world signals tend to have heavy-tailed characteristics, the work in this thesis revolves around examining the presence of non-Gaussian characteristics in real-time noises using FoSP tool i.e., α-stable distribution tool. Subsequently, methods for processing non-stationary signals in a non-Gaussian environment will be designed.

1.4 Historical Background of Time-Frequency (TF) Tools

The non-stationary process offers an alternate explanation for the empirical phenomenon that long-range dependencies are intended to solve [30]. As mentioned before, just like LRD data are analyzed using FoSP tools, non-stationary signals, which are the realization of a non-stationary process, are analyzed using time-frequency (TF) tools. They provide simultaneous localization of time and frequency components to efficiently analyse and process non-stationary signals.

Historically, the concept of time-frequency analysis is related to the joint distribution of position and momentum in Quantum Mechanics [31]. Thus, the concept behind devising time-frequency distribution (TFD) may be traced back to the idea of joint distribution of

densities, which incorporates the utilization of marginals and moments of the density functions, as commonly employed in probability theory. Thus, the construction of TFDs involves the concept of joint distributions, covariations, and marginals to describe the energy density of a signal in both time and frequency domains [32].

In the last few decades, TF tools have emerged as a powerful method for analyzing non-stationary signals and have been applied to diverse fields like seismic signal processing [33], volcanic monitoring [34], fault signal processing [35], biomedical signal processing [36, 37], etc. TF tools have also shown promising results in image processing applications using advanced processing methods such as machine learning and deep learning [37, 38].

With the initial classification of TF tools into linear, quadratic and higher-order representations, the focus was on improving the *resolution* of TF tools. Typical examples falling in this category are short-time Fourier transform (STFT) [39], Wavelet transform (WT) [40], Wigner-Ville distribution (WVD) [32, 41, 42, 43].

Inspired by the advantages offered by fractional Fourier transform (FrFT) [44] in filtering, a new perspective to the established analytical TF tools was introduced, leading to the development of time-fractional frequency tools like short-time fractional Fourier transform (STFrFT) [45], fractional Wavelet transform (FrWT) [46] and fractional Stockwell transform (FrST) [47]. This new category of tools based on the FrFT kernel improved robustness by offering the flexibility of FrFT parameter φ, which helps extract better characteristic information of signal by introducing time-fractional frequency resolution.

However, most of the research related to FrFT kernel-based TF tools is limited to geophysics, and there is an opportunity to explore its advantages in the biomedical field. Therefore, the aim of this research is first to explore the performance of FrFT kernel-based TF tool for biomedical applications.

Furthermore, most of the above-mentioned TF tools emphasize the analysis of real-time signals in the presence of a Gaussian noise environment. Nevertheless, recent literature studies have revealed that the effectiveness of these current TF techniques declines when impulsive noise is present [48]. Hence, to enhance the versatility of TF tools, new definitions using fractional lower-order statistics (FLOS) have been *proposed*, referred to as fractional lower-order time-frequency (FLO-TF) tools. These tools are based on fractional lower-order statistics (FLOS) and incorporate the FLO parameter ρ. In contrast to their TF counterpart, FLO-TF tools provide better performance in the presence of a non-

Gaussian α-stable distribution noise environment [49, 50]. However, their performance is still limited by poor resolution, which results in loss of information when reconstructing.

In order to address the limitations of current FLO-TF tools, this thesis proposes a novel design strategy that utilizes FrFT kernel. The objective is to improve performance in terms of resolution, reconstruction, and robustness in noise environments that range from impulsive to Gaussian.

1.5 Contribution of Research Work

For over 100 years, the electrocardiogram (ECG) has been used to evaluate human cardiac activity. It is a non-invasive technique that transforms the electric impulses evolving from the heart into a time-varying signal and any deviation from the normal ECG pattern is reflected in the subject's ECG recording. Thus, it provides information about the electrophysiology of the heart and ischemic changes occurring in the heart; hence, is contemplated as a fundamental tool for monitoring cardiovascular disorders (CVDs). However, ECG analyzing systems designed to capture subtle abnormal changes in ECG patterns for timely and accurate diagnosis of fatal heart diseases still face challenges due to the *non-stationary* nature of ECG signals. Also, the chances of a wrong diagnosis of ECG signals increase if noises and distortions are not dealt with at the initial stage. Therefore, initial research work aims to design the denoising and QRS complex detection employing time-fractional frequency analysis. With the advantages of hybridizing the concept of ST with FrFT, the obtained spectrogram plays a key role by providing a fine signal resolution and avoiding the overlap between essential components present in the signal and various noises corrupting the ECG signal.

Furthermore, as mentioned before, ECG gets corrupted by various impulsive noises and artifacts, which can cause problems in analyzing the underlying condition of the heart. The possible reason for these impulsive noises is electromyogram (EMG) or muscle noise, powerline interference and drift in ECG caused by baseline wander. However, in conventional ECG signal processing techniques, artifacts are assumed to follow the Gaussian distribution. This is why we usually use additive white Gaussian noise, for proving the robustness of algorithms under noisy conditions (physiological and environmental). However, it has been proved that various noises existing in nature do not follow the assumption of the Central Limit Theorem, which forms the backbone for assuming noise to be Gaussian. Hence, an investigation study has been presented to prove

the existence of non-Gaussian α-stable distribution noise nature in noises corrupting ECG signals.

Subsequently, as traditional linear filtering techniques are ineffective for reducing impulsive noises and preserving the subtle notches and spurs in ECG signal, further research on non-linear filtering alternatives using morphological filters (MFs) is put forward. The *proposed* MF has the potential to suppress ECG noises and offer beat adaption, ultimately improving reconstruction performance.

Lastly, the time-frequency analysis and processing methods are again explored to provide enhanced performance in a non-Gaussian α-stable distribution noise environment. The *proposed* novel tool has the capability of dealing with Gaussian as well as impulsive noise as its formulation is based on FLOS. Additionally, considering the *robustness*, *reconstruction* and *resolution* ability of *proposed* tool, application on electroencephalogram (EEG) epileptic detection is explored.

Thus, the research encapsulated in this thesis revolves around exploring – *non-stationary* nature of signals and solutions for dealing with a *non-Gaussian* noise environment.

1.6 Organization of Thesis

The research work is structured in seven chapters. The first two chapters describe the theme of the presented work with its introductory and state-of-the-art works, while the main work of the thesis is presented in chapters three and onwards.

Chapter 2: Literature Survey

Central premise of the thesis is covered with an extensive review of research work pertaining to morphological filters, fractional-order signal processing and time-frequency signal analysis and processing. This will serve as a prerequisite for the subsequent chapters by highlighting the motivation, research gaps, objectives and research methodology carried out in this thesis.

Chapter 3: ECG Signal Processing Using Fractional Stockwell Transform (FrST)

This chapter explores the idea of TF tools based on the FrFT kernel, i.e., FrST, in processing non-stationary ECG signals. The methods for FrST-based denoising and FrST-based QRS

complex detection are devised and their performance is compared against well-established methods. Contrary to the classical approaches, the performance of the *proposed* methods are dependent on three variable FrST parameters (a, p and q), resulting in a dramatic improvement for both denoising and QRS complex detection in terms of their respective performance metric parameters.

Chapter 4: Investigation of α-Stable Distribution Noise Analysis Model for ECG Signals

This chapter addresses the question, "*Is Gaussian distribution noise appropriate for practical scenarios*?" by investigating the characteristics of real-time noises. The presence of a non-Gaussian α-stable distribution is demonstrated by employing several statistical techniques on noise data obtained from standard databases. The main highlight of this chapter is the evidence of performance degradation obtained by incorporating the *proposed* α-stable distribution noise on existing R-peak detection methods and deep learning (DL) models, which are designed with the implicit assumption of normality.

Chapter 5: Design of Morphological Filter for ECG Processing Considering α-Stable Distribution Noise

Following the conclusion drawn from Chapter 4, the design of denoising and QRS complex detection is *proposed* for ECG signals, considering the scenario of a practical noise model, i.e., α-stable distribution noise model. Owing to the need to design solutions for noises ranging from impulsive to Gaussian, the branch of non-linear morphological filtering is used. With the *proposed* fractional structuring element and morphological operations, the designed filter served for noise suppression and better adaption to the changes in ECG signal morphology. This improved reconstruction, followed by better detection of QRS complex, compared to established methods.

Chapter 6: Introduction of Novel Time-Frequency Tool for α-Stable Distribution Noise Environment

Extending the idea of FrST in conjunction with the non-Gaussian α-stable distribution noise concept, a new tool based on fractional lower-order statistics (FLOS) is put forward

in this chapter. With an intensive comparison of the *proposed* FLO-FrST with existing state-of-the-art tools, the application of EEG epileptic detection using DL is presented using the *proposed* tool. Also, validation and comparison are provided with literature methods and using different CNN models to indicate the potential of the *proposed* FLO-FrST tool.

Chapter 7: Conclusion and Future Scope

This chapter provides concluding remarks on the research encapsulated in this thesis. In addition, future prospects have been presented built around the potential of the *proposed* methods.

Chapter 2

Literature Survey

2.1 Overview of ECG Signal Analysis and Processing

Over the last four decades, methods to analyze and process ECG signals have gained enormous attention, as ECG is the most popular tool for effectively evaluating heart disorders like cardiac arrhythmia and myocardial infarction. However, due to the *non-stationary* nature of ECG signals and their susceptibility to various noises, it is necessary to devise methods for enhancing diagnostic information of ECG signals.

A brief description of different noises corrupting ECG signals, its preprocessing and detection of QRS complex are summarized below.

2.1.1 ECG Noise Analysis

As stated before, ECG signals tend to get distorted by various physiological and environmental factors, even with a controlled acquisition setup. Therefore, to design preprocessing mechanisms for its accurate monitoring, understanding the main sources of noise is essential. The following categories provide an overview of different noises by considering all the perturbations affecting ECG [51, 52].

- **Muscle noise**: ECG is acquired by electrodes which are attached to patient body. These electrodes acquire the electric potential generated by heart muscle and other active muscles. Thus, muscle noise is caused by contraction of muscles also known as electromyogram (EMG). It is a high-frequency noise whose spectrum overlaps with ECG spectrum. Methods designed to address this noise reduction often result in distorting the essential ECG components.
- **Baseline wander**: It is a low-frequency noise originating from physiological factors like respiration or body movements. This noise affects the isoelectric line of captured signal and thus misleading the analysis.
- **Powerline interference (PLI)**: This is a narrowband noise with frequency centered at 50/60 Hz. This power supply type of noise can result in sporadic impulse.

- **Artifacts of motion**: These are caused by loss of electrode contact due to the motion of patients, resulting in sharp changes. This results in a slow and gradual shift in baseline of ECG. These artifacts resemble baseline wander but are more troublesome as they appear to follow the characteristics of an ECG signal.
- **Other interferences of physiological and non-physiological origin**: Mother ECG appearing in fetal ECG is an example of physiological interference, which cannot be controlled. Additionally, interference caused due to phonocardiogram (PCG), vibromyogram (VMG) and vibroarthrogram (VAG) also affect the morphology of ECG. On the other hand, electric interference caused by instruments used in acquiring ECG or present near the acquisition apparatus, such as electromagnetic interference, instrumentation noise etc., are of non-physiological origin.

2.1.2 Preprocessing of ECG Signals

Preprocessing in general is a process of removing noises and artifacts interfering with signal of interest and its enhancement for processing stages. This stage is foremost after acquiring the signal, and methods used in this stage decide the quality of subsequent stages and overall process involved in interpreting underlying signal. In the context of ECG processing normalization, resampling and ECG denoising are few blocks involved in preprocessing. ECG denoising is a significant block of this stage, which involves removing artifacts and noises and performing operations like baseline correction.

The significance of this stage lies in the fact that during signal acquisition, ECG gets corrupted by various noise and artifacts (physiological and non-physiological origin), whose frequency mostly lies within the band of interest (0.05-100 Hz) [51, 52].

Over the years, an extensive survey has been conducted in this field and a wide variety of signal processing methods to denoise ECG signals have been established.

Conventionally, preprocessing of ECG was done using time-domain techniques as they were independent of spectral content required to filter out noise from signals. On the other hand, frequency domain techniques were implemented to get desired response characteristics based on spectral information [51]. Many algorithms based on adaptive filtering [51, 53] such as LMS and RLS were also developed for canceling noise from ECG signals as they could track time-varying morphology of ECG signal. To filter out noise from ECG signal without distorting its characteristic waveform, Savitzky-Golay filtering

technique [54] was also developed, which is a widely accepted tool in the research community.

Recently, various decomposition-based techniques [55, 56, 57, 58, 59, 60] are introduced and are quite effective in handling ECG signals. Among them, empirical mode decomposition (EMD) based techniques are quite popular as they adaptively decompose signal into IMFs and process signal components based on different frequency ranges.

In addition to these techniques, fractional-order filters [61, 62, 63] have proved advantageous over integer-order filters such as Wiener filters, Kalman filters, etc., as they can better model real-world problems. In contrast to integral filters, fractional integral filters do not have unity weights for getting weighted summed output of a signal. Some of these methods also provide zero-phase filtering, which is desirable for preserving the features of signal [61].

2.1.3 QRS Complex Detection

The goal of preprocessing stage is to suppress noises and enhance the interpretability of fiducial points of ECG signal namely P, Q, R, S and T. These fiducial points correspond to the depolarization and repolarization mechanisms related to the conduction system of heart. Thus, they contain important information that can be manipulated in different ways. For example, any change in their morphological pattern indicates cardiac arrhythmia, wave interval timings of QRS complex provides information about heart rate variability (HRV), and other features extracted from these beats can help identify various heart disorders. Among these points, QRS complex is the most prominent component in ECG waveform, which plays a key role in analyzing ECG signals. In the sequel of preprocessing ECG signals, detection of QRS complex holds significant importance, as its accurate detection plays a decisive role in feature extraction, classification and hence in the overall interpretation of ECG signal for suitable diagnosis. Therefore, huge research is available with a focus on correctly identifying the QRS complex and their brief description is grouped into the following three categories:

Signal Derivative-based methods: Pan and Tompkins [64] presented the algorithm for detecting QRS complex in real-time based on linear filtering techniques and nonlinear transformations. Hamilton and Tompkins [15] modified this algorithm by optimizing the involved decision rules. Many detectors based on first derivative and the combination of

Hilbert transform were also developed to detect QRS complex [65]. Furthermore, fractional derivatives have recently been introduced to detect QRS complex [66, 67].

Digital filtering methods: This involves removal of undesired frequency components using preprocessing techniques such as window-based filtering [68], median filtering [69], and adaptive filtering [53, 70, 71, 72], along with suitable thresholding to detect R-peaks.

Time-frequency-based methods: Numerous methods based on joint time-frequency analysis tools have been developed to detect QRS complexes. The techniques based on wavelet transform utilize decomposition mechanism using different wavelet functions and soft and hard-based thresholding [73]. On the other hand, Stockwell transform (ST) utilizes Gaussian window (known to have best time-frequency bandwidth product) for extracting complex features [74]. Also, Empirical Mode Decomposition (EMD) based techniques are popular as they decompose signal into various IMFs and process components with different frequency ranges [55]. Apart from these, Hilbert transform-based techniques are also popular for finding R-peaks [75].

2.2 Preliminaries of Morphological Filters (MFs)

Morphological Filters (MFs) are a category of nonlinear filters utilized in processing impulsive signals. By virtue of their intrinsic qualities and solid mathematical foundation, they are highly suitable for managing sudden and localized fluctuations in a signal. A comprehensive overview of its fundamentals along with its applications are presented below:

2.2.1 Basics of MFs

The fundamental concept of MF revolves around nonlinearly transforming the shape of a signal interacting with another signal referred to as structuring element (SE). This interaction involves different morphological operations (MOs) performed on underlying signal using suitable SE. The two key components required for designing MF are described below.

2.2.1.1 Concept of Morphological Operations (MOs)

Four fundamental MOs constituting the main frame of MSP are *erosion*, *dilation*, *opening* and *closing*. They are elaborated with their mathematical formulation in the subsequent paragraphs.

Let $f(n)$ be an original 1-D discrete signal that represents function over the domain $F = (0,1,\dots.,N-1)$. Let $g(m)$ be the SE that is discrete function over a domain $G = (0,1,\dots\dots.M-1)$ $(M \leq N)$. Mathematically, four basic operators are defined as follows [76]:

i. *Erosion*: This operation is derived from Minkowski subtraction performed on two sets or the intersection performed on two functions equivalently. Intuitively, erosion is a shrinking process and it reduces peaks present in signals. Mathematically, it is represented as:

$$(f \ominus g)(n) = \min\{f(n+m) - g(m)\}\{1 \leq n \leq N; 1 \leq m \leq M\} \quad (2.1)$$

ii. *Dilation*: Derived from Minkowski addition performed on two sets or equivalently the union operation performed on two functions. Dilation is an expanding process and it smoothens the peaks present in signal and is mathematically described as:

$$(f \oplus g)(n) = \max\{f(n-m) + g(m)\}\{1 \leq n \leq N; 1 \leq m \leq M\} \quad (2.2)$$

iii. *Opening*: This is cascade operation of the above two operations, i.e., *erosion* followed by *dilation* and is represented as:

$$(f \circ g)(n) = ((f \ominus g) \oplus g)(n) \quad (2.3)$$

iv. *Closing*: This operation is attained by performing a *dilation* operation followed by *erosion* and is represented as:

$$(f \blacksquare\ g)(n) = ((f \oplus g) \ominus g)(n) \quad (2.4)$$

where $\ominus$, $\oplus$, $\circ$ and $\blacksquare$ denote erosion, dilation, opening and closing operations, respectively.

Nonetheless, each MO possesses distinct characteristics and is selected according to an intended task. For instance, erosion and opening exhibit high-pass characteristics and dilation and closing exhibit low-pass characteristics. This enables the utilization of these MOs for purposes like noise reduction and feature extraction. In addition to the operations mentioned above, literature has documented various MOs that have been employed in mechanical fault diagnosis and is founded on the combination of these fundamental operators (morphological top-hat and morphological gradient operators, etc.) [14, 76, 77].

2.2.1.2 Concept of Structuring Element (SE)

In order to perform morphological filtering on the underlying signal, geometric features of the signal are modified by applying morphological transformations (i.e., MO) with another

signal referred to as SE. It is characterized by its shape, length and height. Performance of MF is governed by the choice of SE along with suitable MO.

In the literature, many SE shapes are defined such as flat SE, dome-shaped SE, triangular SE and half-wave of sine waveform [31, 32, 33]. The selection of SE solely depends on signal characteristics and application for which MF is to be applied. For example, if an aim is to extract signal features, shape of SE is chosen to be like the shape of signal. If an aim is to remove noise, flat SE is used to smooth the regions where noise is present. MF is generally a shape-processing filtering approach and SE is like a probe that executes the filtering mechanism using the intended MO. After selecting a particular shape for SE, length of SE is then determined by

$$\begin{cases} L_s > M; segment\ of\ signal\ is\ retained \\ L_s < M; segment\ of\ signal\ is\ removed \end{cases} \tag{2.5}$$

where M is length of SE and L_s denotes segment of signal under consideration.
Furthermore, various theories are reported in the literature which employ MO multiple times (multi-scale morphological filtering [78]) using different SEs to process different scales of underlying signal. The concept of time-varying SE [79] is *proposed* to reduce the complexity of multi-scale morphological filtering and different approaches to optimize the length of SE in conjunction with MO are *proposed* for various image processing applications [80, 81] as well as for mechanical fault detection [82].

2.2.1.3 Demonstration of MF

With viewpoint of illustrating the effect of different MOs as well as providing the essence of working with SE, a simulated signal of following specifications is considered.

- Two small “positive” and “negative” impulses of length 4 sampling points
- Two large “positive” and “negative” impulses of length 6 sampling points

And for demonstration purposes, SE characterized by following attributes is chosen.

Shape: *Flat*

Height: *Zero*

Length: 3, 4, 5, and 6 sampling points, therefore for simplicity SEs will be denoted as $SE_{L3,}$ SE_{L4} SE_{L5} and SE_{L6}.

Moving further, to demonstrate the output of fundamental MOs firstly in **Figure 2.1**, output of *dilation* in accordance with different lengths of SE is depicted with following observations:

Impact on negative impulses

- Short negative impulse: As negative impulse length is 4, SE_{L4} SE_{L5} and SE_{L6} completely suppresses its amplitude to zero (reference level of signal), whereas SE SE_{L3} only partially reduces the amplitude as depicted.
- Large negative impulse: SE_{L6} completely suppresses the amplitude whereas, other SEs only reduce the amplitude with worst reduction shown by SE_{L3}.

Impact on positive impulses

- All SEs flatten (or smooth) the amplitude of impulses, with maximum flattening shown by SE_{L6} and minimum by SE_{L3}.

  Thus, overall behavior of dilation is to suppress negative amplitudes (also referred to as valleys) and flatten positive ones (referred as peaks).

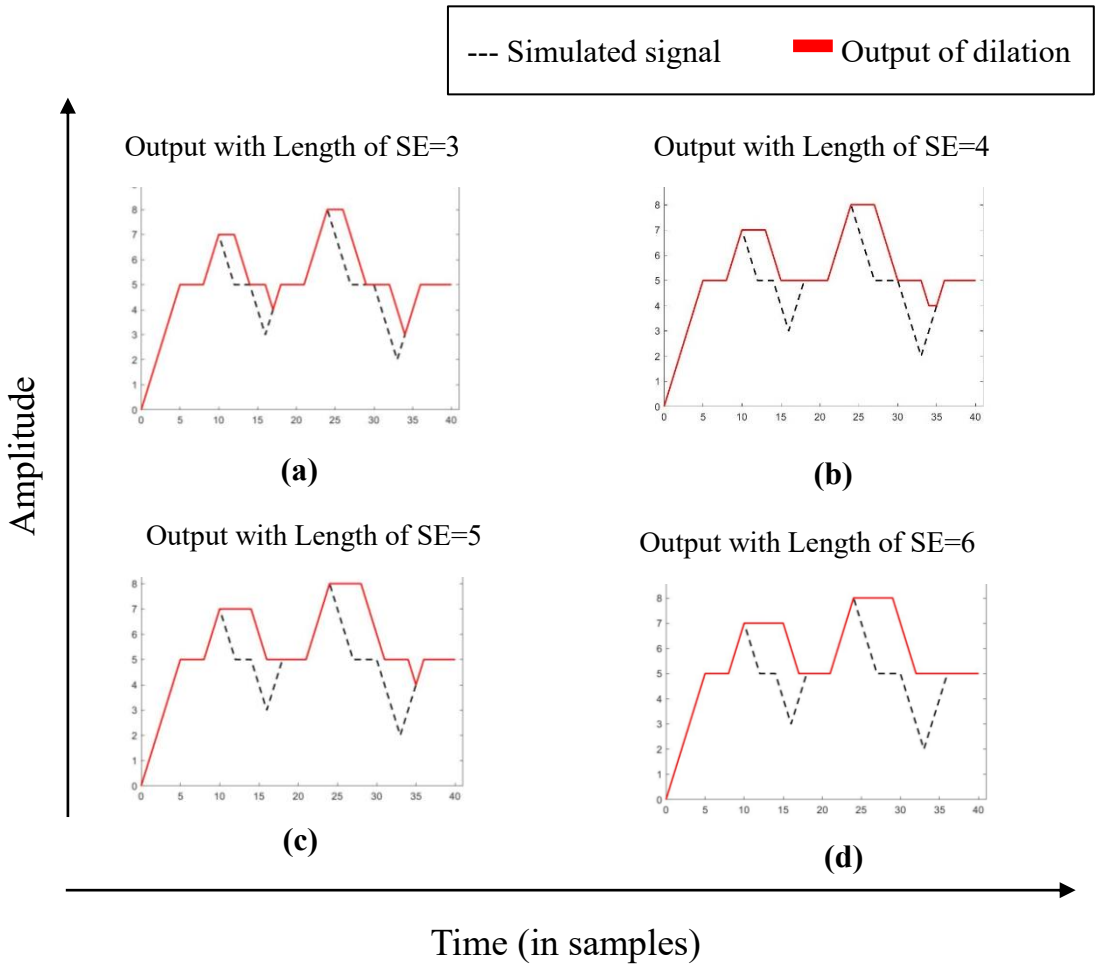

Figure 2.1 Demonstration of *dilation* using different structuring element (SE) of different length **(a)** Using SE_{L3} i.e., SE of length 3 **(b)** Using SE_{L4} i.e., SE of length 4 **(c)** Using SE_{L5} i.e., SE of length 5 **(d)** Using SE_{L6} i.e., SE of length 6.

Next, to depict the *erosion* **Figure 2.2** is shown with a suitable explanation as follows:

Impact on positive impulse

- For shorter impulse of length 4, SE_{L4}, SE_{L5} and SE_{L6} completely suppresses its amplitude to zero (reference level of signal), whereas SE_{L3} only reduces the amplitude.

Impact on negative impulses

- All SEs flatten (or smooth) the amplitude of impulses, with maximum flattening shown by SE_{L6} and minimum by SE_{L3}.
- For large impulse, only SE_{L6} is able to completely suppress the peak, whereas other SEs show partial suppression, with worst performance shown by SE_{L3}.

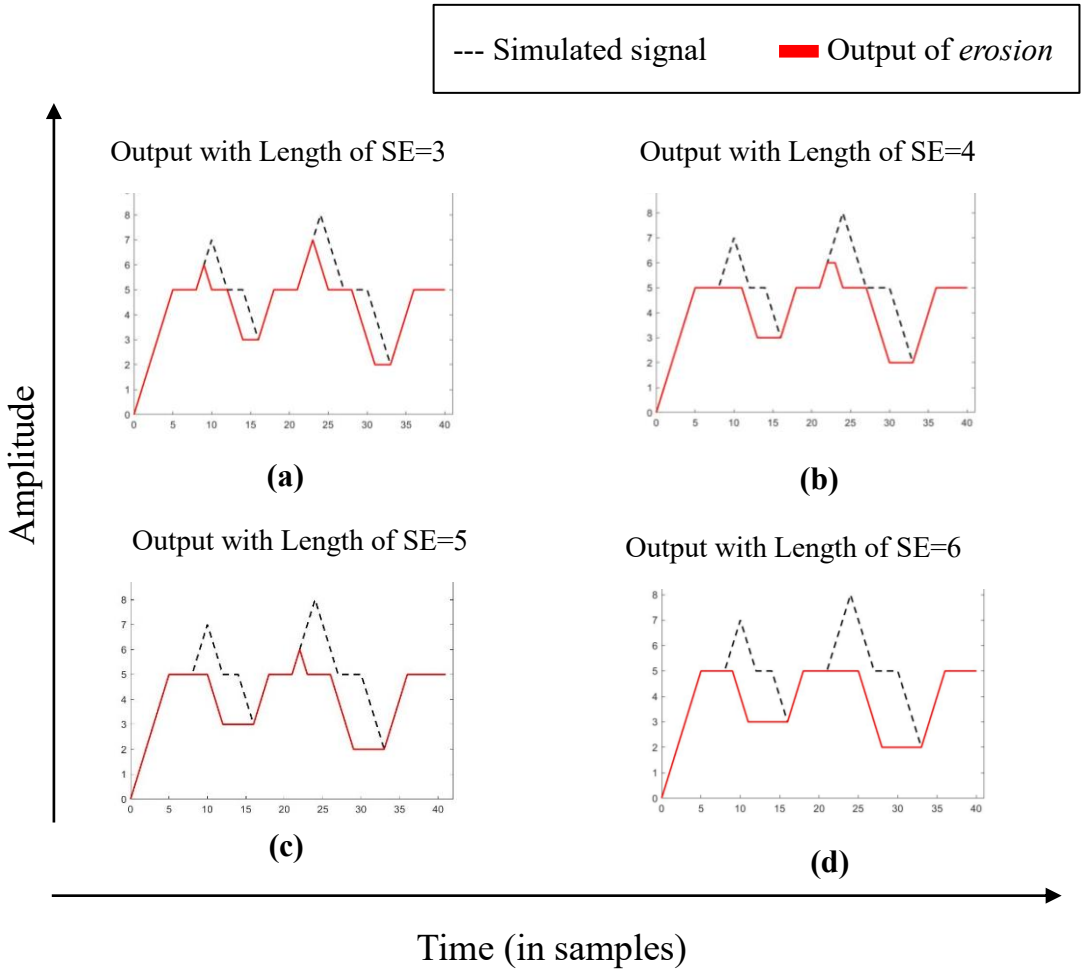

Figure 2.2 Demonstration of *erosion* operation using different structuring element (SE) of different length **(a)** Using SE_{L3} i.e., SE of length 3 **(b)** Using SE_{L4} i.e., SE of length 4 **(c)** Using SE_{L5} i.e., SE of length 5 **(d)** Using SE_{L6} i.e., SE of length 6.

Here, point worth mentioning is that *erosion* is the dual operation of *dilation* in terms of set complementation. Hence, performance of *erosion* on positive impulses is similar to the performance of *dilation* on negative impulses.

Furthermore, performance of *opening,* which is a cascade operation of *erosion* followed by *dilation*, is depicted in **Figure 2.3** with following observations:

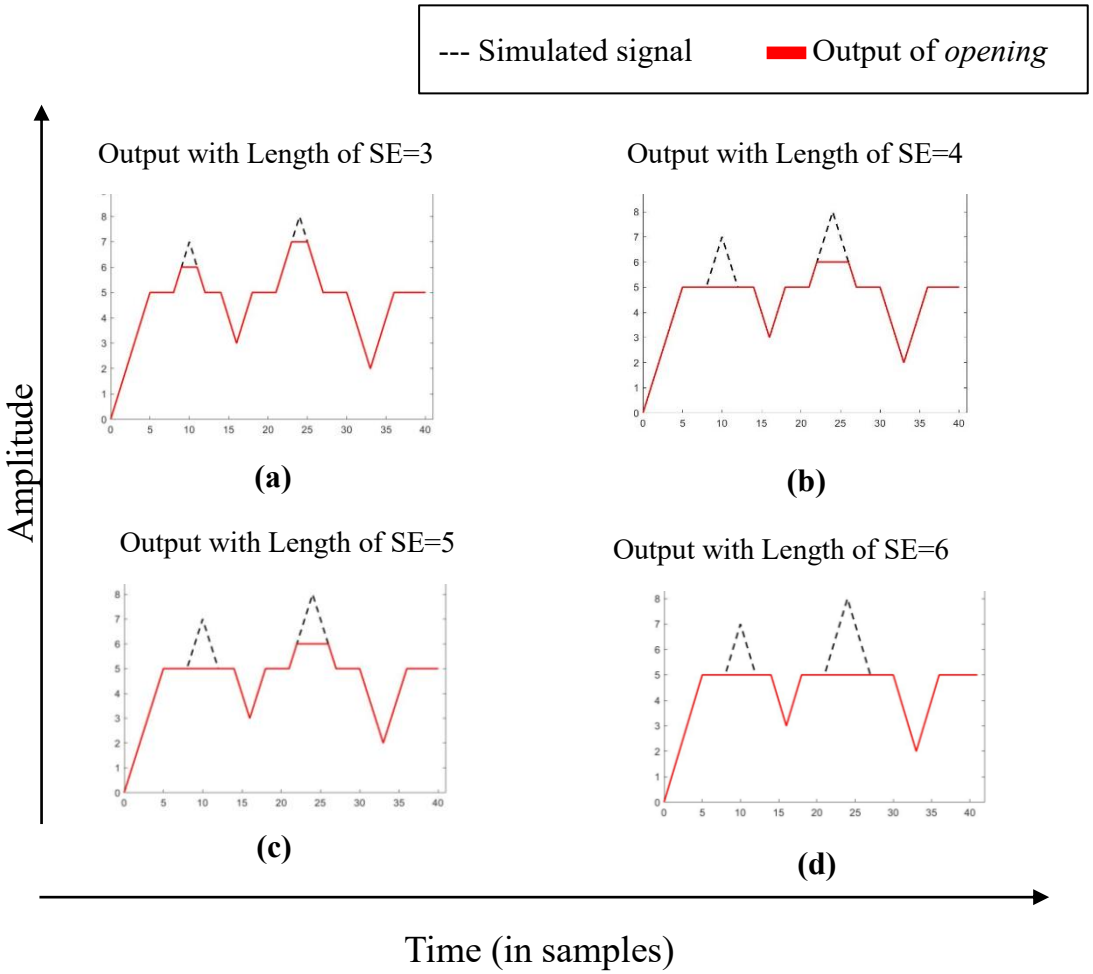

Figure 2.3 Demonstration of *opening* operation using different structuring element (SE) of different length **(a)** Using SE_{L3} i.e., SE of length 3 **(b)** Using SE_{L4} i.e., SE of length 4 **(c)** Using SE_{L5} i.e., SE of length 5 **(d)** Using SE_{L6} i.e., SE of length 6.

Impact on negative impulses

- Inheriting the characteristics of *erosion*, *opening* operation retains negative impulses and therefore, no impact is observed by using SE_{L3},SE_{L4}, SE_{L5} and SE_{L6} on negative impulse.

Impact on positive impulses

- Inheriting the characteristics of *dilation*, *opening* operation reduces the positive impulses. For shorter impulse, SE_{L4}, SE_{L5} and SE_{L6} are equally effective and for larger impulse, only SE_{L6} completely removes the impulse.

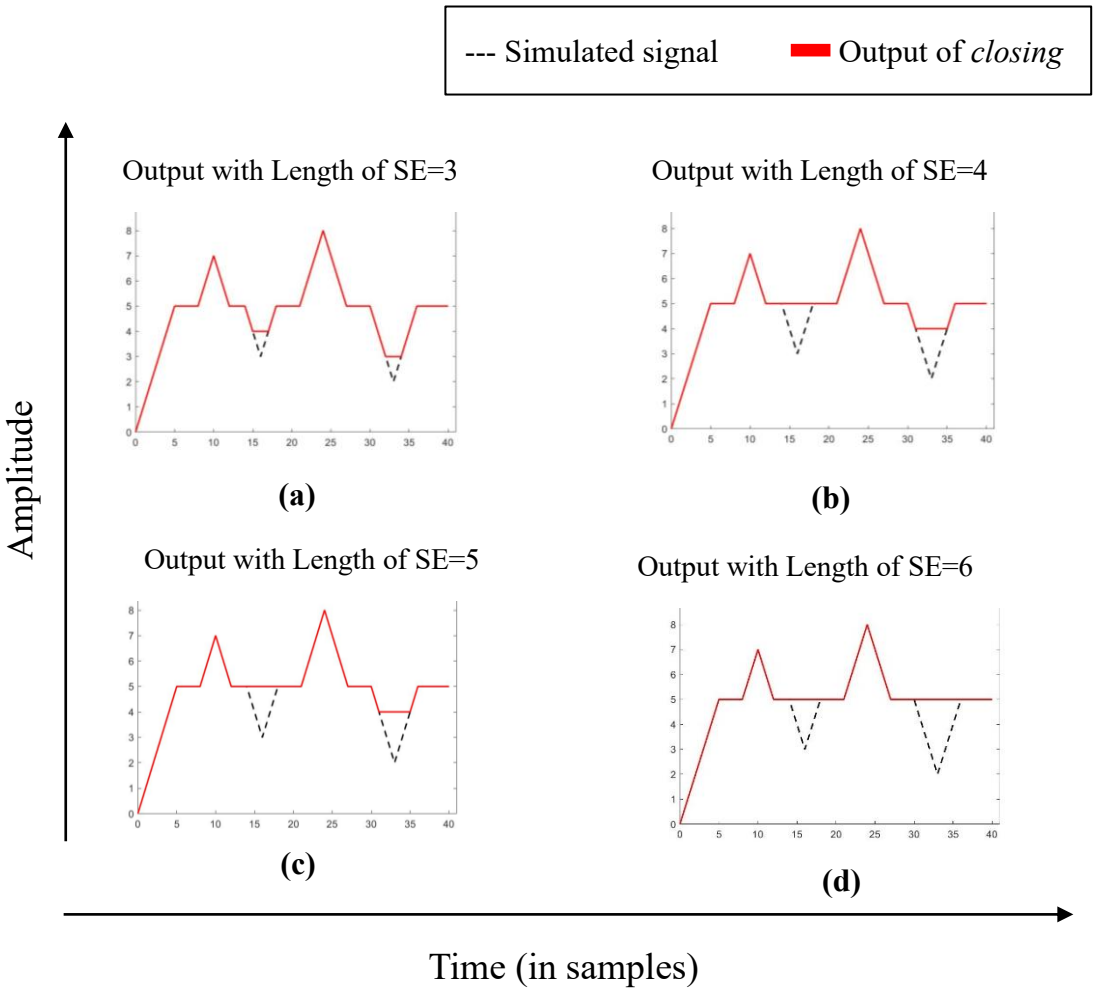

Figure 2.4 Demonstration of *closing* operation using different structuring element (SE) of different length **(a)** Using SE_{L3} i.e., SE of length 3 **(b)** Using SE_{L4} i.e., SE of length 4 **(c)** Using SE_{L5} i.e., SE of length 5 **(d)** Using SE_{L6} i.e., SE of length 6

Lastly, the performance of *closing* is shown in **Figure 2.4** with details as follows:

Impact on positive impulses

- As *closing* is derived from first performing *dilation* followed by *erosion*, positive impulses are preserved; hence, all SEs perform equally on positive impulses.

Impact on negative impulses

- Reduction of negative peaks observed with SE_{L4}, SE_{L5} and SE_{L6} is equally effective in suppressing amplitude of shorter impulse. Furthermore, only SE_{L6} is able to completely suppress larger impulse.

Finally, to summarize the performance of different MOs, **Table 2.1** gives an overview of their characteristics.

Table 2.1 Summary of morphological operations (MOs)

S. no	Name of the MO	Symbol	Salient features
1	Dilation	$(f \oplus g)$	Reduces the negative peaks and smoothens positive peaks
2	Erosion	$(f \odot g)$	Reduces the positive peaks and smoothens negative peaks
3	Opening	$(f \circ g)$	Removes positive peaks and retains the negative peaks
4	Closing	$(f \blacksquare g)$	Removes negative peaks and retains the positive peaks

Note: f is signal of interest and g represents SE.

2.2.2 Applications of MFs in Signal Processing

Owing to the advantages offered by MFs, they have been extensively employed in biomedical signal processing and mechanical fault processing and their brief description is given below:

2.2.2.1 MFs in ECG Signal Processing

Numerous works have been done in the field of ECG signal processing incorporating morphological filtering methods. Morphological filtering methods are known to suppress noise and extract features from signal [83]. The pioneering work of applying morphological filtering on ECG was done by Chu and Delp in 1989 [13]. An algorithm based on the

combination of opening and closing was developed to suppress the impulsive and background noise in ECG signal. Later, Trahanias *et al.* [84] in 1993 introduced the concept of morphological peak-valley extraction operator for detecting QRS complex in ECG signals. As morphological processing is a computationally efficient method, Sun *et al.* [85] in 2002 presented a modified morphological filtering algorithm for signal conditioning. Additionally, multi-scale morphological derivate was introduced to improve the noise sensitivity of single-scale [86]. Besides that, various QRS complex detection methods based on morphological filtering were developed, and this concept has also been incorporated into wearable devices [87]. Furthermore, the idea of adaptive morphological filtering was also formulated to reject broadband noises affecting ECG signal. These were based on an adaptive structuring element (SE), shape, size, and weight of which were changed based on previously detected QRS complex [88].

Considering the advantages of MFs, such as its simple and computationally effective mechanism, it has been utilized in the development of wearable sensors for ECG [87] and has been paired with established techniques to assist in identifying ECG's characteristic components [89, 90].

Apart from the applications of MFs in ECG signal processing, methods for EEG signal preprocessing based on MF have also been reported [11, 12, 91].

2.2.2.2 MFs in Mechanical Fault Processing

MFs are extensively employed in applications specific to mechanical engineering. Among various works, various variations of MFs are reported in the domain area of bearing fault detection of rotating machinery and vibration analysis for detection of machine defects. A brief summary of MFs related to the domain of mechanical fault processing is presented as follows:

Lv *et al.* [76] presented a new MF based on averaging the best combination of difference operators. This new filter enhances the accuracy of detecting positive and negative impulses. SE length is determined by introducing a new indicator called Teager energy kurtosis, which further increases the effectiveness of filter introduced for feature extraction. Li *et al.* [92] *proposed* a new novel scheme for feature extraction based on a mathematical morphological filter (MMF) along with a grey relations analysis scheme. Various approaches are discussed to determine the analysis scale to be used for MMF. Comparisons are performed with the kurtosis criterion-based MMF and spectral kurtosis criterion-based

MMF, and superiority is tested using the feature selection results obtained by detecting train axle-bearing faults.

Meng *et al.* [93] made an approach to deal with fault detection of rolling element bearing based on MF combined with a translational invariant wavelet as a pre-filter. At a later stage, the *proposed* method utilized ensemble empirical mode decomposition to extract defect information. The efficiency of *proposed* method is evaluated by measuring signals from defective bearings with different fault types.

Zhang *et al.* [94] constructed a morphological gradient filter using concept of SE, whose length parameter is decided by α-stable distribution. The parameter α is used as an indicator to reflect the faults diagnosis due to its strong relation with impulse signal. The frequency spectrum of various gradient filters is observed, and dilation-erosion gradient filter has shown good performance in enhancement of impulse signal.

Hu *et al.* [95] studied the concept of mathematical MF for vibration signal analysis. The filter characteristics are described through frequency response analysis, and relationship between SE length and MF's cut-off frequency is put forward to quantitatively select SE. Better computational speed and filtering of impulses are found in *proposed* filter.

Li *et al.* [79] presented time-varying morphological filtering (TMF) for rolling element fault detection. SE chosen for this purpose is no longer fixed and adjusts adaptively according to the extreme points of signal. The method employed has high computational efficiency and can extract features accurately. Also, some novel SEs are explored to improve the performance of TMF.

Li *et al.* [96] presented a novel signal-processing scheme for rolling element-bearing fault detection. The advantage of closing and opening based gradient operator along with denoising characteristic of convolution operator is utilized to design morphological convolution operator (MCO). MCO is then introduced into lifted morphological undecimated wavelet to enhance detection ability.

Yu *et al*. [97] *proposed* the enhanced form of MF based on combinations of MOs for robust feature extraction for vibration signals.

Liang *et al*. [98] amalgamated the concepts of mathematical morphology with other signal processing methods, like signal segmentation, to extract the hidden features from intrinsic modes to enhance the accuracy of fault diagnosis.

2.3 Preliminaries of Fractional-Order Signal Processing (FoSP)

Knowledge of *process*, such as stochastic or deterministic, is essential in understanding reasons behind the cause of complex phenomena. Conventional signal processing aids by providing various avenues to address such scenarios. For example, backed by a strong mathematical background, statistical models help to understand the phenomenon of signal and noise generation. Here, the catch is models are based on certain *assumptions*. However, to deal with practical applications where signals exhibit properties that change with time (*non-stationary*), such *assumptions* do not hold firm, leading to inaccuracies in analysing the underlying signal.

To understand these *assumptions* and *models*, this section first introduces conventional assumptions, followed by a description of the tools needed to address realistic characteristics, namely *non-Gaussian* and *non-stationary*.

2.3.1 Conventional Assumptions

First assumption: The data to be analyzed is normally distributed.

In conventional signal processing, normal distribution also referred to as Gaussian distribution forms the foundation for modeling and processing signals. Mathematicians have extensively studied this distribution model and resulting algorithms are usually of a simple linear nature and can be implemented in real-time. For example, the additive white Gaussian noise (AWGN) assumption in communication theory greatly simplifies the design and analysis of receiver structures [49].

Gaussian distribution also known as the bell curve has its mathematical origins in the work of several mathematicians, including Abraham de Moivre (1713), Legendre (1805), Robert Adrain (1808), Pierre Simon de Laplace (1810, 1811, 1878-1912) with significant contributions from Carl Friedrich Gauss (1795). Originally utilized in the realm of astronomy to quantify errors, this concept now plays a crucial role in the domains of physics, machine learning, economics, and engineering [99, 100].

Mathematically for a random variable X, with mean μ and standard deviation σ, **Table 2.2** summarizes the statistics of Gaussian distribution.

Moreover, this distribution holds unique properties, such as cumulants above order two being zero. Therefore, it is frequently used to describe uncertainty in various applications. Another feature of Gaussian distribution is that the Fourier transform of Gaussian distribution is again Gaussian distribution itself and therefore has significance in properties

like convolution and uncertainty and has practical implications in various fields such as probability theory, signal processing, quantum mechanics, to name a few. Therefore, the simplicity and characteristics of this distribution make it a useful tool for applying this model to various aspects of signal processing and other scientific and engineering fields. Additionally, the applicability of Gaussian distribution is supported by central limit theorem (CLT), which is a key concept of probability theory given by:

Central Limit Theorem (CLT)

Let X_1,X_2,... ... X_n, be a sequence of independent and identically distributed (i.i.d) random variables with mean μ and finite variance σ^2. Then, a sequence of sums given as [101]:

$$S_n = \frac{1}{\sigma\sqrt{n}}\left(\sum_{i=1}^{n} X_i - n\mu\right) \tag{2.6}$$

such that its distribution function weakly converges to standard Gaussian distribution, i.e., to a zero-mean Gaussian variable with the same variance as X_i. CLT theoretically justifies the appearance of Gaussian statistics in real life. Furthermore, to understand CLT, an informal description is stated as follows: if the sample size of data under consideration contains at least 30 independent observations and is lightly *skewed*, then distribution can be well approximated by Gaussian distribution, i.e., all the parametric procedures and statistical procedures, designed for Gaussian distribution can be applied. Nevertheless, on

Table 2.2 Statistics of Gaussian distribution

Notation	$\mathcal{N}(\mu, \sigma^2)$
Range of Parameters	$-\infty < \mu < \infty; \sigma > 0$
PDF	$\frac{1}{\sqrt{2\pi}\sigma} e^{-(x-\mu)^2/2\sigma^2}$
CDF	$\frac{1}{2}\left(1 + erf\left(\frac{(x-\mu)}{2\sigma^2}\right)\right)$
First moment; *mean*	μ
Second moment; *variance*	σ^2
Third moment; *skewness*	0
Fourth moment; k*urtosis*	3

Here $erf(x)$ is the Gauss error function given by $\frac{2}{\sqrt{\pi}}\int_0^x e^{-t^2}$

carefully examining CLT, following constraints are observed, leading to second, third, and fourth assumptions as follows:

Second assumption: *Independent and identical distribution (i.i.d.)*

Third assumption: *finite variance*

Fourth assumption: *lightly skewed*

Furthermore, some questions were brought up in practical applications for analyzing real-time data, like "*what if variables have non-identical distribution*?" "*what if variables possess infinite variance?*" Hence, the generalized central limit theorem (GCLT) was devised to address the ***second*** and ***third*** assumptions. For the ***fourth assumption***, i.e., modeling skewed data, α-stable distribution was used as they are used to describe data with a heavy-tailed nature.

Lastly, in light of the deficiencies observed in CLT and with subsequent introduction of GCLT, α-stable distribution emerges as a crucial tool in the field of FoSP. It incorporates the necessary characteristics to model heavy-tailed distributions.

2.3.2 Introduction to First FoSP tool—α-Stable Distribution

With the need to characterize impulsive phenomenon, an important class of non-gaussian distributions — α-stable distribution [49], was introduced by Levy [102] in 1925 and later rigorously studied by various researchers [103, 104, 105]. These are heavy-tailed distributions widely used for modeling impulsive phenomena. α-stable distribution family is the generalization of Gaussian distribution with infinite variance and heavy tail. The following sections illustrate basic definitions and features of this distribution.

2.3.2.1 Definition of α-Stable Distribution

α-stable random variable is represented by a characteristic function due to a lack of closed-form expressions of its probability density functions (PDF). Mathematically represented by (2.7) and denoted by $S(\alpha, \beta, \gamma, \delta)$, where; α is characteristic exponent (also known as stability parameter); measuring *thickness* of tails, β is symmetry parameter; measuring skewness, γ is scale parameter; measuring dispersion and δ is location parameter. For a random variable x, characteristic function $\theta(t)$ of a univariate stable distribution function $F(x)$ has the form [49]

$$\theta(t) = \begin{cases} \exp\left\{j\delta t - \gamma|t|^{\alpha}\left[1 + j\beta sgn(t)\tan\frac{\alpha\pi}{2}\right]\right\}, if\ \alpha \neq 1 \\ \exp\left\{j\delta t - \gamma|t|^{\alpha}\left[1 + j\beta sgn(t)\frac{2}{\pi}\log|t|\right]\right\}, if\ \alpha = 1 \end{cases} \quad (2.7)$$

where the symbol $j^2 = 1$, 't' corresponds to the continuous variable of time and sgn is signum function given by

$$sgn(t) = \begin{cases} 1, if\ t > 0 \\ 0, if\ t = 0 \\ -1, if\ t < 0 \end{cases} \quad (2.8)$$

and the four parameters are conformed in range

$$0 < \alpha \leq 2, -1 \leq \beta \leq 1, \gamma > 0 \text{ and } -\infty < \delta < \infty \quad (2.9)$$

Some of the distributions which belong to the family of α-stable distributions are reported in **Table 2.3**.

Furthermore, the impact of four α-stable distribution parameters on its PDF is demonstrated in **Figure 2.5** with variation in α, β, γ and δ shown in **Figure 2.5 (a)**, **(b)**, **(c)** and **(d)**, respectively.

- The change in α parameter contributes to "thickness" of tails in density function. As the value of α approaches zero, impulsive characteristic increases, i.e., tail becomes thicker and more data is centered around the central location. At $\alpha = 2$, the density curve corresponds to Gaussian distribution (for any γ, δ).
- The β factor is responsible for skewness of distribution. Negative values of β, make distribution skewed towards left side and positive values make distribution more concentrated towards the right side, with the center of the axis being at zero. This parameter helps understand heavy tail behavior.
- The scale factor γ is similar to variance of Gaussian distribution, and its value corresponds to the dispersion of distribution.
- The location parameter δ, decides shift and scale of α-stable distribution. Also, its value corresponds to mean for $1 < \alpha \leq 2$ and median for $0 < \alpha < 1$.

Table 2.3 Some special cases of α-stable distribution

Name	Notation	Closed-form expression
Standard α-stable distirbution	$S(2,\beta,1,0)$	Do-not exists
Symmetric α stable (SαS)	$S(\alpha,0,\gamma,\delta)$	Do-not exists
Gaussian distribution	$S(2,0,\gamma,\delta)$	Exists
Cauchy distribution	$S(1,0,\gamma,\delta)$	Exists
Levy stable distribution	$S\left(\frac{1}{2},1,\gamma,\delta\right)$	Exists
Pearson distribution	$S\left(\frac{1}{2},-1,\gamma,\delta\right)$	Exists

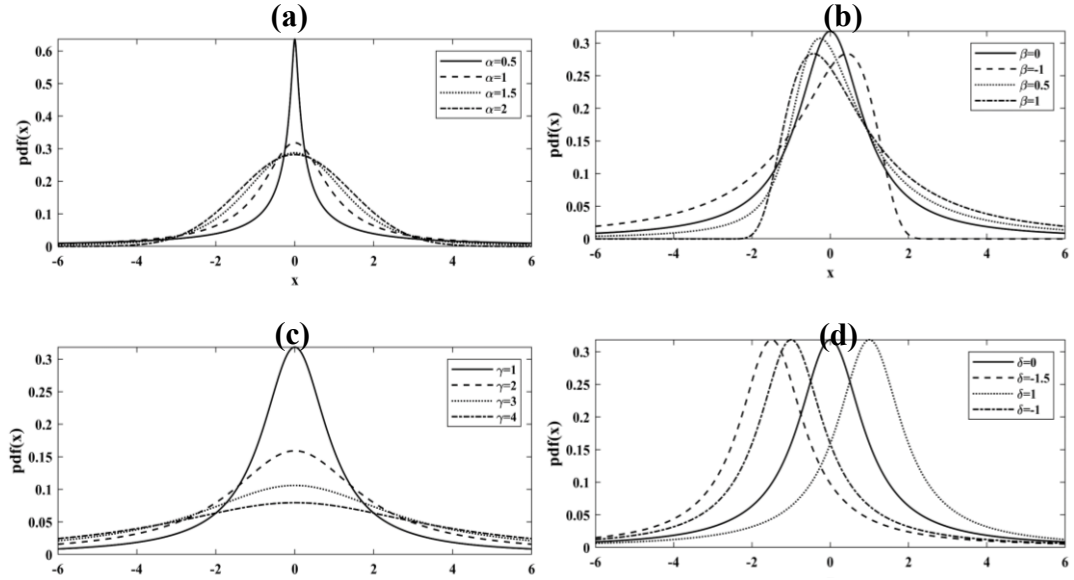

Figure 2.5 α-stable probability density function $S(\alpha,\beta,\gamma,\delta)$ at different values of α-stable distribution parameters **(a)** Density function of $S(\alpha,0,1,0)$ by varying α parameter, **(b)** Density function of $S(1,\beta,1,0)$ by varying by varying β parameter, **(c)** Density function of $S(1,0,\gamma,0)$ by varying γ parameter, **(d)** Density function of $S(1,0,1,\delta)$ varying δ parameter. Note: x is a random variable

2.3.2.2 Properties of α-Stable Distribution

The justification for using α-stable distributions is backed by two most important properties stated below [49].

i. **Stability Property:** A random variable Y is said to have stable distribution if and only if for all Y_1, Y_2 independent variables with the same distribution as Y and for arbitrary constants a_1, a_2, there are constants a and b such that:

$$a_1 Y_1 + a_2 Y_2 \stackrel{d}{=} aY + b \tag{2.10}$$

where $X \stackrel{d}{=} Z$ signifies both X and Z have the same distributions [49] .

ii. **Generalized Central Limit Theorem (GCLT)**: For a sequence $\{Y_i\}$ of independent and identically distributed (i.i.d) random variables, the necessary and sufficient condition for Y to be the limit of distribution having form

$$S_n = \frac{1}{a_n}\left(\sum_{i=1}^{n} Y_i - b_n\right);\ i = 1,2,\cdots n,\ n \in \mathbb{Z},\ a_n \in \mathbb{R}^+ \text{ and } b_n \in \mathbb{R} \tag{2.11}$$

is only if Y is a stable random variable. Here, if the i.i.d. Y_i's have finite variance, then the limit of distribution is Gaussian, as stated in Central Limit Theorem (CLT).

2.3.2.3 Features of α-Stable Distribution

The basic properties of α-stable distributions are detailed in [106]. However, for better understanding, some characteristics worth mentioning about α-stable distribution are listed below.

i. No closed-form expressions exist for α-stable distributions.
ii. α-stable distributions have algebraic tails and, therefore, are known to have thicker/heavier tails than Gaussian distributions, characterized by exponential tails.
iii. For α-stable distributions, the *mean* only exists for $\alpha > 1$; and is zero for $\alpha \in (1,2)$
iv. For α-stable distributions, except for the limiting case $\alpha = 2$ (Gaussian case), all have infinite variance.
v. Higher-order moments do not exist for α-stable distributions and for $1 < \alpha < 2$, fractional lower-order moments (FLOMs) of order p are defined with $p < \alpha$. For details on FLOMs, refer [49] .

2.3.2.4 Parameter Estimation Tests

Accurate estimation of parameters is the key to signal modeling. Parameter estimation is one of the best ways to check if chosen model is the "best fit" for underlying signal data.

Unfortunately for α-stable distributions, conventional methods in statistics are not used for parameter estimation due to lack of proper closed-form density functions (which only exist for stable distributions –Gaussian, Cauchy, Levy and Pearson distribution). As this distribution includes Gaussian distribution as its special case, therefore these tests hold for both α-stable distribution and Gaussian distribution. Some widely used parameter estimation methods for α-stable distributions fall into four categories:

a) Quantile methods based on order statistics- Based on the quantiles of distribution, this method was introduced by Fama and Roll [107] and was extended by McCulloch [108] to estimate all four parameters for cases where $\alpha \in [0.6,2]$.
b) Empirical Characteristic function (ECF) method- Koutrouvelis [109] developed a method to estimate the sample's characteristic function using Koutrouvelis's regression-type method. Later, Kogon and Williams [110] presented a Fourier-based method to estimate the ECF.
c) Logarithmic moments method- As statistical moments $E[|.|^p]$of stable distributions only exist for $p < \alpha$ (where α is characteristic exponent); therefore, FLOMs were introduced by Nikias [111] in 1995 for symmetric stable distributions. Later, challenges in the computation of gamma function and inversion of Sinc function for FLOM were eliminated by introducing Logarithmic moments [101]. This method is based on computing the differentiation with respect to order p.
d) Maximum Likelihood method- This method is based on maximizing the log-likelihood function by numerically estimating stable PDF. Estimation of stable PDF is performed using fast Fourier transform (FFT) or the method given by Nolan [112].

In the presented work, *parameter estimation tests* given by McCllouch [108] and Kogon and Williams [110] will be utilized to estimate the parameters of considered data.

2.3.2.5 Applications of α-Stable Distribution Model

By considering the improvements attained by incorporating models that can analyze real-time phenomena, α-stable distribution model has contributed to various domains listed below.

Seismic signal processing

Yue *et al.* [113] studied statistical characteristics of seismic traces and concluded that the distribution of real seismic traces should be heavy-tailed and asymmetric. QQ plots and

sample variance experiments were used to illustrate this. Following this assumption, the Kogon–Williams characteristic estimation method was applied to estimate the α-stable distribution parameters from seismic traces.

Wireless communication

Chen *et al*. [114] *proposed* the design of new detectors based on SαS distribution, which outperformed existing detectors, giving improved accuracy for wireless sensing systems.

Powerline communication

Sanchez *et al*. [115] presented the application of α-stable model to synthesize noise in power-line. The motivation behind this model is the evidence obtained from statistical properties of marginal distribution of noise found in power-line communication systems.

Image processing

Sadreazami *et al*. [116] *proposed* a new image-denoising method in contourlet domain using α-stable family of distributions. Denoising in the transformed domain improves performance at recovering signals from noisy data. Therefore, contourlet coefficients, which have proven to be highly non-Gaussian with heavy tails, are modeled using α-stable distribution. The results show a high peak SNR and improved visual quality of denoised images.

EEG signal processing

Wang *et al*. [117] analyzed the effect of α-stable distribution in noise suppression for seizure detection from scalp EEG. Due to the heavy tails and asymmetric properties of α-stable distribution, it is a powerful tool in modeling impulsive noises in EEG, which usually cannot be handled by the Gaussian distribution. The method's superiority is proved by testing the *proposed* method with the existing approaches. Results demonstrate a better detection rate and less false alarms.

ECG signal processing

Talbi *et al.* [118] developed an α-stable based parametric modeling method for the application of ECG compression. This attempt outperformed in terms of providing a better-quality compressed signal compared to existing modeling methods like Gaussian wavelet-based models.

Pander [119] described modeling of muscle noise using α-stable distribution and suggested the use of a nonlinear filter for its removal, owing to the impulsive characteristics of muscle noise.

Hamlili *et al.* [120] examined the effect of various impulsive noise models, including α-stable distribution and concluded that regardless of filtering, α-stable distribution noise model has the most adverse effect on ECG signals.

Yu *et al.* [121] incorporated α-stable distribution model to analyze the bearing faults. Also, a new statistical measure was reported to measure the non-Gaussian characteristics of bearing faults, and based on obtained results, it was concluded that, owing to the impulsive nature of bearing faults, α-stable distribution-based models offer better performance.

Classification

Luan *et al*. [122] *proposed* a classification feature by considering α-stable distribution for statistical modeling of noise, which resulted in providing robust performance in impulsive noise environments.

2.3.3 Introduction to Second FoSP tool—Fractional Fourier Transform (FrFT)

FrFT is a useful tool for analyzing time-varying signals and LRD signals since it is both practically and mathematically more versatile. FrFT, as the extended concept of Fourier transform (FT) offered immense significance in all domains and applications that utilized FT. It has been applied in several areas of signal and image processing [123, 124, 125, 126, 127] and has served as the foundation of multiple tools, such as fractional correlation, fractional power spectrum, and fractional convolution [27, 128].

Initially discovered as an idea of fractional power of Fourier operator by Codon [codon] and Namias in solving mathematical problems in 1929, FrFT was reintroduced as a tool related to quantum mechanics and optics by Namias and Ozaktas [28, 123] in 1980s. Subsequently, it has received significant attention from the research community for examining its properties and applications, resulting in notable developments in the disciplines of fractional calculus, signal processing and imaging processing [29].

2.3.3.1 Definition of FrFT

FrFT is a unitary transform that maps signal representation to an intermediate domain between time and frequency by varying fractional rotation parameter φ related to fractional order parameter a by $\varphi = a\pi/2$. FrFT of a signal $x(t)$ and its inverse is mathematically defined by the following expressions [123, 127]:

$$X^{\varphi}(u_{\varphi}) = \mathcal{F}_{\mathcal{F}}^{\varphi}[x(t)] = \int_{-\infty}^{\infty} K_a(t, u_{\varphi}) x(t) dt \tag{2.12}$$

$$x(t) = \int_{-\infty}^{\infty} K_{-a}(t, u_{\varphi}) X^{\varphi}(u_{\varphi}) du_{\varphi} \tag{2.13}$$

where $0 < |a| < 2$ and $\mathcal{F}_{\mathcal{F}}^{\varphi}(\cdot)$ denotes FrFT operator. Also, u_{φ} denotes fractional Fourier frequency and $K_a(t, u_{\varphi})$ is FrFT kernel. The transform kernel is defined by the following equation [127]:

$$K_a(t,u_{\varphi}) = \begin{cases} \sqrt{\dfrac{1-j\cot\varphi}{2\pi}}\, exp\left[j\left(\dfrac{t^2+{u_{\varphi}}^2}{2}\right)\cot\varphi - ju_{\varphi}t\ \csc\varphi\right], & \varphi \neq n\pi \\ \delta(t-u_{\varphi}) & if\ \varphi = 2n\pi \\ \delta(t+u_{\varphi}) & if\ \varphi+\pi = 2n\pi \end{cases} \tag{2.14}$$

which coincides with FT kernel at $a = 1$ i.e., for $\varphi = \pi/2$.

2.3.3.2 Properties of FrFT Kernel

FrFT is also defined as the decomposition of signal in terms of chirp signals, which are orthogonal basis functions analogous to sinusoids in the context of FT. However, on analyzing FrFT definition in (2.12), the following characteristics are observed:

i. It can be ascertained FrFT kernel is responsible for decomposition of a signal as chirp signals.
ii. FrFT kernel is composed of a time shift and phase factor along with a fixed sweep rate $\frac{1}{2}\cot\varphi$, such that:

$$K_a(t,u_{\varphi}) = e^{-j\frac{u_{\varphi}^2}{2}\tan\varphi}\, K_a(t-u_{\varphi}\csc\varphi\,, 0) \tag{2.15}$$

Furthermore, the beauty of FrFT kernel lies in the following properties:

i. Symmetry

$$K_a(t,u_{\varphi}) = K_a(u_{\varphi},t) \tag{2.16}$$

ii. Unitary

$$K_a^{-1}(t,u_{\varphi}) = K_{-a}(t,u_{\varphi}) = K_a^{*}(t,u_{\varphi}) \tag{2.17}$$

where $(.)^{*}$ is the complex conjugate denoting Hermitian conjugation.

iii. Orthogonal

$$\int_{-\infty}^{\infty} K_a(t,u_{\varphi})K_a(t,v_{\varphi})dt = \delta(u_{\varphi}-v_{\varphi}) \tag{2.18}$$

iv. Additive

$$\int_{-\infty}^{\infty} K_a(t,u_{\varphi})K_b(m,u_{\varphi})du_{\varphi} = K_{a+b}(t,m) \tag{2.19}$$

2.3.3.3 Discrete Fractional Fourier Transform (DFrFT)

The potential applications of FrFT in fields of science and engineering has led to a demand for its practical implementation. Due to the quadratic exponential kernel and integration

operator in the mathematics of FrFT, it was impractical to compute it because of the significant memory demands, computational time and numerical inaccuracies. As a result, researchers have periodically *proposed* methods for the discrete version of FrFT.

To effectively capture the essence of continuous FrFT, a discrete version of FrFT must meet the following requirements.

i. The closest approximation to continuous FrFT
ii. Boundary condition, i.e., at a=1 corresponding to $\varphi = \pi/2$, discrete FrFT must be reduced to a discrete Fourier transform (DFT).
iii. Unitary property
iv. Additivity of index

Several definitions have been documented in literature for digital computation of FrFT and they can be grouped into six types namely: sampling-type DFrFTs [129, 130], group theory type DFrFTs [131], eigenvector decomposition type DFrFTs [132, 133], quadratic phase transform-type DFrFTs [134, 135], chirp-Z transform-type DFrFTs [136] and linear combination-type DFrFTs [137, 138, 139].

Additionally, a thorough examination of the literature on DFrFTs has revealed that sampling-type and eigenvalue decomposition-type DFrFTs are most often employed based on their closest resemblance to the abovementioned properties [140]. Furthermore, upon reviewing these two definitions, it is found that eigenvalue decomposition-type DFrFTs have higher computation requirements and lack closed-form expressions. Therefore, the sampling-type DFrFT given by Pei *et al.* [89] will be utilized for the presented work.

2.3.3.4 Applications of FrFT

FrFT is a powerful mathematical tool due to its ability to rotate the time-frequency plane. This distinct advantage has resulted in its use across various fields, including but not limited to filtering, signal reconstruction, feature extraction, pattern recognition, and image encryption. This section discusses the applications of FrFT which have significantly contributed to *proposing* tools from the thesis perspective.

FrFT as a time-frequency (TF) tool

TF representations provide an intuitive way to analyze signals simultaneously in time and frequency domains. Upon reviewing the basic definition of FT, signal's FT can be regarded as rotation of $\pi/2$ in a counterclockwise direction by an integer order operator $\mathbb{F}$. Also, repeated applications of $\mathbb{F}$ results in the following transformations across the TF plane, i.e.,

i. Rotation by zero will correspond to the identity operator, i.e., $\mathbb{F}^0 = \mathbb{I}$

ii. Rotation by $\pi/2$, results in FT, i.e., $\mathbb{F}^{\frac{\pi}{2}} = \mathbb{F}$

iii. Successive rotations by angle ϑ_1 and ϑ_2 are equivalent to a single rotation ϑ_1+ϑ_2 i.e., $\mathbb{F}^{\vartheta_1} + \mathbb{F}^{\vartheta_2} = \mathbb{F}^{\vartheta_1+\vartheta_2}$

iv. Rotation by 2π corresponds to the identity operator again, i.e., $\mathbb{F}^{2\pi} = \mathbb{I}$

Similarly, FrFT can be regarded as rotation by a non-integer number a, which results in representing signal across a fractional axis given by u_φ and v_φ, making an angle $\varphi = a\pi/2$ with time and frequency axes, respectively, as shown in **Figure 2.6**.

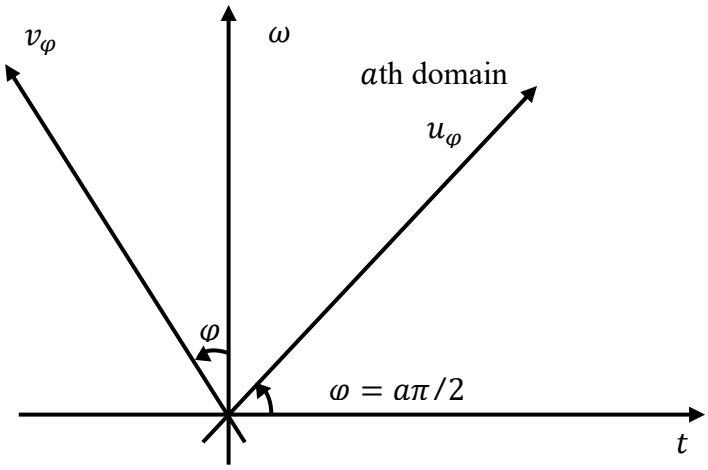

Figure 2.6 Time fractional-frequency plane

This interpretation of FrFT has resulted in its association with several TF tools like Wigner Distribution (WD) and Short-time Fourier transform (STFT). The equivalence between rotating the TF plane is obtained using WD or STFT in a clockwise direction by $\varphi = a\pi/2$ corresponds to performing FrFT [44], resulting in following relation between (t, f) and (u_φ, v_φ) coordinates

$$\begin{bmatrix} u_\varphi \\ v_\varphi \end{bmatrix} = \begin{bmatrix} \cos\varphi & \sin\varphi \\ -\sin\varphi & \cos\varphi \end{bmatrix} \begin{bmatrix} t \\ f \end{bmatrix} \tag{2.20}$$

Furthermore, FrFT is also interpreted as TF transform with chirp as a basis function, thus establishing the relationship between FrFT and chirp transform. Additionally, this link has been further extended by resulting in a relation between wavelet transform (WT) and FrFT, where the chirp function is used as wavelet transform kernel [141, 142].

All these connections of FrFT have resulted in the development of fractional Fourier domain [141, 142], eventually resulting in extensions of convolution, compaction, filtering

and multiplexing in a fractional domain. These extensions have been successfully employed in the arenas of filter design [45, 127, 143, 144], compression [145, 146], and multiplexing [147, 148] making FrFT one of the most valuable tools in signal and image processing.

In addition to being recognized as a time-frequency tool and its connection with other well-known time-frequency tools, it has demonstrated adaptability in creating new tools, such as FrFT kernel-based time-frequency tools (explained in Section 2.4.2).

FrFT as a Feature-Extraction Tool

FrFT provides flexibility in terms of fractional rotation parameter φ, which eventually helps in analyzing different characteristics of signal and image under consideration. With an extension of correlation in the fractional domain [149], many applications involving a comparison between two signals (or image patterns) like matched filtering [124], pattern recognition [150] and object detection [151] have been improvised. Additionally, to facilitate classification, FrFT is employed to enhance the feature-extraction process [152, 153, 154, 155]. Also, FrFT has been utilized to achieve variation in window function parameters, which further proves advantageous in practical applications such as image compressions [125, 145].

Finally, applications mentioned above served as inspiration for the presented work, which resulted in adopting FrFT kernel-based TF for processing ECG signals in Chapter 3. The design of novel SE is backed up by applying FrFT as a feature-extracting tool. Lastly, in Chapter 6, a novel tool known as FLO-FrST, which is constructed upon FrFT and FLOS, is formulated.

2.4 Concept of Time-Frequency (TF) Tools

TF tools are fundamental block of Time-Frequency Signal Analysis and Processing (TFSAP) field, with diverse applications spanning various domains such as biomedical, finance, engineering, and physics. In recent decades, TF tools have garnered significant attention from researchers globally and evolved as an essential component for devising advanced solutions for real-world problems.

This section is segregated into three parts aimed at offering a concise overview of TF tools, followed by a description of prevalent TF tools and applications of TF tools.

2.4.1 Overview of TF Tools

Time-domain and frequency-domain representations of a signal are two classical methods that offer insights into different aspects of signal. The time-domain representation provides information about signal's temporal characteristics, such as its start, end, and strength over time. On the other hand, frequency-domain representation reveals various frequencies present in the signal, including their magnitudes. However, for signals with time-varying spectral content (non-stationary signals), these representations do not provide simultaneous information about both aspects. For example, the magnitude spectrum created by representing signal in frequency domain merely reveals the frequencies present in signal. However, it does not provide any information about the specific times when these frequencies occur.

Therefore, the concept of time-frequency (TF) representation was introduced to provide simultaneous localization of time and frequency components and efficiently analyze and process non-stationary signals. This section briefly describes the fundamental concepts that are essential for comprehending the realm of TF tools.

2.4.1.1 Non-Stationary Signals

A non-stationary signal is one whose statistical structure varies with time. For example, the mean, variance, correlation (covariance) etc., change as time passes. For a stationary signal $s(t)$, whose power spectrum defined by (2.21) is independent of time and autocorrelation $r(\tau) = \mathrm{E}[x(t+\tau)x(t)]$ is sufficient to describe the statistical properties of signal $s(t)$ [156].

$$S(\omega) = \int_{-\infty}^{\infty} r(\tau) e^{-j\omega\tau} d\tau \tag{2.21}$$

In contrast for non-stationary signals, spectral properties change with time; hence, for analyzing such signals, time-dependent power spectrum representation is needed, which is achieved using TF tools.

2.4.1.2 Shortcomings of Fourier Transform (FT)

FT is the most popular transform for stationary signals, offering time-independent power spectra. It provides a comprehensive description of frequency components prevalent in a signal. However, the disadvantage of classical representations in both time and frequency domains is their lack of localization concerning the excluded variable (t or ω). The inadequacy of FT is outlined in points below [37]:

i. The magnitude spectrum indicates frequencies within the signal but does not provide information about the specific timing of those frequencies.
ii. It is unsuitable for depicting abrupt changes or sharp angles, as it requires many Fourier components to represent such discontinuities accurately.
iii. Inability to localize time and frequency together.
iv. Not effective in analyzing time-varying signals and non-stationary signals.

Furthermore, analyzing a signal's frequency content has been invaluable in many different applications, making Fourier transform (FT) an important tool for signal analysis. However, need to analyze problems in real time that involve changing characteristics led to the development of TF tools.

2.4.1.3 Uncertainty Principle

The uncertainty principle, originating from quantum mechanics and established by Heisenberg in 1927, asserts the impossibility of accurately determining both position and momentum of a particle simultaneously [157]. Subsequently, Gabor expanded this idea to signal and information theory in 1940s [158] and ever since it has also been known as the Heisenberg-Gabor uncertainty principle in signal processing.

Additionally, within the context of signal processing, this principle states that it is impossible to localize signal $x_s(t)$ and its Fourier transform (FT) $X_s(\omega)$. If a signal is limited to an interval length of Δt and its FT is bandlimited by $\Delta\omega$, then [159]:

$$\Delta t\, \Delta\omega \geq \frac{1}{2} \tag{2.22}$$

However, Leon in [32] explained that Δ should be understood as standard deviation. Therefore, another interpretation of abovementioned equation is that if Δt is the standard deviation of time marginal represented as T^2 and $\Delta\omega$ is the standard deviation of frequency marginal, denoted as B^2, given by [32]

$$T^2 = \sigma_t^2 = \int (t - \langle t \rangle)^2 |x_s(t)|^2 dt \tag{2.23}$$

$$B^2 = \sigma_\omega^2 = \int (\omega - \langle \omega \rangle)^2 |X_s(\omega)|^2 d\omega \tag{2.24}$$

Then (2.22) is modified as

$$\sigma_t^2 \sigma_\omega^2 \geq \frac{1}{4} \tag{2.25}$$

or equivalently

$$TB \geq \frac{1}{2} \tag{2.26}$$

This presents the idea of *time-bandwidth product* (TBP), calculated by multiplying a signal's bandwidth by its duration [37]. TBP is an alternative explanation of the uncertainty principle that helps comprehend a crucial aspect of TFD, namely *resolution*. TBP quantifies the trade-off between time and frequency resolution and establishes a threshold for the minimum level of TF resolution required for signal analysis. To achieve good resolution in both time and frequency domains simultaneously, TBP should be minimized in an ideal scenario.

2.4.2 Preliminaries of TF Tools

Over the past few decades, concept of time-frequency analysis has taken a big leap, and various tools have been developed. Owing to their fundamental characteristic of simultaneously distributing signal energy over both time and frequency, TF tools offer better interpretation of information. This is why TF tools are also referred to as time-frequency distributions (TFDs) or time-frequency representations (TFRs). To familiarize with established TF tools from a thesis point of view, established TF tools are grouped into three parts: TF tools based on Fourier kernel, TF tools based on FrFT kernel, and TF tools based on fractional lower order statistics (FLOS). Furthermore, every group is accompanied by a description of TF tools, which are important from the thesis perspective for better understanding.

2.4.2.1 Group I: TF Tools based on Fourier Kernel

As the name suggests, TF tools employ the Fourier kernel. To delve deeper, it can be said that, as Fourier analysis deals with decomposing signal into orthogonal basis function, i.e., sines and cosines, on the same front, when this concept is amalgamated with TF tools, signal decomposition is attained using *TF atoms* localizing signal in time and frequency domains. Furthermore, TF tools in this group are the primitive tools that were initially developed since the concept of TF tools was first formulated in 1940s. The tools that are part of this group are STFT, CWT, WVD, and ST. Additionally, as per rich literature these tools belong to the category of linear (STFT, CWT and ST) and quadratic (WVD) methods. A description of the tools is listed below:

i. **Short-time Fourier transform (STFT)**: Also called windowed Fourier transform, STFT performs Fourier transform on the overlapping or non-overlapping signal

segments and then combines results to obtain TF representation. These are mathematically represented as [160] :

$$STFT(\tau,\omega) = \int_{-\infty}^{\infty} x_s(t) w(t-\tau) e^{-j\omega t} dt \tag{2.27}$$

where $x_s(\tau)$ is signal, $w(\tau - t)$ is window function, which is multiplied with segment of the signal under consideration.

STFT employs a window function to segment the signal. Based on this, literature has reported many variants of STFT, where different windows like rectangular, triangular, Hanning, Kaiser, etc., are employed for localizing signals in the time-frequency plane [161].

Additionally, STFT is governed by the uncertainty principle. Therefore, its performance is limited by the trade-off between time and frequency, which was removed by introduction of the Gabor transform which introduced Gaussian window function [158] for STFT formulation.

ii. **Continuous Wavelet transform (CWT)**: Instead of using a Fourier kernel, CWT localizes time and frequency domain by applying a wavelet-based signal decomposition technique. It is mathematically represented as [37, 160]:

$$WT(a,b) = \int_{-\infty}^{\infty} x_s(t) \frac{1}{\sqrt{a}} \Psi^* \left(\frac{t-b}{a}\right) dt \tag{2.28}$$

where $x_s(\tau)$ is signal, $\Psi^* \left(\frac{t-b}{a}\right)$ is a wavelet function with location parameter b and scale parameter a.

CWT offers variable TF resolution as it employs different wavelet scales for analyzing different frequencies of signals. They perform better than the previously discussed STFT tool, whose fixed resolution limits its performance.

iii. **Wigner-Ville Distribution (WVD)**: They employ the autocorrelation function of signal to form TF representation. The mathematical formulation of WVD is given as [160]:

$$WVD(t,\omega) = \int_{-\infty}^{\infty} x_s\left(t+\frac{\tau}{2}\right) x_s^*\left(t-\frac{\tau}{2}\right) e^{-j\omega\tau} d\tau \tag{2.29}$$

Additionally, literature has reported that the mathematical formulation of WVD can be seen as FT of a time-varying signal kernel [37]. Wigner distribution was initially introduced in quantum mechanics and later introduced for signal analysis by Ville

in 1960s; therefore, it is referred to as Wigner-Ville distribution. It is better than STFT and CWT in capturing the time-varying nature of signal, but cross-terms hinder its effectiveness.

iv. **Stockwell transform (ST)**: It is a time-frequency analysis tool that combines the properties of STFT and CWT. It was established by Stockwell in 1996 [162]. ST provides resolution dependent on frequency, sustaining a direct relationship with Fourier spectrum. It is an extension of the idea of STFT and is based on a moving and scalable Gaussian window. So far, it has been the most powerful Joint Time-Frequency Analysis (JTFA) tool. Mathematically, ST of a signal is defined as [162, 163]:

$$S(\tau, f) = \frac{|f|}{\sqrt{2\pi}} \int_{-\infty}^{+\infty} x_s(t) e^{\frac{-(t-\tau)^2 f^2}{2}} e^{-j2\pi f t} dt \tag{2.30}$$

where $x_s(t)$ is signal of interest, f is signal frequency, τ is window's function controlling parameter, which decides the position of Gaussian window on time axis t.

2.4.2.2 Group II: TF tools based on FrFT Kernel

Since FrFT is the generalization of conventional FT, tools in this group are the generalization of conventional tools formed by replacing FT kernel with FrFT kernel [164]. This amalgamation of FrFT with TF tools has improved their concentration.

i. **Short-time fractional Fourier transform (STFrFT)**: This tool is developed by using STFT of signal with fractional Fourier transformed window and is mathematically given by [165]:

$$STFrFT(\tau, u_\varphi) = \int_{-\infty}^{+\infty} x_s(\tau) w(\tau - t) K_a(t, u_\varphi) d\tau \tag{2.31}$$

where $x_s(\tau)$ is signal, $w(\tau - t)$ is window function and $K_a(t, u_\varphi)$ is FrFT kernel. It was introduced to analyze multicomponent and non-chirp signals.

ii. **Fractional wavelet transform (FrWT)**: It is the generalization of traditional CWT, which introduces non-integer translations and dilations of the wavelet by adding fractional parameter φ. Mathematically represented as [46]:

$$\mathrm{Fr}WT(a, b) = \frac{1}{\sqrt{a}} \int_{-\infty}^{\infty} X_s^{\varphi}(u_\varphi) \Psi^* \left(\frac{u_\varphi - b}{a}\right) du_\varphi \tag{2.32}$$

where $X_s^{\varphi}(u_\varphi)$ is FrFT of $x_s(t)$, which is computed by (2.12).

iii. **Fractional Stockwell transform (FrST)**: It is the latest time-fractional frequency analysis tool, which adopts FrFT kernel instead of the Fourier kernel as in existing time-frequency transforms. FrST is simply the extension of ST from time-frequency domain to a time-fractional frequency domain.

For a signal $x(t)$, an a^{th} order FrST is defined and its inverse is defined as [47]:

$$FrST_x^a(\tau, u_\varphi) = \int_{-\infty}^{+\infty} x_s(t) g(\tau - t, u_\varphi) K_a(t, u_\varphi) dt \tag{2.33}$$

$$x_s(t) = \int_{-\infty}^{+\infty} \left\{ \int_{-\infty}^{+\infty} FrST_x^a(\tau, u_\varphi) d\tau \right\} K_a^*(t, u_\varphi) du_\varphi \tag{2.34}$$

where $K_a(t, u_\varphi)$ is kernel function of FrFT, $g(\tau - t, u_\varphi)$ is a scalable Gaussian window function depending on time t and u_φ defined by [47]:

$$g(t, u_\varphi) = \frac{|u_\varphi \csc \varphi|^p}{\sqrt{2\pi} q} \exp\left(\frac{-t^2 (u_\varphi \csc \varphi)^{2p}}{2q^2} \right) \tag{2.35}$$

where p and q are window adjustment parameters that control window shape based on signal characteristics. The window function defined in (2.35) has its width proportional to fractional Fourier frequency u_φ, which makes FrST somewhat similar to ST. Thus, FrST has two window adjusting factors (p and q) controlling the resolution of Gaussian window and a fractional order parameter (a). Hence FrST is a multi-resolution fractional transform with three degrees of freedom, allowing for a more flexible operation.

2.4.2.3 Group III: TF Tools based on Fractional Lower-Order Statistics (FLOS)

These tools were an improvised version of Group I tools, designed to function effectively in non-gaussian environments as well. To explain further, for instance, the mathematical formulation of WVD involves the autocorrelation function, an essential operation within the category of second-order moments. When encountering impulsive noise, which is more accurately represented by a non-Gaussian α-stable distribution, the higher-order moments become unbounded, and second-order moments cease to exist. As a result, need to find alternatives grew, leading to the introduction of fractional lower-order statistics (FLOS), which is how the idea of fractional lower-order time-frequency representation (FLO-TFR) originated in the first place. Another possible explanation for the decline of TF tools in the presence of impulsive noise may be linked to the concept of linear space. TF tools are

frequently utilized for non-stationary signals that involve Gaussian processes, and it is established that linear space produced by Gaussian processes is a Hilbert space. However, when impulsive behavior arises, α-stable distribution is naturally involved. In this case, the linear space of the stable process is metric space for $\alpha \in (0,1)$ and Banach space when $\alpha \in [1, 2)$. Therefore, the inevitable introduction of non-linearity when addressing problems in Banach and metric space could cause TF degradation [49].

The concept of fractional lower-order covariance was introduced with the development of α-stable distribution in modeling impulsive phenomena in signal processing applications[49]. Furthermore, considering the limitations associated with obtaining unfavorable outcomes with TF tools when encountering impulsive noise, fractional lower-order covariance was employed in developing the fractional lower-order Wigner Ville distribution (FLO-WVD) [48]. Later, concept of detecting signals in unknown time-frequency / time-scale offset was extended to the case of impulsive noise for receivers [166]. The idea of FLO-WVD was extended with introduction of FLO polynomial WVD (FLO-PWVD) to address the problem of resolution in polynomial phase signals [167]. With the implementation of TF tools for analyzing mechanical faults [35], TF tools with FLOS concept were modified to analyze and process non-Gaussian impulsive behavior of bearing faults [35]. With the advantages of ST in providing good resolution in TF domain, fractional lower-order Stockwell transform (FLO-ST) was introduced in [168] with its application in filtering for machine fault diagnosis. For the analysis of drive end accelerometer in α-stable distribution noise environment, linear chirplet transform (LCT) was combined with FLOS [169, 170]. Apart from design modifications resulting in various FLO-TFDs, spectrum methods based on α-stable statistical tools [171, 172, 173] and applications in spectrum sensing were also introduced [174].

A brief description of some tools belonging to this group, which are important from a thesis perspective, are described below:

i. **Fractional lower-order short-time Fourier transform (FLO-STFT)**: This variant was introduced to improve the performance of STFT in α-stable distribution noise environment. It is defined as [175]:

$$FLO - STFT(\tau, \omega) = \int_{-\infty}^{\infty} x_s^{\langle \rho \rangle}(t) w(t-\tau) e^{-j\omega t} dt \tag{2.36}$$

where $(.)^{\rho}$ is fractional lower-order operator with with $0 \leq \rho \leq 1$ and is defined as:

$$x_s^{<\rho>}(t) = \frac{|x_s(t)|^{\rho+1}}{x_s^*(t)} \tag{2.37}$$

ii. **Fractional lower-order Stockwell transform (FLO-ST)**: This modified variant improved the performance of ST for α-stable distribution environment. It is mathematically given by [168]:

$$FLO-ST(\tau,f) = \frac{|f|}{\sqrt{2\pi}} \int_{-\infty}^{+\infty} x_s^{\langle\rho\rangle}(t) e^{\frac{-(t-\tau)^2 f^2}{2}} e^{-j2\pi f t} dt \tag{2.38}$$

2.4.3 Applications of TF Tools

The undeniable success of TF tools in recent decades can be attributed to their wide-ranging applications. Their range of applications spans various disciplines in science and engineering, where they are utilized for a multitude of tasks, including but not limited to non-stationary signal processing and analysis, feature extraction, filtering, and data compression [37, 176].

The focus of this section is to outline the applications of the groups mentioned above.

Applications of Group I Tools: These tools are widely employed in the field of signal processing of seismic signals [33], biomedical signals [36, 160], vibration analysis [35], and speech and audio signals [37]. Furthermore, these tools are also incorporated with post-processing approaches [37, 177] like synchro-squeezing, synchro-extracting and reassignment to improve the energy concentration and reducing the cross terms as for the case of WVDs. These post-processing methods are widely employed in biomedical signals to improve the performance of intended application at hand [178]. Also, these tools have been utilized for feature extraction in machine learning applications in biomedical signals and deep learning, resulting in improved accuracy [179].

Applications of Group II tools: These tools are commonly used for analyzing time-varying signals and estimating spectra of signals that include noise due to the added benefit of having an extra fractional Fourier domain. With potential applications of these tools in seismic signal processing, detection, and estimation, their scope is limited to analyzing seismic signals and geophysics domain [45, 46, 47, 180, 181].

Applications of Group III tools: As mentioned before, the domain of these tools is strictly limited to mechanical fault signal analysis, where the bearing faults are known to encompass impulsive nature [50, 168, 174].

2.5 Statistical Tools

Statistical tools represent an extensive collection of analytical methods that enable the examination of many attributes of raw data, facilitating significant insights and conclusions. It includes methods such as data analysis, descriptive statistics, inferential statistics, regression analysis, and non-parametric tests. In the subsequent sections, statistical tests are illustrated to study the deviation of data from normality assumption, as it is key aspect when dealing with data in practical scenarios [182]. Here, tests are described to illustrate the deviation from normality and resemblance with α-stable distribution, which is *proposed* in the presented work. Four categories of statistical tests: visual inspection, statistical moments, parameter estimation, and hypothesis test are summarized below:

2.5.1 Tests based on Visual Inspection

This category includes simplest methods for identifying the characteristics of distribution based on their graphical representation. The tests used in *proposed* work are described below.

2.5.1.1 Histogram

It is a popular visualization tool in statistics and is based on graphical representation of the frequency of data under consideration. It reflects the shape of distribution, and for the normally distributed data, bell-shaped histogram is obtained. On the other hand, if the data representation is skewed (right or left), then distribution of data is asymmetric and has longer tails.

2.5.1.2 QQ plot

In this, quantiles of the sample dataset are plotted against theoretical quantiles obtained using the normal distribution. The points form a straight line if both follow the same distribution, and if departure is observed from the line, then it indicates the deviation from the normal distribution.

2.5.2 Statistical Moment Theory

The concept of moments in statistics plays a crucial role in describing distribution properties. Statistical moments are widely used in estimation theory and hypothesis testing [182, 183]. Generally, moments are defined by the expected value of a random variable and are denoted by $E[|.|^k]$, where $k \in \mathbb{Z}$. The most commonly used moments are:

2.5.2.1 *Mean*, the First Moment

It is a measure for finding the central position of distribution and is given by

$$\mu = \sum xP(X = x) \tag{2.39}$$

where x is a random variable, $P(X)$ represents PDF of x, and μ is the mean of distribution. Additionally, for a data series $\{d_i\}$, *mean* is calculated by:

$$\mu = \frac{1}{n}\sum_{i=1}^{n} d_i \tag{2.40}$$

To study and concur with this characteristic of α-stable distribution, the running mean method is also used for the computations in *proposed* work [101] which is mathematically computed as

$$Running\ mean, \bar{X}_n = \frac{1}{N-1}\sum_{s=1}^{n} X_s \tag{2.41}$$

where N are the total samples in distribution and X_s is the distribution samples at $s = 1, \cdots, N$.

2.5.2.2 *Variance*, the Second Moment about *Mean*

It is a measure of the spread of distribution about the mean value and is defined as

$$\sigma^2 = E((X - \mu)^2) \tag{2.42}$$

For data series, *variance* is given by:

$$\sigma^2 = \frac{1}{n}\sum_{i=1}^{n} (\mathrm{d_i} - \mu)^2 \tag{2.43}$$

For α-stable distributions, variance is finite at $\alpha = 2$ (Gaussian case) and has infinite variance at $\alpha < 2$. The running variance test is conducted on sample data to support this. If variance converges, the distribution follows Gaussian characteristics, and if variance diverges, the distribution falls in the non-Gaussian α-stable family of distributions. Mathematically, running variance is computed as [101]

$$Running\ Variance = \frac{1}{n-1}\sum_{s=1}^{n} (X_s - \bar{X}_n)^2 \tag{2.44}$$

where $\bar{X}_n$, is the running mean as computed in (2.41).

2.5.2.3 *Skewness*, the Third Moment

It is the symmetry measure used for identifying asymmetric distributions. Mathematically, the skewness of a distribution is represented as [184]

$$Skewness = E\left(\left(\frac{X-\mu}{\sigma}\right)^3\right) = \frac{E((X-\mu)^3)}{\sigma^3} \tag{2.45}$$

For data series, it is given by:

$$Skewness = \sqrt{\frac{1}{n}\sum_{i=1}^{n}\frac{(\mathrm{d_i}-\mu)^3}{\sigma}} \tag{2.46}$$

In the case of α-stable, distributions are mostly skewed due to the presence of outliers, and hence, skewness is a useful shape-based measure to identify the non-Gaussian α-stable distributions.

2.5.2.4 *Kurtosis*, the Fourth Moment

It calculates the amount of extreme data present in distribution and is mathematically given by [184]

$$Kurtosis = E\left(\left(\frac{X-\mu}{\sigma}\right)^4\right) = \frac{E\left((X-\mu)^4\right)}{\sigma^4} \tag{2.47}$$

And for data series, it is computed as:

$$Kurtosis = \sqrt{\frac{1}{n}\sum_{i=1}^{n}\frac{(\mathrm{d_i}-\mu)^3}{\sigma^2}} \tag{2.48}$$

Kurtosis is a measure to find the "*tailedness*" of distribution. The value for Gaussian distribution is 3; for non-Gaussian and heavy-tailed distributions, the value is either greater than 3 or the higher-order moments do not exist.

2.5.3 Non-Parametric Tests

Statistical tests are essential for analyzing data and making quantitative decisions. They are categorized into parametric and non-parametric tests. Parametric tests rely on specific assumptions relating to the independence of samples, normal distribution of underlying data, similarity to normal distribution, and equal variances among distributions. Moreover, when the underlying distribution deviates from a normal distribution, parameter tests are conducted following certain transformations, which researchers have noted can distort the results. Non-parametric tests are referred to as "distribution-free tests" because they require minimal assumptions about the data and were developed to address the issue of assumption violation present in parametric tests.

This section introduces non-parametric tests used to analyse data and determine the significance of α-stable distribution behaviour, which challenges the assumption of normality.

2.5.3.1 Chi-Square Goodness-of-Fit Test

The assumption of normality is an obvious concept with CLT. CLT straightforwardly implies that if the samples are more than 30, regardless of the actual shape of its distribution, it tends to follow the normal distribution. However, before relying on Gaussian assumption, it is important to ascertain the presence of outliers and check if a serious deviation from normality exists. Therefore, hypothesis tests must also be performed to assess the normality assumption [184].

In the presented work, *Chi-square goodness-of-fit* test will be performed on the random variables and noisy samples. Introduced by Snedecor and Cochran in 1989 [185], it tests the hypothesis if the given sample follows specific distribution.

For the Chi-Square test, the hypothesis used in *proposed* work is defined as:

Null hypothesis, H_o: The sample data follows *Normal* distribution.

Alternate hypothesis, H_A: The sample data do not follow *Normal* distribution.

Also, to perform this test, the sample data is divided into k bins and Chi-Square test statistic is computed as

$$\chi^2 = \sum_{i=1}^{k} (o_i - e_i)^2 / e_i \tag{2.49}$$

where, o_i and e_i represents the observed and expected frequency of i^{th} cell, χ^2 is the data sample with a distribution approximated as a Chi-Square distribution with k-1 degrees of freedom. For the significance level equal to a and critical value χ_a^2, the null hypothesis is accepted when $\chi^2 < \chi_a^2$, indicating a good fit. On the other hand, we reject the H_o in favor of H_A, when $\chi^2 > \chi_a^2$.

2.5.3.2 Kolmogorov-Smirnov (KS) Test

The Kolmogorov-Smirnov (KS) test is a distribution-free goodness-of-fit test. It is used to determine whether the given samples/ underlying probability distribution is similar to the hypothesized distribution based on quantification measure called KS statistic or D-statistic [186, 187]. KS test statistic value is computed as

$$KS\ test\ statistic = \max|F(X_i) - R(X_i)|, \forall\ i = 1,2,\cdots,N \tag{2.50}$$

where $F(X_i)$ is the computed eCDF of sample and $R(X_i)$ is the reference CDF.

There are two types of this test:

(i) One-sample KS test: It evaluates the difference between empirical cumulative distribution function (eCDF) of sample and CDF of any known continuous distribution as depicted in **Figure 2.7(a)**.

(ii) Two-sample KS test: It measures the difference between eCDF of the samples [188], as illustrated in **Figure 2.7 (b)**.

2.5.4 Wasserstein Distance

Wasserstein distance provides a special way to compare probability distributions. It originated from the concept of optimal transport problem [189, 190] and is also known as Earth Mover's Distance. It is widely employed as a statistical inference tool and goodness-of-fit tool in statistics. For comparing two distributions, this distance is measured as:

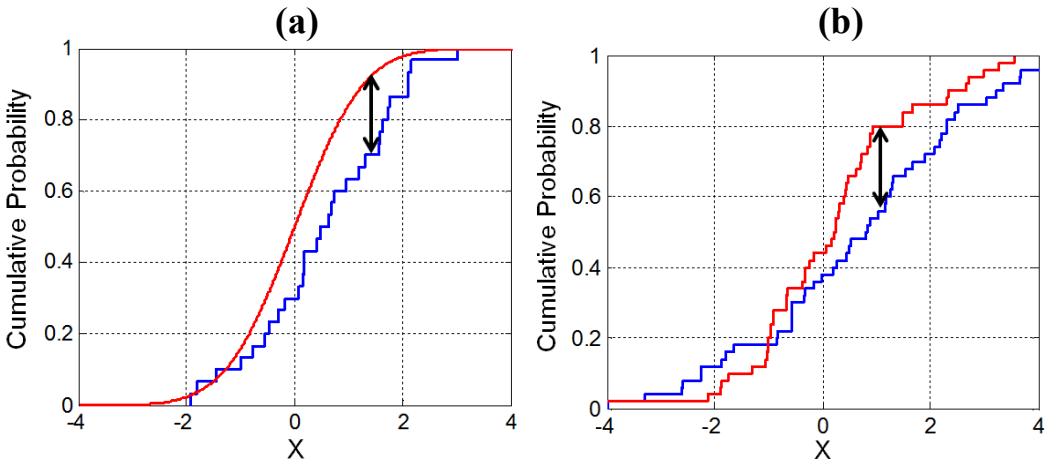

Figure 2.7 Illustration of Kolmogorov-Smirnov (KS) test, **(a)** One-sample KS test, *blue line* depicts eCDF of sample and *red line* depicts CDF of reference distribution and black arrow represents KS test statistic, **(b)** Two-sample KS test, *red and blue line* depicts eCDF of two samples and black arrow represents KS test statistic.

$$W_{dd} = \left(\frac{1}{n} \sum_{i=1}^{n} \| A(X_i) - B(X_i) \| \right)^{dd} \quad \forall\, i = 1,2,\cdots,N \tag{2.51}$$

where W_{dd} denotes dd-Wasserstein distance, $A(X_i)$ is the empirical distributions of underlying data, $B(X_i)$ is the distribution obtained using estimated parameters. For the present work, $dd = 1$ will be employed, i.e., 1-Wasserstein distance will be used to compare two distributions. Comparing the measure values for evaluating goodness-of-fit, one can ascertain that less value of W_{dd} will correspond to less distance and hence will signify better fit.

Furthermore, this distance is only defined for distributions with finite moments and therefore, for α-stable distribution W_{dd} is only defined for $1 \leq \alpha \leq 2$.

2.5.5 Statistical Distributions

Statistical distributions, commonly referred to as probability distributions, constitute important branches within the realm of statistics and probability theory. They are basically mathematical functions and offer valuable insights into the characteristics of a process. Various distributions that are suitable for modelling non-Gaussian processes have been documented in the literature. These distributions are specifically designed to handle outliers and exhibit heavier tails than the Gaussian distribution. This section provides an overview of the distribution models that will be employed in thesis.

2.5.5.1 Gaussian Mixture Distribution (GMD)

This distribution is composed of M number of multivariate Gaussian distributions. The PDF of GMD is given by [191] :

$$f_{GMD}(x) = \sum_{i=1}^{M} \pi_i \, \mathcal{N}\left(x; \mu_{GMD_i}, \mathrm{K}_{GMD_i}\right) \tag{2.52}$$

where π_i represents component proportion with constraint $\sum_{i=1}^{M} \pi_i = 1$, μ_{GMD_i} is the mean of i^{th} component, K_{GMD_i} is the covariance matrix and $\mathcal{N}\left(x; \mu_{GMD_i}, \mathrm{K}_{GMD_i}\right)$ is the density function of multivariate Gaussian distribution.

Even though this model is based on Gaussian distributions, GMDs can be tailored to capture the heavy-tailed nature of distribution. Based on the combination of multiple Gaussian distributions with different means and covariances, GMD tends to provide a good fit for heavy-tailed distribution. This distribution is widely employed in machine learning.

2.5.5.2 Generalized Gaussian Distribution GGD)

As the name depicts, this is a generalization of Gaussian distribution, which offers more flexibility than Gaussian distribution. The PDF of this distribution is defined with three parameters, namely location parameter μ_{GGD}, scale parameter α_{GGD} and shape parameter β_{GGD} is given by [192]:

$$f_{GGD}(x) = \frac{\beta_{GGD}}{2\alpha_{GGD}\Gamma\left(\frac{1}{\beta_{GGD}}\right)} e^{\left|\frac{-(x-\mu_{GGD})}{\alpha_{GGD}}\right|^{\beta_{GGD}}} \tag{2.53}$$

where, $-\infty < \mu_{GGD} < \infty$, $\alpha_{GGD} > 0$, $\beta_{GGD} > 0$ and $\Gamma(.)$ is gamma function.

Laplace distribution, Gaussian distribution and uniform distributions are the special cases of GGD at β_{GGD} =2, $\beta_{GGD} = 1$ and $\beta_{GGD} = \infty$, respectively.

GGDs are commonly used in various fields such as biomedical, machine learning, and economics to model data with non-Gaussian and heavy-tailed characteristics due to their flexible shape parameter compared to traditional Gaussian distributions [193].

2.5.5.3 t Location-Scale Distribution (tLSD)

This distribution belongs to the family of location-scale distributions and is used for modeling heavier tails. Mathematically, tLSD is defined as [194]:

$$f_{tLSD}(x) = \frac{\Gamma\left(\frac{\upsilon_{tLSD}+1}{2}\right)}{\sigma_{tLSD}\sqrt{\nu_{tLSD}\pi}\,\Gamma\left(\frac{\nu_{tLSD}}{2}\right)}\left[\frac{\nu_{tLSD} + \left(\frac{x-\mu_{tLSD}}{\sigma_{tLSD}}\right)^2}{\nu_{tLSD}}\right]^{-\left(\frac{\nu_{tLSD}+1}{2}\right)} \tag{2.54}$$

with location parameter μ lying in range $(-\infty, \infty)$, scale parameter $\sigma_{tLSD} > 0$, shape parameter $\nu_{tLSD} > 0$ and $\Gamma(.)$ is the gamma function.

This distribution is also referred to as nonstandard student t distribution, and with $\sigma_{tLSD} = 1$ and $\mu_{tLSD} = 0$, this distribution approaches student t distribution. Additionally, as the shape parameter $\nu_{tLSD} \to \infty$ this distribution approaches Gaussian distribution and for small values of ν_{tLSD} , heavy tails are achieved.

2.6 Dataset Description

Several benchmark databases are available at Physionet [123] to facilitate the analysis and evaluation of *proposed* methods. They provide a large collection of clinical and physiological data for an iterative improvisation of the *proposed* method. Since its establishment, every algorithm *proposed* for preprocessing, classification, etc., has been evaluated in its database. Hence, it serves as a standard comparison framework to validate performance with state-of-the-art literature methods.

To validate the methods *proposed* in this thesis, the following databases will be used in different chapters.

2.6.1 MIT-BIH Arrhythmia Database

One of the firstly established databases by Moody and Mark [195], collected from the Beth Israel Hospital Arrhythmia Laboratory, provides an exclusive set of ECGs obtained from analyzing 4000 long-term Holter recordings. Database referred to as the Massachusetts

Institute of Technology-Beth Israel Hospital (MIT-BIH) Arrhythmia Database contains 48 records of ECGs of length around 30 minutes, sampled at 360 Hz and 11-bit resolution over a 10mV range.

These 48 recordings (100 to 234) are grouped into two sets, with the first group (100-124, with 23 random records) providing a representative sample of waveforms and artifacts encountered in routine clinical use. The second group (200 to 234, with 25 selected records), containing abnormalities, illustrates variations in the morphology of QRS and various rhythmic features [196].

Additionally, this database contains various beat annotations, which help in describing certain events within the recording. The beat classes–N, S, V, F, Q described as normal beat (N), supraventricular ectopic beat (S), ventricular ectopic beat (V), fusion beat (F) and unknown beat (Q) containing information regarding unclassifiable beat, are among the five beat classes of Arrhythmia recommended by the American National Standards Institute (ANSI) and Association for Advancement of Medical Instrumentation (AAMI). The last four classes contain significant information regarding abnormalities; hence, their detection and classification is important for diagnostic purposes[197, 198, 199].

For example, record 104 from the first group contains a total of 2229 annotated beats with 163 normal beats of class N, 2 premature ventricular contraction (PVC) beats of class V, 1380 paced beats, and 18 unclassifiable beats of class Q and 666 fusion beats of class F. Record 208 from group second contains total of 2955 beats with 1586 normal beats of class N, 2 premature or ectopic supraventricular (SVPB) beats of class S, 992 PVC beats of class V, 373 fusion beats of class F and 2 unclassifiable beats of class Q.

In the context of research presented in this thesis, **Chapters 3** and **5** will utilize this database to assess the efficacy of methods *proposed* for denoising and QRS complex detection of ECG signals.

2.6.2 MIT-BIH Noise Stress Test Database

Created by Moody *et al*. [200], this database comprises two types of recordings. The first type includes 3 recordings of 30 minutes each, containing predominantly noises present in ambulatory ECG recordings. It consists of baseline wander (*bwm*), muscle artifact (*mam*), i.e., EMG artifact and electrode motion artifact (*emm*). The second type includes 12 recordings of 30 minutes created by adding a calibrated amount of electrode motion artifact, i.e., *emm* noise to ECG records 118 and 119 from MIT-BIH Arrhythmia database. These

noisy segments of these recordings have signal-to-noise ratios of -6, 0 6, 12, 18, and 24 dB [201].

This database will be used in **Chapters 3** and **4** to validate the performance of *proposed* denoising method and establish the presence of α-stable distribution noise characteristics in real-time noises, respectively.

2.6.3 European ST-T Database

Created by Taddei *et al*.[202], this database is employed for assessing the performance of algorithms for identifying morphological changes in ST segment and T-wave of ECG signals. The database has a total of 90 recordings, each lasting two hours. The recordings have a sampling frequency of 250Hz and a resolution of 12 bits, covering a range of 20mV. The recordings in this database have myocardial ischemia and show abnormalities depicting medication effects, ventricular dyskinesia and hypertension. Additionally, some excerpts indicate the instance of ST displacement and shifted T-wave [203].

This database will be referred in **Chapter 3** to establish the effectiveness of *proposed* denoising method and prove its versatility over different databases.

2.6.4 Motion Artifact Contaminated ECG Database

Designed by Behravan *et al*. [204], this database is employed to study the impact of physical activities on the ECG signal. It contains short-duration ECG signals of three types: standing, walking and single jump. With a sampling rate of 500Hz and 16-bit resolution, the database comprises of signals with 4000 samples [205].

This database will be used in **Chapter 4** to investigate the characteristics of motion artifacts affecting ECG signals.

2.6.5 Examples of Electromyograms Database

This database is composed to analyze the functionality of muscles and associated nerves. It helps measure muscular contractions, which can further help analyze the dysfunction in nerves and muscles. This database comprises three EMG signals obtained from three subjects with neurological disorders. The signals used in this database were recorded at a sampling rate of 50 kHz and then were down-sampled to 4 kHz [206].

This database will be used in **Chapter 4** to study the behavior of muscular artifacts (EMGs) in ECG signals,

2.6.6 CHB-MIT Scalp EEG Database

Worked upon by Ali Shoeb [207] as a part of his doctoral thesis, this database consists of EEG recordings with intractable seizures. It includes recordings from 24 subjects collected through 23 channels (some contain 24 or 26 channels) with a sampling rate of 256 Hz with 16-bit resolution. Combinedly, this database contributes to 198 excerpts of seizures [208]. This database will be employed in **Chapter 6** for the classification of interictal and preictal EEG.

2.7 Motivation

- The study and analysis of ECG signals are not limited to clinical and health care nowadays; they have also been used as a potential tool for designing biometric systems. Therefore, designing a model by replicating real-time scenarios could improve the performance of ECG-based devices.
- R-peak plays a vital role in diagnosing ECG signals. Also, literature has reported that features based on R-R intervals are most efficient and contribute to the classification. However, impulsive noise affects these the most and consecutively classification performance degrades. Therefore, analyzing the noise influencing ECG signals followed by its preprocessing are the two highly demanded processes to reduce false alarms, but they are often neglected.
- The conceptualization of designing SE with FrFT is to replicate the advantages of fractional-based filtering with improved computational efficiency. It is well known that MFs exhibit simple calculations based on minimum-maximum and addition-subtraction operations, compared to integration, multiplication, and summation in linear filters. Therefore, MFs offer simple computation and good computational efficiency. By bringing together the design of MFs employing FrFT, morphological filtering with benefits of fractional filtering could be achieved.

2.7.1 Research Gaps

The following research gaps have been identified after a thorough review of the literature. Addressing them would be beneficial in expanding the boundaries of signal processing field.

- There is a scope to expand the applicability of TF tools based on FrFT kernel in the field of ECG signal processing. An additional benefit of including fractional Fourier

domain is increased likelihood of localizing signal components, which can aid in the elimination of noisy counterparts and hence improve the overall diagnosis of ECG signal.

- Validating the performance of any state-of-the-art method associated with ECG signals is based on the addition of additive white Gaussian noise (AWGN) or utilizing real-time noises present at standard databases: *bwm, emm, mam*. However, the underlying problem, which is less focused is that their results may not reflect significant improvement when dealt with real-world scenarios. As reported in the literature, performance of filters degrades when non-gaussian environment is detected. Therefore, there is a scope to investigate the nature of noises and then design the solution based on noise environment that could possibly be encountered.
- With extensive survey of the literature, it has been observed that there has been a surge in applications areas focusing on the design of SE and mostly literature is focused on designing new MOs. Therefore, design methods for SE are possible scope of research. Additionally, they have the essence of window functions, so there is a possibility of designing SE by combining the advantages of existing windows as per intended application.
- MFs are employed for impulsive noises, and literature reports that FrFT, with its variable fractional order parameter a, could be a possible contender for extracting features. Therefore, there is a scope to amalgamate both concepts to design an adaptable filter for signal-processing applications.
- FLO-TF tools have opened a new research domain by having a versatile nature in dealing with impulsive as well as Gaussian noise. However, their application areas are restricted to mechanical fault signals; hence, they could be employed in the domain of biomedical signals to achieve robust performance against different noise scenarios.

2.7.2 Objectives of the Research

The following objectives are *proposed* based on the initial studies, the literature survey (as reported), and the established understanding.

I. The areas of morphological signal processing, FOC, α-stable noise distribution and FLO-TFD/TFD will be reviewed in depth and simulated accordingly.

II. The design methods for implementing morphological filter (MF) based on FOC will be studied and analyzed in SαS environment.
III. A novel fractional lower-order time-frequency distribution (FLO-TFD) method will be investigated based on FLO statistics.
IV. The application of the *proposed* MF for suitable signal processing applications and the comparative study with the existing techniques will be done.

2.8 Research Methodology

In order to bridge the gap between the prevailing research work and real-time solutions based on established methods, workflow for attaining the abovementioned objectives is illustrated in **Figure 2.8.** The basic aim of this thesis is centered on improving the analysis of non-stationary signals using TF tools. ECG signals are chosen for present study, as they are considered the most valuable tool for analyzing human heart and happens to be of a non-stationary nature as well. Furthermore, analyzing the prevailing design methods and their incorporated validation methodology helped to gain significant perspective about the noise analysis models, which led to the establishment of another important aspect of the thesis, i.e., analyzing *non-Gaussian* nature of noises corrupting ECG signals.

With formulated research gaps, the core idea of thesis is to analyze *non-stationary* signals using time-frequency (TF) tools and designing new methods for dealing with a *non-Gaussian* noise environment. Building upon it, a new domain of TF tools based on the FrFT kernel is initially explored for analyzing non-stationary nature of ECG signals. This leads to designing methods for denoising and QRS complex detection based on the advantage of processing signals in a transformed domain. Subsequently, there existed a need to validate processing methods by using real-time noise and varying levels of additive white Gaussian noise (AWGN), which eventually led to investigating the nature of ECG noises. Thus, an extensive simulation study is conducted to analyze the behavior of noises corrupting ECG signals using statistical tests.

Based on this, α-stable distribution noise analysis model is put forward as it has the virtue of encompassing noise environments ranging from Gaussian to impulsive. Considering this noise analysis model, a solution for ECG processing is then *proposed* using morphological filters (MFs), which belong to the class of nonlinear filters offering better performance in

impulsive noise environments. This led to the amalgamation of structuring element (SE) and FrFT concepts in designing novel structuring element i.e., FrSE, which on conjunction with morphological operation (MO) formulated *proposed* MF (referred to as $MF_{FrSE\&MO}$) that could adapt to the shape of ECG signal and suppress noise. Furthermore, to formulate the solution for analyzing *non-stationary* signals under a *non-Gaussian* environment, the concept of TF tools is revisited to develop a more effective solution with higher resolution compared to current TF tools by proposing fractional lower-order fractional Stockwell transform (FLO-FrST) tool. The potential of this tool is then proved by designing an classification method using another non-stationary signal namely EEG. All the simulations for achieving outlined objectives have been done using MATLAB software (version 2022b) installed in a system with an Intel®Core i5CPU 1.7 GHz processor with 16 GB RAM.

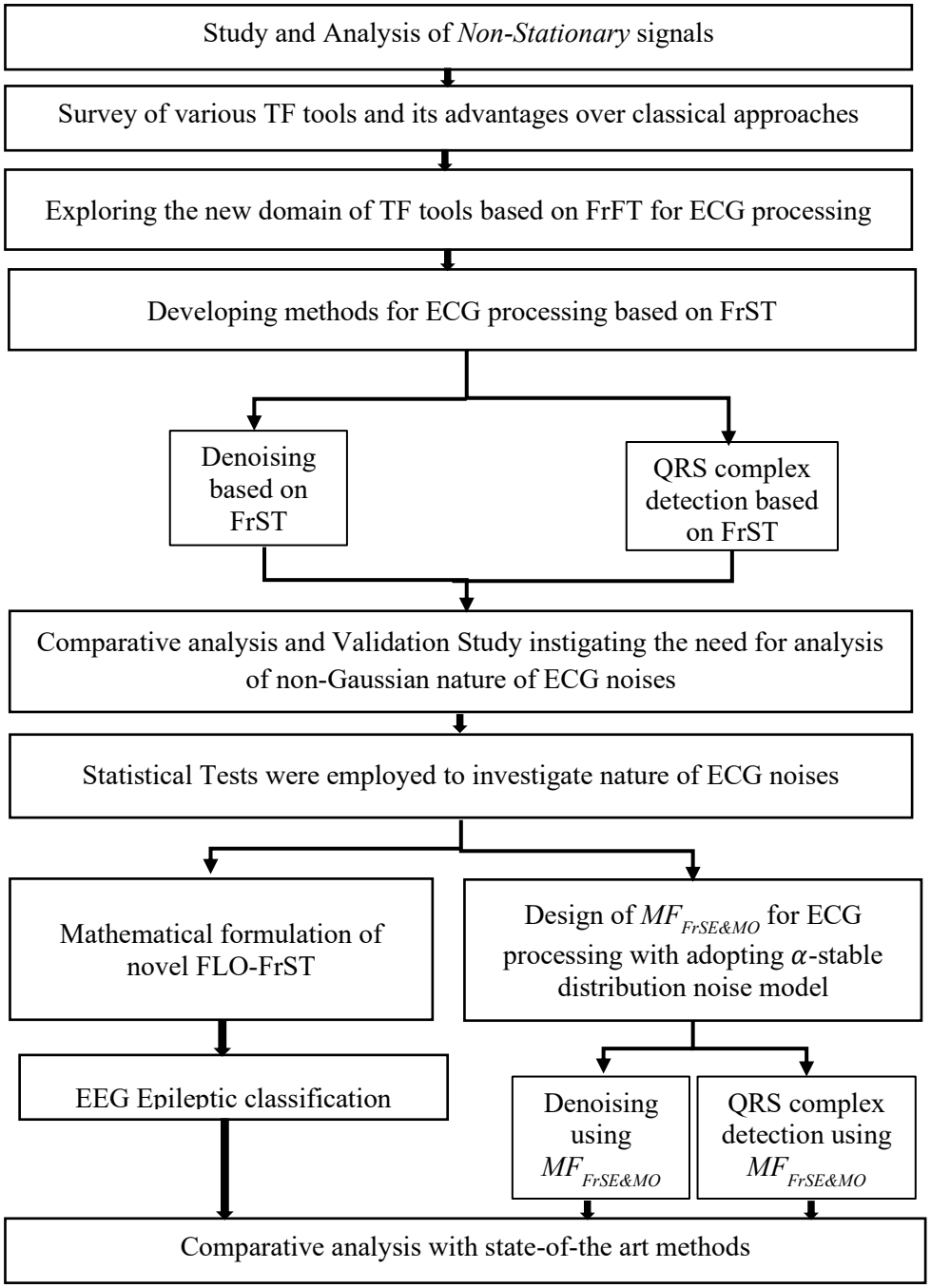

Figure 2.8 Flow chart describing the workflow of thesis

Chapter 3

ECG Signal Processing using Fractional Stockwell Transform (FrST)

TF tools have emerged as a powerful method for analyzing non-stationary signals and have been extensively applied in various fields of signal processing [33, 34, 35, 36, 37]. They jointly display time and frequency domain information, allowing better processing perspectives for non-stationary signals. Under the research on TF tools, new tools based on fractional Fourier transform (FrFT) have been widely utilized to improve TF resolution and extract the information from the time-fractional frequency domain, which otherwise is absent in the TF tools introduced in the first place.

To explore the potential of these improved TF tools in processing one of most important non-stationary signal found in nature, this chapter delves into designing ECG processing methods using this extended time-fractional frequency concept. It validates the performance with established methods through intensive simulation study.

3.1 Time-frequency Analysis of ECG Signal using Fractional Stockwell Transform (FrST)

ECG is a non-stationary signal with a quasiperiodic nature exhibiting physiological variations in morphology. The analysis and processing of this tool have consistently been a prominent research subject due to its widespread use in identifying human cardiac conditions. Among several techniques reported in the literature, TF tools have attained a distinguished recognition in capturing and analyzing the time-varying nature of ECG signals as discussed in Section 2.1.

To examine and develop ECG processing techniques using FrST [47] a description of the FrST algorithm is first presented. Subsequently, an analysis of ECG using FrST spectrogram is discussed.

3.1.1 Computation of FrST

An efficient algorithm has been derived, as illustrated in **Figure 3.1**, for computing FrST of the signal. Different steps are described in the flowchart, followed by their detailed mathematics. To compute the FrFT of underlying signal and Gaussian window, we will use discrete fractional Fourier transform (DFrFT) algorithm described in [130]. To provide a more detailed process of mathematical analytical formulation, details are presented as follows:

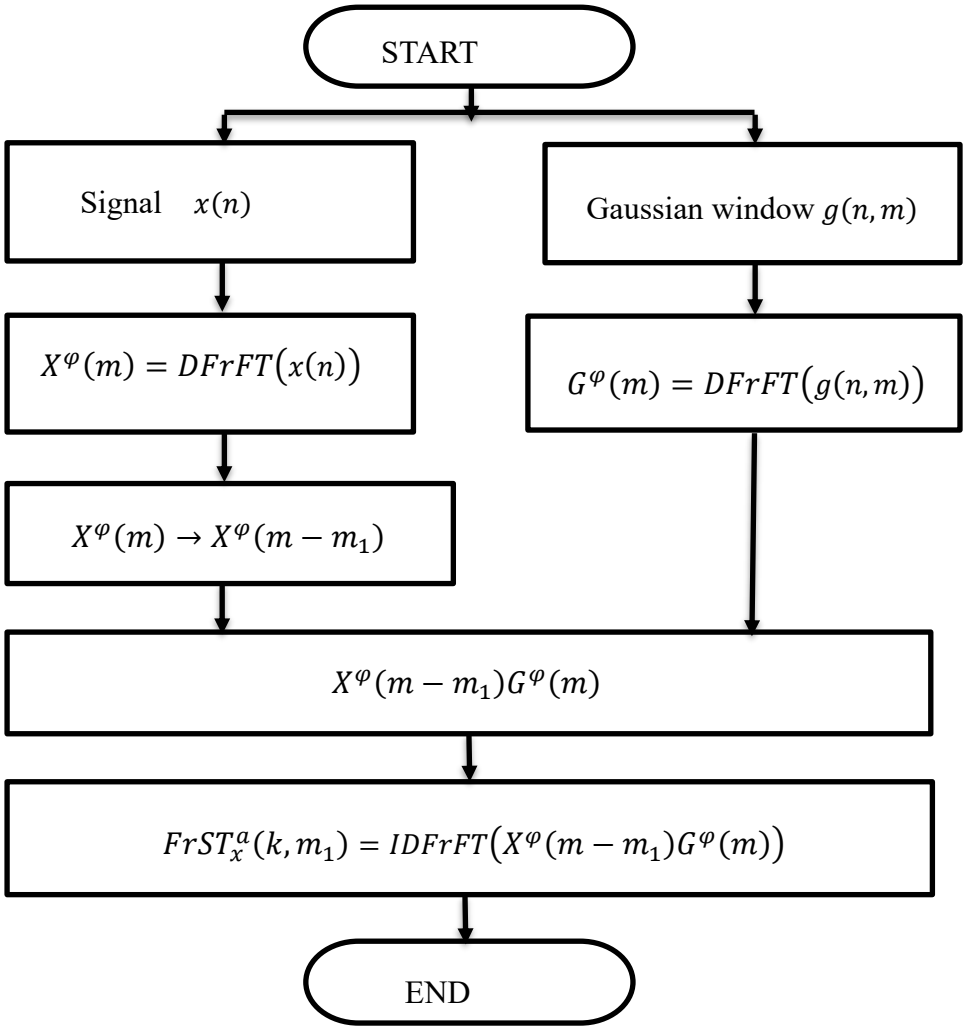

Figure 3.1 *Proposed* flowchart for computing FrST

First, the signal of interest, represented by $x(n)$, is sampled at regular intervals Δt. The DFrFT of the signal is then calculated as

$$X^{\varphi}(m) = \sum_{n=-N}^{N} K_a(n,m)\ x(n) \tag{3.1}$$

where $n = -N, -N+1, \cdots, N-1, N$, and $m = -M, -M+1, \cdots, M-1, M$ (with $M \geq N$). Furthermore, with Δu_{φ} as the sampling interval, the kernel $K_a(m,n)$ is defined by:

$$K_a(n,m) = \sqrt{\frac{1 - j\ \cot\varphi}{2\pi}}\,\Delta t \exp\left(\frac{j}{2}\cot\varphi\, m^2 \Delta {u_{\varphi}}^2\right)\exp\left(-j\csc\varphi\, n\, m\, \Delta u_{\varphi}\, \Delta t\right)\exp\left(\frac{j}{2}\cot\varphi\, n^2 \Delta t^2\right) \tag{3.2}$$

Additionally, the sampling intervals Δu_{φ} and Δt must also satisfy the constraint:

$$\Delta u_{\varphi}\ \Delta \mathrm{t} = \mathrm{S}2\pi \sin\varphi/(2M+1) \tag{3.3}$$

where $|S|$ is some integer prime to $(2M+1)$.

Similarly, for computing the DFrFT of Gaussian window, firstly, FrFT of the window is computed by:

$$G^{\varphi}(u_{\varphi}) = \mathcal{F}_{\mathcal{F}}^{\varphi}\left(g(t,u_{\varphi})\right) = \frac{|u_{\varphi}\csc\varphi|^{p}}{\sqrt{2\pi}}\sqrt{\frac{1 - j\cot\varphi}{\left(u_{\varphi}\csc\varphi\right)^{2p} - j\,q^2\cot\varphi}}\exp\left(\frac{\cot\varphi\left(u_{\varphi}\csc\varphi\right)^{2p} + jq^2}{\left(u_{\varphi}\csc\varphi\right)^{2p} - jq^2\cot\varphi}\right) \tag{3.4}$$

which can be further simplified as:

$$G^{\varphi}(u_{\varphi}) = \frac{|u_{\varphi}\csc\varphi|^{p}}{\sqrt{2\pi}}\sqrt{\frac{1 - j\cot\varphi}{\left(u_{\varphi}\csc\varphi\right)^{2p} - j\,q^2\cot\varphi}}\exp\left(\frac{\left(\left(u_{\varphi}\csc\varphi\right)^{4p} - q^4\right)\cot\varphi + jq^2\csc^2\varphi\left(u_{\varphi}\csc\varphi\right)^{2p}}{\left(u_{\varphi}\csc\varphi\right)^{4p} + q^4\cot^2\varphi}\right) \tag{3.5}$$

where $G^{\varphi}(u_{\varphi})$ has been deduced by substituting the value of $u = |u_{\varphi}\csc\varphi|^{2p}/q^2$.

Now, DFrFT of Gaussian window is obtained by replacing the variables t with $n\Delta t$ and u_{φ} with $m\Delta u_{\varphi}$ in (3.5), the following formula is obtained:

$$G^{\varphi}(m) = \frac{|m\Delta u_{\varphi}\csc\varphi|^{p}}{\sqrt{2\pi}}\sqrt{\frac{1 - j\cot\varphi}{\left(m\Delta u_{\varphi}\csc\varphi\right)^{2p} - j\,q^2\cot\varphi}}\exp\left(\frac{\left(\left(m\Delta u_{\varphi}\csc\varphi\right)^{4p} - q^4\right)\cot\varphi + jq^2\csc^2\varphi\left(m\Delta u_{\varphi}\csc\varphi\right)^{2p}}{\left(u_{\varphi}\csc\varphi\right)^{4p} + q^4\cot^2\varphi}\right) \tag{3.6}$$

Subsequently, spectrum of the underlying signal, designated as $X^{\varphi}(m)$, is multiplied with the shifted version of the DFrFT of the Gaussian window, represented as $G^{\varphi}(m)$. The inverse DFrFT (IDFrFT) of this obtained product is then calculated by

$$z(n) = \sum_{m=-M}^{M} K_a^{*}(m,n) Z^{\varphi}(m) \tag{3.7}$$

Here, the Hermitian property of DFrFT kernel, i.e. $K_a^*(k,m) = K_{-a}(k,m)$ is utilized to define the IDFrFT of signal.

Finally, FrST of signal obtained is given by:

$$FrST_x^a(k,m_1) = \sum_{m=-M}^{M} K_a^*(k,m)X^{\varphi}(m-m_1)G^{\varphi}(m) \tag{3.8}$$

Moreover, the method used to calculate FrST utilizes DFrFT with the lowest level of complexity [130]. To compute FrST of a signal, a total of two DFrFT and one IDFrFT computations are required i.e., a total of $4P + P\log_2 P$ multiplication operations, where P represents the length of output and is equal to $2M + 1$.

3.1.2 FrST Spectrogram Analysis of ECG Signals

In terms of developing processing methods for ECG signals based on TF tools, spectrogram analysis plays a crucial role. Therefore, to examine FrST spectrogram of ECG, this section provides a simulation study for qualitative analysis of the FrST spectrogram.

For demonstration, ECG record 100 from MIT-BIH Arrhythmia Database is used as an example. Furthermore, since FrST comprises three independent parameters— a, p, and q— simulations to demonstrate variations in FrST resolutions are conducted by keeping two of these parameters constant (any one of a, p, and q will do in this case; a constant value of 0.6 is used only for experimentation) and varying the third parameter.

To illustrate the superiority of FrST over ST, the ST spectrogram of ECG is shown in **Figure 3.2** and FrST spectrograms are shown in **Figures 3.3**, **3.4**, and **3.5**. Moreover, the spectrogram is a mathematical representation that depends on three variables: time, frequency, and signal power at each specific location. The hues in these figures represent the magnitude of the signal's power: *red* represents a high-power level, whereas *blue* represents a low power level. Comparing these distinct spectrograms reveals the following distinguishing aspects.

i. FrST spectrograms have better energy concentration and resolution than ST, as can be visually inspected from FrST spectrograms depicted in **Figures 3.3**, **3.4** and **3.5**.
ii. The spectrogram of ST shows fixed resolution, whereas variability in resolution is observed in the FrST spectrogram by changing FrST parameters (a, p, q) as illustrated in **Figures 3.3, 3.4** and **3.5**.

Furthermore, the following observations are obtained to elaborate on the effect of FrST parameters in achieving variable resolution.

Impact of changing window adjustment parameters p and q: On analyzing **Figures 3.3 (a)** and **3.3(b)**, it is observed that as the value of p increases, resolution becomes sharp. Similarly, on analyzing **Figure 3.4** the effect of variation in resolution is observed as the value of q is increased. These changes in obtained resolutions for analysis of ECG signal are in accordance with the fact of Gaussian window described in [47], i.e., the width of Gaussian window becomes narrower when the value of p increases and hence improving the resolution and vice-versa for parameter q.

Impact of changing fractional parameter a: Fractional parameter a is known to enhance the resolution obtained by varying window adjustment parameters [47], which has been illustrated in **Figure 3.5**. A smaller value of parameter a leads to scalloping loss, which is smearing of frequencies due to spectral leakage. However, it provides improved time resolution, as seen in **Figure 3.5(a)**. Furthermore, for larger values of a, there is an enhancement in frequency resolution while compromising time resolution, as depicted in **Figure 3.5(c)**. Significantly improved time and frequency resolution occurs at a=0.4, for the chosen set of parameters, as shown in **Figure 3.5(b)**.

By examining these simulation findings, it is possible to deduce that the FrST tool offers far greater flexibility than traditional tools like ST and WT and, considering its three degrees of freedom, much superior time and frequency resolution [40, 162].

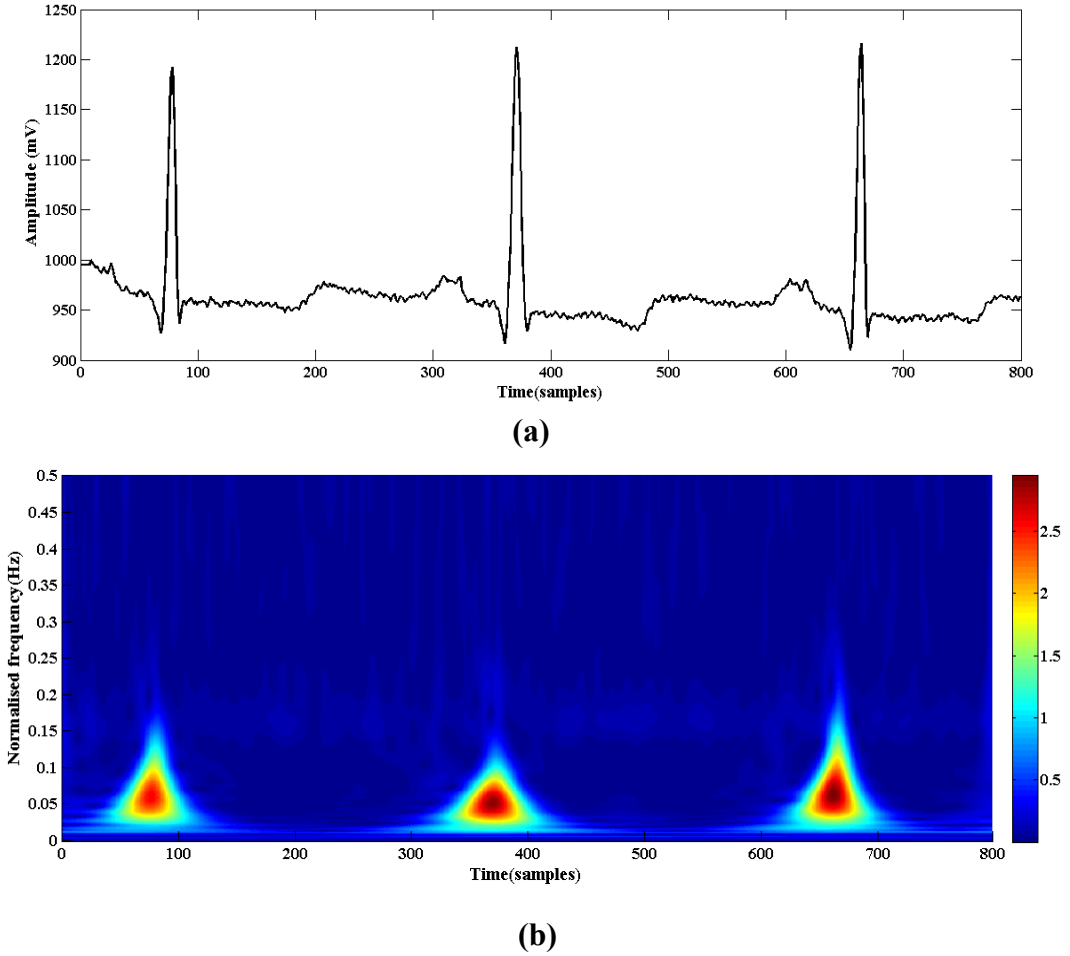

Figure 3.2 (a) Time domain representation of ECG record no. 100**, (b)** ST spectrogram for ECG record no. 100 with color-bar depicting the relationship of power values: *red*: high power and *blue*: low power**.**

a= 0.6, $\boldsymbol{p}$ **=0.4**, q = 0.6

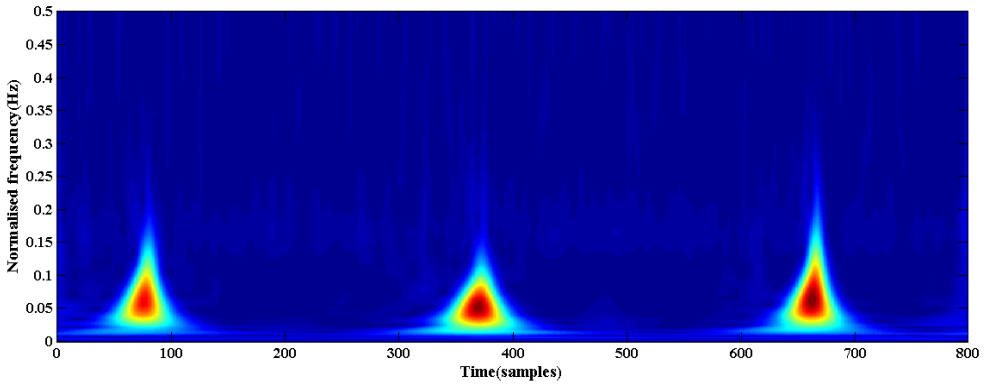

(a)

a= 0.6, $\boldsymbol{p}$ **=0.8**, q = 0.6

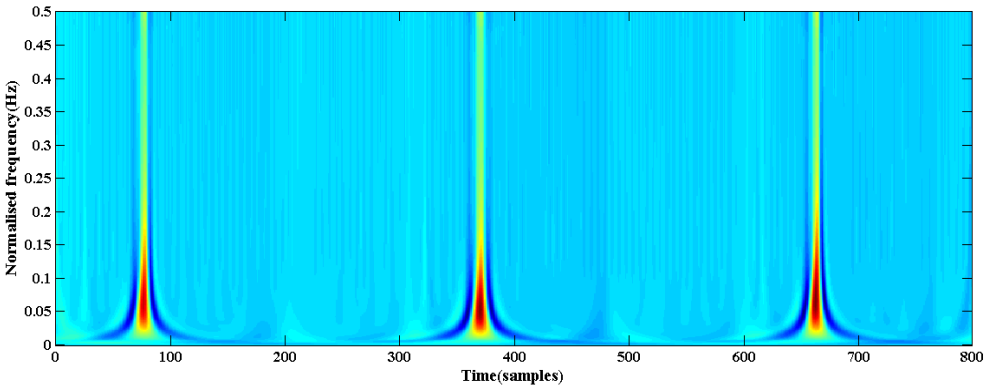

(b)

Figure 3.3 (a) FrST spectrogram for ECG record no. 100 at a= 0.6, p= 0.4 and q=0.6**, (b)** FrST spectrogram for ECG record no. 100 at a= 0.6, p= 0.8 and q=0.6**.**

a= 0.6, p =0.6, $\boldsymbol{q = 0.3}$

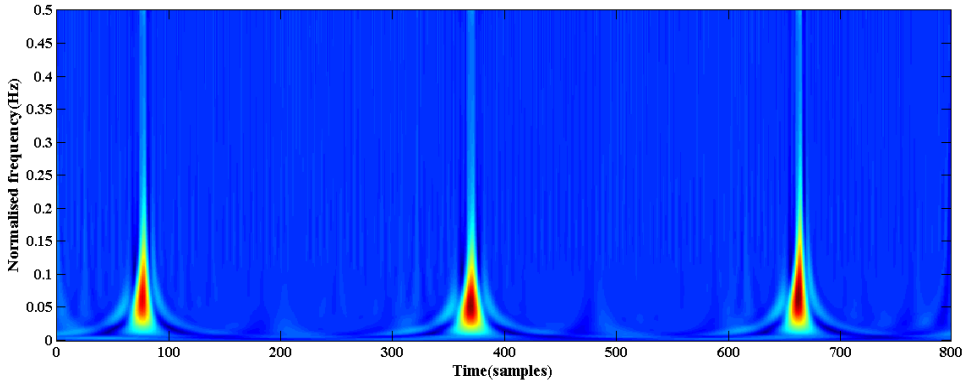

(a)

a= 0.6, p =0.6, $\boldsymbol{q = 0.9}$

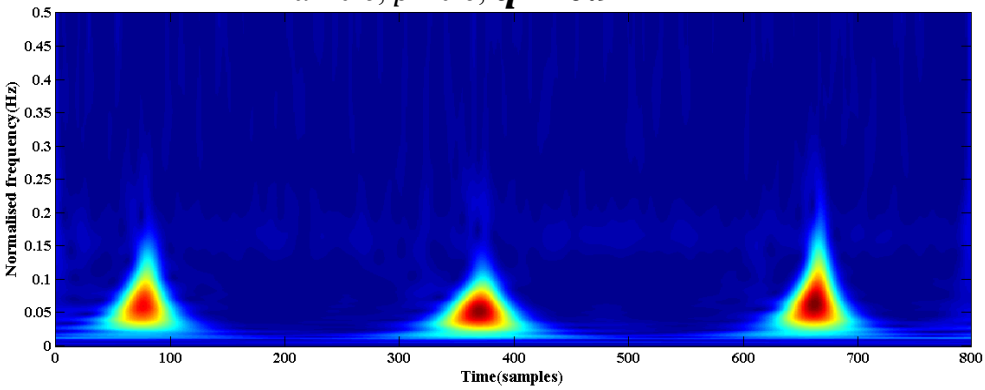

(b)

Figure 3.4 (a) FrST spectrogram for ECG record no. 100 at a= 0.6, p= 0.6 and q=0.3**, (b)** FrST spectrogram for ECG record no. 100 at a= 0.6, p= 0.6 and q=0.9**.**

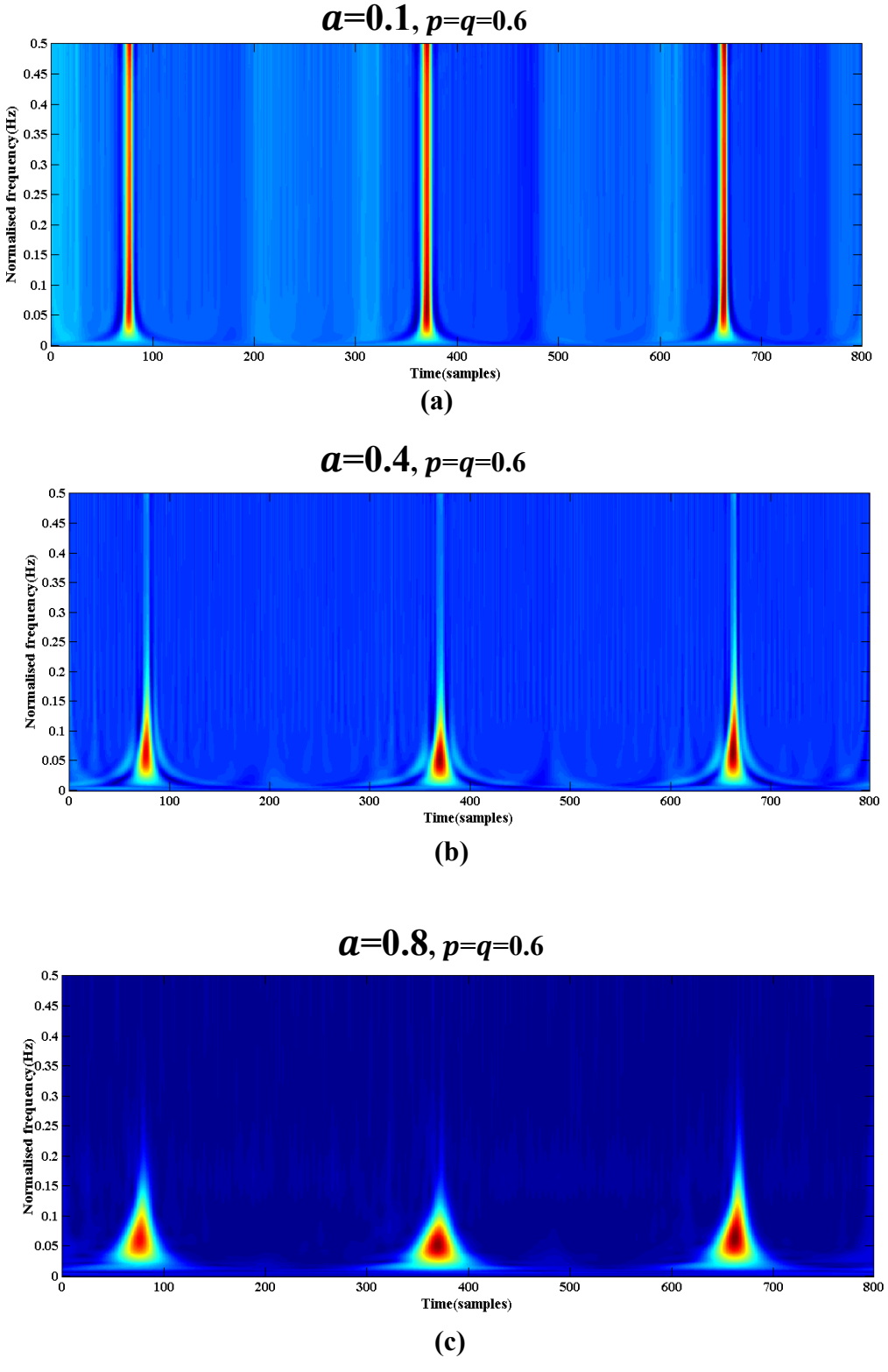

Figure 3.5 (a) FrST spectrogram for ECG record no. 100 at a= 0.1, p= 0.6 and q=0.6**,** **(b)** FrST spectrogram for ECG record no. 100 at a= 0.4, p= 0.6 and q=0.6**,** **(c)** FrST spectrogram for ECG record no. 100 at a= 0.8, p= 0.6 and q=0.6.

3.2 ECG Signal Denoising using FrST

Denoising is a crucial step for accurate diagnosis of ECG signals as during acquisition, ECG has a tendency to get contaminated by unwanted noises and artifacts, as discussed in Section 2.1. These noises significantly impact the morphology of ECG signals, posing challenges in accurately interpreting the information related to biomarkers, namely P-QRS-T.

Classical signal processing algorithms used for removing and suppressing the interfered noises were based on time and frequency domain filtering [51, 52]. One of the limitations of such classical algorithms was that they could not track the time-varying morphology of signal, resulting in inaccurate detection of QRS complex. Due to the non-stationary nature of ECG signals, TF tools [5] like ST, WT, and EMD have recently been introduced for ECG signal processing and analysis. However, the following shortcomings persist in using these tools:

- Selection of wavelet and choice of thresholding (hard and soft) in WT method [209].
- The presence of redundant information while transforming signal using the ST method at the initial stage, which when processed further leads to distortions and loss of useful information [210].
- Poor signal retrieval in EMD based methods [55] .

Hence, with various methods introduced for denoising ECG signals, getting a high reconstruction rate and better retaining significant information is still an open problem.

Thus, to successfully reduce distortions and maintain the information content of signal, a new tool called FrST, which combines the qualities of ST and FrFT, has been used to build a denoising method. Based on suggested FrST approach, the block diagram is depicted in **Figure 3.6**. It consists of five stages, which are discussed below.

Stage 1: In the given illustration, the ECG signal is taken from the MIT-BIH Arrhythmia Database [196]. To assess the effectiveness of *proposed* FrST-based algorithm, signals are intentionally distorted by introducing additive Gaussian noise (AWGN) generated using MATLAB. The resulting noisy signal is given by $x_n[n] = x_o[n] + \sigma[n]$, is obtained by adding Gaussian distribution noise $\sigma[n]$ to the original ECG $x_o[n]$.

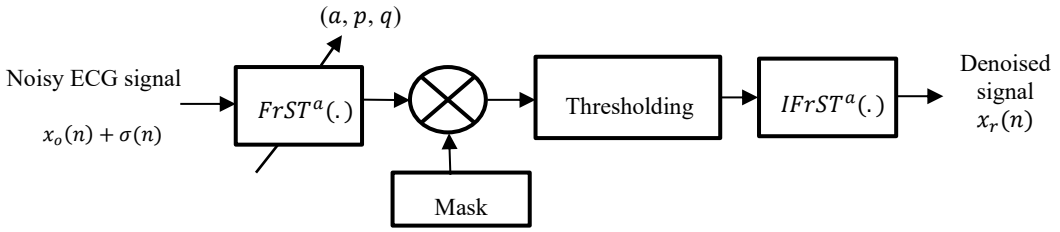

Figure 3.6 Block diagram for *proposed* denoising method

Stage 2: The *proposed* FrST algorithm is then applied to the noisy ECG signal using the procedure detailed in Section 3.1.1.

Stage 3: Time and fractional Fourier frequency domain spectrum is subsequently utilized to eliminate high-frequency components that are present in the noisy ECG data. The bandwidth of the original ECG lies in the range of 0.05-100 Hz, with significant information lying up to the frequency of 200 Hz. Therefore, the time-frequency mask employed in this stage is defined such that it is unity up to 200 Hz and zero above 200 Hz.

Stage 4: Unwanted frequencies present between QRS complexes are removed from the masked output of previous stage using proper threshold level, which is known to play a crucial role in ECG denoising process. The improper threshold level may lead to distortion, so adaptive thresholding technique is applied, which only permits three times less standard deviation of the noisy signal [209, 210].

Stage 5: Finally, with inverse FrST formulation, the processed spectrum is reconstructed back to time domain, resulting in a denoised signal.

The key step in the *proposed* denoising method is the computation of FrST spectrogram. This method provides simultaneous good time and frequency resolution, allowing for accurate identification and separation of signal and noise components. With careful analysis of these components and the knowledge of underlying noises corrupting ECG signals, the resulting FrST spectrogram can effectively remove noise from ECG signal. The quality of ECG signal is significantly improved and the same has been demonstrated using qualitative and quantitative performance metrics in next sections.

3.2.1 Performance Metric Parameters

For quantitative analysis between *proposed* denoising method and the existing state-of-the-art methods [55, 209, 210], three performance metrics— root mean square error (*RMSE*), percent root mean square difference (*PRD*) and improved signal-to-noise ratio (*imp_SNR*) are chosen. These performance metric parameters statistically assess the quality of denoised signal obtained after simulations. Also, all three performance metrics namely, *RMSE*, *PRD* and *imp_SNR,* collectively depend on fractional parameter a and two window adjustment parameters p and q.

The performance metric parameters are calculated as [211]:

$$RMSE = \sqrt{\frac{\sum_{n=0}^{N-1}[x_o(n) - x_r(n)]^2}{N}} \tag{3.9}$$

$$PRD = \sqrt{\frac{\sum_{n=0}^{N-1}[x_o(n) - x_r(n)]^2}{\sum_{n=0}^{N-1}[x_o(n)]^2}} \times 100 \tag{3.10}$$

$$imp\_SNR[dB] = SNR_{output}[dB] - SNR_{input}[dB] = 10\log\left[\frac{\sum_{n=0}^{N-1}[x_r(n) - x_o(n)]^2}{\sum_{n=0}^{N-1}[x_o(n) - x_n(n)]^2}\right] \tag{3.11}$$

where $x_o(n)$ is original ECG signal, $x_r(n)$ is reconstructed denoised signal, $x_n(n)$ is noisy ECG signal and N is length of the signal.

Usually, visual inspection is used for the clinical acceptability of the denoised signal. But here, quantitative analysis is also carried out to measure the level of distortion in the denoised signal compared to the original signal. The metric parameter *RMSE* measures the error between original signal and reconstructed (denoised) signal. The smaller its value, better the preserved information content. Performance metric *PRD* is a quality measure used for evaluating the real performance of the algorithm. A lower *PRD* value indicates superior performance. The *imp_SNR* reflects the difference between the noise level present before and after applying the algorithm. The greater the value of *imp_SNR*, the better the effect.

For conventional methods [55, 209, 210, 212], the quality of denoised signal is based on fixed value of involved parameters. On the other hand, *proposed* method gives the flexibility of having three variable parameters, thus giving three degrees of freedom and increasing robustness over other state-of-the-art methods.

3.2.2 Simulation Results

Numerical simulations carried out to assess the effectiveness of *proposed* method are divided into two sections: simulations to determine optimal values for the FrST parameters (a, p, and q) and performance evaluation of *proposed* method to compare it with existing techniques using aforementioned performance metric parameters.

Furthermore, for facilitating analysis of our *proposed* method, ECG signals from standard databases *MIT-BIH Arrhythmia* [196] (with MLII lead as a reference for original signal) and *European ST-T database* [203] (modified limb lead MLIII is chosen as reference) are selected. Moreover, to illustrate the denoising performance, MATLAB generated AWGN to replicate the practical noise environment is employed to distort ECG signal. Here, 5 dB, 10 dB and 15 dB noise levels are generated to validate performance of *proposed* method. Also, real-time noise and artifacts from *MIT-BIH Noise Stress Test Database* [200, 201] are considered.

Additionally, aforementioned performance metric parameters are used for an intuitive quantitative analysis between ST-based denoising and the *proposed* denoising method in a *noisy environment*.

Thus, firstly the effect of variation of FrST parameters (a, p, q) on the *proposed* denoising method is examined for computing optimal value set of involved FrST parameters. Secondly, the performance of *proposed* method based on the computed value set is recorded for comparison purposes.

3.2.2.1 Parameter-based Performance Evaluation of *Proposed* Denoising Method

As previously stated, *proposed* method provides three degrees of freedom, allowing for increased flexibility in accomplishing the denoising process. Hence, to develop an effective denoising technique, it is necessary to have high resolution across time-fractional frequency plane. Consequently, it is essential to calculate the optimal-set of values for these parameters. The higher the resolution, the greater the likelihood of obtaining localized components, reducing the possibility of information overlapping with noise, and resulting in higher-quality denoised signal.

For simulation purposes, MIT-BIH ECG record number 100 (only taken for experimentation) of a time span of 100 seconds (36,000 samples) is artificially corrupted with 15 dB AWGN. This noisy signal is passed through *proposed* denoising model

illustrated in **Figure 3.6**. Here, a noise level of 15 dB is chosen to evaluate the *proposed* method's efficacy in an extremely noisy environment right from the beginning.

Furthermore, an attempt has been made to analyze the variability of all performance metric parameters *RMSE, PRD* and *imp_SNR* by changing values of FrST parameters a, p and q. For analysis purposes, simulations are performed by keeping two FrST parameters constant (here, 0.5 is taken only for experimentation) and the third parameter is varied as 0.1, 0.3, 0.5, 0.7, 0.9, 1.1 and 1.3, respectively. The simulation results are recorded in **Tables 3.1, 3.2** and **3.3** for a, p and q. Also, a graphical depiction of these results is depicted in **Figures 3.7**, **3.8** and **3.9**.

Examining the results recorded in **Table 3.1**, it is evident that the resulting *RMSE* values at a=0.3, 0.5, 0.7, 0.9, 1.1 and 1.3 are significantly lower than those obtained using ST method (corresponding to $a = p = q = 1$, as reported in [47]). Therefore, the *proposed* method achieves better reconstruction capability, and hence maximum information content is preserved in the denoised signal.

Next as per **Table 3.2**, the variation of various performance metric parameters is presented by varying window adjustment parameter_1, i.e., p. On analyzing values of $p = 0.3$, 0.5, 0.7, 0.9, 1.1 and 1.3, it is observed that lower values of *RMSE* are obtained as compared to conventional ST method. For instance, *RMSE* value obtained for ST method is 0.15051, whereas, with *proposed* method, the lowest value of 0.0325 is obtained at p=0.7, which is much lower than conventional ST method. This depicts that the obtained denoised ECG signal is much less distorted than noisy ECG signal, and useful information content is preserved. Also, the examination of *imp_SNR* values shows a maximum improvement of 28.15431 dB (at $p = 0.9$) and a minimum improvement of 22.48855 dB (at p=0.3), which are significantly higher than the value of 12.68183 dB obtained for conventional ST method.

Finally, the variation of second window adjustment parameter_2, i.e. q is recorded in **Table 3.3** for different performance metric parameters and an *imp_SNR* value of 25.95269 dB is obtained for a= p= q =0.5, which is much higher than ST method value of 12.68183 dB.

Table 3.1 Performance results varying a and with $p = q = 0.5$.

a	p	q	*RMSE*	*PRD*(%)	*imp_SNR*(dB)
0.1	0.5	0.5	0.18131	18.13178	22.24773
0.3	0.5	0.5	0.07728	7.7266	22.78265
0.5	0.5	0.5	0.04336	4.33641	25.95269
0.7	**0.5**	**0.5**	**0.03947**	**3.94693**	**26.59749**
0.9	0.5	0.5	0.04842	4.84152	24.60438
1.1	0.5	0.5	0.04842	4.84152	24.60438
1.3	0.5	0.5	0.03947	3.94693	26.59749
1	**1**	**1**	**0.15051**	**15.05162**	**12.68183**

Bold value indicates the minimum *RMSE*, minimum *PRD* (%) and maximum *imp_SNR* (dB) obtained by varying parameter a and values of metric parameters obtained using ST method.

Table 3.2 Performance results varying p and with $a = q = 0.5$.

a	p	q	*RMSE*	*PRD*(%)	*imp_SNR*(dB)
0.5	0.1	0.5	0.38505	38.50443	22.5313
0.5	0.3	0.5	0.11181	11.18027	22.48855
0.5	0.5	0.5	0.04336	4.33641	25.95269
0.5	0.7	0.5	0.04276	4.27466	25.23005
0.5	**0.9**	**0.5**	**0.0325**	**3.25167**	**28.15431**
0.5	1.1	0.5	0.03468	3.46952	25.18319
0.5	1.3	0.5	0.03423	3.42294	24.89507
1	**1**	**1**	**0.15051**	**15.05162**	**12.68183**

Bold value indicates the minimum *RMSE*, minimum *PRD*(%) and maximum *imp_SNR* (dB) values obtained by varying parameter p and values of metric parameters obtained using ST method.

Table 3.3 Performance results varying q and with $a = p = 0.5$.

a	p	q	*RMSE*	*PRD*(%)	*imp_SNR*(dB)
0.5	0.5	0.1	0.02344	2.34529	25.59744
0.5	0.5	0.3	0.03933	3.93381	25.00798
0.5	**0.5**	**0.5**	0.04336	4.33641	**25.95269**
0.5	0.5	0.7	0.06686	6.68521	23.43531
0.5	0.5	0.9	0.07464	7.4648	24.1778
0.5	0.5	1.1	0.07049	7.04953	24.64526
0.5	0.5	1.3	0.05786	5.78557	25.5137
1	**1**	**1**	**0.15051**	**15.05162**	**12.68183**

Bold value indicates the maximum *imp_SNR* (dB) values obtained by varying parameter q and values of metric parameters obtained using ST method.

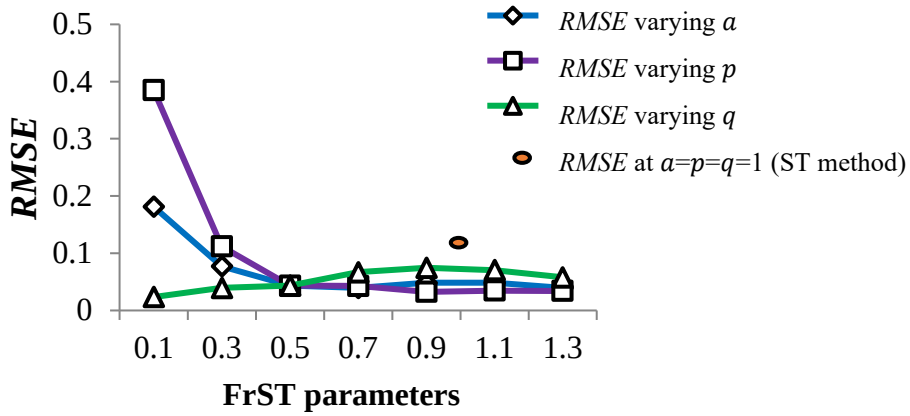

Figure 3.7 General trend in *RMSE* with variation in a, p and q.

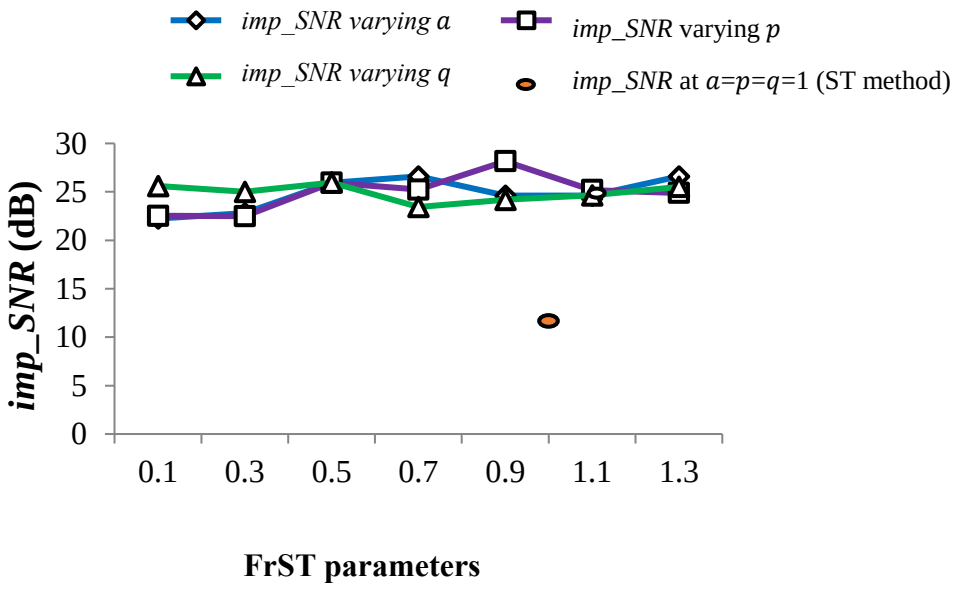

Figure 3.8 General trend in *imp_SNR* (dB) with variation in a, p and q

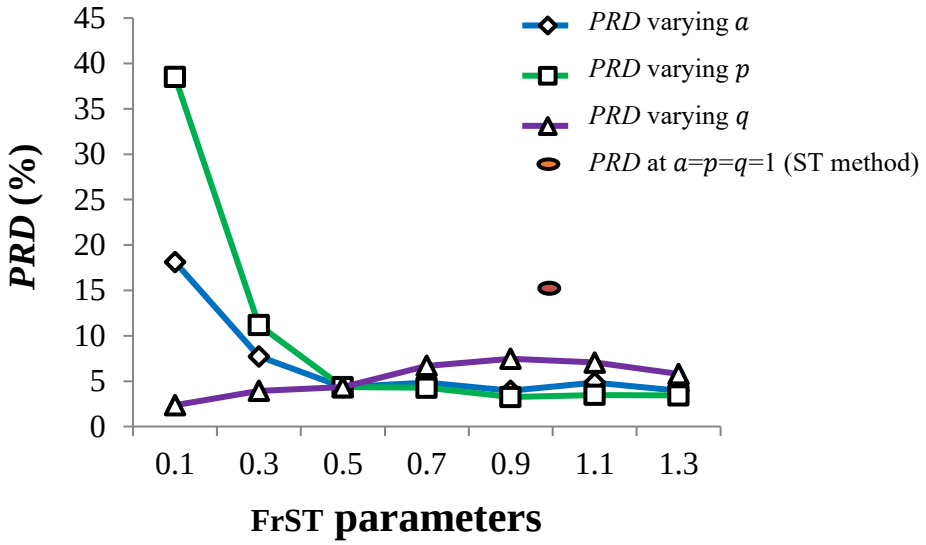

Figure 3.9 General trend in *PRD* (%) with variation in a, p and q.

Upon examining these observations, it has been determined that the ideal range for FrST parameters (a, p, q) is between 0.5 and 0.7. Any combination of FrST parameters (a, p, q) within the specified range would yield favorable outcomes for the suggested approach. Therefore, optimal value set of (0.5, 0.5, 0.5) is selected to evaluate the performance of *proposed* method and demonstrate its comparison with other methods.

3.2.2.2 Performance Evaluation of *Proposed* Denoising Method on MIT-BIH ECG Records

For evaluating the performance of *proposed* method, 10 ECG records were selected with few artifacts, i.e., 100, 101, 102, 103, 113, together with less common arrhythmia records, i.e., 201, 214, 217, 231, and one with an abnormal shape, noise, and artifacts, i.e., ECG record 207. The selected records encompass variety of artifacts and waveform variations that might be encountered in routine clinical use.

Next, selected ECG records are corrupted with MATLAB generated AWGN of level 5 dB, 10 dB and 15 dB. This is done to effectively assess the performance of *proposed* method and ensure a fair comparison with existing methods. The output of different steps described in Section 3.2 are shown in **Figure 3.10**. The illustrations give an insight into the results obtained after each stage of *proposed* algorithm.

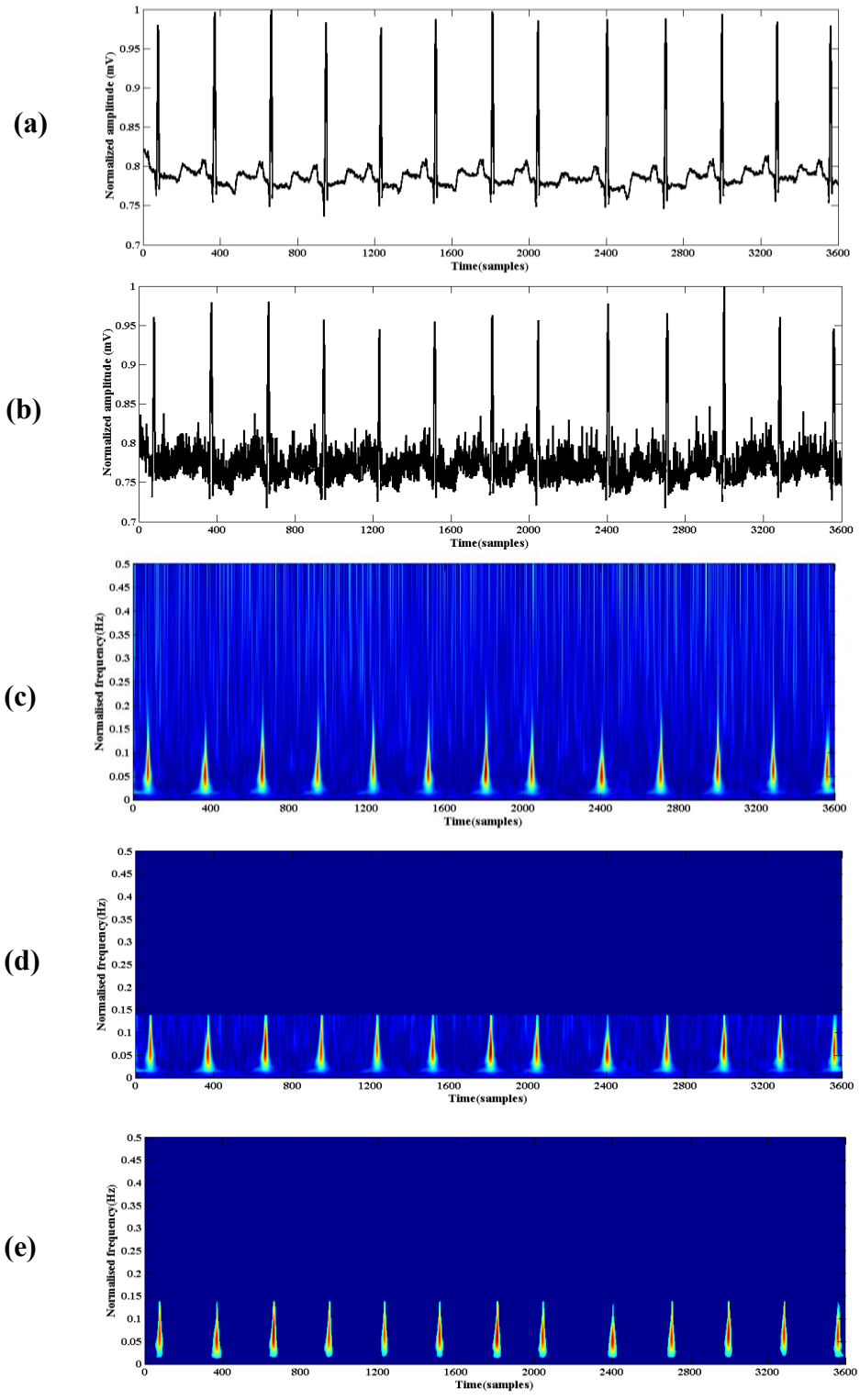

Figure 3.10 Different stages of *proposed* method: **(a)** Time domain representation of ECG record no. 100, **(b)** Time domain representation of ECG record no. 100 corrupted with 10dB additive white Gaussian noise, **(c)** FrST spectrogram for noisy ECG record no. 100 at a= 0.5, p= 0.5 and q=0.5, **(d)** FrST spectrogram of ECG after masking, **(e)** FrST spectrogram of ECG after adaptive thresholding.

For experimentation purposes and with reference to the obtained value set derived in Section 3.2.2.1, denoising process is performed at $a = p = q = 0.5$. Quantitative analysis using ST method is also performed on the same records for comparison purposes.

In order to make quantitative comparisons, the experimentation is conducted on segments of ECG recordings that are 11 seconds long. A total of 162 segments are used to cover the whole 30-minute length of each ECG record. The performance metric parameters for a single record are generated by averaging performance metric parameters of these segments.

The experimentation results at different noise levels for both methods are tabulated in **Tables 3.4**, **3.5** and **3.6**. The performance metric parameters obtained at 5 dB input noise level are reported in **Table 3.4**. The obtained metric values show a notable decrease in *RMSE* values and a considerable increase in *imp_SNR* values for *proposed* method, demonstrating a considerably more substantial improvement than the conventional ST method.

Analyzing the results tabulated in **Table 3.5** recorded at 10 dB input noise level, a minimum *RMSE* value of 0.022 is achieved for ECG record 207 compared to 0.1179 obtained for the same record using the ST method. Also, a maximum *SNR* improvement of 25.2731 dB is achieved using *proposed* method for ECG record 201, which is much higher than 11.0387 dB obtained using ST method.

Similarly, by investigating the results tabulated in **Table 3.6**, it can be seen that minimum value of *imp_SNR* (17.767 dB) achieved using *proposed* method is still higher than the maximum value of *imp_SNR* (14.163 dB) achieved using ST method. This ascertains that even if the noise levels increase, *proposed* method performs better than ST method.

Furthermore, overall performance of *proposed* method and ST method based on statistical measure *RMSE* is compared in **Figure 3.11**. The average *RMSE* values are plotted against different input noise level. The bar graphs clearly show that RMSE values for *proposed* method are much lower than ST method. Hence, this proves that *proposed* method is capable of better retaining the required information content in ECG signals, and at the same time it offers better noise-removing ability.

Table 3.4 Comparison of *proposed* method and ST method at 5 dB input noise level

ECG record no.	Input noise level	ST method		***Proposed* method a=0.5, p=0.5, q=0.5**	
		RMSE	***imp_SNR***	***RMSE***	***imp_SNR***
100	5 dB	0.1291	3.5375	0.0161	23.144
101	5 dB	0.1224	4.0058	0.0146	23.9942
102	5 dB	0.1693	1.12146	0.0185	22.0023
103	5 dB	0.137	3.414	0.0169	22.9156
113	5 dB	0.1482	2.186	0.0177	22.3592
201	5 dB	0.1009	5.8195	0.0113	26.3795
207	5 dB	0.1169	4.4233	0.0112	26.4917
214	5 dB	0.1198	4.0875	0.0164	23.0122
217	5 dB	0.1519	1.9868	0.0174	22.4858
231	5 dB	0.1097	5.0924	0.0156	23.5468

Note: recorded *imp_SNR* values are in dB

Table 3.5 Comparison of *proposed* method and ST method at 10 dB input noise level

ECG record no.	Input noise level	ST method		***Proposed* method a=0.5, p=0.5, q=0.5**	
		RMSE	***imp_SNR***	***RMSE***	***imp_SNR***
100	10 dB	0.1313	8.7687	0.0293	22.4876
101	10 dB	0.1246	9.2403	0.027	23.2303
102	10 dB	0.1713	6.4986	0.0354	20.949
103	10 dB	0.1394	8.6448	0.031	22.1491
113	10 dB	0.1502	7.4805	0.0322	21.6816
201	10 dB	0.1025	11.0387	0.0215	25.2731
207	10 dB	0.1179	9.7643	0.022	25.1852
214	10 dB	0.1223	9.3301	0.0303	22.2291
217	10 dB	0.1539	7.2883	0.0324	21.6374
231	10 dB	0.1119	10.2653	0.0285	22.8002

Note: recorded *imp_SNR* values are in dB

Table 3.6 Comparison of *proposed* method and ST method at 15 dB input noise level

ECG record no.	Input noise level	ST method		*Proposed* method a=0.5, p=0.5, q=0.5	
		RMSE	*imp_SNR*	*RMSE*	*imp_SNR*
100	15 dB	0.1552	12.5655	0.0807	19.0699
101	15 dB	0.1491	12.9199	0.0786	19.2892
102	15 dB	0.1914	10.759	0.0936	17.767
103	15 dB	0.1635	12.3742	0.0855	18.515
113	15 dB	0.1722	11.5786	0.0851	18.5711
201	15 dB	0.1306	14.143	0.0751	19.6527
207	15 dB	0.1419	13.3693	0.0774	19.41
214	15 dB	0.1474	12.9619	0.0831	18.7897
217	15 dB	0.1745	11.4683	0.0871	18.3946
231	15 dB	0.138	13.6527	0.082	18.8998

Note: recorded *imp_SNR* values are in dB

The robustness offered by *proposed* method is depicted in **Figure 3.12**. As the noise level increases, ST method tends to show lesser improvement in SNR. On the other hand, corresponding values demonstrate the strength and effectiveness of *proposed* method in handling higher levels of noise. This indicates that *proposed* method can denoise signals more effectively, even in the presence of significant noise.

Lastly in **Figure 3.13**, the performance of selected ECG records at input noise level of 15 dB is depicted in terms of *PRD* values. This performance metric measures the quality of denoised signal, and it is known from the rich literature that its value must be lower for proper reconstruction of signal. Here, *PRD* values at 15 dB noise input are plotted to prove the superiority of *proposed* method over ST method. Its lower values mean better reconstruction capability, leading to better quality of denoised signal.

Therefore, based on chosen performance metrics (*RMSE*, *imp_SNR* and *PRD*) and with the added advantage of FrST parameters (a, p, q), we can conclude that *proposed* method offers better denoising ability and is more robust than existing denoising methods.

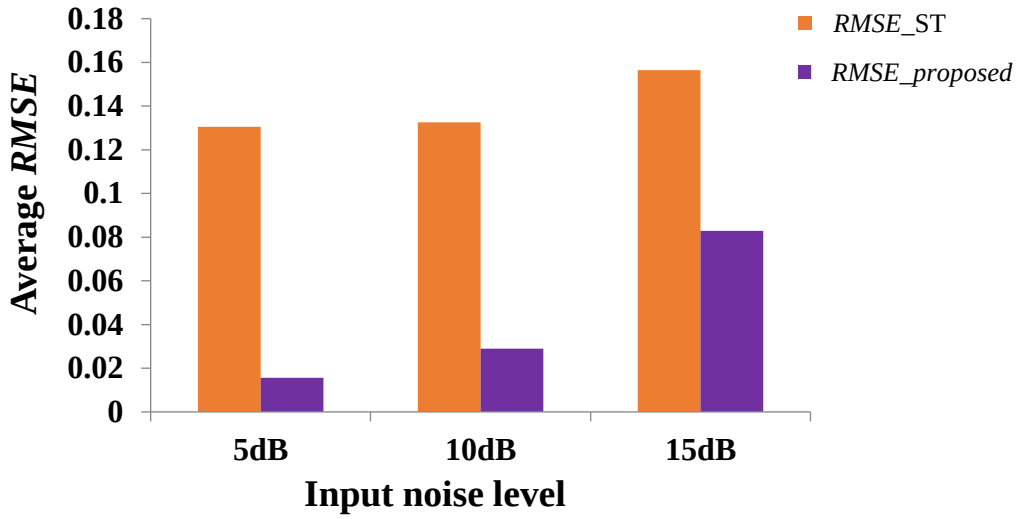

Figure 3.11 Comparison of average *RMSE* for *proposed* method and ST method at different input noise levels.

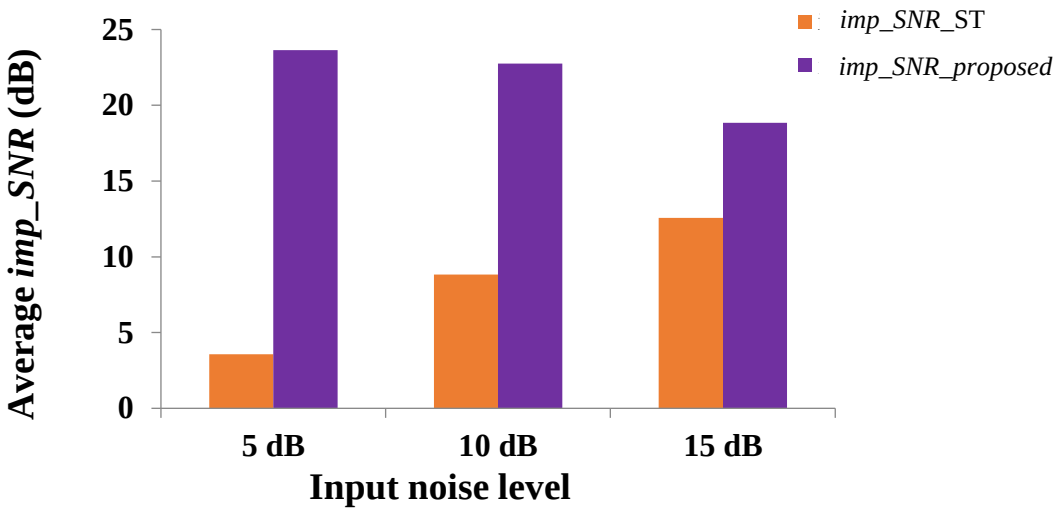

Figure 3.12 Comparison of average *imp_SNR* (dB) for *proposed* method and ST method at different input noise levels.

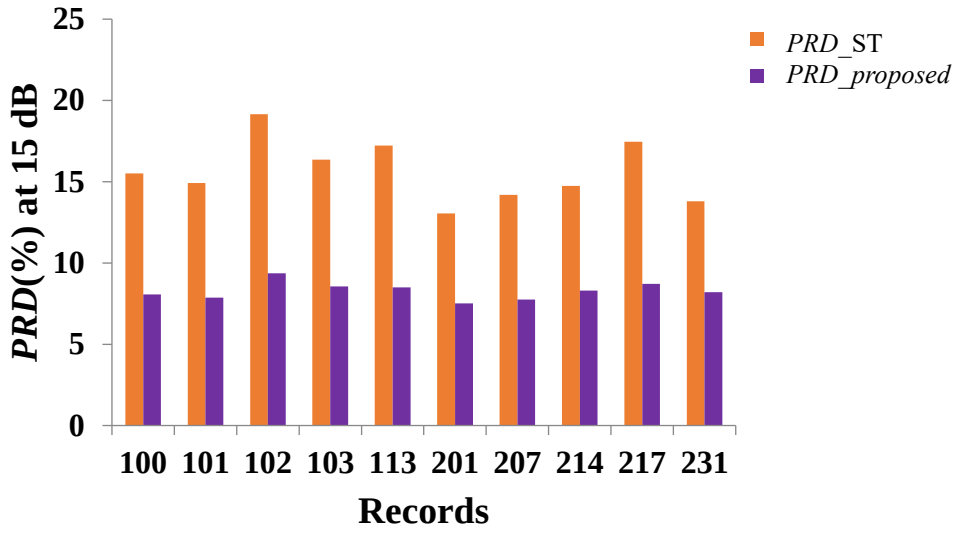

Figure 3.13 Performance comparison of *PRD* (%) obtained for all ECG records at 15dB input noise level using *proposed* method and ST method.

3.2.2.3 Performance Evaluation of *Proposed* Method with Real Noises

To prove the robustness of *proposed* method, different artifacts and noises from MIT-BIH Noise Stress Test Database [200, 201] are added to two randomly selected MIT-BIH records, 100 and 222. Results recorded in **Tables 3.7** and **3.8** were obtained by corrupting ECG records with five types of noise, namely baseline wander (bwm), electrode motion artifact (emm), muscle artifacts (mam) also known as EMG, noise records: 118e and 119e calibrated at 12dB noise level of motion artifacts.

By analyzing the results tabulated in **Tables 3.7** and **3.8**, it is evident that *proposed* method obtains better results in terms of *RMSE* and *imp_SNR* than the ST method. The *imp_SNR* values obtained in **Table 3.8** are plotted in **Figure 3.14**. Bar plots of obtained *imp_SNR* values clearly validate the robustness offered by *proposed* method in terms of better noise removing ability leading to better reconstruction of ECG signal. This highlights the strength of *proposed* method in terms of robustness against different noise types.

Table 3.7 Comparison results for *RMSE* values obtained using *proposed* and ST method for different types of noises taken from *MIT-BIH Noise Stress Test Database*

	ST method		***Proposed* method**	
Noises ↓ **ECG records** →	100	222	100	222
Baseline (bwm)	0.1951	0.1641	0.0397	0.0411
EMG (mam)	0.8609	1.2066	0.1277	0.2097
Electrode Motion (emm)	0.1224	0.1895	0.0507	0.0616
118e	1.4214	0.9673	0.1322	0.3241
119e	0.9698	0.7348	0.1296	0.152

Table 3.8 Comparison results for *imp_SNR* (dB) obtained using *proposed* and ST method for different types of noises taken from *MIT-BIH Noise Stress Test Database*

	ST method		***Proposed* method**	
Noises ↓ **ECG records** →	100	222	100	222
Baseline (bwm)	8.7144	10.0379	25.0793	25.4952
EMG (mam)	10.1388	14.2114	25.2086	21.5302
Electrode Motion(emm)	16.2448	15.409	26.746	25.7584
118e	11.6429	15.3342	35.5686	28.3762
119e	9.6312	12.7036	30.3537	29.7277

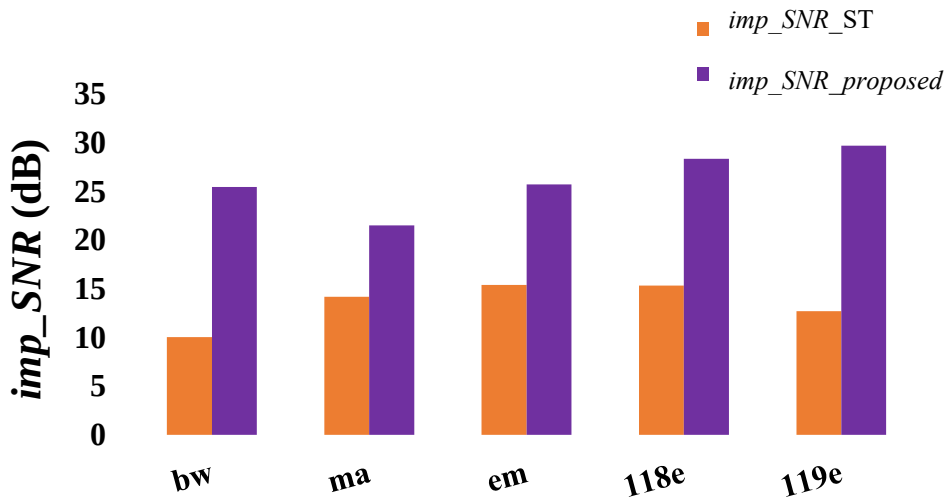

Figure 3.14 Comparison of *imp_SNR* (dB) values obtained using the *proposed* method and ST method for different types of noise.

3.2.2.4 Performance Evaluation of *Proposed* Method on ECG Signals from European ST-T Database

In order to justify the effectiveness of *proposed* method over databases other than MIT-BIH, ECG records from the *European ST-T Database* [203] are also considered. This database was designed to monitor the quality of ambulatory ECG systems (as mentioned in Section 2.6.3). Four ECG records namely e0103, e0104, e0105 and e0106, are selected for the simulation study. These records are affected with abnormalities such as baseline ST segment displacement and episodes of shifts resulting in apparent S-wave and T-wave changes.

For simulations, selected records are corrupted with 15dB AWGN noise, as shown in **Figure 3.15** (here, noisy ECG record e0104 is shown with its spectrogram) and corresponding quantitative results are recorded in **Table 3.9**. The signal's length is limited to 15,000 samples and modified limb lead MLIII is chosen as reference.

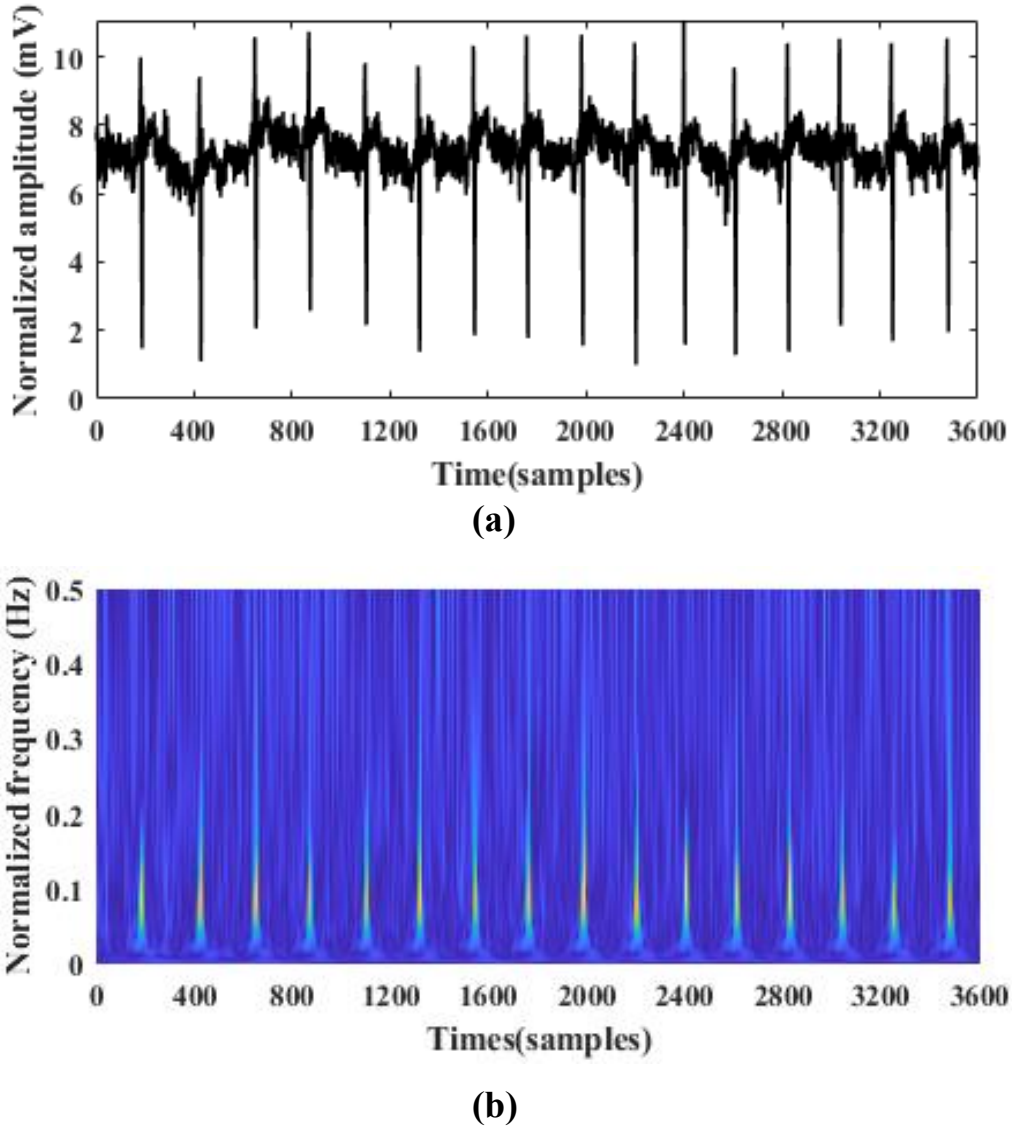

Figure 3.15 (a) Time domain representation of ECG record no. e0104 from *European ST-T Database* corrupted with 15dB additive white Gaussian noise, **(b)** FrST spectrogram for noisy ECG at a= 0.5, p= 0.5 and q=0.5

As per **Table 3.9**, *proposed* method has obtained lower values of *RMSE* and much higher values of *imp_SNR* as compared to ST method. This proves the effectiveness of *proposed* method and thus making it a suitable contender for ECG pre-processing techniques.

Table 3.9 Comparison results for *proposed* method and ST method at 15 dB input noise level for *European ST-T Database* ECG records

ECG records no.	ST method		***Proposed* method *a*=0.5, *p*=0.5, *q*=0.5**	
	RMSE	***imp_SNR***	***RMSE***	***imp_SNR***
e0103	0.1453	16.4603	0.0469	24.6292
e0104	0.1569	15.7564	0.057	22.0665
e0105	0.1145	19.1578	0.0505	23.1446
e0106	0.1187	18.9624	0.0424	24.1596

3.2.2.5 Comparison of *Proposed* Method with State-of-the-Art Methods

For comparing the performance of *proposed* method with other state-of-art methods, full-length ECG records similar to the ones presented in other simulation studies [58, 209, 210] are selected, i.e., ECG records 100, 101, 103 and 113. The *imp_SNR* of selected records at input noise level of 5 dB is shown in **Figure 3.16**.

It is evident from the graphical depiction that *proposed* method outperforms conventional ST and WT methods in showing SNR improvement. Also, our *proposed* method shows significant improvement compared to Fourier decomposition-based [58] method in which the signals are corrupted with a 5 dB input level noise of two types: power line interference (*PLI*) noise and baseline wander (*bwm*).

Hence, it can be stated that our *proposed* method has the potential to denoise ECG signals and can be a good substitute in the preprocessing stage of a computer-aided ECG analyzing system.

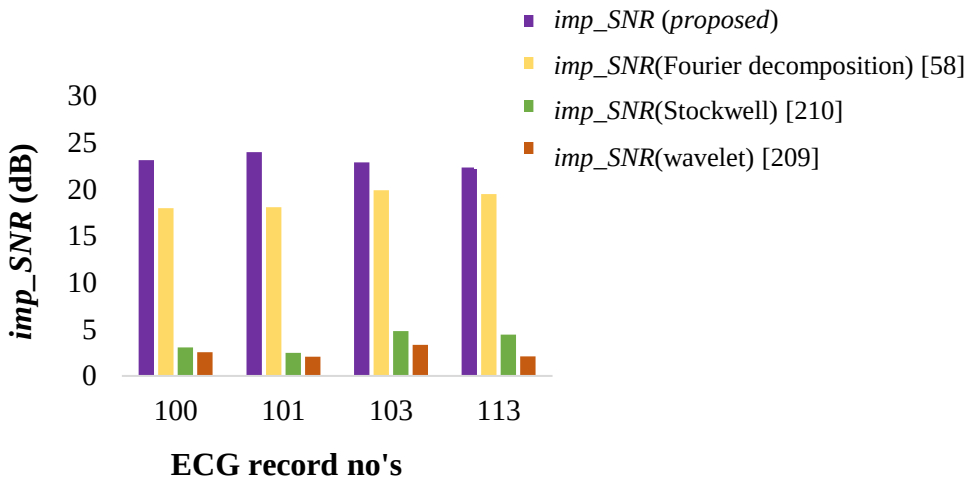

Figure 3.16 Comparison of obtained *imp_SNR* (dB) of *proposed* method with other state-of-art methods.

3.3 QRS Complex Detection of ECG Signals based on FrST

QRS complex, the most prominent component in ECG waveform, plays a key role in analyzing ECG signals and provides an effective basis for various front-end ECG signal processing measures. However, due to physiological variability of QRS complex and noise encountered during acquisition, the morphology of ECG gets affected. So, computer-aided diagnosis for accurately delineating the QRS complex is needed to assist physicians and doctors in providing suitable medical intervention to patients.

Researchers have established a wide variety of QRS detection methods. Initially, the QRS detector developed by Pan and Tompkins [64] based on linear filtering techniques and nonlinear transformations was used. To enhance the performance of this algorithm, Hamilton and Tompkins [213] introduced modification by optimizing the involved decision rules. Many detectors based on the first derivative and involving combination of Hilbert transform were also developed to detect QRS complex [65]. However, these algorithms were based on processing in time and frequency domains and hence suffered from the limitation of tracking time-varying morphology of ECG signal and made the detection of QRS complex erroneous.

To overcome this, numerous methods based on TF tools have been developed for detecting QRS complexes. The techniques based on WT utilize the decomposition mechanism using

different wavelet functions and soft and hard-based thresholding [73]. On the other hand, ST method utilizes Gaussian window known to have the best time-frequency bandwidth product to extract the complex features [74, 162]. Also, Empirical Mode Decomposition (EMD) based techniques are popular as they decompose signal into various IMFs and process components with different frequency ranges [55].

The application and thorough study of rich literature prove the significance of using FrFT and ST for studying the time-varying nature of signals. However, most of the literature mainly contributes to the work done by both of these tools in isolation. Hence, an attempt has been made to amalgamate the concepts of FrFT and ST. FrST provides the modification in frequency-dependent resolution provided by ST. It utilizes window adjustment parameters (p and q) to achieve higher fractional-frequency resolution by adjusting the fractional order parameter (a), which helps in extracting characteristic information of signal better.

In this section, ambiguities of time-varying morphology of ECG signal faced by existing state-of-the-art methods are addressed by incorporating FrST-based five-stage methodology for QRS complex detection, depicted in **Figure 3.17.**

Stage 1 Computation of FrST: Based on the algorithm described in Section 3.1.1, FrST of ECG signal is computed. Here, ECG signals are taken from MIT-BIH Arrhythmia Database [196].

Stage 2 Calculation of Fractional Stockwell Shannon Energy Envelope (FrSShnE): Shannon energy (ShnE) is among the nonlinear transformation methods used to transform a bipolar ECG signal into a unipolar signal for detecting R-peaks. It is defined as the averaged energy spectrum and is used for enhancing QRS complexes using a single-sided threshold mechanism [214]. The ShnE method significantly changes QRS amplitude values and highlights low and medium-level QRS better than other methods. Hence, ShnE is adopted for further processing in the *proposed* method. Here, the advantage of improved resolution provided by FrST is combined with ShnE method to compute FrSShnE envelope. The envelope

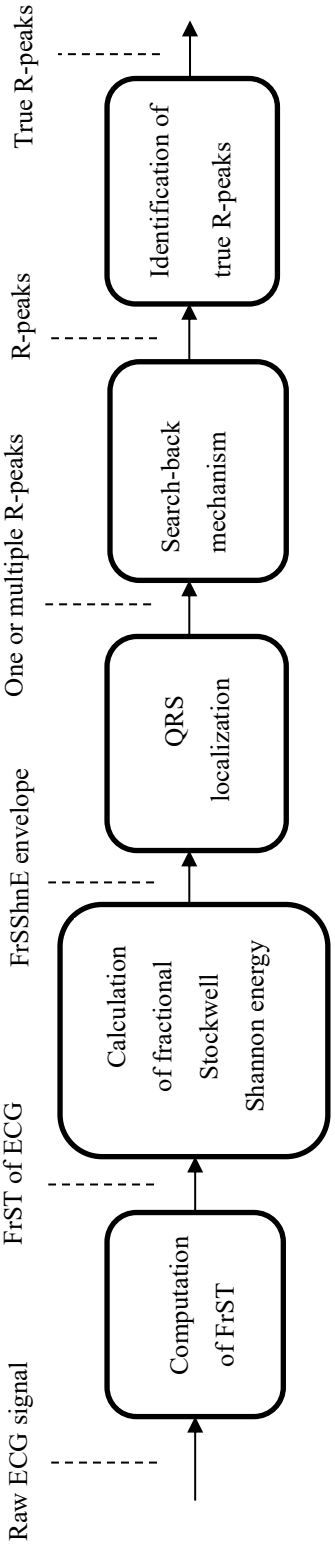

Figure 3.17 *Proposed* block diagram for QRS complex detection

is extracted for 5-22.5 Hz as QRS complexes are more prominent in this frequency range. FrSShnE envelope is defined by:

$$FrSShnE(k) = -\sum_{m=m_o}^{m_1} [FrST(k,m)]^2 log[FrST(k,m)]^2 \quad (3.12)$$

with m_o and m_1 corresponding to lower and upper limit of selected frequency and index k indicates row of FrST matrix.

Stage 3 QRS Complex Localization: In this stage, localization is performed to detect QRS complex. It is accomplished by comparing the position of extracted FrSShnE envelope with a detection threshold. This threshold plays a major role in detecting R-peaks. If threshold is greater than or lower than the required level, number of false negative (FN) and false positives (FP) increases, respectively. Various QRS detectors reported in the literature [64, 213, 215] employ different thresholding schemes to estimate the detection threshold levels. Usually, QRS detectors work well with the threshold coefficients in the range of 0.3 to 0.4 and therefore, in *proposed* methodology, detection threshold is given by

$$\lambda = 0.3\max(FrSSE_n) \quad (3.13)$$

where $FrSShnE_n = FrSShnE/|max(FrSShnE)|$ is chosen for accurate localization of QRS complex. The procedure for calculating QRS localization process using the normalized FrSShnE envelope is as follows:

i. For finding FrSShnE envelope associated with QRS complex, detection threshold is applied on the computed $FrSShnE_n(k)$ using (3.13). The positions (k) where $FrSShnE_n(k) \geq \lambda$, are considered and the positions where $FrSSE_n(k) < \lambda$ are discarded.

ii. If multiple peaks are detected within the difference of 36 samples (100 ms), then the one with lower energy is eliminated. Also, in identifying the complex positions, refractory blanking (200 ms i.e., 72 samples) is considered for eliminating the multiple detections of QRS complex and false detection corresponding to T-wave [74].

Stage 4 Search-back algorithm: It is a method that re-evaluates previously rejected QRS peaks when the significant time has elapsed without detection. Therefore, a secondary threshold is applied within 150% of the current RR interval by using new threshold of 0.5 times the threshold value selected in Stage 3 [65, 73, 74, 213, 216].

Stage 5 Identification of true R-peak: The location of detected R-peaks may vary slightly from the annotated time instants of true R-peaks. So, to find the real position of R-peak, largest amplitude within ± 25 samples of the identified location is searched and correct time of occurrence of the detected R-peak is determined [216]. Also, if the detected R-peak does not lie within 50 ms of the annotated time frame, it is considered as FP.

3.3.1 Performance Metric Parameters

To illustrate the performance of *proposed* method, four performance metric parameters: *Sensitivity*, *Positive Predictivity*, *Error Rate* and *Detection Accuracy* are chosen. The four performance metric parameters are collectively dependent on fractional order parameter a and two window adjustment parameters p and q, respectively.

The performance metric parameters are defined as follows [211]:

$$Sensitivity = \frac{TP}{TP + FN} \tag{3.14}$$

$$Positive\ Predictivity = \frac{TP}{TP + FP} \tag{3.15}$$

$$Error\ Rate = \frac{FN + FP}{Total\ detected\ beats} \tag{3.16}$$

$$Detection\ Accuracy = \frac{TP}{TP + FP + FN} \tag{3.17}$$

where *TP*, *FP*, and *FN* are similar to four labels of confusion matrix (used for classification), indicating correct and wrong detection of QRS complex. The parameter *TP* is true positive; indicating correct detection of QRS complex, *FP* is false positive; indicating the number of falsely detected QRS complexes and *FN* is false negative; indicating the number of missed QRS complexes.

For classical QRS detection algorithms [55, 64, 65, 73, 74, 213, 216, 217, 218], process rarely involves any variable parameter on which output result visualization (qualitative analysis) and performance metric (quantitative analysis) depends. Contrary to the classical approaches, performance of *proposed* algorithm is dependent on three variable parameters a, p and q. This provides three degrees of freedom and as a result increases the flexibility of QRS detection process.

ECG records present in the selected database contains different types of annotation beats such as *normal beat*, *premature ventricular extraction*, *paced beat*, the *fusion of paced and normal beat*, the *fusion of ventricular and normal beat* and *unclassifiable beat*. The detection of QRS complex of these beats is considered as *TP*. Total of all R-peaks detected from these beats combines to form *TPs* (109494 beats) present in MIT-BIH database. The ECG records also contain non-beat annotations such as *ventricular flutter wave*, *non-R-peaks* (P-wave, T-wave, and U-wave), and isolated *QRS like artifacts* which are treated as *FP* if detected.

3.3.2 Simulation Results

The *proposed* method utilizes three degrees of freedom, which means three FrST parameters (a, p and q) may be varied to achieve desired results. For accurate delineation of QRS complex, an optimal value set of FrST parameters is required. Finding an optimal value set for FrST spectrogram of ECG signal usually implies high energy distribution (resolution) over time-fractional Fourier frequency domain. This optimal time-fractional frequency concentration will contribute in achieving a better FrSShnE envelope and better localization of QRS complex.

Numerical simulations carried out to assess the effectiveness of *proposed* method are divided into two sections: simulations to determine the optimal values for FrST parameters (a, p, and q) and performance evaluation of *proposed* method to compare it with existing techniques using the aforementioned performance metric parameters.

3.3.2.1 Parameter-based Performance Evaluation of *Proposed* Detection Method

For computing the optimal value set, an approach based on quantitative analysis is followed, in which a small length of the ECG record is initially considered. For experimental purposes, a time span of 5 minutes (108,000 samples) is considered. FrST spectrogram for different segments of ECG waveform is analyzed for detecting R-peaks by varying fractional order parameter (a) and window adjustment parameters (p and q). The simulations are performed by keeping two parameters (any two out of a, p and q) constant at a time (here, a constant value of 0.5 is taken only for experimentation) and the third one is varied as 0.1, 0.3, 0.5, 0.7, 0.9 and 1.1, respectively. The results for ECG record no. 119 are tabulated in **Tables 3.10**, **3.11** and **3.12**. The variation of true positives (*TP*), false positives (*FP*) and false negatives (*FN*) with FrST parameters have been investigated in

Figures 3.18, **3.19** and **3.20** for ECG record no. 119, respectively. The results are verified for every annotated beat from the database [196].

On examining the results presented in **Tables 3.10**, one can determine the effect of varying FrST parameters on *TP*, *FP*, and *FN*. The results for fractional order parameter α = 0.5 and 0.7 have maximum *TP* =108, whereas for fractional order parameter less than 0.5 (α = 0.1 and 0.3) and more than 0.7 (α = 0.9 and 1.1) has a smaller number of *TP*s as can be seen from **Figure 3.18**. Furthermore, the trend of detecting true beats decreases for lower and higher values of α and better results are obtained at α = 0.5 and 0.7.

Next, from **Table 3.11** we can see that the results for window adjustment parameter_1 i.e., p = 0.1, 0.3 and 0.9 show poor performance in terms of achieved *TP* and give the worst value at minimum value of p = 0.1 with *TP* = 83. Thus, as value of p approaches the lower values, the error in detection of true peaks becomes greater.

Lastly, from **Table 3.12** we can infer that for window adjustment parameter_2 i.e., q =0.9 and 1.1, shows poor performance by achieving the worst count of *TP* =21 at q = 1.1. Thus, the trend of detecting accurate beats improves as the value of q approaches 0 and it deteriorates for the values approaching 1.

Next, the variation of *FP* with respect to FrST parameters is shown in **Figure 3.19**. The results show that the maximum number of wrongly detected QRS complexes are obtained at α =0.9 and 1.1, with each giving *FP*= 4. Also, at p =0.1, 0.3, 0.9 and 1.1 and q = 0.7, 0.8

Table 3.10 Performance results **varying α** and keeping $p = q = 0.5$ for ECG record 119

α	p	q	Total Beats	True Positives (*TP*)	False Positives (*FP*)	False Negatives (*FN*)
0.1	0.5	0.5	108	104	2	4
0.3	0.5	0.5	108	108	1	1
0.5	0.5	0.5	108	**108**	**0**	**0**
0.7	0.5	0.5	108	108	0	1
0.9	0.5	0.5	108	107	4	2
1.1	0.5	0.5	108	107	4	2

Bold values indicate the maximum TP and minimum FP and FN obtained by varying the parameter α.

and 0.9, the results have shown wrong detection, giving the maximum number at p =0.1 with *FP* =33 and at q =1.1 with *FP* =36, respectively.

Similarly, examining the results shown in **Figure 3.20**, count of missed QRS complexes is worst for higher values of q, i.e., at q = 1.1, *FN* obtained a value of 87. For other parameters, the worst count is achieved at p = 0.1 and a =0.1 with *FN*= 25 and *FN*=4, respectively.

Moreover, the reason behind the observed trend of variation in *TP*, *FP* and *FN* for different values of FrST parameters a, p and q can be ascertained with the concept of resolution of ECG signal in the time-fractional frequency plane. Window adjustment parameters (p and q) play a key role in deciding the resolution of the signal spectrum, as demonstrated in Section 3.1.2. As the value of p approaches 0 (or q approaches 1), fractional Gaussian window [47, 219] becomes wider, resulting in poor resolution and decreasing the accuracy of detecting QRS complex. Thus, **Tables 3.10**, **3.11** and **3.12** summarize the effect of varying FrST parameters on *TP*, *FP* and *FN* using *proposed* method.

Hence, the optimal value set of FrST parameters (as concluded by repeated simulations) is found to lie within the range of 0.4 to 0.6, which is deduced by eliminating all erroneous cases of wrong detection. Any combination of (a, p, q) lying in the range of 0.4 to 0.6 will contribute to better detection of QRS complex. In subsection 3.3.2.2, the value set of (0.5, 0.51, 0.51) is chosen to assess the performance of *proposed* method on all ECG records available in the selected database.

Table 3.11 Performance results **varying p** and keeping $a = q = 0.5$ for ECG record 119

a	p	q	Total Beats	True Positives (*TP*)	False Positives (*FP*)	False Negatives (*FN*)
0.5	**0.1**	0.5	108	83	33	25
0.5	**0.3**	0.5	108	103	15	5
0.5	**0.5**	0.5	108	**108**	**0**	**0**
0.5	**0.7**	0.5	108	**108**	**0**	**0**
0.5	**0.9**	0.5	108	101	4	7
0.5	**1.1**	0.5	108	108	10	0

Bold values indicate the maximum TP and minimum FP and FN obtained by varying the parameter p.

Table 3.12 Performance results **varying** q and keeping $a = p = 0.5$ for ECG record 119

a	p	q	Total Beats	True Positives (*TP*)	False Positives (*FP*)	False Negatives (*FN*)
0.5	0.5	**0.1**	108	**108**	**0**	**0**
0.5	0.5	**0.3**	108	**108**	**0**	**0**
0.5	0.5	**0.5**	108	**108**	**0**	**0**
0.5	0.5	**0.7**	108	108	1	0
0.5	0.5	**0.9**	108	103	10	5
0.5	0.5	**1.1**	108	21	36	87

Bold values indicate the maximum TP and minimum FP and FN obtained by varying the parameter q.

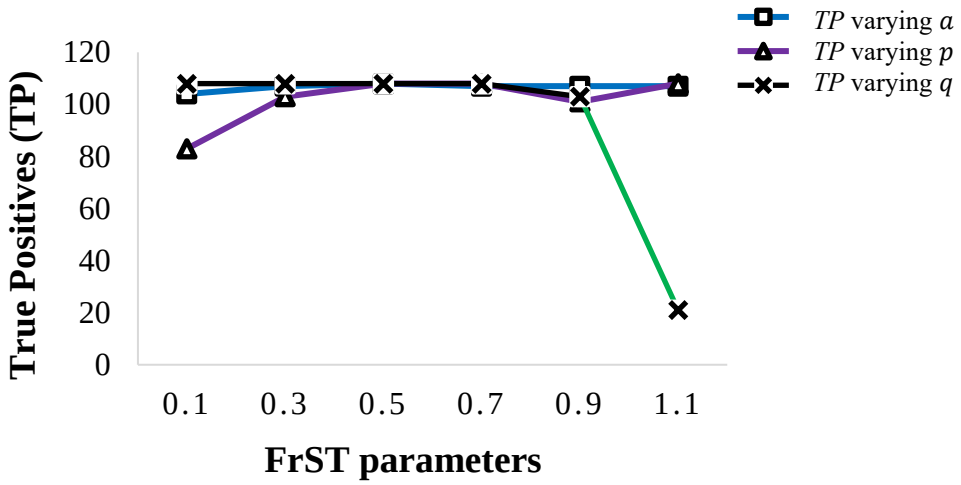

Figure 3.18 Variation of *TP* with FrST parameters (a, p and q) for ECG record no. 119

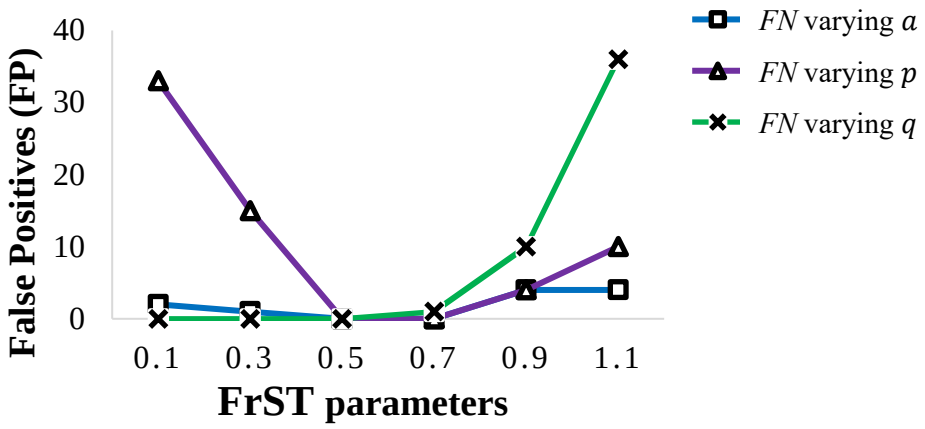

Figure 3.19 Variation of *FN* with FrST parameters (a, p and q) for ECG record no. 119

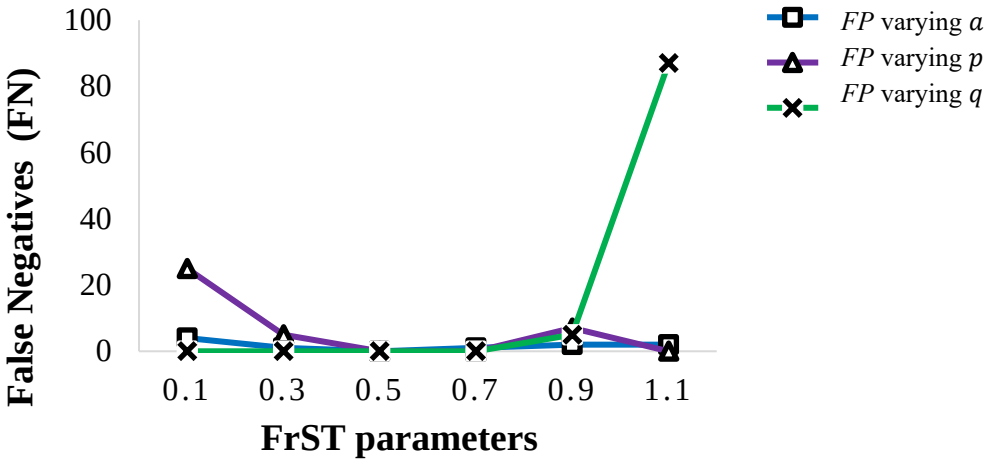

Figure 3.20 Variation of *FP* with FrST parameters (a, p and q) for ECG record no. 119

3.3.2.2 Performance Evaluation of all MIT-BIH ECG records

The performance of *proposed* method is investigated for all 48 records available at MIT-BIH Arrhythmia database [196]. The output waveforms obtained from different stages of *proposed* method are shown in **Figure. 3.21**. The results depicted in **Figure 3.21(a)** is the original ECG signal, **Figure 3.21(b)** illustrates FrST spectrum of ECG signal and **Figure 3.21(c)** shows normalized FrSShnE plot of the associated signal with marked R-peak instants.

For quantitative analysis, statistical parameters, namely *Sensitivity*, *Positive Predictivity*, *Error Rate* and *Detection Accuracy* are calculated at $a = 0.5$, $p = 0.51$, $q = 0.51$ as explained in subsection 3.3.2.1. The experimental results for performance evaluation on ECG records are tabulated in **Table 3.13**. Furthermore, the experiments are conducted on every 15-second-long segment of the ECG record and therefore there are a total of 120 segments that add up to 30 minutes of record length. The computation time of every segment is 29 sec.

The *proposed* method provides an *Error Rate* of 0.03%, which is lowest among those obtained by any other methods reported in well-established literature [55, 74, 217, 218, 220, 221]. *Error Rate* less than 0.2% is achieved for the following records: 101, 104, 105, 200, 201, 207, 208, 210, 214, and 228, and for the rest of the records, it is 0%. Only record 203 gives an *Error Rate* of 0.5%.

The performance comparison of *proposed* method with other methods is reported in **Table 3.14**. The *proposed* technique has clearly demonstrated superior performance by accurately detecting 99.99% of all beats. Of the total 48 records, 38 give 0% *Error Rate*, 100% *Sensitivity* and 100% *Positive Predictivity*. Total number of obtained *FP* and *FN* are 29 and 8 respectively, which is much less than other literature methods [55, 74, 217, 218, 220, 221].

The *proposed* method has reported a highest *Error Rate* of 0.5% for ECG record no. 203, which is much less than *Error Rate* reported for corresponding record utilizing [74] method. This record is the most challenging record containing sudden amplitude changes of R-peak. Also, this record is corrupted with muscle artifact and baseline shifts, which makes it difficult to localize the QRS complex accurately. With the optimal value set, *proposed* method manages to give *FN*=5 and *FP*=10.

For comparing the ability of *proposed* method over ST method [74], a small segment from 1260.8 sec. to 1262.4 sec. of ECG record no. 208 is selected, as illustrated in **Figures 3.22** and **3.23**. In these illustrations, first waveform shows the marked instants of R-peaks present for ECG record no. 208. The blue square highlights the R-peak of an *unclassifiable beat* and a non-R-peak corresponding to a *QRS-like artifact*. The *green* triangle corresponds to accurate detection of R-peak and *red* triangle corresponds to false detection.

The main features distinguishing *proposed* method from ST method are as follows:

(i) *Proposed* method shows better resolution than ST method, as depicted in **Figures 3.22(b)** and **3.23(b)**.

(ii) The envelope extracted using FrSShnE in **Figure 3.23(c)** accurately traces significant peaks in ECG signal as compared to the envelope extracted using SShnE in case of ST method as shown in **Figure 3.22(c)**.

(iii) Better R-peak detection of *unclassifiable beats* is achieved by *proposed* method giving FN =0, in contrast to ST method with FN=1 as shown in **Figure 3.22 (c)**.

Finally, the results of erroneous records (104, 105, 107, 108, 201, 203, 208 and 228) obtained with *proposed* method and ST method are compared in **Table 3.15**. Less number of FP and FN are obtained using *proposed* method.

Hence, it can be concluded that *proposed method* outperforms ST method in every aspect, i.e., better performance in terms of performance metric parameters, detection of unclassifiable beat, and fewer false detections

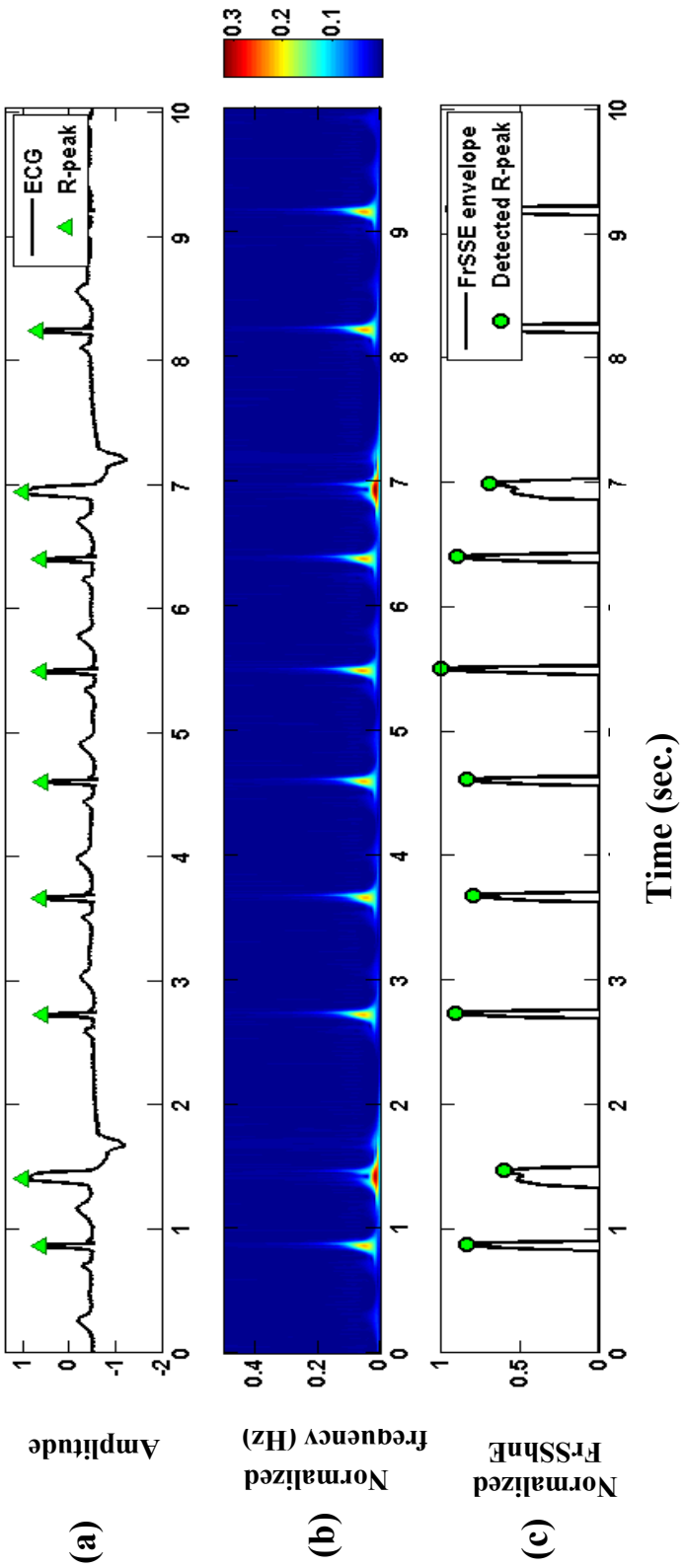

Figure 3.21 (a) Waveform of ECG record no. 119, **(b)** FrST spectrogram with color-bar scale showing the relationship between amplitude and color, **(c)** Fractional Stockwell Shannon energy (FrSShnE) plot with marked instants of detected R-peaks.

Table 3.13 Performance of *proposed* algorithm for QRS complex detection

Record No.	**Annotated** Beats	**Detected Beats**	**TP**	**FN**	**FP**	**Sensitivity**	**Positive Predictivity**	**Detection Accuracy**	**Error Rate**
100	2273	2273	2273	0	0	100.00	100.00	100.00	0.00
101	1865	1867	1865	0	2	100.00	99.89	99.89	0.11
102	2187	2187	2187	0	0	100.00	100.00	100.00	0.00
103	2084	2084	2084	0	0	100.00	100.00	100.00	0.00
104	2229	2232	2228	1	4	99.96	99.82	99.78	0.22
105	2572	2573	2571	1	2	99.96	99.92	99.88	0.12
106	2027	2027	2027	0	0	100.00	100.00	100.00	0.00
107	2137	2137	2137	0	0	100.00	100.00	100.00	0.00
108	1763	1763	1763	0	0	100.00	100.00	100.00	0.00
109	2532	2532	2532	0	0	100.00	100.00	100.00	0.00
111	2124	2124	2124	0	0	100.00	100.00	100.00	0.00
112	2539	2539	2539	0	0	100.00	100.00	100.00	0.00
113	1795	1795	1795	0	0	100.00	100.00	100.00	0.00
114	1879	1879	1879	0	0	100.00	100.00	100.00	0.00
115	1953	1953	1953	0	0	100.00	100.00	100.00	0.00
116	2412	2412	2412	0	0	100.00	100.00	100.00	0.00
117	1535	1535	1535	0	0	100.00	100.00	100.00	0.00
118	2278	2278	2278	0	0	100.00	100.00	100.00	0.00
119	1987	1987	1987	0	0	100.00	100.00	100.00	0.00
121	1863	1863	1863	0	0	100.00	100.00	100.00	0.00
122	2476	2476	2476	0	0	100.00	100.00	100.00	0.00
123	1518	1518	1518	0	0	100.00	100.00	100.00	0.00
124	1619	1619	1619	0	0	100.00	100.00	100.00	0.00
200	2601	2602	2601	0	1	100.00	99.96	99.96	0.04
201	1963	1964	1963	0	1	100.00	99.95	99.95	0.05
202	2136	2136	2136	0	0	100.00	100.00	100.00	0.00
203	2980	2985	2975	5	10	99.83	99.66	99.50	0.50
205	2656	2656	2656	0	0	100.00	100.00	100.00	0.00
207	1860	1863	1860	0	3	100.00	99.84	99.84	0.16
208	2955	2957	2955	0	2	100.00	99.93	99.93	0.07
209	3005	3005	3005	0	0	100.00	100.00	100.00	0.00
210	2650	2651	2650	0	1	100.00	99.96	99.96	0.04
212	2748	2748	2748	0	0	100.00	100.00	100.00	0.00
213	3251	3251	3251	0	0	100.00	100.00	100.00	0.00
214	2262	2261	2261	1	0	99.96	100.00	99.96	0.04
215	3363	3363	3363	0	0	100.00	100.00	100.00	0.00
217	2208	2208	2208	0	0	100.00	100.00	100.00	0.00
219	2154	2154	2154	0	0	100.00	100.00	100.00	0.00
220	2048	2048	2048	0	0	100.00	100.00	100.00	0.00
221	2427	2427	2427	0	0	100.00	100.00	100.00	0.00

Table 3.13 *continued*

Record No.	Annotated Beats	Detected Beats	TP	FN	FP	Sensitivity	Positive Predictivity	Detection Accuracy	Error Rate
222	2483	2483	2483	0	0	100.00	100.00	100.00	0.00
223	2605	2605	2605	0	0	100.00	100.00	100.00	0.00
228	2053	2056	2053	0	3	100.00	99.85	99.85	0.15
230	2256	2256	2256	0	0	100.00	100.00	100.00	0.00
231	1571	1571	1571	0	0	100.00	100.00	100.00	0.00
232	1780	1780	1780	0	0	100.00	100.00	100.00	0.00
233	3079	3079	3079	0	0	100.00	100.00	100.00	0.00
234	2753	2753	2753	0	0	100.00	100.00	100.00	0.00
Total	109494	109515	109486	8	29	**99.99**	**99.97**	**99.97**	**0.03**

Table 3.14 Comparison with other methods

Methods	Sensitivity	Positive Predictivity	Error Rate
***Proposed* method**	**99.99**	**99.97**	**0.03**
Li *et al.* (2018) [221]	99.87	99.93	-
Sahoo *et al.* (2016) [220]	99.88	99.61	0.5
Rakshit *et al*. (2016) [218]	99.95	99.88	0.16
Sabharwal *et al.* (2016) [217]	99.9	99.9	0.16
Li *et al*. (2014) [55]	99.94	99.87	0.19
Zidelmal *et al*. (2014) [74]	99.84	99.91	0.25

Bold values indicate the highest Sensitivity and Positive Predictivity and lowest Error Rate

Table 3.15 Comparison of the number of *FN* and *FP* obtained with ST and *proposed* method

Records	ST method FN	*Proposed* method FN	ST method FP	*Proposed* method FP
104	9	**1**	5	**4**
105	22	**1**	10	**2**
107	0	**0**	2	**0**
108	23	**0**	20	**0**
201	25	**0**	4	**1**
203	11	**5**	9	**10**
208	3	**0**	2	**2**
228	7	**0**	4	**3**

Bold values indicate the lowest FN and lowest FP

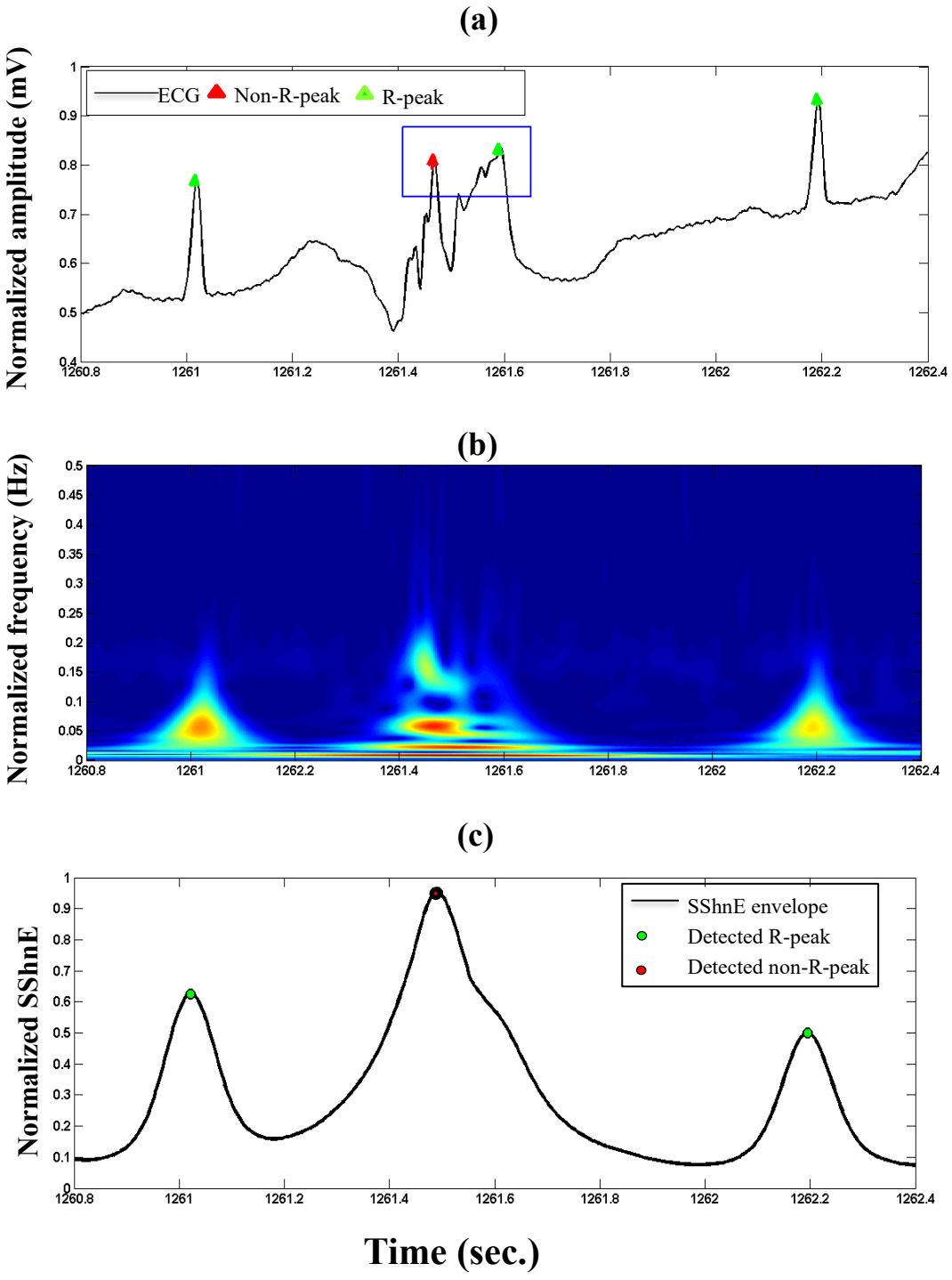

Figure 3.22 (a) ECG record no. 208 with marked instants of R-peaks, (**b)** ST spectrogram, **(c)** Stockwell Shannon energy (SShnE) plot

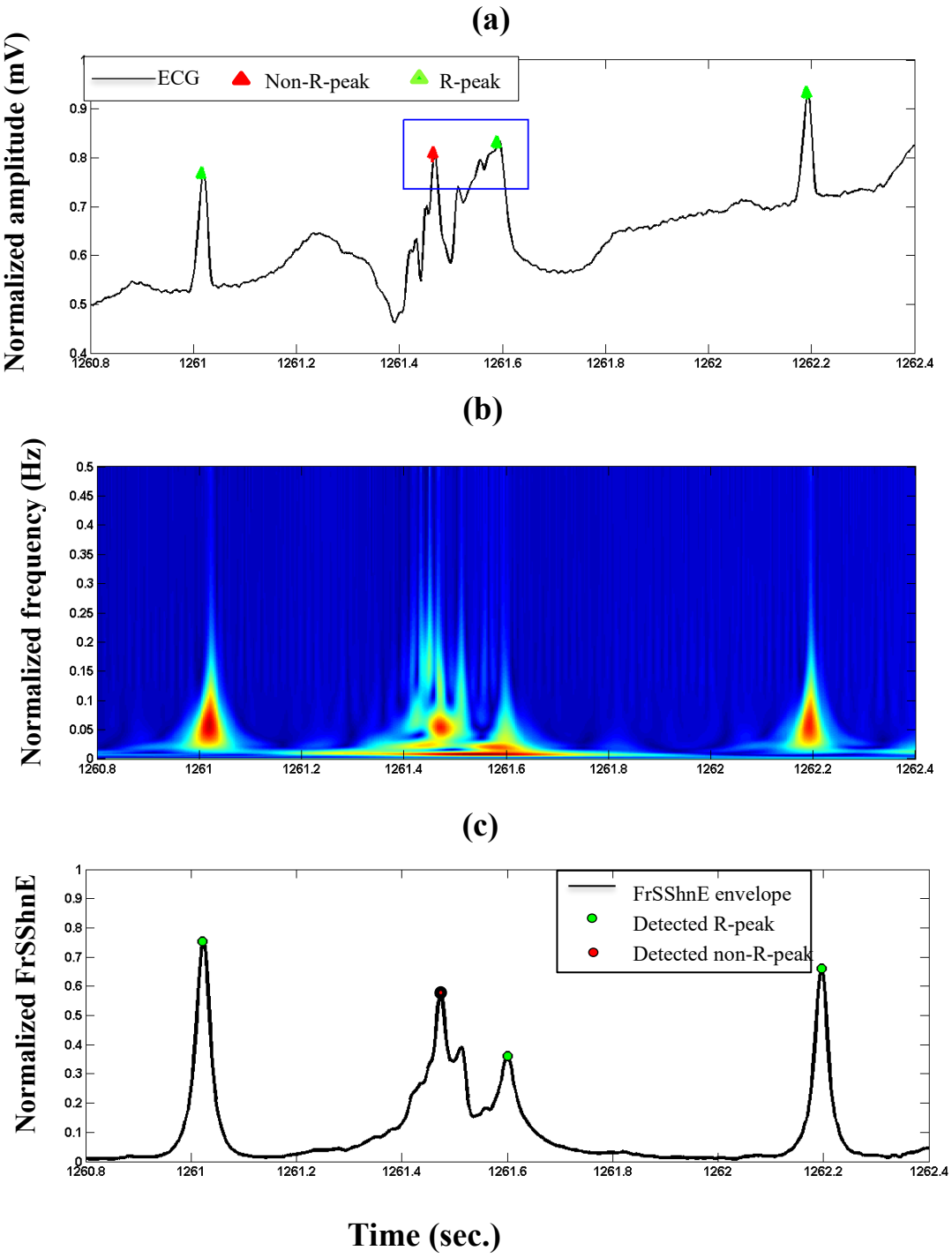

Figure 3.23 (a) ECG record no. 208 with marked instants of R-peaks, **(b)** FrST spectrogram, **(c)** Fractional Stockwell Shannon energy (FrSShnE) plot

3.4 Summary

This chapter proposes the design of denoising and QRS complex detection methods based on FrST. In the pursuit of exploring the application of FrST in non-stationary ECG signal processing, a computation algorithm for FrST is designed. From the qualitative analysis of spectrograms obtained using FrST tool and another established method, i.e., ST tool, it has been observed that FrST spectrograms outperform ST spectrogram by allowing better resolving ability and flexibility, which has enhanced the detection of QRS complex and also, improved the reconstruction performance.

Furthermore, in order to discuss the performance of FrST-based denoising, simulation studies have shown that, not only is resolution improvement achieved with FrST, but also noise corrupting ECG signal can be suppressed by varying fractional order parameter a. At the same time, information present can be enhanced by window adjustment parameters p and q. Also, comparison and validation of *proposed* method are depicted using different levels of AWGN noise levels and different real-time noises. Also, two databases are referred to prove the generalizability of *proposed* method in handling a wide variety of ECG signals. The results obtained depict robustness and superiority of *proposed* method over state-of-the-art methods. The three degrees of freedom ascertained that the combination of ST and FrFT i.e., FrST, outperforms the existing methods.

Additionally, the performance of FrST-based QRS complex detection has proved that, apart from offering fine resolution, incorporating the FrST concept with Shannon energy resulting in FrSShnE, is advantageous in detecting low and medium amplitude QRS complexes and hence, improving the performance of detection. Furthermore, it has been observed that the resolving ability achieved by varying FrST parameters has improved the detection of QRS complex of *unclassifiable beats*. The overall performance metric measures provide outstanding results in terms of *Sensitivity* (99.99%), *Positive Predictivity* (99.97%), *Error Rate* (0.03%) and *Detection Accuracy* (99.97%), which clearly validates the superiority of *proposed* method over other well-established methods.

When addressing the first issue of non-stationarity with the FrST tool, it was necessary to evaluate the proposed method by employing real-time noise and varying levels of AWGN, as shown in the denoising part of this chapter. This validation, which utilizes a Gaussian noise model, prompts a genuine curiosity about exploring the characteristics of real-time noises. The purpose is to determine whether the longstanding assumption of employing a

Gaussian model accurately replicates the behavior of real-world scenarios, or if a more comprehensive model should be adopted for assessing the robustness of any signal processing technique. Therefore, as a major contribution to the research work carried out in the thesis, an intensive investigation study is demonstrated with statistical tools to prove the existence of non-Gaussian nature in practical scenarios. Subsequently the use of α-stable distribution as noise analysis model is *proposed* as a better alternative to Gaussian distribution model for processing ECG signals.

Chapter 4

Investigation of α-Stable Distribution Noise Analysis Model for ECG Signals

The work presented in this chapter establishes the groundwork for using non-Gaussian framework (which shares similar characteristics with existing state-of-the-art Gaussian distribution model) for noise analysis. It attempts to establish the utility of *proposed* model *by analyzing behavior of existing noises using a model that is more adequate for practical scenarios—* α-stable *distribution.*

4.1 Need for Adopting Noise-Analysis Model other than Gaussian Distribution Model

The choice of filtering method is a significant factor influencing the performance of ECG processing and analysis system [58, 222]. If noises impacting ECG signal are not given enough importance, adopting any noise-reduction approach may be unsuccessful, leading to undesirable distortion in true ECG morphology. Therefore, investigating the characteristics of ECG noises can be beneficial in designing noise-reduction and filtering methods.

The noises present in real-time scenarios may not always have Gaussian nature. Additionally, since real-time noise sources may not always produce noise with finite variance, the central limit theorem (CLT) does not apply to these noise sources. Thus, Gaussian assumption may not always be valid (as discussed in Section 2.3.1). Under non-Gaussian conditions, degradation in the performance of conventional Gaussian-based techniques may result in inaccurate predictions or false alarms. Furthermore, following factors highlight the current scenario.

- At the time of ECG signal acquisition, it gets corrupted by various impulsive noises and artifacts, which can cause problems in analyzing underlying condition of the heart. However, in conventional ECG signal processing techniques, artifacts are

- assumed to follow Gaussian distribution. This is why we usually use additive white Gaussian noise (AWGN) to prove algorithms' robustness under noisy conditions (physiological and environmental).
- Traditional signal processing methods such as adaptive filters [223], use statistical moments (specifically second-order moments) and criterion of least squares (i.e., LMS, RLS criterion) to develop filtering techniques to remove such noises. However, this criterion no longer applies to non-Gaussian cases, and filtering may result in signal distortion. So processing techniques need to adopt more robust noise analysis approach to better replicate the environmental conditions.
- Also, looking at the diverse applications involving ECG signals, such as wearable healthcare devices and biometrics, the importance of automated noise analysis is highly demanded for reducing false alarms. The need to distinguish between noisy excerpts and true ECG morphology is required to eliminate cases of misleading and inaccurate diagnosis.

Therefore, the main objective of this chapter is to introduce an alternative noise model and establish its efficacy to be beneficial for biomedical signal processing applications.

4.2 Analytical Investigation of Noises using Statistical Tests

From the viewpoint of investigating the characteristics of Gaussian and non-Gaussian scenarios, this section is partitioned into two sections. Initially, statistical tests are executed on variables generated by MATLAB. Then based on the analysis derived, characteristics of real-time noises that corrupt ECG signal are examined for comprehending deviation from or similarity to Gaussian distribution.

Nevertheless, our investigation will revolve around four categories of statistical tests: *visual inspection*, *statistical moments*, *parameter estimation* and *non-parametric tests*.

4.2.1 Simulated Variables

To assist in understanding the behavior of real-time noises in next section, statistical analysis on MATLAB-generated random variables of Gaussian nature (denoted as G1, G2 and G3) and non-Gaussian α-stable nature (denoted as A1, A2, and A3) is performed in this section. The random variables- G1, G2, G3, A1, A2 and A3 are plotted in **Figure 4.1,** and the parameters at which these are generated are recorded in **Table 4.1**. For experimental

purposes, a sample size of 2000 is chosen. Additionally, α-stable random variables used in this study are generated using the method described in [224].

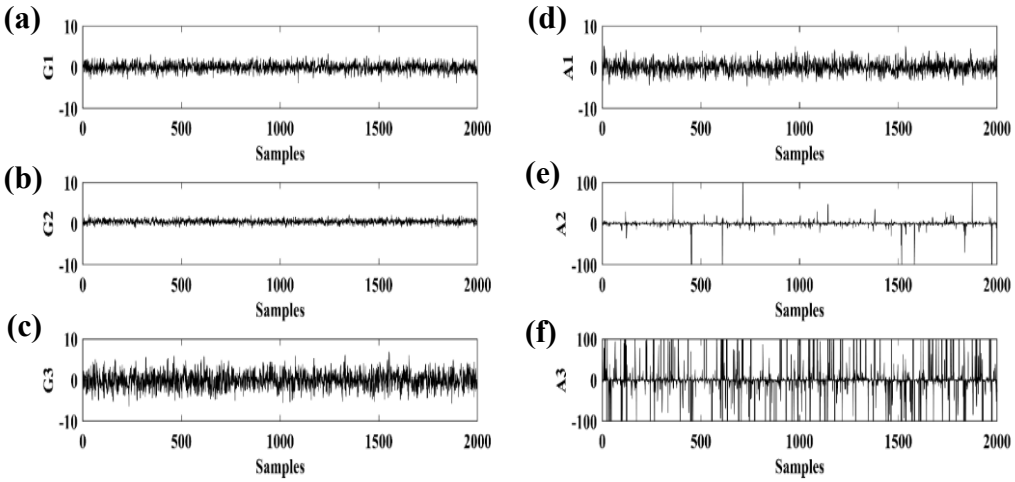

Figure 4.1 Representation of random variables of Gaussian and non-Gaussian nature: **(a)** G1, **(b)** G2, **(c)** G3, **(d)** A1, **(e)** A2 and **(f)** A3

Table 4.1 Parameters at which distribution of Gaussian and non-Gaussian random variables is generated.

Variables	Notation	Type
G1	$\mathcal{N}(0,1)$	Gaussian nature
G2	$\mathcal{N}(1,0.5)$	Gaussian nature
G3	$\mathcal{N}(5,2)$	Gaussian nature
A1	$S(2,0,1,0)$	Non-Gaussian α-stable nature
A2	$S(1.4,-0.2,1,0)$	Non-Gaussian α-stable nature
A3	$S(0.5,0,1,0)$	Non-Gaussian α-stable nature

4.2.1.1 Tests based on Visual Inspection

This category includes the most straightforward methods for identifying distribution characteristics based on their graphical representation.

(i) **Histogram**: The histograms for random variables (both Gaussian and α-stable nature) are generated and shown in **Figure 4.2**. Based on the concept of histogram outlined in Section 2.5.1.1, it can be deduced that the distribution of G1, G2, and G3 follows a normal, Gaussian distribution as evidenced by the bell-shaped histogram shape and symmetry about the mean. Furthermore, for variable A1, which represents the limiting case ($\alpha = 2$) of α-stable distribution, the histogram obtained is similar to that of Gaussian variables (G1, G2, and G3). Histograms for A2 and A3 indicate that most of data is centered around prominent peaks. This indicates that the distribution characteristics of A2 and A3 deviate from normality, becoming asymmetrical and exhibiting peaks.

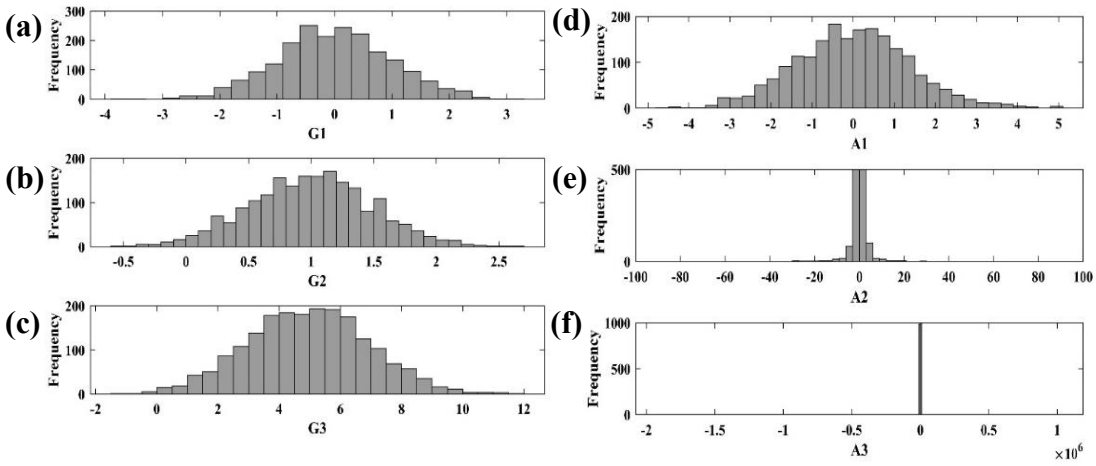

Figure 4.2 Histograms showing the distribution of Gaussian and non-Gaussian random variables: **(a)** G1, **(b)** G2, **(c)** G3, **(d)** A1, **(e)** A2 and **(f)** A3

(ii) **QQ-plot**: QQ plots of random variables are shown in **Figure 4.3** with GQ representing the quantiles of Gaussian distribution (here, we have used standard Gaussian distribution with mean=0 and variance=1) and RQ represents quantiles of the sample, for which, type of distribution has to be identified as *Gaussian* or *non-Gaussian*.

Upon examining **Figure 4.3**, it is evident that the data points for G1, G2, G3 and A1 are accurately aligned, as depicted in **Figures 4.3(a)**, **4.3(b)**, **4.3(c)**, and **4.3(d)** respectively. Here, the linear relationship or straight line indicates the Gaussian structure of the distribution. However, in the case of A2 (**Figure 4.3**(e)) and A3 (**Figure 4.3** (f)), there is observable divergence at the endpoints of GQ line. This deviation is characterized by extended tails, providing evidence that the distribution of A2 and A3 is *non-Gaussian*.

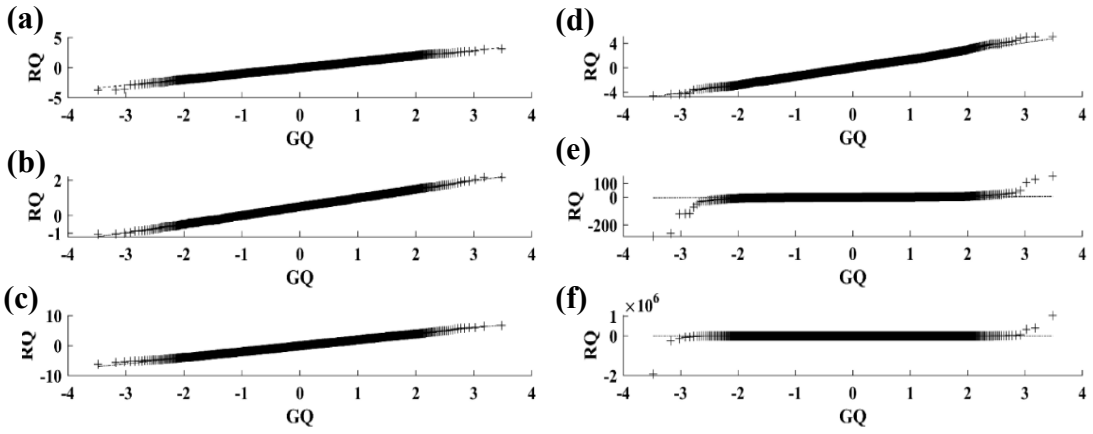

Figure 4.3 QQ plots of Gaussian and non-Gaussian random variables: **(a)** G1, **(b)** G2, **(c)** G3, **(d)** A1, **(e)** A2 and **(f)** A3

4.2.1.2 Statistical Moment Theory

The values of these statistical moments for the random variables are given in **Table 4.2**.

(i) **Mean- the First Moment**: Transitioning to the examination of random variables based on this concept, it is observed that the mean of Gaussian variables G1, G2, and G3 is in line with μ value with which the Gaussian distribution was generated, as reported in **Table 4.1**.

Furthermore, from the viewpoint of analyzing for non-Gaussian characteristics, it is described in Section 2.5 that for α-stable variables, mean is zero for $\alpha > 1$ and is undefined for $\alpha < 1$. Therefore, upon examining mean values for α-stable variables, it is observed that the mean for A1 $(\alpha = 2)$ is 0.00 and 0.07 for A2 $(\alpha = 1.4)$, which complies with the concept of mean for α-stable distribution.

Furthermore, to prove the concept of finite mean for Gaussian variables and the infinite mean concept for α-stable variables, the *running mean* is computed and their graphs are shown in **Figure 4.4**. The *running mean* graphs for variables G1, G2, G3, A1 and A2 converges to a finite value and for A3$(\alpha = 0.5)$ mean exhibits a large negative value. The large value attained for A3 aligns with the notion of undefined mean as outlined for α-stable distribution family [49].

(ii) **Variance- the Second Moment about Mean**

To represent the concept of variance, it is observed that the values of variance for G1, G2, and G3, as presented in **Table 4.2**, correspond to the value σ^2 i.e., variance at which distributions were generated, as tabulated in **Table 4.1**.

Furthermore, to understand this concept from non-Gaussian point of view, *the running variance* method is illustrated in **Figure 4.5**. As stated in Section 2.3, for α-stable distribution, variance is infinite for $\alpha < 2$. Therefore, as shown in **Figure 4.5**, variances of all variables converge to specific value except for A2 and A3, where the graph appears to diverge and has very large value. This diverging behavior explains the behavior of α-stable variables and justifies the concept of infinite variance as described for α-stable distribution family [49].

(iii) **Skewness- the Third Moment**

Before analyzing skewness values obtained for generated random variables, it is worth mentioning that the skewness coefficient values are constrained in the range of $[-1,1]$. Now, on analyzing values from **Table 4.2**, values of skewness for variables with *Gaussian* nature (G1, G2, G3 and A1) seem to lie within the range as expected for Gaussian distribution. But for α-stable variables with $\alpha < 2$ (i.e., for A2 and A3), the skewness values obtained do not even comply with the range of skewness used in descriptive statistics for analyzing real data [184] . This proves that the third moment does not exist for α-stable variables. Hence, skewness could help to differentiate between Gaussian and non-Gaussian behavior.

(iv) **Kurtosis- the Fourth Moment**: On analyzing Kurtosis values from **Table 4.2**, Gaussian variables: G1, G2 G3 and A1 have kurtosis value close to 3, whereas, for A2 and A3, the values are high enough and do not comply with the acceptable range for kurtosis used in descriptive statistics [184]. Thus, from skewness and kurtosis values, we can conclude that higher-order statistics do not exist for α-stable variables A2 and A3 and have non-Gaussian nature.

Therefore, statistical moments hold a significant place in analyzing deviations from normality and are advantageous in identifying non-Gaussian characteristics.

Table 4.2 Statistical moments of Gaussian and non-Gaussian random variables.

	Gaussian			**Non-Gaussian**		
	G1	**G2**	**G3**	**A1**	**A2**	**A3**
Mean	-0.01	1	4.96	0.00	0.07	-264.45
Variance	0.99	0.49	1.98	1.41	11.75	50758.79
Skewness	-0.01	-0.01	0.06	0.12	-11.76	-22.70
Kurtosis	3.03	2.99	2.90	3.25	323.62	1126.22

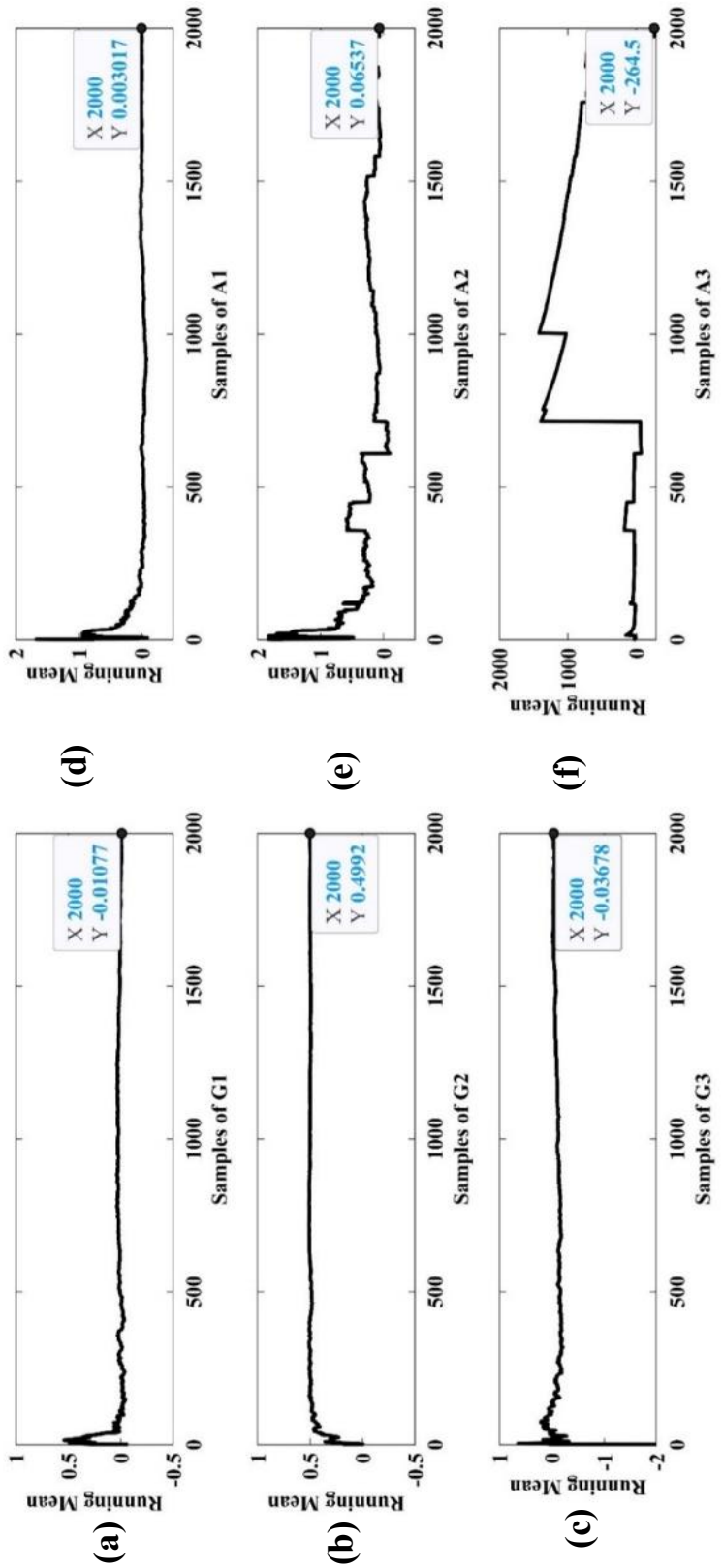

Figure 4.4 Running Mean plots for random variables: **(a)** G1, **(b)** G2, **(c)** G3, **(d)** A1, **(e)** A2 and **(f)** A3

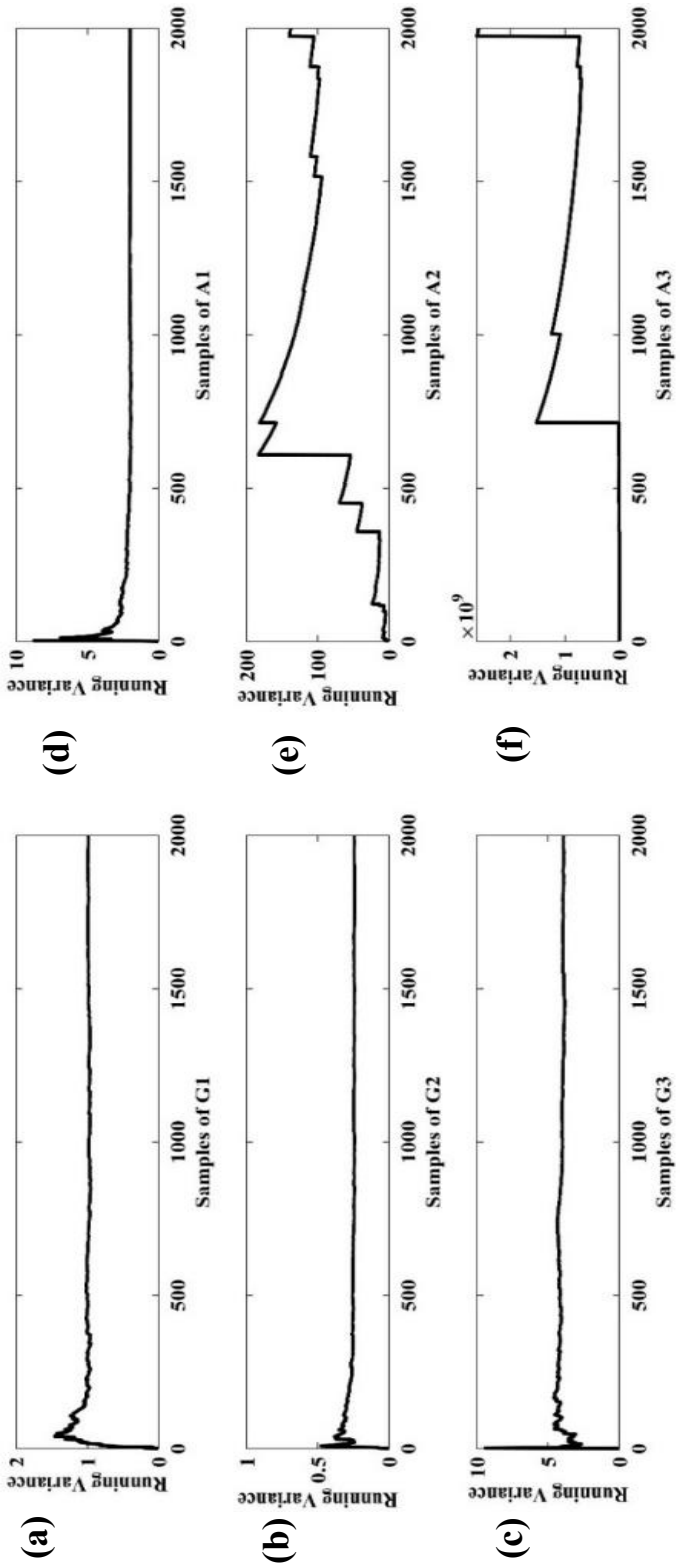

Figure 4.5 Running Variance plots for random variables: **(a)** G1, **(b)** G2, **(c)** G3, **(d)** A1, **(e)** A2 and **(f)** A3

4.2.1.3 Chi-Square Goodness-of-Fit Test

As demonstrated in Section 2.5.3.1, this test is a normality test performed on the generated variables (Gaussian and α-stable variables) to check the hypothesis that if variables follow normal distribution, or they show deviation from normality assumption. The results are recorded in **Table 4.3**, with hypothesis defined as:

Null hypothesis, H_O: The sample data follows the *Normal* distribution.

Alternate hypothesis, H_A: The sample data do not follow the *Normal* distribution.

On analyzing obtained values, it is observed that for G1, G2, G3 and A1– the *chistat* value, χ^2 values are less than the χ_a^2 computed at a significance level, $a = 0.05$. This implies that our null hypothesis (H_o) is true and variables follow normal distribution, i.e., have a Gaussian nature and *normal* distribution is a good fit for these variables.

On the other hand, for A2 and A3 the *chistat* value χ^2 is greater than the χ_a^2 computed at the same significance level. Therefore, it shows that our null hypothesis (H_o) is rejected in favor of alternate hypothesis that *normal* distribution is not a good fit for these variables.

Table 4.3 Chi-Square goodness of fit test performed on MATLAB generated variables

	Gaussian			**Non-Gaussian**		
	G1	**G2**	**G3**	**A1**	**A2**	**A3**
h	0	0	0	0	1	1
p	0.176	0.7712	0.5096	0.147	<0.00001	<0.00001
df	6	7	7	6	1	1
$\boldsymbol{\chi^2}$	8.9577	4.0743	6.2609	9.6397	5.10E+45	5.16E+116
$\boldsymbol{\chi^2_{0.05}}$	11.07	12.592	12.592	11.07	3.841	3.841

Note: Here, **h**= is the hypothesis value, **p**= probability of observing the result values in favour of the null hypothesis, $\boldsymbol{df}$ is the degree of freedom, $\boldsymbol{\chi^2}$ is the observed Chi-square test statistic and $\boldsymbol{\chi^2_{0.05}}$ is the Chi-square test statistic obtained at significance level $\boldsymbol{a = 0.05}$ for a given degree of freedom.

4.2.1.4 Parameter Estimation Tests

This section intends to verify the correctness and effectiveness of parameter estimation methods in handling the sample-given data. **Table 4.4** and **Table 4.5** records the results obtained from the estimation tests– McCllouch [108] and Kogon and Williams [110], respectively. On comparing the results obtained using methods mentioned above with previously attained **Table 4.1** (which contains the actual parameters, at which corresponding variables were generated in the first place), following observations are made:

(i) Both methods (**Tables 4.4 and 4.5**) are effective in estimating the distribution parameters for both types of variables: Gaussian distributed as well as non-Gaussian α-stable distributed.

(ii) The results in **Table 4.5** display a higher level of accuracy than those outlined in **Table 4.4**, so Kogon and Williams method will be employed for the *proposed* study later.

Subsequently in next section, chosen parameter estimation will be employed along with significance tests to find the "best fit" among distributions for the underlying data.

Table 4.4 Parameter Estimation using McCllouch method

	G1	**G2**	**G3**	**A1**	**A2**	**A3**
$\boldsymbol{\alpha}$	1.87	1.96	2.00	1.92	1.26	0.59
$\boldsymbol{\beta}$	-0.09	-0.14	-0.01	0.01	-0.21	0.10
$\boldsymbol{\gamma}$	0.68	0.34	1.41	0.97	0.97	0.95
$\boldsymbol{\delta}$	-0.01	0.51	-0.02	0.01	0.14	-0.15

Table 4.5 Parameter estimation using Kogon-William's method

	G1	**G2**	**G3**	**A1**	**A2**	**A3**
$\boldsymbol{\alpha}$	2.00	2.00	2.00	1.98	1.26	0.49
$\boldsymbol{\beta}$	1.00	-1.00	-1.00	0.97	-0.27	-0.08
$\boldsymbol{\gamma}$	0.70	0.35	1.41	0.98	0.99	0.97
$\boldsymbol{\delta}$	-0.02	0.50	-0.06	-0.03	0.61	0.00

4.2.2 Experimental Study on Real-Time Noises Corrupting ECG Signals

The literature has always used additive white Gaussian noise for ECG signal processing to validate and test the noise-removal methods. Also, the trend of using Gaussian distribution noise is supported by the fact that this noise model allows easy analytical manipulation. However, as the real-time noises have higher amplitudes, impulsive nature and are asymmetric, therefore in this section, we shift our focus from Gaussian assumption and attempt to analyze the statistical behavior of noises corrupting ECG signals. Based on the results and analysis drawn from the statistical tests in preceding section, this section will investigate the behavior of real-time noises.

For investigating behavior of real-time noises corrupting ECG signals, real-time noise data from three Physionet databases [225];

- Motion Artifact Contaminated ECG Database [204, 205]: The database also has ECGs acquired during different physical activities
- Examples of Electromyograms [206]: This database is used for intensive analysis of EMG signals.
- MIT-BIH Noise Stress Test Database [201]: This database contains noises– "baseline wander", "electrode motion artifact", and "muscle artifact" (commonly called EMG), whose frequency content overlaps with ECG signals.

For experimental purposes and to analyze statistical characteristics of noises, the full length of segments available in the database are considered.

4.2.2.1 Database 1- Motion Artifact Contaminated ECG Database

This database [205] consists of signals acquired to study the impact of physical activities on ECG signal. The database comprises three types of ECG: *standing ECG*, *walking ECG* and *single jump ECG*.

As our *proposed* work aims to study the characteristics of noise contaminating ECG signals, this database helps investigate the characteristics of *motion artifacts* in ECG. Three signals each from standing, walking, and jumping are selected for experimental purposes. Statistical tests described in Section 4.2 are then applied, and results are recorded in **Figures 4.6-4.9** and **Tables 4.6-4.7**. Here, M1, M2, and M3 denote the three motion artifacts corresponding to *standing*, *walking* and *jumping*.

- **Visual Statistical Tests:** On applying test based on *histograms,* it can be observed from **Figure 4.6** that for available samples, the histograms obtained have large tails on the right side and are asymmetric.

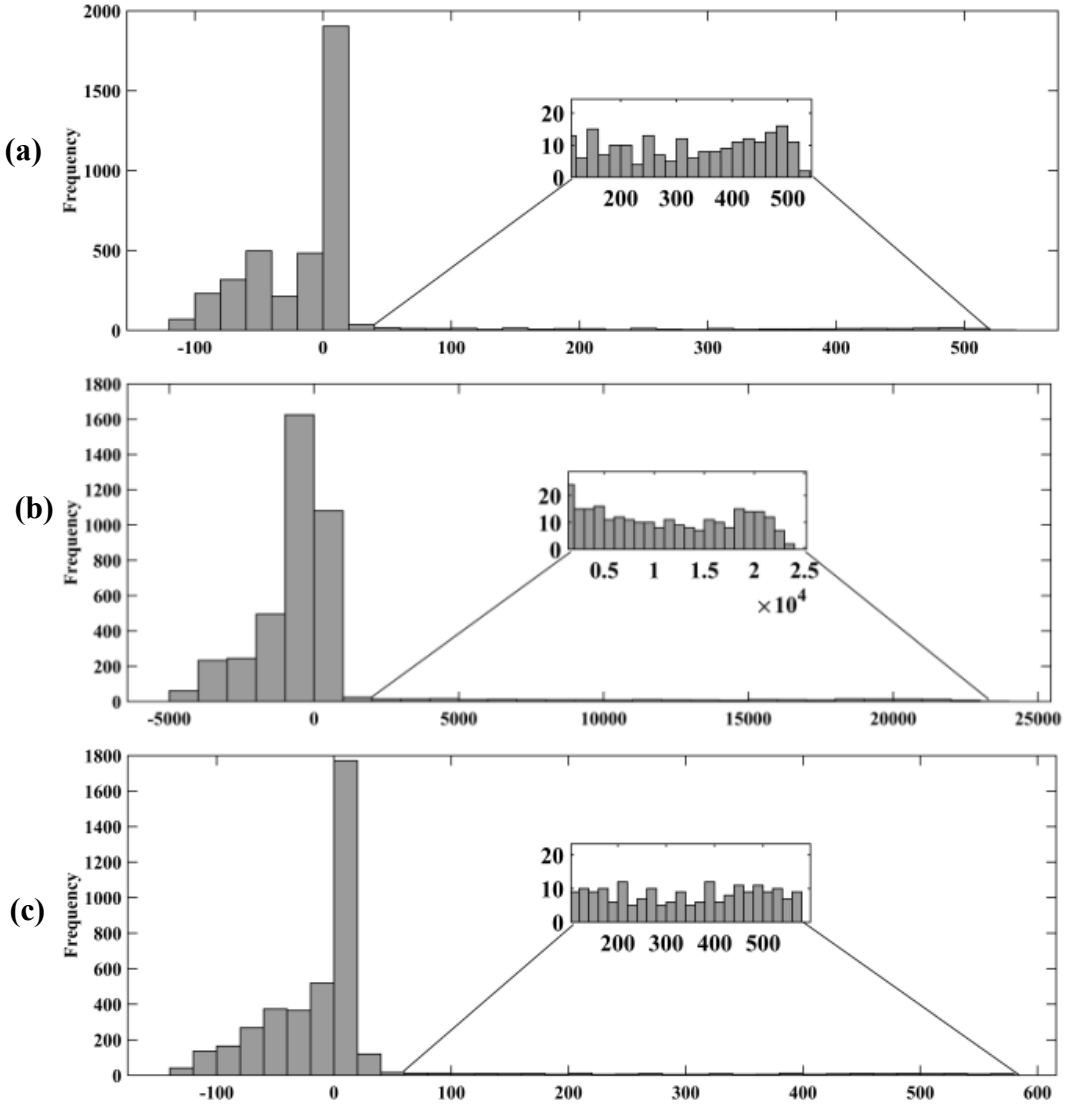

Figure 4.6 Histograms for different motion artifacts from Motion Artifact Contaminated ECG Database **(a)** M1, **(b)** M2 and **(c)** M3
M1 represents the motion artifact in standing, M2 is the motion artifact due to walking and M3 is motion artifact caused due to the jumping from Motion Artifact Contaminated ECG Database.

- Next, on observing the QQ plots in **Figure 4.7**, all three plots depicting the behavior of *standing* (M1), *walking* (M2), and *jumping* (M3) ECGs have clearly shown high deviation on the upper end, whereas the bottom end coincides with the straight line. This concludes that the motion artifact data obtained is highly right-skewed and does not follow the Gaussian distribution.

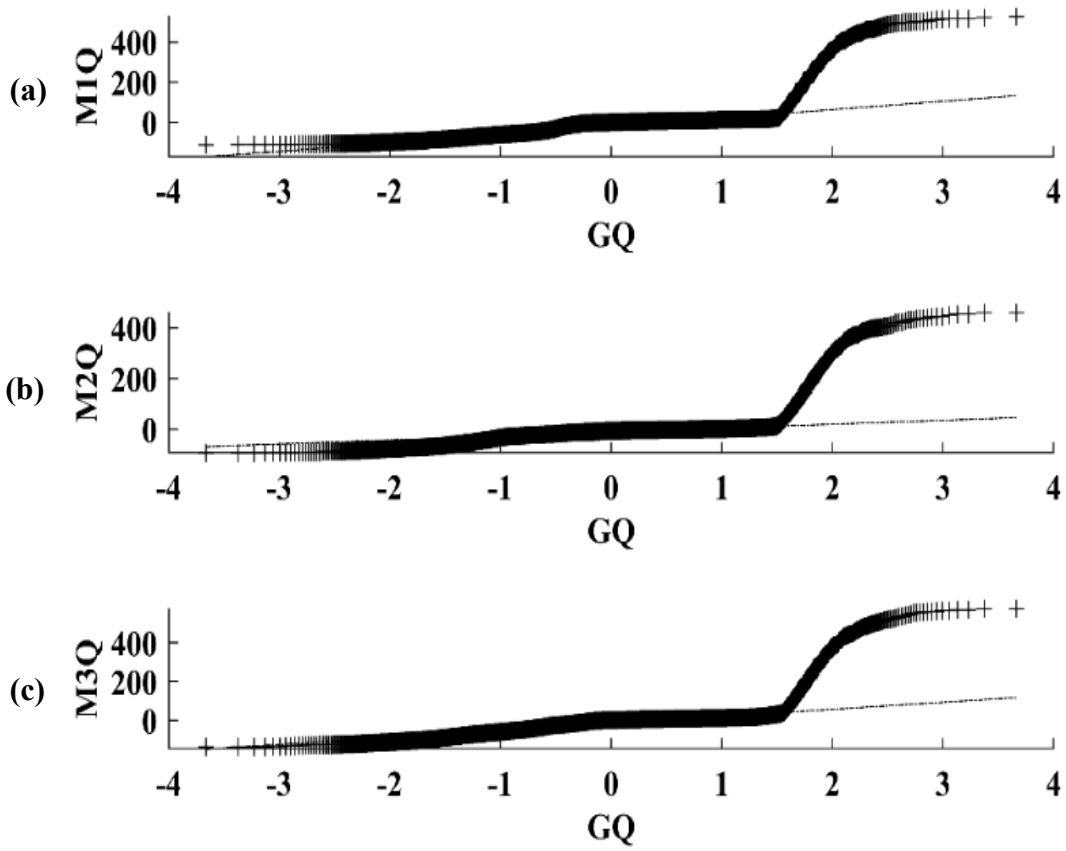

Figure 4.7 QQ plots for different motion artifacts from Motion Artifact Contaminated ECG Database **(a)** M1, **(b)** M2 and **(c)** M3
M1 represents the motion artifact in standing, M2 is the motion artifact due to walking and M3 is motion artifact caused due to the jumping from Motion Artifact Contaminated ECG Database.

- **Statistical Moments**: Next on examining the *statistical moments* values (of three motion artifacts, *standing* (M1), *walking* (M2), and *jumping* (M3), reported in **Table 4.6**, it is observed that skewness value is greater than 1, which does not comply with the usual range of skewness (-1 to 1) as described in Section 2.5 and illustrated in Section 4.2.1.2. Furthermore, the large right tail values depicted in the histogram (**Figure 4.6**) and QQ plot (**Figure 4.7**) are quantified by kurtosis value greater than 3, which surely signifies non-Gaussian behavior.

  Furthermore, to study the behavior of statistical moments from α-stable distribution point of view, *running mean* and *running variance*, plots are generated as shown **Figures 4.8** and **4.9**, respectively.

  On analyzing **Figure 4.8**, it is evident that the *running mean* either converges to zero or diverges. This behavior of *running mean* reveals certain similarities to the characteristics of α-stable distribution (as described in Section 2.4).

  Additionally, the *running variance* curves appear to diverge, as depicted in **Figure 4.9**. Specifically, large value is observed in the last sample (marked in the blue box). This divergence is evident for all signals, indicating that these signals possess infinite variance and thus display the α-stable characteristics.

Table 4.6 Statistical moments of different motion artifacts from Motion Artifact Contaminated ECG Database

Statistical moments	Standing (M1)	Walking (M2)	Jumping (M3)
Mean	-0.03	10.84	-0.01
Variance	88.56	71.77	92.62
Skewness	3.57	4.09	3.68
Kurtosis	18.27	21.90	19.59

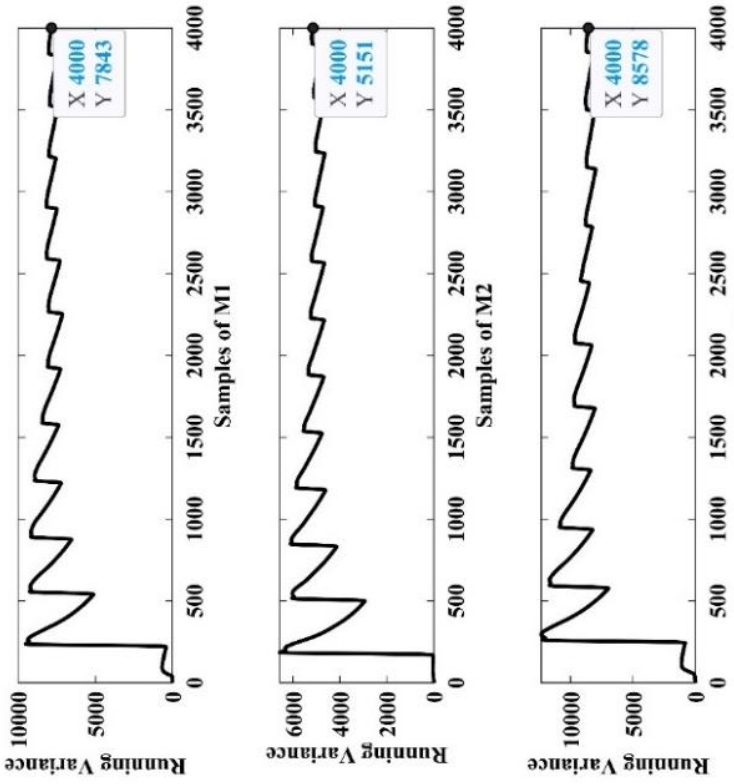

Figure 4.9 Running variance for different motion artifacts from Motion Artifact Contaminated ECG Database **(a)** M1, **(b)** M2 and **(c)** M3

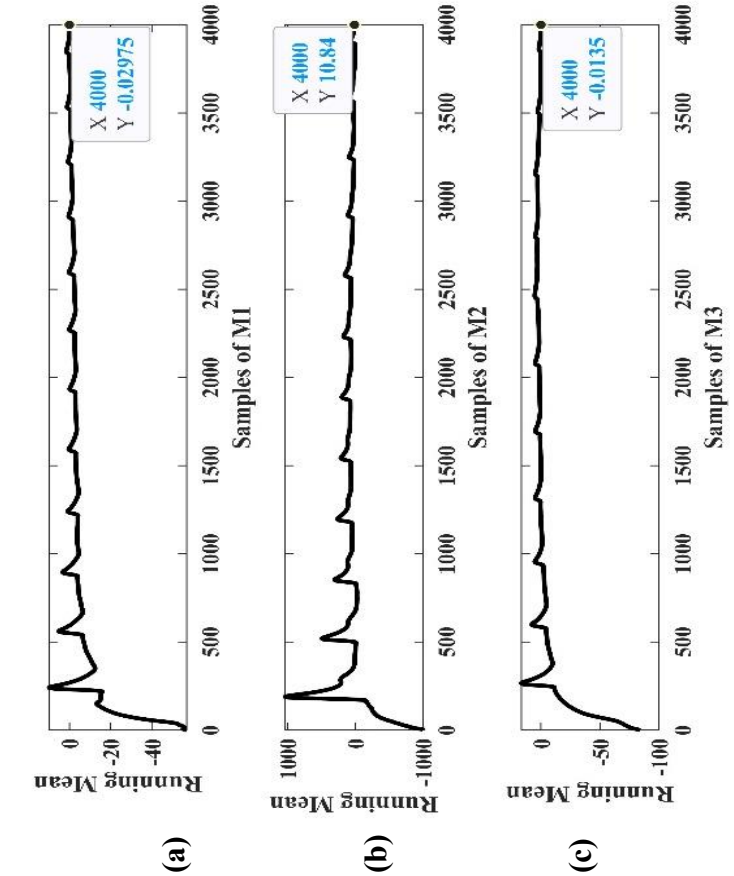

Figure 4.8 Running mean for different motion artifacts from Motion Artifact Contaminated ECG Database **(a)** M1, **(b)** M2 and **(c)** M3

- **Parameter Estimation Test**: Finally, to quantify the abovementioned traits of signal approaching α-stable distribution nature, Kogon and Williams's estimation method is applied to estimate the parameters of sample data's distribution and results are recorded in **Table 4.7**.

  Upon analyzing the data, it is observed that α parameter values obtained for *standing* and *jumping* are below 2 and even lower than 1 for *walking* signal. This proves the presence of impulsive behavior and highlights the absence of Gaussian nature, clearly indicating that the α-stable distribution noise model is a suitable choice for real-time scenarios.

Table 4.7 Parameter estimation of different motion artifacts from Motion Artifact Contaminated ECG Database using the Kogon-William's method

Estimated parameters	Standing (M1)	Walking (M2)	Jumping (M3)
$\boldsymbol{\alpha}$	1.26	0.88	1.22
$\boldsymbol{\beta}$	-1.00	-0.98	-1.00
$\boldsymbol{\gamma}$	21.84	7.99	21.48
$\boldsymbol{\delta}$	34.13	-11.20	18.93

4.2.2.2 Database 2- Examples of Electromyograms Database

This database comprises three EMG signals obtained from three subjects with neurological disorders [206]: *EMG_healthym*, *EMG_myopathym*, and *EMG_neuropathym*, respectively. To investigate the statistical behavior of these EMG signals, statistical tests were applied and results are recorded in **Figures 4.10-4.13** and **Tables 4.8-4.9**. Here, *EMG_healthym*, *EMG_myopathym*, *EMG_neuropathym* denoted as E1, E2, and E3, respectively

- **Visual Statistical Tests:** The histograms displayed in **Figure 4.10** illustrate that the distribution does not follow normal bell-shaped curve. Instead, the forms of histograms have prominent peaks in the center. Specifically in **Figure 4.10 (c)**, most of the data is concentrated in central region. Next, the QQ plots in **Figure 4.11** indicate the existence of outliers at both lower and upper extremes i.e., long tails are present on both sides. This reveals that the data have an asymmetric distribution, which in turn suggests that data are not Gaussian in nature, but rather follow a non-Gaussian distribution.

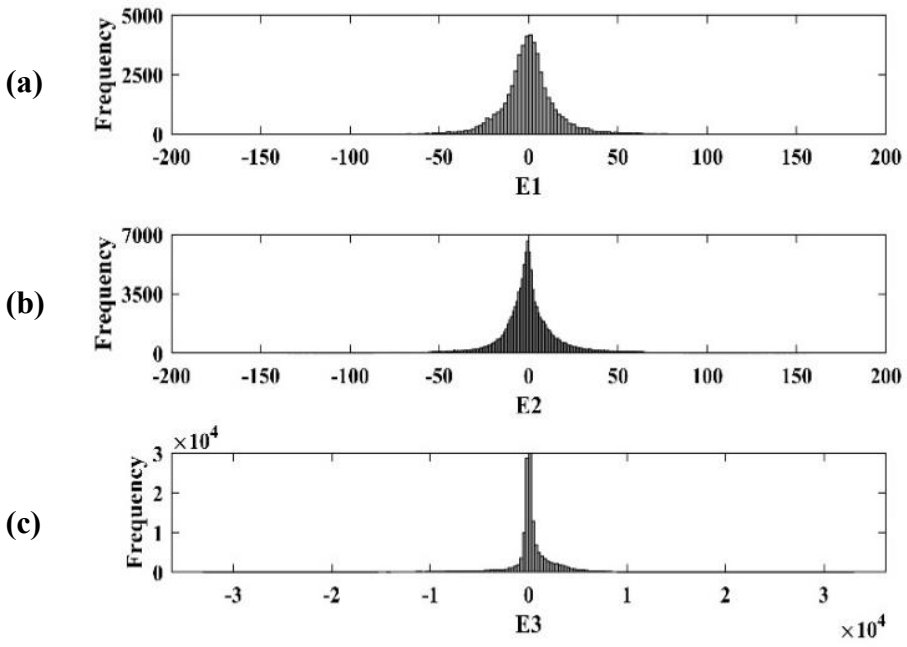

Figure 4.10 Histograms for different EMGs from Example of Electromyograms Database **(a)** E1, **(b)** E2 and **(c)** E3.
E1 represents the EMG_healthym signal, E2 is the myopathym signal and E3 is the EMG_neuropathym signal from Examples of Electromyograms Database.

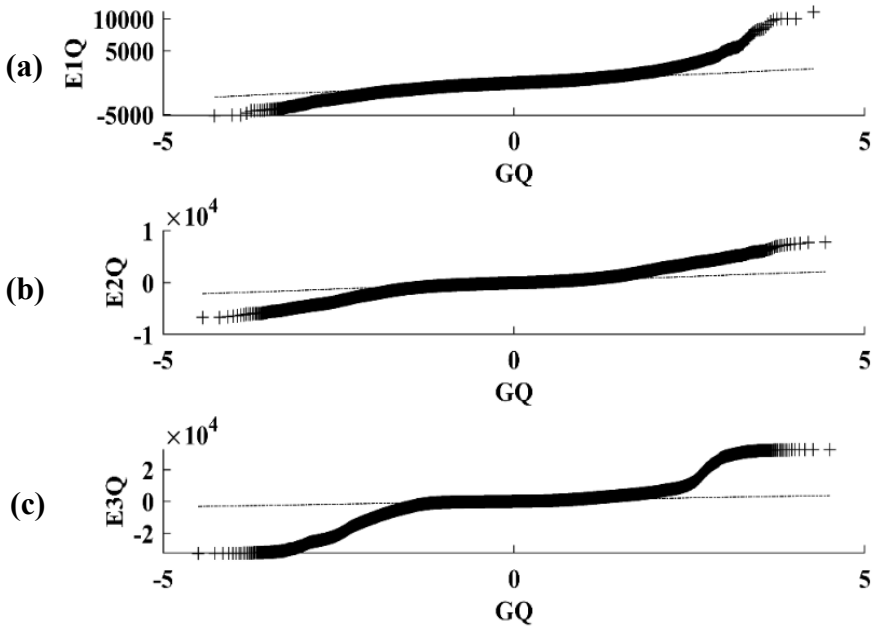

Figure 4.11 QQ plots for different EMGs from Example of Electromyograms Database **(a)** E1, **(b)** E2 and **(c)** E3
E1 represents the EMG_healthym signal, E2 is the myopathym signal and E3 is the EMG_neuropathym signal from Examples of Electromyograms Database.

- **Statistical Moments:** For quantifying the results obtained using visual inspection, statistical moments are recorded in **Table 4.8**. It is evident from the long tails with peaky centers that the data is asymmetric and as a result, skewness values do not fall between -1 and 1. Likewise, kurtosis and variance values are high enough to indicate the presence of outliers and heavy tails, as described in Section 4.2.1.2.

Table 4.8 Statistical moments of different EMGs from Example of Electromyograms Database.

Statistical moments	EMG_healthym (E1)	EMG_myopathym (E2)	EMG_neuropathym (E3)
Mean	0.04	0.07	49.76
Variance	815.77	970.30	3883.90
Skewness	1.07	0.29	-1.40
Kurtosis	14.10	9.43	24.95

In order to examine α-stable behavior, *running mean* and *running variance* plots are shown in **Figures. 4.12** and **4.13**, respectively. On analyzing **Figure 4.12**, it is apparent that the *running mean* either converges to zero or diverges for signals in this database. Moreover as represented in **Figure 4.13**, *running variance* curves have large values at the last sample (highlighted in the blue box) for each signal, indicating divergence in the curve and implying an infinite variance. Therefore based on these data, it is accurate to state that the behavior of EMG signals does not conform to Gaussian assumption.

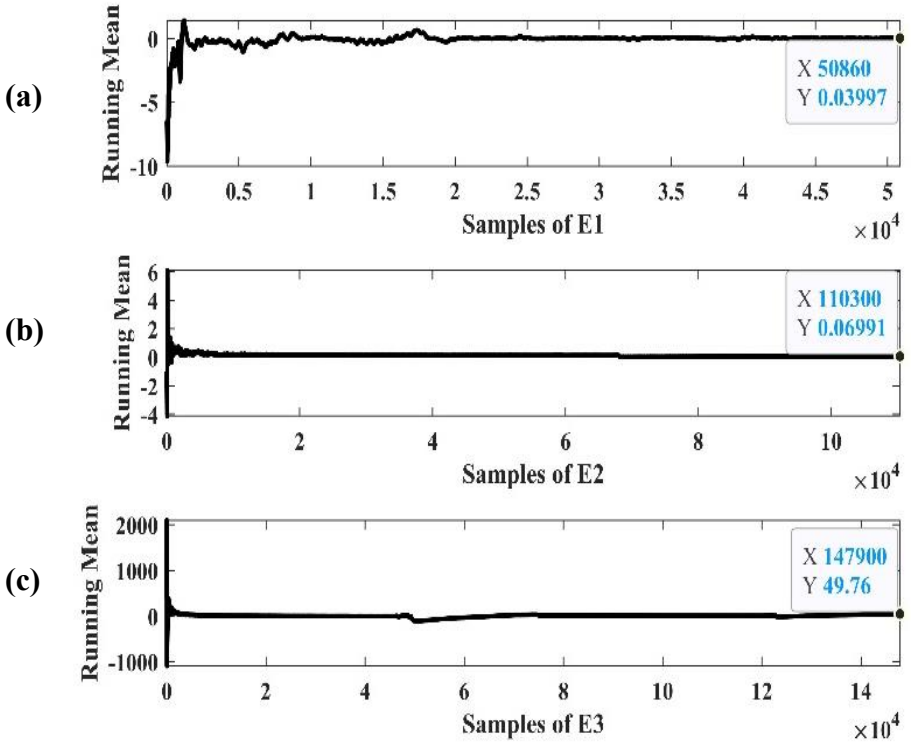

Figure 4.12 Running mean plots for different EMGs from Example of Electromyograms Database **(a)** E1, **(b)** E2 and **(c)** E3.

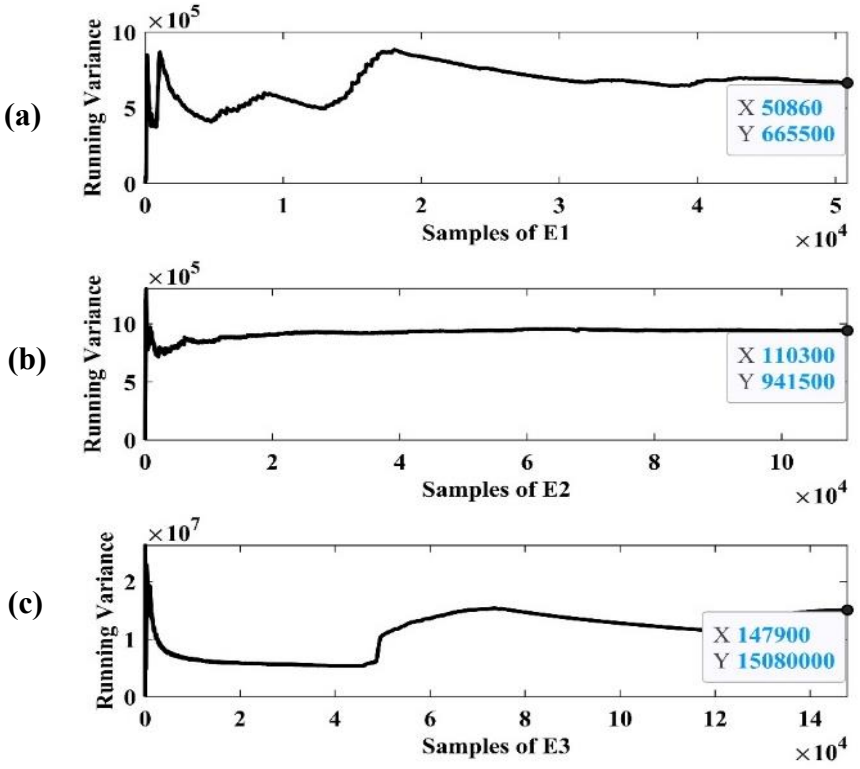

Figure 4.13 Running Variance plots for different EMGs from Example of Electromyograms Database **(a)** E1, **(b)** E2 and **(c)** E3

- **Parameter Estimation Test**: Lastly, the process of determining values of parameters is carried out to model the underlying distribution and the results are recorded in **Table 4.9**. Based on the data, it is derived that the α value for E1 and E2 signals is below 2, while for E3, α value is even below 1. This shows the presence of impulsive behavior, confirming our previous assumption to represent noise behavior using α-stable distribution.

Table 4.9 Parameter estimation of different EMGs from Example of Electromyograms Database using the Kogon-William method.

Estimated parameters	EMG_healthym (E1)	EMG_myopathym (E2)	EMG_neuropathym (E3)
$\boldsymbol{\alpha}$	1.64	1.33	0.77
$\boldsymbol{\beta}$	-0.02	0.16	0.55
$\boldsymbol{\gamma}$	405.70	358.39	460.10
$\boldsymbol{\delta}$	-21.22	-52.23	66.58

4.2.2.3 Database 3- MIT-BIH Noise Stress Test Database

This database [201] is widely referred, as it contains signals that predominantly include the most troublesome noises like muscle artifacts (*mam*), electrode motion artifacts (*emm*), and baseline wander (*bwm*). As discussed in Section 4.2.1, different statistical tests are applied to study the behavior of such noises. The signal length available in this database is 650,000 samples, so their behavior is studied by dividing each signal into lengths of 50,000 (a total of thirteen segments per signal). Also *mam*, *emm* and *bwm* are denoted as N1, N2 and N3.

- **Parameter Estimation Test**: Firstly, to model the behavior of noises, the Kogon-Williams parameter estimation method is applied to thirteen segments and the results are recorded in **Tables 4.10-4.12**. From the recorded values of characteristic α for *mam* noise in **Table 4.10**, it is evident that all the thirteen segments have value of $\alpha < 2$. Furthermore, six of these segments have value of $\alpha < 1.5$. Similarly, **Table 4.11** (*emm* noise) and **Table 4.12** (*bwm* noise) indicate that all thirteen segments have value of $\alpha < 2$. It is worth noting that four segments for *emm* noise and two segments for *bwm* noise have values close to 2 (specifically, more than or equal to 1.90). The overall α parameter attained for all three noisy signals is smaller than 2, which proves the existence of impulsive behavior and hence confirms the characteristics of α-stable distribution.

Table 4.10 Parameter estimation performed on full-length "mam" data from MIT-BIH Noise Stress Test Database.

Segment no:	α	β	γ	δ
1	1.66	-0.18	18.63	-1.31
2	1.76	0.44	20.19	0.29
3	1.79	-0.66	16.54	-2.30
4	1.65	0.69	17.73	1.13
5	1.60	0.39	18.95	0.73
6	1.38	0.10	16.35	-0.08
7	1.47	0.21	20.99	0.64
8	1.46	0.21	13.30	1.36
9	1.39	0.26	19.29	2.53
10	1.31	0.10	33.57	-0.61
11	1.44	0.04	24.16	0.79
12	1.59	-0.14	10.32	-0.78
13	1.58	0.03	14.47	-0.74
Average	**1.54**	**0.12**	**18.81**	**0.13**

Bold represents the overall averaged values of estimated parameters

Table 4.11 Parameter estimation performed on full-length "emm" data from MIT-BIH Noise Stress Test Database.

Segment no:	α	β	γ	δ
1	1.93	-1.00	80.88	-3.20
2	1.90	-0.12	77.04	0.00
3	1.75	0.76	94.94	2.88
4	1.67	1.00	92.77	24.80
5	1.86	1.00	113.96	15.61
6	1.67	1.00	92.29	25.48
7	1.98	0.71	91.10	-3.81
8	1.99	0.30	73.33	0.30
9	1.84	1.00	101.76	13.24
10	1.67	1.00	95.20	27.27
11	1.82	1.00	102.99	14.96
12	1.72	1.00	93.51	23.15
13	1.85	1.00	95.18	10.93
Average	1.82	0.67	92.69	11.66

Bold represents the overall averaged values of estimated parameters

Table 4.12 Parameter estimation performed on full-length "bwm" data from MIT-BIH Noise Stress Test Database.

Segment no:	α	β	γ	δ
1	1.95	-1.00	55.36	-2.79
2	1.54	-0.15	60.72	-8.89
3	1.55	0.06	39.21	4.53
4	1.31	-0.45	32.24	-21.78
5	1.34	-0.08	30.11	-1.43
6	1.87	-1.00	51.36	-8.19
7	1.76	0.65	74.72	9.14
8	1.68	-1.00	29.06	-7.03
9	1.78	0.56	75.51	10.83
10	1.67	-0.89	29.64	-4.03
11	1.21	-0.46	22.36	-25.42
12	1.98	-1.00	55.99	1.97
13	1.62	0.13	58.40	0.54
Average	**1.64**	**-0.36**	**47.28**	**-4.04**

Bold represents the overall averaged values of estimated parameters

- **Visual Inspection Method**: One random segment was chosen from each signal to depict the results obtained through this method. Their histograms and the QQ plots are depicted in **Figure 4.14** and **4.15,** respectively. Once again, histograms exhibit asymmetry and distinct peak at the center. Also, QQ plots display divergence on both sides. This clearly indicates the presence of non-Gaussian α-stable distribution characteristics.
- **Statistical Moments**: From the results recorded on evaluating one segment of each type: *bwm*, *emm* and *mam* in **Table 4.13** it is evident that signals do not show values of skewness and kurtosis within expected ranges. Additionally, the value attained at last sample depicts divergence for *running mean* and *running variance* curves as shown in **Figures 4.16** and **4.17**. This hint towards the presence of α-stable nature of distribution in these signals.

Therefore, we can conclude that these noises deviate from Gaussian assumption and follow non-Gaussian α-stable distribution characteristics.

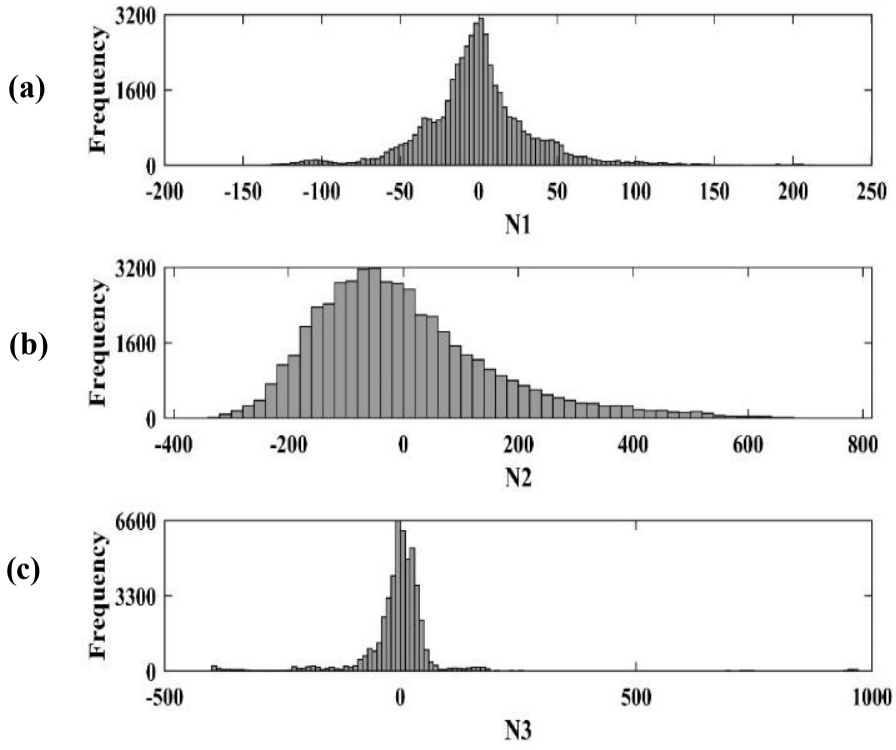

Figure 4.14 Histograms for different noises from MIT-BIH Noise Stress Test Database. **(a)** N1, **(b)** N2 and **(c)** N3.

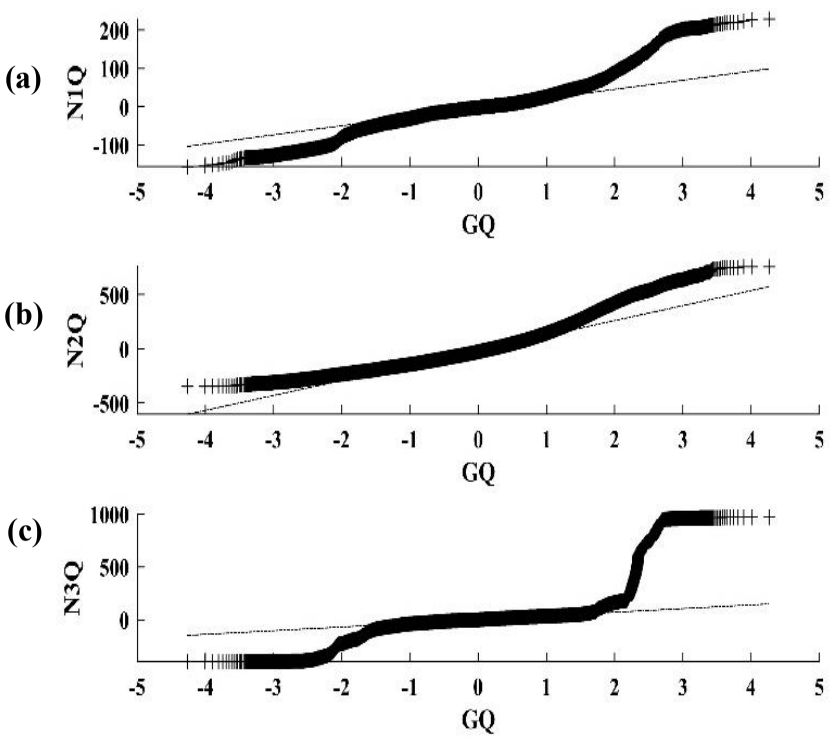

Figure 4.15 QQ plots for different noises from MIT-BIH Noise Stress Test Database **(a)** N1, **(b)** N2 and **(c)** N3

N1 represents the segment from muscle artifact (mam) noise, N2 is the segment from electrode motion (emm) noise and N3 is the signal segment from baseline wander (bwm) noise from MIT-BIH Noise Stress Test Database.

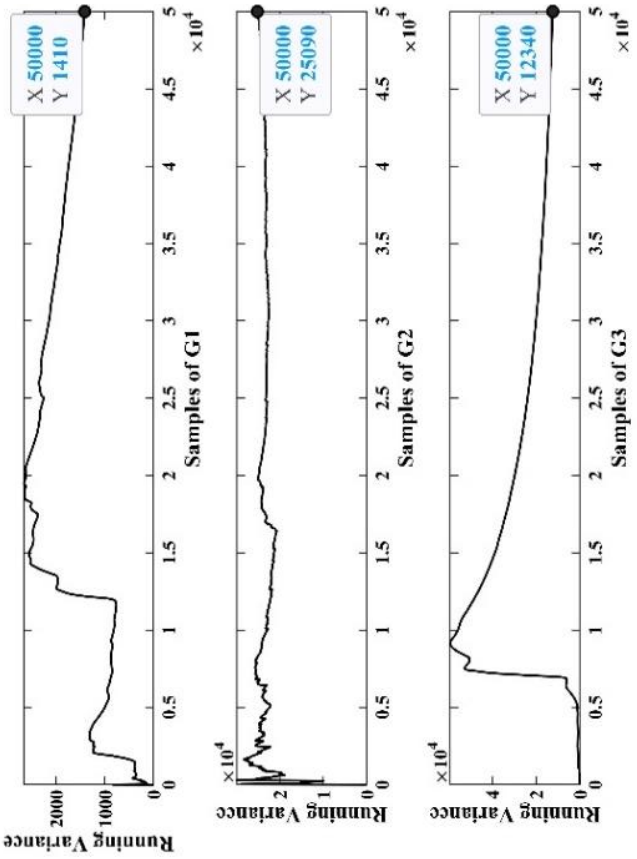

Figure 4.17 Running Variance plots for different noises from MIT-BIH Noise Stress Test Database **(a)** N1, **(b)** N2 and **(c)** N3

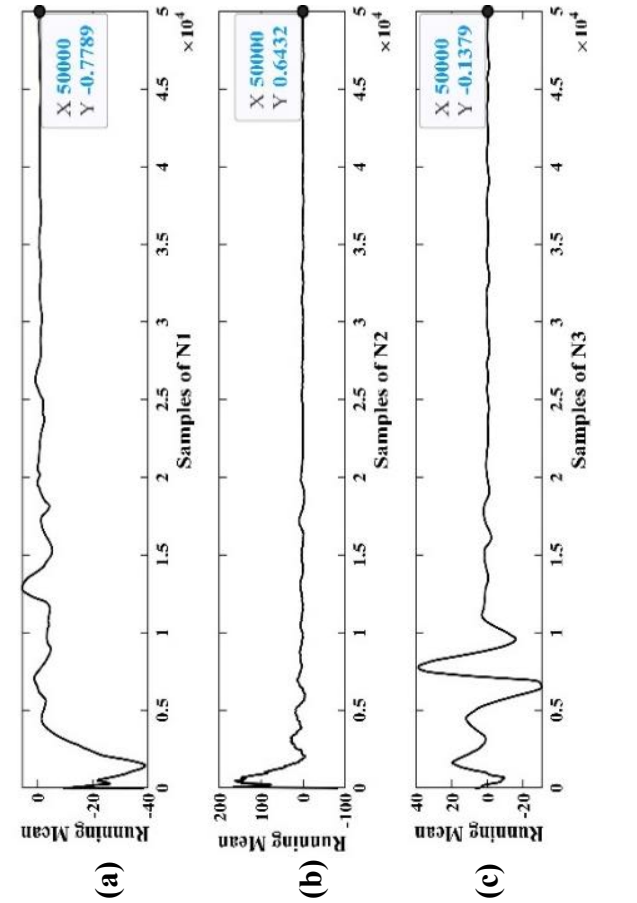

Figure 4.16 Running mean plots for different noises from MIT-BIH Noise Stress Test Database **(a)** N1, **(b)** N2 and **(c)** N3

Table 4.13 Statistical moments of random noisy segments extracted from "mam", "emm", and "bwm" signal.

Statistical moments	mam (N1)	emm (N2)	bwm (N3)
Mean	-0.78	0.64	-0.14
Variance	37.56	158.41	111.09
Skewness	0.77	1.08	3.58
Kurtosis	7.68	4.52	35.93

4.2.2.4 Chi-Square Goodness-of-Fit Test on Selected Databases

Chi-square goodness of fit is performed on above-discussed signals to determine if these signals follow normal distribution and the results are recorded in **Table 4.14**. Upon analyzing the obtained values for all signals, it is evident that the computed χ^2 values are greater than the χ_a^2 computed at 0.05 significance. This implies that null hypothesis (H_o) is rejected in favor of the alternate hypothesis and normal distribution is not a good fit for these signals. This further strengthens our *proposed* argument that a different model, such as α-stable distribution model, should be utilized to simulate real-world noises instead of Gaussian distribution.

Table 4.14 Chi-Square goodness of fit test performed on real-time noise excerpts from each selected database.

	E1	E2	E3	M1	M2	M3	N1	N2	N3
h	1	1	1	1	1	1	1	1	1
p	<0.00001	<0.00001	<0.00001	<0.00001	<0.00001	<0.00001	<0.00001	<0.00001	<0.00001
df	2	3	3	3	3	3	3	6	3
χ^2	15008.02	54753.81	110104.5	3849.934	5676.653	1761.2761	281470.02	137653.5	98421.2
$\chi^2_{0.05}$	5.991	7.815	7.815	7.815	7.815	7.815	7.815	5.991	7.815

4.2.2.5 Comparison of *Proposed* Noise Model with other Literature based Non-Gaussian Models

As demonstrated using the statistical results in previous sections, Gaussian distribution cannot handle real-time noises due to their asymmetric and heavy-tailed characteristics. Thus, in order to validate the use of *proposed* α-stable distribution, various other non-Gaussian distribution models present in literature, which have been *proposed* as a viable alternative like *Generalized Gaussian distribution (GGD)* [192], *Gaussian Mixture distribution (GMD)* [226], along with *t Location-Scale distribution (tLSD)* [194] are investigated. The performance of these distributions is analyzed using two statistical measures: Kolmogorov–Smirnov (KS) test statistic [227] and Wasserstein distance [189].

Furthermore, for comparative analysis three real-time signals: M2 (*walking*), E3 (*EMG_neuropathym*) and N1 (*mam*), which were previously mentioned in Section 4.2.2.1, 4.2.2.2 and 4.2.2.3 respectively, are taken into consideration.

Method: In order to apply the statistical measures, firstly estimates to the aforementioned distributions are obtained using the method described in [228]. Furthermore, in order to remove any bias, this parameter estimation method is different from the one used in previous sections, as it is simply based on minimizing the maximum distance between the empirical cumulative density function (eCDF) of the underlying data and estimated CDF of the distribution.

The estimated parameters for different distributions for selected signals is presented in **Table 4.15-4.17**. On analyzing these results, it is evident that N1, M2 and E3 have heavy tails and follow impulsive characteristics. This is justified with the obtained values as explained below:

- For α-stable distribution: Value of $\alpha < 2$ for N1(*mam*) and it is $\alpha < 1$ for both M2(*walking*) and E3(*standing*).
- For GGD, shape parameter $\beta < 1$ for all examined signals, implying a heavier tail than normal distribution.
- For GMD, the covariance parameter indicating significant dispersion exceeds 100 for various Gaussian components in GMD.
- Finally, for tLSD, the values for shape parameter are approximately 2 indicating the presence of heavy tails.

Thus, it can be stated that these signals have impulsive nature and Gaussian distribution model is not a suitable contender for modelling these noises. To quantify the obtained results, statistical measures-based analysis is performed which is described in next two sections.

Table 4.15 Estimated parameters for different distributions corresponding to N1, N2 and N3

Parameter description		Input real-time data		
		N1(mam)	N2(emm)	N3(bwm)
		α-stable distribution		
α	stability parameter	1.57	1.8	1.84
β	symmetry parameter	0.12	0.71	0.66
γ	scale parameter	19	95.28	23.02
δ	location parameter	-2.31	10.66	-3.80
		Generalized Gaussian distribution (GGD)		
μ_{GGD}	location parameter	-1.06	-0.26	-3
α_{GGD}	scale parameter	23.17	59.46	36.03
β_{GGD}	shape parameter	0.93	2.10	1.30
		Gaussian Mixture distribution (GMD)		
μ_{GMD}	means parameter	[-2.21; 6.95]	[25.48; -16.92]	[4.0414; -8.1963]
K_{GMD}	covariance parameter	[562.526;5.36E+03]	[1.38E+03; 1.17E+03]	[1.80E+03; 298.6483]
	Component proportion	[0.812; 0.188]	[0.3886; 0.6114]	[0.6253;0.3747]
		t Location-Scale distribution (tLSD)		
μ_{tLSD}	location parameter	-1.74	-0.44	-2.07
σ_{tLSD}	scale parameter	23.06	40.95	29.12
ν_{tLSD}	shape parameter	2.8	2.87E+06	5.73

Note: Here, GMD distribution is estimated using two components and values are given by [first component respective parameter value; second component respective parameter value].

Table 4.16 Estimated parameters for different distributions corresponding to M1, M2 and M3

Parameter description		Input real-time data		
		Standing (M1)	Walking (M2)	Jumping (M3)
		α-stable distribution		
α	stability parameter	0.79	0.82	0.76
β	symmetry parameter	-0.70	-0.57	-0.63
γ	scale parameter	11.08	7.03	10.98
δ	location parameter	3.88	-3.2	3.63
		Generalized Gaussian distribution (GGD)		
μ_{GGD}	location parameter	0.47	0.00	0.46
α_{GGD}	scale parameter	2.43	2.58	2.41
β_{GGD}	shape parameter	0.40	0.44	0.40
		Gaussian Mixture distribution (GMD)		
μ_{GMD}	means parameter	[-17.80; 312.74]	[-6.78; 22.63]	[-17.9827; 333.7128]
σ_{GMD}	covariance parameter	[1.30E+03;1.95E+04]	[111.29; 2.06E+04]	[1.45E+03;2.35E+04]
	Component proportion	[0.9462; 0.0538]	[0.762;0.238]	[0.9489; 0.0511]
		t Location-Scale distribution (tLSD)		
μ_{tLSD}	location parameter	4.28	-3.94	58.7
σ_{tLSD}	scale parameter	9.90	8.3	378.1
ν_{tLSD}	shape parameter	0.72	0.92	0.74

Note: Here, GMD distribution is estimated using two components and values are given by [first component respective parameter value; second component respective parameter value].

Table 4.17 Estimated parameters for different distributions corresponding to E1, E2 and E3

Parameter description		Input real-time data		
		E1(EMG_healthym)	E2(EMG_myopathym)	E3(EMG_neuropathym)
		α-stable distribution		
α	stability parameter	1.51	1.21	0.79
β	symmetry parameter	0.029	0.13	0.27
γ	scale parameter	389.543	331.73	418.04
δ	location parameter	-21.536	-59.89	62.93
		Generalized Gaussian distribution (GGD)		
μ_{GGD}	location parameter	0.39	0.381	0.41
α_{GGD}	scale parameter	2.402	2.40	2.40
β_{GGD}	shape parameter	0.2656	0.263	0.24
		Gaussian Mixture distribution (GMD)		
μ_{GMD}	means parameter	[70.3764;-25.401]	[-62.468;143.468]	[73.36; 9.91]
K_{GMD}	covariance parameter	[1.85E+06;1.88E+05]	[1.25E+05;2.64E+06]	[1.60E+05;4.03E+07]
	Component proportion	[0.2861;0.7139]	[0.679;0.321]	[0.628; 0.372]
		t Location-Scale distribution (tLSD)		
μ_{tLSD}	location parameter	-16.947	-50.647	58.7
σ_{tLSD}	scale parameter	471.572	378.51	378.1
ν_{tLSD}	shape parameter	2.60	1.56	0.74

Note: Here, GMD distribution is estimated using two components and values are given by [first component respective parameter value; second component respective parameter value].

4.2.2.5.1 **Comparative Analysis using Kolmogorov–Smirnov (KS) Test Statistic**

The KS statistical significance test is applied on the estimated parameters of considered distributions, to determine the presence of statistical errors in estimations and results are tabulated in **Table 4.18**. To compare the performance of the aforementioned distributions, a smaller value of KS test statistic will imply better estimation and thus correspond to a better distribution fit for the respective signal.

Results and Discussion: Examining the KS test statistic values, it is demonstrated that the α-stable distribution model yields the lowest values for all signals. Hence, it can be stated that α-stable distribution exhibits a superior fit compared to other distributions mentioned in the literature.

Table 4.18 KS test statistic value computed for different distributions corresponding to each data

Dataset	α-stable	GGD	GMD	tLSD
N1 (mam)	**0.016**	0.028	0.024	0.020
N2 (emm)	**0.011**	0.023	0.020	0.026
N3 (bwm)	**0.021**	0.027	0.034	0.051
M1 (standing)	**0.097**	0.170	0.218	0.185
M2 (Walking)	**0.069**	0.256	0.120	0.135
M3 (jumping)	**0.088**	0.159	0.191	0.175
E1(EMG_healthym)	**0.016**	0.100	0.025	0.022
E2(EMG_myopathym)	**0.031**	0.111	0.036	0.032
E3 (EMG_neuropathym)	**0.030**	0.117	0.078	0.075

Bold represents the minimum KS test statistic value

4.2.2.5.2 Comparative Analysis using Wasserstein Distance

Wasserstein distance measures the distance between two distributions. Also, as mentioned in Chapter 2 (Section 2.5.4), this measure is defined for only α-values greater than 2, therefore the results tabulated in **Table 4.19**, are only obtained for datasets which have value of $\alpha > 1$ i.e., N1, N2, N3, E1 and E2. Performance is compared for all distributions, and lesser distance signifies better fit.

Results and Discussion: On analyzing the Wasserstein distance values, it is observed that α-stable distribution model yields lowest values for all signals (who satify this condition). Hence, it is again proved that α-stable distribution is a betterfit compared to the other distributions mentioned in the literature.

Table 4.19 Wasserstein distance value computed for different distributions corresponding to N1, N2, N3, E1 and E2

Dataset	α-stable	GGD	GMD	tLSD
N1 (mam)	**0.204**	0.209	0.210	0.21
N2 (emm)	**0.06**	0.14	0.16	0.25
N3 (bwm)	**0.14**	0.23	0.25	0.35
E1(EMG_healthym)	**0.16**	0.25	0.19	0.3
E2(EMG_myopathym)	**0.14**	0.23	0.25	0.29

Bold represents the minimum Wasserstein distance

4.3 Shortcomings of using Gaussian Distribution Noise Model with Practical Implications

This section demonstrates the effectiveness of *R-peak detection* techniques and *deep learning models* in the presence of two types of noise: Gaussian distribution and α-stable distribution. Through this study, we aim to demonstrate the behavior of two ECG processing stages when designed with the implicit assumption of Gaussian distribution noise.

4.3.1 Impact of Literature-based Different Noise Analysis Models on R-peak Detection

As discussed in Section 2.1, R-peaks are the most prominent waveform and contain crucial information related to the state of heart. Therefore, its detection is integral to ECG signal analysis and processing algorithms. Unfortunately, ECG signals are highly prone to noises during acquisition; thus, owing to the need for automated ECG signal analysis and processing, various methods for R-peak detections have been *proposed* in the literature. These established methods can be broadly categorized into methods based on signal derivatives [64, 229], digital filtering [68, 71] and time-frequency tools such as wavelets [55, 73], as previously described in Section 2.1.3.

Furthermore, within the extensive range of methodological approaches utilized for R-peak detection, most follow fundamental framework of preprocessing and decision-making. The preprocessing stage aims to eliminate artifacts and disturbances while enhancing important signal components. Decision-making involves using thresholding to identify the distinctive properties of ECG. Despite high detection rates and excellent accuracy offered by existing R-peak detection algorithms, their real-time deployment is hindered by false alarm rates, with the primary causes of false alarms listed below:

(i) The failure to differentiate between noises and ECG components can misidentify noise as a normal beat, resulting in a false positive (referred to as *FP*).
(ii) The severely distorted ECG may be misclassified, leading to inaccurate measurements required for feature extraction.

So, to emphasize the importance of using suitable noise analysis model in accurately detecting R-peaks and reducing false alarms, the performance of state-of-the-art methods is evaluated in Gaussian and α-stable distribution noise environments.

4.3.1.1 Simulation Results

To demonstrate the behavior of R-peak detection, three R-peak detection methods are utilized from the categories mentioned above: signal-derivative, wavelet, and filtering. The performance of these methods is analyzed under traditionally used Gaussian noise model and the *proposed* α-stable distribution noise model at four input noise levels— 5 dB, 10 dB, 15 dB and 20 dB, respectively. For this, the full-length records; 100, 101, 102, 103, 104, 105, 106, 107, 108, 109 from MIT-BIH Arrhythmia Database are considered. Annotations available at the MIT-BIH directory are used to validate the true count of R-peaks present in each record. Comparison of performance under different noises, the quantitative measures namely *Sensitivity*, *Positive Predictivity*, *Detection Accuracy* and *Error Rate* are chosen (already defined in Section 3.3.1).

In addition, to showcase the impact of selecting an appropriate noise analysis model on true detections, a portion of record 105 (segment: 660s-675s) that is affected by 10 dB Gaussian distribution noise and 10 dB α-stable distribution noise is depicted in **Figure 4.18**, along with the results of selected R-peak detection methods. The raw ECG segment is displayed in the image, with Gaussian-based outcomes shown on the left side and α-stable based outcomes on the right side.

According to an extensive survey of rich literature, higher *TP* and lower *FN*, *FP* values indicate a good detection performance. Upon visual inspection of **Figure 4.18**, it is evident that Gaussian noise has minimal impact on the morphology of ECG signal. On contrary, the presence of α-stable distribution noise has distorted the morphology of ECG significantly, making it more challenging to identify the true R-peaks. Moreover, from the number of *TP*, *FP* and *FN* obtained for different methods, it can be deduced that for the case of Gaussian noise, there is a clear and accurate detection with no instances of missed detections or false detections. On the other hand for α-stable, which is a more suitable model for the representation of practical noises, the performance of existing techniques has degraded, leading to inaccurate detections. Specifically, *FP*=3 for wavelet-based R-peak detection method, *FP*=2 for signal derivative-based R-peak detection method, and *FP*=8 and *FN*=2 for filtering-based R-peak detection method.

Additionally, **Table 4.20** represents the simulation results recorded for these methods in the presence of Gaussian and α-stable distribution noise for four noise levels. Here, the average

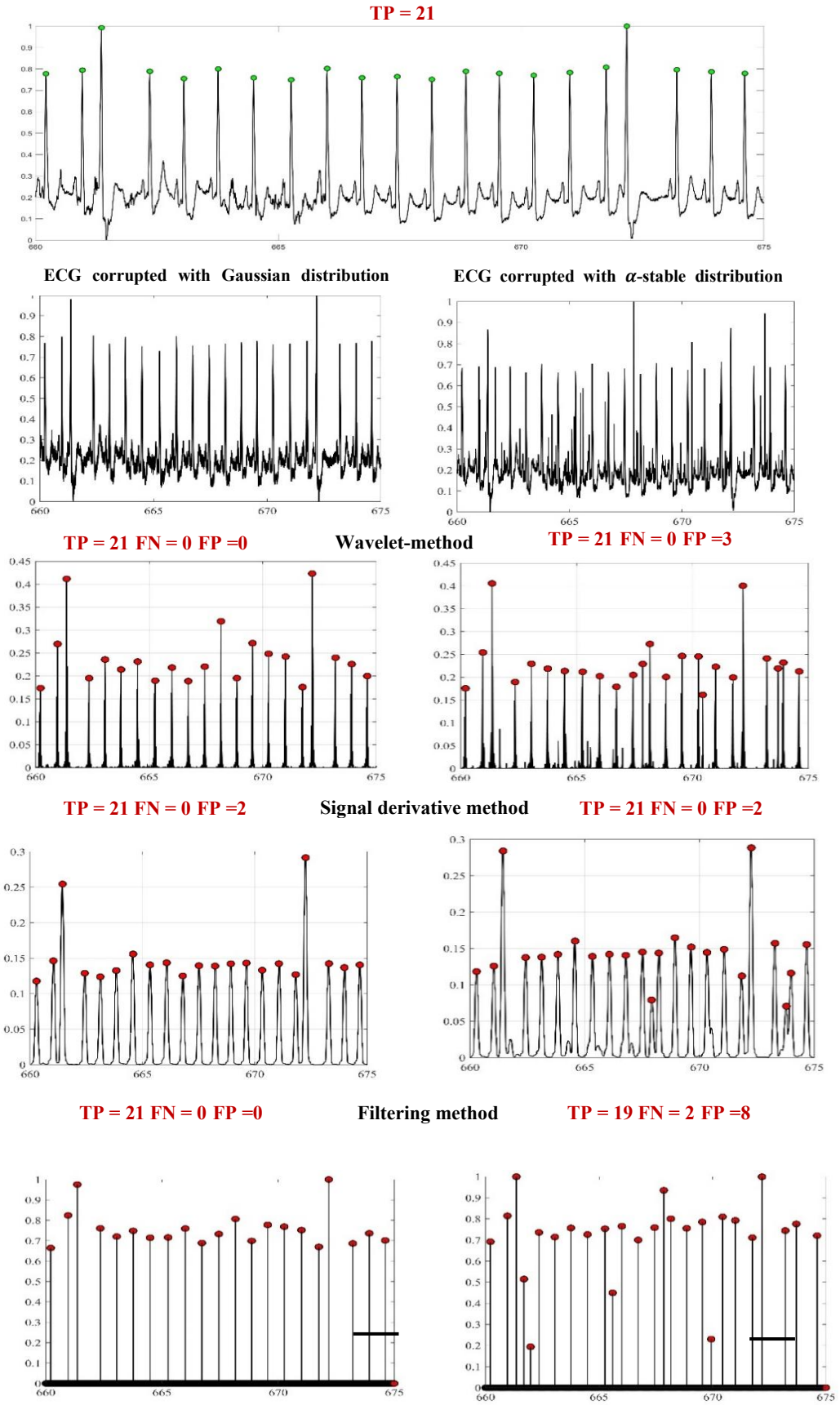

Figure 4.18 Performance in terms of (TP, FN and FP) for different R-peak detection methods applied on ECG segment corrupted with 10 dB Gaussian and α-stable distribution noise.

Sensitivity, *Positive Predictivity*, *Detection Accuracy* and *Error Rate* is computed after simulations for full-length records (i.e., 100, 101, 102, 103, 104, 105, 106, 107, 108, and 109).

Analyzing the results tabulated in **Table 4.20**, it is ascertained that the performance of the established approaches will deteriorate when subjected to α-stable distribution noise, in contrast to their performance in Gaussian environment. For example, at 15 dB noise level, the wavelet method shows *Sensitivity* of 99.55% in Gaussian noise, which drops to 63.76% in α-stable distribution noise, and the *Error Rate* increases from 0.81 % to 41.64%. Similarly, the *Error Rate* increased from 1.06 % to 38.33 % for the signal-derivative-based method at 15dB noise level.

Furthermore, observing the general trend of Sensitivity, *Positive Predictivity*, *Detection Accuracy* and *Error Rate*, in the presence of both noises, it can be concluded that, although established selected methods can correctly detect a significant number of true peaks, false detections (both missed and incorrect detections) have increased at all noise levels. To further illustrate this, **Figure 4.19** shows a comparison of obtained *Sensitivity*, *FN* and *FP* values averaged over all selected records for both Gaussian (■) and α-stable distribution case (■). The obtained bar charts clearly demonstrate that there is a significant drop in the performance and effectiveness of existing methods in managing noise as the noise level increases, particularly in the case of α-stable distribution noise.

In the light of abovementioned observations, it is imperative to emphasize how crucial it is to use appropriate noise model while developing techniques for ECG signal analysis.

Table 4.20 Comparison of R-peak detection methods in presence of Gaussian and α-stable distribution noise.

R-peak Detection Method	Input Noise (dB)	Gaussian				α-stable			
		Sensitivity	**Positive Predictivity**	**Detection Accuracy**	**Error Rate**	**Sensitivity**	**Positive Predictivity**	**Detection Accuracy**	**Error Rate**
Wavelet based	5.00	99.84	99.87	99.71	0.29	96.86	96.19	93.42	6.58
	10.00	99.73	99.78	99.51	0.49	88.50	92.33	83.13	16.87
	15.00	99.55	99.64	99.19	0.81	63.76	77.48	58.36	41.64
	20.00	99.16	99.29	98.48	1.52	33.90	47.91	30.18	69.82
Signal - Derivative based	5.00	99.72	99.72	99.45	0.55	96.61	98.45	95.21	4.79
	10.00	99.63	99.67	99.32	0.68	85.89	97.49	84.29	15.71
	15.00	99.46	99.47	98.94	1.06	63.12	94.98	61.67	38.33
	20.00	99.05	98.98	98.09	1.91	42.98	90.67	41.37	58.63
Filtering based	5.00	99.73	99.69	99.43	0.57	98.38	98.04	96.48	3.52
	10.00	99.53	99.46	99.00	1.00	98.12	95.57	93.89	6.11
	15.00	99.09	99.00	98.13	1.87	78.26	88.03	73.17	26.83
	20.00	98.67	97.02	95.86	4.14	25.96	71.95	25.46	74.54

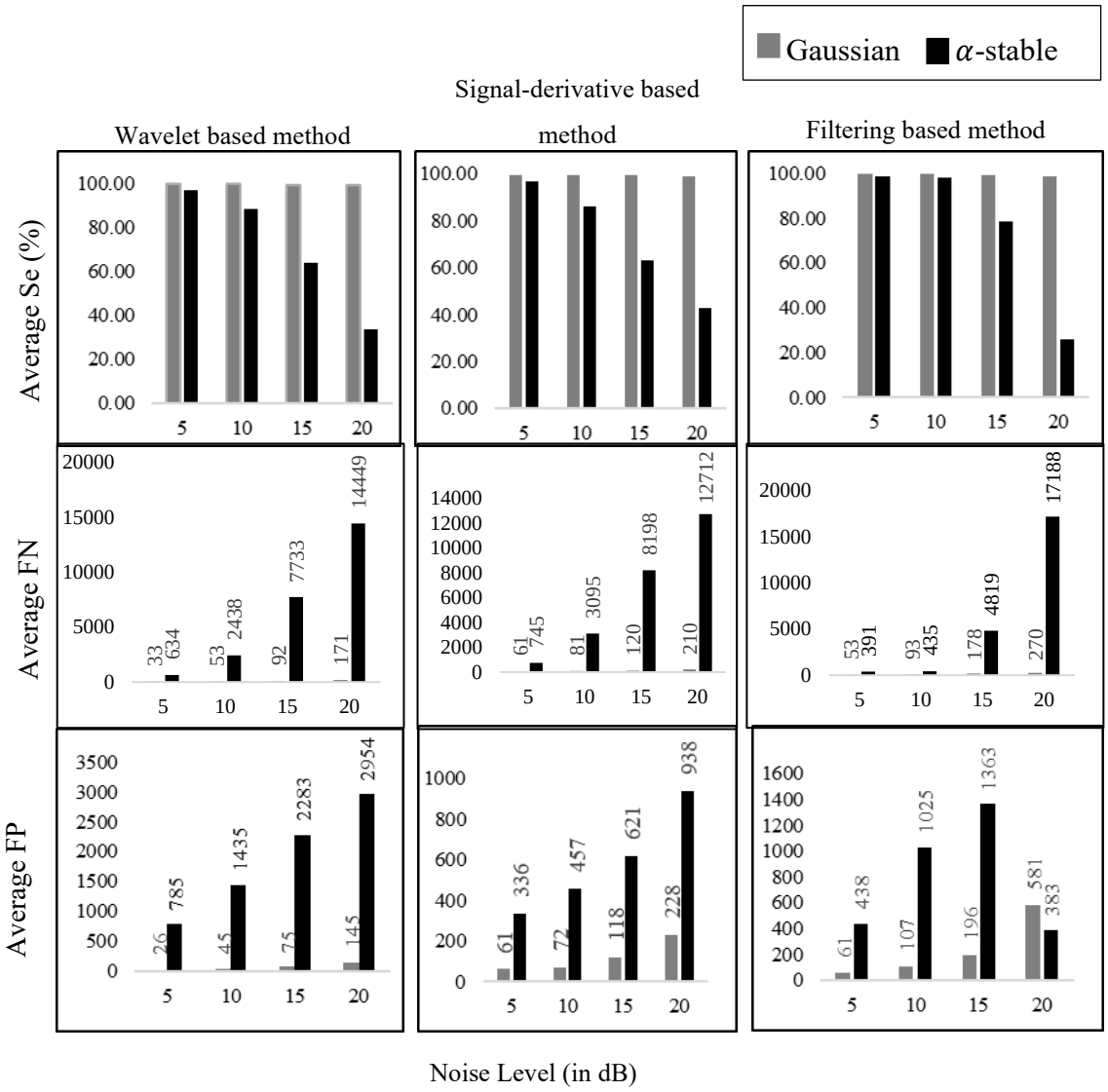

Figure 4.19 Illustration of averaged performance metric parameters in Gaussian and α-stable distribution noise

4.3.2 Impact on Different Noise Analysis Models on Classification Stage: employing Deep Learning Models

Interpretation and identification of ECG signals is a useful indicator for diagnosing cardiovascular disorders (CVDs). Therefore, with advancements in signal processing techniques like machine learning (ML) and deep learning (DL) methods, various computer-aided diagnosis (CAD) methods have been established to classify ECG signals for early detection of CVDs [230, 231].

In general, the fundamental framework of CAD method employs a preprocessing stage, a feature extraction stage followed by classification [231, 232]. The preprocessing stage focuses on removing artifacts and noise, followed by segmentation. In the feature extraction stage, various time features, frequency features, time-frequency features, etc., are extracted from ECG segments, and an effective feature set is used to train the machine learning model for classification [233]. On the other hand, DL models involve automatic feature learning for effective classification [233]. Even though these CAD methods have high accuracies, when they are deployed in real-time, their performance degrades due to following reasons:

i. Different noise environments can be encountered e.g., in wearable devices, captured ECG signals may be severely distorted with motion artifacts.
ii. As different subjects (patients) have different ECG morphologies, only considering Gaussian distribution noise model-based validation of CAD method, may result in overfitting as data involves uniform distributed noisy samples.

Thus, this section demonstrates the adverse impact of using conventional noise-analysis model (Gaussian distribution noise model) on classification by taking into account the classification of three ECG signals of type arrhythmia (ARR), congestive heart failure (CHF) and normal sinus rhythm (NSR). Furthermore, to emphasize the choice of using *proposed* noise analysis model, this section demonstrates the impact of performance on DL-based classification in contrast to ML-based classification. The reason is solely based on the fact that DL is an advanced processing method than ML, so if DL-based performance is degraded, it is implicit to have degradation of ML-based classification in the same environment. To demonstrate and emphasize the importance of noise analysis model, the approach followed is outlined below:

i. Firstly, the DL model is trained on data without considering the corrupted data. This DL model will be referred to as *DL model trained on true data* for simplicity.

ii. Next, the DL model is trained on data considering the effect of Gaussian noise (conventional noise analysis model) referred to as *DL model trained on Gauss data*.

iii. After training model using above mentioned points, performance of these models is tested under two scenarios – Gaussian distribution noise data (i.e., signals affected with Gaussian distribution noise) and α-stable distribution noise data (i.e., signals affected with α-stable distribution noise).

4.3.2.1 Simulation Results

To demonstrate the whole process, this section is divided into three parts. Firstly, training scenarios are described, with details of training performance. Then, the testing phase is demonstrated with description of introduction of newly generated dataset and testing results. Finally, quantitative analysis is provided for overall classification.

A. Training scenarios are detailed below:

- ***Training process***: In the presented demonstration, the DL model used is based on Continuous Wavelet Transform (CWT) and Convolutional Neural Network (CNN) [230] . The training process for *DL model trained on true data* and *DL model trained on Gauss data* involves transfer learning with the AlexNet CNN model using ECG dataset available at github [234]. For simulation purposes, 600 images from each category (ARR, CHF, NSR) are employed with 70/30 ratio to divide dataset into training and testing sets. The configuration parameters were set to following: 'Max Epochs'= 8, 'Initial Learning Rate' = 1×10^{-4}, 'Mini Batch Size' = 20 and 'validation frequency' =10 with remaining parameters set to default values.
- ***Training Results***: Training results for *DL model trained on true data* are depicted in **Figure 4.20(a)** and **20(b)**. On analyzing the training progress for *DL model trained on true data* i.e. **Figure 4.20(a)**, it is illustrated that a validation accuracy of 90.56% is achieved with loss curve converging to zero. Also, on analyzing the confusion matrix in **Figure 4.20(b)**, it is observed that DL model has achieved 165 correct predictions for ARR, 160 correct predictions for CHF and 164 correct predictions for NSR.

  Furthermore, the training results for another model, i.e., *DL model trained on Gauss data,* are depicted in **Figure. 4.20 (c)** and **4.20 (d)**. This model achieved a validation

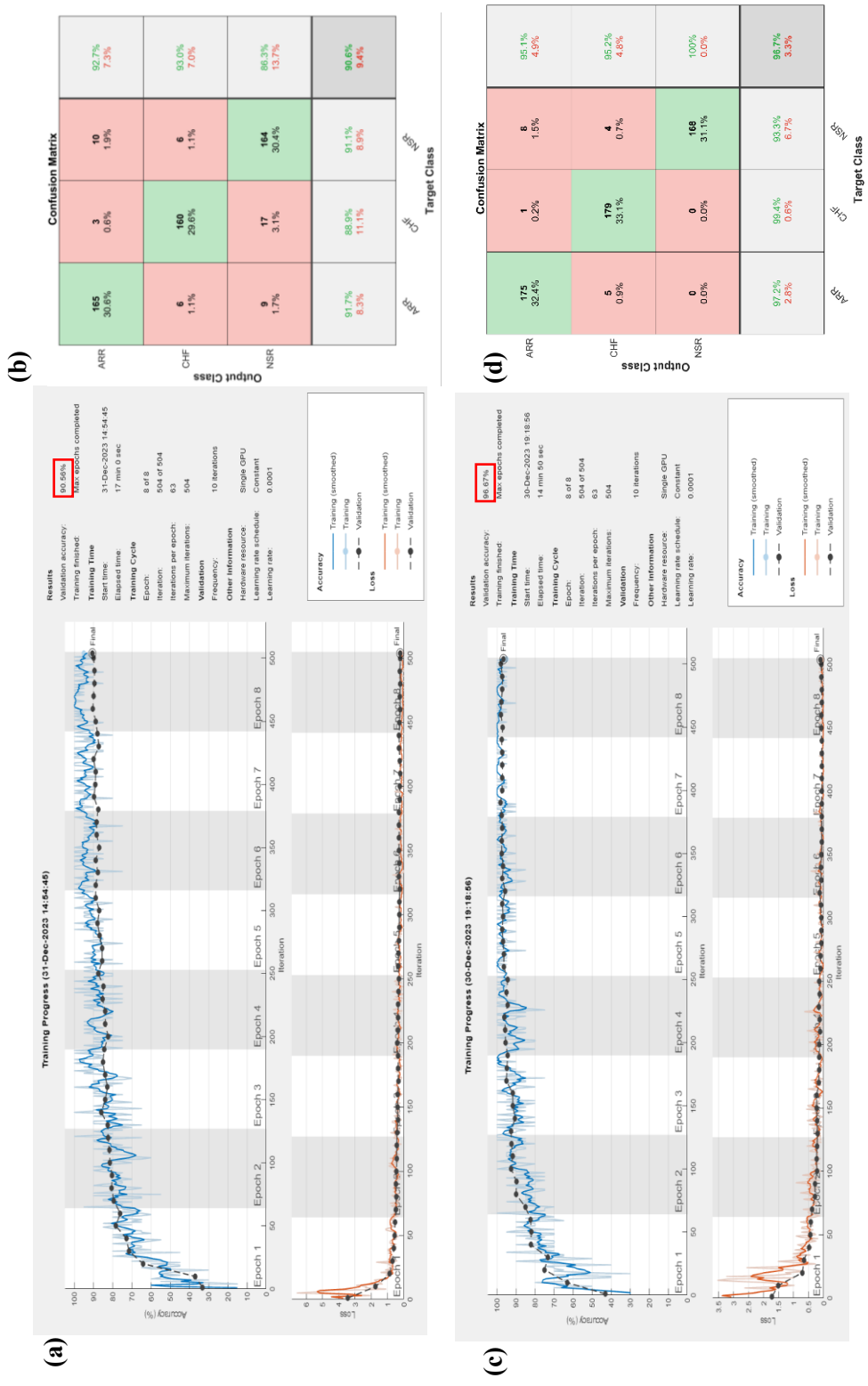

Figure 4.20 Illustration for depicting training results **(a)** Training progress of *DL model trained on True data*, **(b)** Confusion matrix of *DL trained model on True data* **(c)** Training progress of *DL model trained on Gauss data*, **(d)** Confusion matrix of *DL trained model on Gauss data*

accuracy of 96.67 % with 175 correct predictions for ARR, 179 for CHF and 168 for NSR.

B. To illustrate the testing phase incorporating new dataset, details are mentioned below:

- ***Testing on new dataset****:* To evaluate the performance of trained models on data replicating real-time scenarios, following datasets are created:
  (i) New Dataset 1: ECG signals of each category (ARR, CHF, NSR) are corrupted with Gaussian distribution noise at 10dB input noise level. This is used to replicate the traditionally assumed noise environment when deploying the trained model.
  (ii) New Dataset 2: ECG signals of each category (ARR, CHF, NSR) are corrupted with α-stable distribution noise at 10dB input noise level. This dataset replicates the *proposed* noise environment to replicate real-time noises better.

  The important point to note is that the ECG signals used for creating these datasets differ from those used during the training phase.

- ***Results obtained for Testing on new dataset***: In order to demonstrate impact of different noise analysis models, the results of deploying two trained models using new datasets are illustrated in **Figure 4.21**.

  On analyzing the results in **Figure 4.21(a)**, it is observed that under Gaussian environment, the *DL model trained on true data* with accuracy of 90.56% has contributed to testing accuracy of 43%. In contrast, for α-stable distribution environment (**Figure 4.21(b)**), the accuracy is decreased to 33.3%.

  Furthermore, on analyzing the results for *DL model trained on Gauss data* as shown in **Figure 4.21(c)** and **4.21(d)**, the model accuracy of 95.2% is achieved under Gaussian distribution noise environment. It is decreased to 34.3% under α-stable distribution noise environment.

  This demonstration emphasized that models trained by considering only true data or Gaussian data will fail if α-stable distribution noise i.e., the real-time noise scenario is encountered.

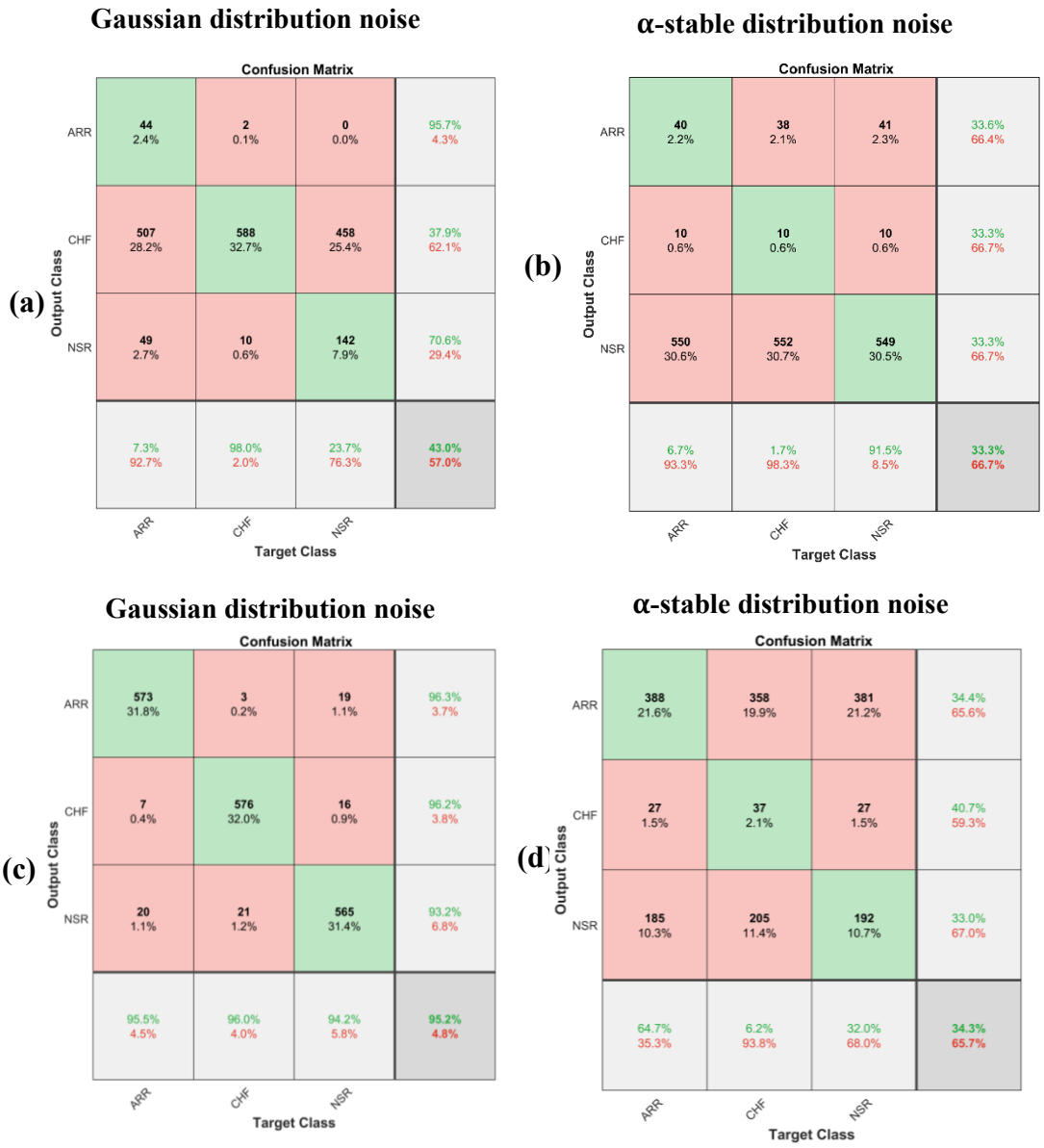

Figure 4.21 Illustration of Testing results with new dataset **(a)** Confusion matrix obtained when testing the *DL trained model on True data* with Gaussian distribution noise data, **(b)** Confusion matrix obtained when testing the *DL trained model on True data* with α-stable distribution noise data, **(c)** Confusion matrix obtained when testing the *DL trained model on Gauss data* with Gaussian distribution noise data, **(d)** Confusion matrix obtained when testing the *DL trained model on Gauss data* with α-stable distribution noise data

C. **Performance Quantification**: To comprehensively assess the performance of this multi-class classification, $Macro_{P_+}$ measure is employed which is given by [235].

$$Macro_{P_+} = \frac{1}{n}\sum_{i=1}^{n} P_{+_i} \tag{4.1}$$

where $Macro_{P_+}$ is the macro positive predictivity (P_+) averaged for three classes: ARR, CHF and NSR.

To provide comparison of two models in their respective noise environments, performance measure $Macro_{P_+}$ of two trained models is computed to assess their overall prediction performance in Gaussian distribution noise and α-stable distribution noise environment and results are depicted in **Figure 4.22**.

Upon examining the outcomes, it is discernible that the performance of *DL model trained on true data* is lowered from 68.05% correct predictions to 33.40% when encountering α-stable noise distribution. Similarly, when a training scenario other than Gaussian distribution is presented, the performance of *DL model trained on Gauss data* drops from 95.23% to 36.03%.

This demonstrates that if the classification model is based on the assumption that noise adheres to Gaussian distribution, the model will not be effective in real-world scenarios. Instead, a more accurate representation of real environment can be achieved by modelling it using an α-stable distribution, as evidenced by the statistical tests conducted in Section 4.2.2.

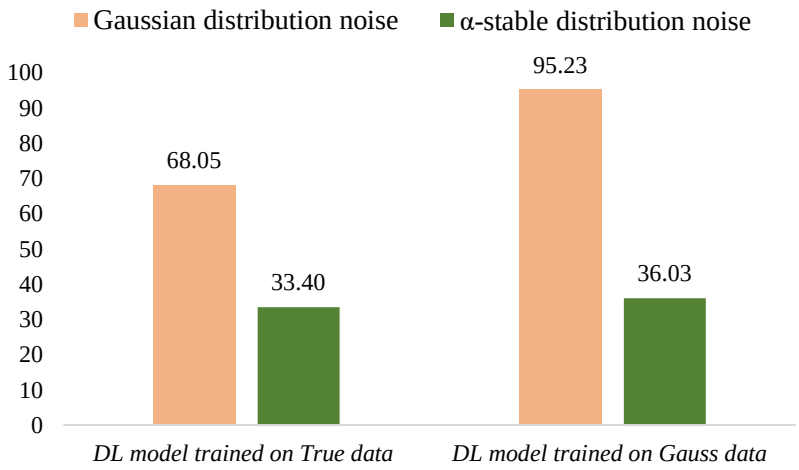

Figure 4.22 Demonstration of testing performance of DL models in terms of $Macro_{P_+}$

4.4 Summary

In the presented work, with rigorous simulation studies and investigation of statistical characteristics of real-time ECG noises, we provided evidence that real-time noises do not have Gaussian nature and instead have asymmetric, long tails with peaky centers.

The work described in the presented work can be summarized in three parts: First, *the statistical tests are applied to determine if the noisy signals are of Gaussian nature*. Second, *based on the results drawn, a new model called α-stable distribution model is suggested and investigated to better approximate the noises distorting ECG signals in real-time circumstances*. *Finally, the impact of using α-stable distribution noise model over Gaussian model in R-peak detection and deep learning is demonstrated to prove the performance degradation of existing methods when actual noise exhibits non-Gaussian nature.*

Hence, the inclusion of α-stable approach as a noise analysis model will contribute to reducing the false alarms and increasing the diagnostic accuracy of the acquired ECG signal.

After establishing the *non-Gassian* characteristics in ECG noises, the next chapter designs the ECG processing methods by adopting the α-stable distribution noise model in the first place.

Chapter 5

Design of Morphological Filter for ECG Processing considering α-Stable Distribution

ECG signals are corrupted by noises that exhibit similar morphology as that of ECG signals. Efficient methods are needed to process signals, but the fundamental problem with existing ones is that they are devised with an implicit assumption that noises follow Gaussian distribution.

After establishing non-Gaussian α-stable distribution nature of ECG noises in **Chapter 4**, this chapter focuses on designing analytical model for morphological filtering, considering α-stable distribution model of noise. This research aims to design an end-to-end processing approach using α-stable distribution noise model. It presents first-of-its-kind filter resulting in improved reconstruction and better detection of distinctive components of ECG signal.

5.1 Notion of Morphological Filter (MF) for ECG Processing

From monitoring the dynamics of human heart for diagnostic purposes to designing ECG-based biometric systems, ECG signals are interpreted for various applications. Furthermore, several techniques, such as feature extraction and classification play a prominent role in interpreting the information present in these signals for various applications. However, to apply these techniques effectively, preprocessing of these signals is essential to remove unwanted artifacts encountered during signal acquisition. Numerous techniques exist in literature, but due to the *non-stationary* nature of ECG signal and the nature of noises interfering with signal, the methods still fail to provide high performance and can introduce distortion resulting in misleading diagnoses.

To emphasize further, the methods for ECG preprocessing should be able to address two concerns:

- First, it should be able to track true morphology of ECG signal. As reported in literature, its shape (i.e., characteristic components) forms the basis of automated ECG processing and analysis algorithms [51].
- Second, it should be robust enough to handle various types of noises for example, Gaussian and non-Gaussian. Here, the point worth mentioning is that sometimes, to design a system focusing on an application involving one biomedical signal (e.g., ECG signal), another biomedical signal (e.g., EMG) is considered an artifact and must be removed.

Therefore, to understand and analyze signals correctly, their preprocessing techniques must be adequately designed taking into account the nature of signals and artifacts involved [222].

In rich literature, several methods have been reported to denoise ECG signals, such as digital filters [51, 236]; adaptive filters [51, 53]; non-linear filtering techniques like median filtering [51, 237]; time-frequency methods like wavelet and empirical mode decomposition (EMD) [212], Fourier decomposition [58] , and machine learning [238], to name a few. Digital filters are employed for suppressing noise, but their performance is affected due to spectral overlap of ECG signal and noise. Non-linear filters have good suppression but have complex structures and require high computations [237]. Adaptive filters can track the morphology of ECG but require a priori information (or reference signal) to filter out the noises [53]. Similarly, wavelet methods face the problem of choosing a suitable threshold level and mother wavelet, thus limiting their use [212].

Owing to the need to design solutions for noises ranging from impulsive to Gaussian, the branch of non-linear morphological filtering is explored in this chapter. Composed of structuring element (SE) and morphological operation (MO), the MF provides a shape-based filtering mechanism to process signals, as explained in Section 2.2.

Based on an intensive survey of rich literature, the state-of-art methods [13, 84, 85, 86, 87, 88, 239, 240] seem to emphasize more on different combinations of MOs, but there has been less focus on designing SE. The SE used in MF has the essence of windows [241] , which are used to design finite impulse response (FIR) filters [68]. The conventional methods [13, 84, 85, 86] based on MF use triangular SE to extract the QRS complex. However, according to the literature, triangular windows have high side lobe levels (SLL), which can lead to errors in identifying characteristic points [241]. The literature suggests

using convolution windows to resolve the trade-off between desired window shape and SLL reduction [241, 242, 243]. Following this interpretation, the cross-convolution window concept is *proposed* in this work for the first time for formulating SE.

In addition to cross-convolution window concept, the *proposed* work employs the concept of fractional Fourier transform (FrFT) in the design of SE. FrFT is extensively employed in signal and image processing [123, 124, 125, 126, 127] domain as it provides flexibility in terms of fractional rotation parameter φ, which eventually helps in analyzing different characteristics of signal and image under consideration. Hence, the SE *proposed* in this work not only adapts to the morphology of ECG beats, but also ensures the removal of various types of noises (Gaussian and non-Gaussian).

5.2 Design of *Proposed* Morphological Filter (MF)

In the context of preprocessing ECG signals, it is imperative to ensure that noise suppression techniques do not result in losing vital information. Hence, the utilization of *proposed* SE in conjunction with *proposed* MO enables adaptation to the non-stationary changes in ECG signals. Additionally, *proposed* methodology ensures suppression of noises and facilitates preservation of distinctive attributes of ECG signals.

As mentioned in Section 2.2, design of MF is determined by the selection of SE and suitable MO based on the intended application. The subsequent sub-sections outline the *proposed* analytical approach to design novel SE and MO for denoising ECG signals using morphological filtering approach.

5.2.1 Formulation of *Proposed* SE—Fractional Structuring Element (FrSE)

SE used in morphological filtering has the essence of windows. Therefore, to minimize the error in reconstruction, the idea is to design a new window with a QRS-like structure with low side lobe level (SLL). To achieve this, the cross-convolution concept is used for designing SE along with the FrFT concept to adapt to the non-stationary nature of ECG signals.

The analytical formulation of whole process is described below.

The window functions $w_1[n]$ and $w_2[n]$ are cross-convolved in time domain as given below:

$$w_c[n] = w_1[n] * w_2[n] \tag{5.1}$$
$$= \sum_{k=-\infty}^{\infty} w_1[k] w_2[n-k]$$

where $*$ represents the convolution operation.

In the subsequent step, FrFT of this cross-convolved window is carried out using the definition of discrete FrFT (DFrFT) [130] given by

$$\mathrm{F}_{\mathcal{F}}^{\varphi}(x[n]) = X_{\varphi}(m) = \sum_{n=0}^{N-1} x[n] K_{\varphi}[n,m] \tag{5.2}$$
$$= \sum_{n=0}^{N-1} x[n] \sqrt{\frac{1-j\cot\varphi}{2\pi}}\, e^{-j\left[\frac{{u_\varphi}^2+n^2}{2}\right]\cot\varphi - jnu_\varphi \csc\varphi} \tag{5.3}$$

Then taking the DFrFT of cross-convolved window $w_c[n]$, we get

$$W_{\varphi}(m) = \sum_{n=0}^{N-1} w_c[n]\, K_{\varphi}[n,m] \tag{5.4}$$
$$= \sum_{n=0}^{N-1} \{\sum_{k=-\infty}^{\infty} w_1[k] w_2[n-k]\}\, K_{\varphi}[n,m] \tag{5.5}$$

Next for causal sequences, (5.5) reduces to

$$W_{\varphi}(m) = \sum_{n=0}^{N-1} \{\sum_{k=0}^{n} w_1[k] w_2[n-k]\}\, K_{\varphi}[n,m] \tag{5.6}$$

Expanding the terms of (5.6) we get

$$W_{\varphi}(m) = \left(\sum_{n=0}^{N-1}\left(\sum_{k=0}^{n} w_1[k] w_2[n-k]\right)\sqrt{\frac{1-j\cot\varphi}{2\pi}}\, e^{-j\left[\frac{{u_\varphi}^2+n^2}{2}\right]\cot\varphi - jnu_\varphi \csc\varphi}\right) \tag{5.7}$$

Finally, the envelope of this new transformed window (obtained in (5.7)) is then extracted (*herein, referred to as* g_r^{φ}) and is morphologically applied to the corrupted ECG signals using *proposed* MO (described in 5.12), discussed later in this section.

The highlighting features of utilizing cross-convolution and FrFT are:

i. A small value of SLL is a desirable feature for constructing SE using window functions as it reduces inaccuracy in identifying characteristic points of ECG beats [51, 68, 222]. Thus, to improve the performance of literature-based MF, cross-convolution approach is employed in designing new window, which resulted in variable SLL, contrary to fixed SLL of window used in literature methods [13, 84, 85, 86, 87, 88, 239, 240].

ii. In order to attain shape flexibility, the design of *proposed* SE (referred to as *FrSE*) utilizes FrFT to address the non-stationary characteristics of ECG signals. Consequently, introduction of the new window has two distinct advantages. Firstly, the utilization of FrFT parameter ensures alignment with QRS-like form of ECG signal, thereby enhancing shape matching. Secondly, the inclusion of variability in SLL contributes to a reduction in reconstruction error and thus facilitates the diagnostic process.

5.2.2 Analytical Aspect of Designing *Proposed* FrSE

Based on an extensive survey conducted on window functions, two window functions chosen for cross-convolution are triangular window [241, 244] and Dolph-Chebyshev [245, 246], which are mathematically represented as follows.

$$Triangular\ window\ [n] = 1 - \frac{|2n|}{N}, 0 \leq |n| \leq \frac{N}{2} \tag{5.8}$$

$$Dolph - Chebyshev\ window\ [n] = \frac{1}{N}\left[\frac{1}{r} + 2\sum_{i=1}^{(N-1)/2}\left(T_{N-1}\left(x_o \cos\frac{i\pi}{N}\right)\right)\cos\left(\frac{2\pi ni}{N}\right)\right], 0 \leq n \leq N \tag{5.9}$$

where

$$x_o = \cosh^{-1}\left(\frac{1}{N-1}\cosh^{-1}\frac{1}{r}\right) \tag{5.10}$$

$$T_N(x) = \begin{cases} \cos(N\cos^{-1}(x)) & , \text{for } |x| \leq 1 \\ \cosh(N\cosh^{-1}(x)) & , \text{for } |x| > 1 \end{cases} \tag{5.11}$$

and r is the required ripple ratio, which contributes to side lobe attenuation [245].

From the viewpoint of developing SE, key points related to window concept are:

i. The advantage of utilizing cross-convolution window in designing new SE resulted in reducing SLL, which in turn reduced error in reconstruction.

ii. The Dolph-Chebyshev window is a variable-type window that offers *minimum main-lobe width (MLW)* for a *given* SLL [241, 244, 245, 246]. On the other hand, triangular window is used due to its resemblance with QRS complex but has a drawback of large *SLL* value (-26.53dB) [241, 243, 244]. Thus, by cross-convolving

these windows, variability in *SLL* is attained, as demonstrated in **Figure 5.1**. Here, the r factor of Dolph-Chebyshev window provides variability in SLL of the newly formulated window. With r changing from 5 to 100 dB, different levels of SLL can be achieved, which are much better than fixed windows like Hamming window (SLL= -42.811 dB), Hann window (SLL= -31.467 dB), and various other windows present in the literature [241].

iii. Also, with the introduction of FrFT order parameter a (where $a = 2\varphi/\pi$), the shape similarity to ECG beat is attained as demonstrated in **Figure 5.2**. Here, the a factor provides flexibility to the shape of cross-convolved window, which further allows new window to adapt to different ECG beats present in the signal. This is a major factor contributing to better reconstruction and enhancing MF performance, and will be illustrated in Section 5.3.

Hence, *proposed FrSE* possesses two degrees of freedom (r and a), which makes the morphological filtering process adaptive in nature in contrast to classical approaches.

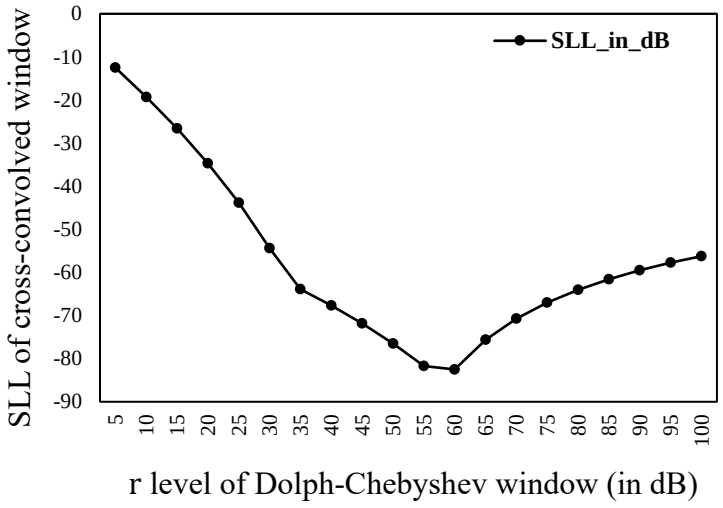

Figure 5.1 Variation of SLL of cross-convolved window with ripple ratio r of Dolph-Chebyshev Window.

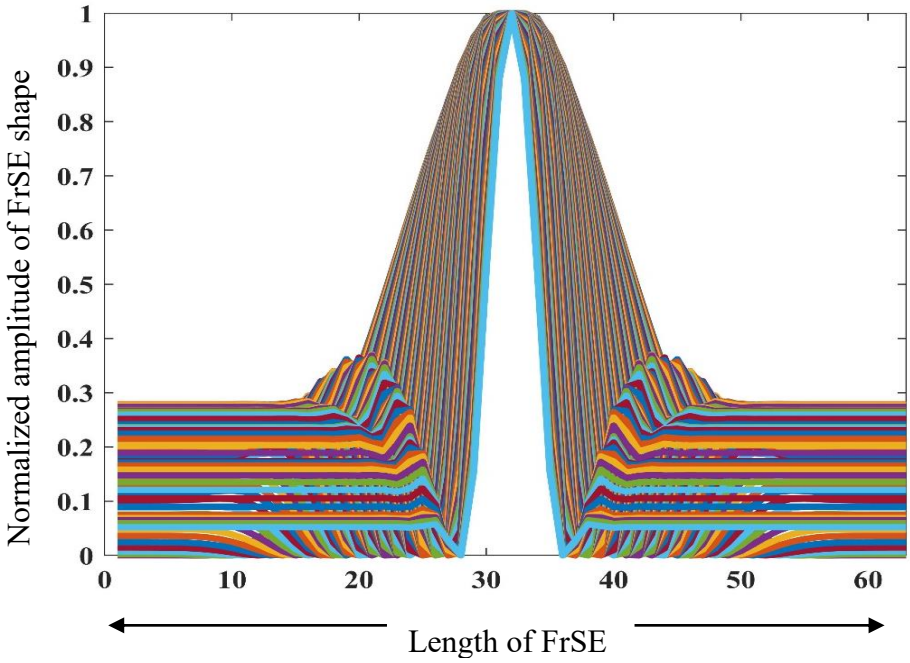

Figure 5.2 Demonstration of shape adaptability with *proposed* FrSE with a varying from 0 to 1.

5.2.3 *Proposed* Morphological Operation (MO)

From the characteristics of different MO described in Section 2.2, the MO *proposed* for denoising ECG signal is represented by

$$x_d = \frac{1}{2}\left(\left(\left(x_n \blacksquare g_r^{\varphi} \circ g_r^{\varphi}\right) \oplus g_{flat}\right) + \left(\left(x_n \blacksquare g_r^{\varphi} \circ g_r^{\varphi}\right) \ominus g_{flat}\right)\right) \tag{5.12}$$

where g_r^{φ} is the novel *FrSE*, $\blacksquare$ is the symbol for closing, $\circ$ is the opening operation, g_{flat} is the flat SE, $\oplus$ represents dilation, $\ominus$ represents erosion, x_d is the resulting denoised signal and x_n is signal of interest.

The operations involved in designing the *proposed* MO are elaborated as:

i. Closing (or opening) removes the negative peaks (or positive peaks). As the shape of QRS complex needs to be preserved, cascade operation of closing followed by opening is chosen. The described operations are expressed as

$$y_{co} = \left(x_n \blacksquare g_r^{\varphi} \circ g_r^{\varphi}\right) \tag{5.13}$$

This MO incorporating *proposed* FrSE (g_r^{φ}) will ensure in preserving true morphology of ECG beat even in the presence of noise.

ii. Next, to remove noises corrupting ECG signal, combination of dilation and erosion operation is applied, which is mathematically described as

$$x_d = \frac{1}{2}\left(\left(y_{co} \oplus g_{flat}\right) + \left(y_{co} \ominus g_{flat}\right)\right) \tag{5.14}$$

The explanation for choosing these operations lies in the fact that dilation (or erosion) is responsible for reducing the positive peaks (or negative peaks). Therefore, *proposed* MO removes the noise without distorting ECG beat. Here, flat SE is chosen to effectively suppress the spurious peaks resulting from noise interference.

5.3 ECG Denoising Methodology

In this study, an attempt has been made to design MF using *proposed FrSE* and *MO* (*herein referred to as* $MF_{FrSE\&MO}$) for denoising ECG signals. In addition, the first-of-its-kind *proposed* methodology incorporates the use of α-stable distribution as a noise analysis model to more accurately simulate real-time noises that interfere with ECG signals. Furthermore, to offer a more comprehensive description of *proposed* denoising approach, this section will commence by explaining the performance metric parameters that have been employed. Following that, several stages of the *proposed* methodology will be outlined.

5.3.1 Performance Metric Parameters (PMP)

In the reported work, different *PMPs* are utilized to measure the efficiency at various stages of denoising algorithm. The general framework of *proposed* denoising process considered in this work can be formulated as follows: $x_n = x_o + \alpha_s$, where x_o is the original ECG signal, α_s is α-stable distribution-based noise model (with $\alpha = 2$ representing Gaussian model), x_n is noisy ECG signal and x_d is the denoised signal.

To illustrate the *proposed* methodology, *PMPs* are classified into three distinct categories, each of which is described as follows:

a) ***PMP for noise quantification*** - To emphasize the impact of using *proposed* α-stable distribution-based noise model, the performance of *proposed* $MF_{FrSE\&MO}$ is quantitatively assessed using signal distortion ratio (*SDR*) and maximum deviation (*Max_dev*), which are defined as [13, 85]

$$SDR = \frac{\sum\|x_o - x_n\|}{\sum\|x_n\|} \tag{5.15}$$

$$Max\_dev = \max_{n=0,\cdots,N} |x_o - x_n| \tag{5.16}$$

Here, *SDR* is used to quantify as well as compare the degradation that results from the introduction of Gaussian distribution noise and α-stable distribution noise in original ECG signal. The large value of *SDR* indicates high level of introduced distortion. Similarly, large value of *Max_dev* signifies the maximum deviation of noisy ECG signal from original ECG signal when corrupted with noises of either type (i.e., Gaussian or α-stable).

b) ***PMP for similarity*** - In order to achieve highest possible alignment between *proposed FrSE* and ECG beat, two similarity measures: cross-correlation (*CC_beat*) and root-mean-square-error (*RMSE_beat*) are used, which are defined as [247]

$$CC\_beat = \frac{\frac{1}{L}\sum(x_{beat} - \overline{x_{beat}})\left(g_r^{\varphi} - \overline{g_r^{\varphi}}\right)}{\sqrt{\frac{1}{L}\left((x_{beat} - \overline{x_{beat}})\right)^2}\sqrt{\frac{1}{L}\left(\left(g_r^{\varphi} - \overline{g_r^{\varphi}}\right)\right)^2}} \tag{5.17}$$

$$RMSE\_beat = \sqrt{\frac{1}{L}\sum\left(x_{beat} - g_r^{\varphi}\right)^2} \tag{5.18}$$

where x_{beat} is ECG beat under consideration and g_r^{φ} is *proposed FrSE* at chosen a and r.

CC_beat quantifies similarity between ECG beat and *proposed FrSE*, with maximum correlation corresponding to 1. On the other hand, a lower *RMSE_beat* value will correspond to less error and hence maximum matching. Additionally, *proposed FrSE* has two degrees of freedom (a and r). Therefore, optimal values of a and r are obtained when *CC_beat* value is closer to one and *RMSE_beat* value is close to zero.

c) ***PMP for evaluation***- To quantitatively assess the performance of overall denoising method using *proposed* $MF_{FrSE\&MO}$, the metrics utilized are defined below [211] :

$$RMSE = \sqrt{\frac{\sum_{n=0}^{N-1}[x_o(n) - x_d(n)]^2}{N}} \tag{5.19}$$

$$imp\_SNR\ [dB] = SNR_{output}[dB] - SNR_{input}[dB] = 10\log\left[\frac{\sum_{n=0}^{N-1}[x_d(n)-x_o(n)]^2}{\sum_{n=0}^{N-1}[x_o(n)-x_n(n)]^2}\right] \quad (5.20)$$

RMSE reflects the error between original and denoised signal. A low *RMSE* value indicates better reconstruction and thus implies that the signal's information is better preserved. The i*mp_SNR* values quantify the noise level before and after applying the *proposed* methodology. Higher values of *imp_SNR* imply better noise removal.

5.3.2 *Proposed* MF based ECG Denoising

ECG denoising model *proposed* in this work employs *proposed* $MF_{FrSE\&MO,}$ which focuses on retaining characteristic components of ECG and subsequently removes the noisy counterpart. The adaptiveness achieved by amalgamating the concept of FrFT (used in designing *FrSE*) with MF for ECG denoising adds the advantage of variable a (related as $a = 2\varphi/\pi$), thereby providing robust performance in Gaussian as well as non-Gaussian environment.

The basic framework for denoising model using *proposed* $MF_{FrSE\&MO}$ is depicted in **Figure 5.3**. This includes corrupting signal with α-stable distribution noise, then applying *proposed FrSE* to ECG segments followed by *proposed MO*, beat-by-beat. Finally, quantitative analysis is performed on output (denoised) signal to check the efficacy of *proposed* method. The *proposed* denoising method is a five-stage process and each stage is described below:

Stage 1—**Noise Addition**: To evaluate the performance of *proposed* method, ECG signals from MIT-BIH Arrhythmia Database [196] are used. These signals are artificially corrupted with α-stable distribution noise model, which is more effective in simulating environmental conditions [49].

Stage 2 —**Beat-to-beat segmentation**: In ECG signals, as each heartbeat is characterized by a distinct waveform, therefore *proposed FrSE* is used at beat-to-beat level to process each ECG beat independently. For simulation purposes, using the sliding window technique [248, 249], a segment length of 200 samples is taken to cover the entire ECG beat.

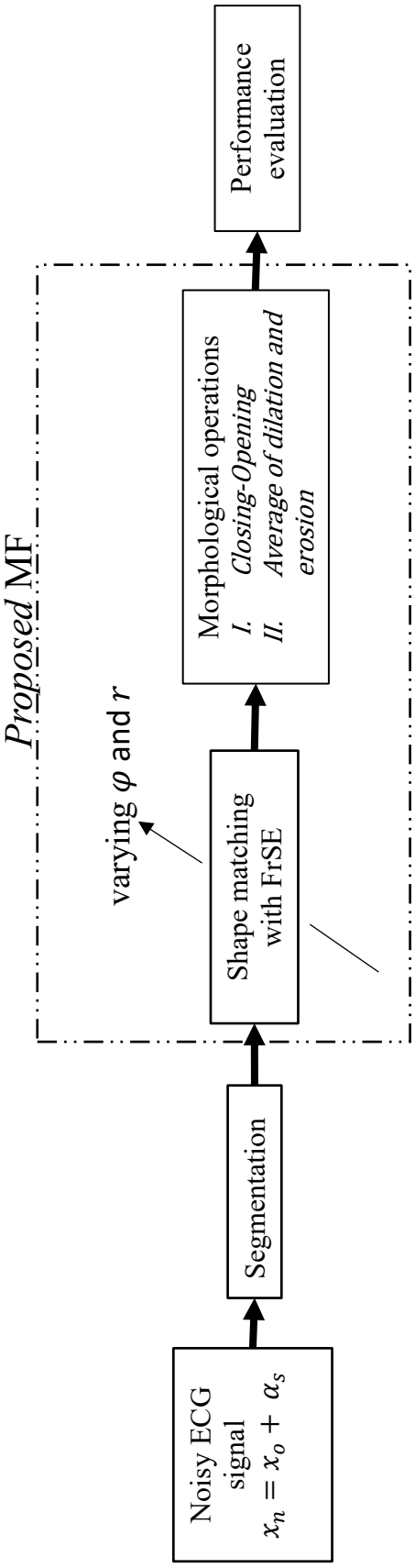

Figure 5.3 Block diagram for ECG denoising using *proposed* MF

Stage 3 —**Shape matching with *FrSE***: After beat segmentation, the selected segment with one beat is compared with *proposed FrSE* by varying *fractional* order parameter a according to the relation $a = 2\varphi/\pi$. Additionally, by altering parameter a, values of *PMP for similarity* (*CC_beat* and *RMSE_beat*) are evaluated, as illustrated in **Figure 5.4 (a)**. The value of a at which *CC_beat* is maximum and *RMSE_beat* is minimum is referred to as $a_{optimal}$ (as highlighted in **Figure 5.4(a)**). At this point, *proposed FrSE* most closely resembles the shape of ECG beat under consideration, as demonstrated in **Figure 5.4 (b)**.

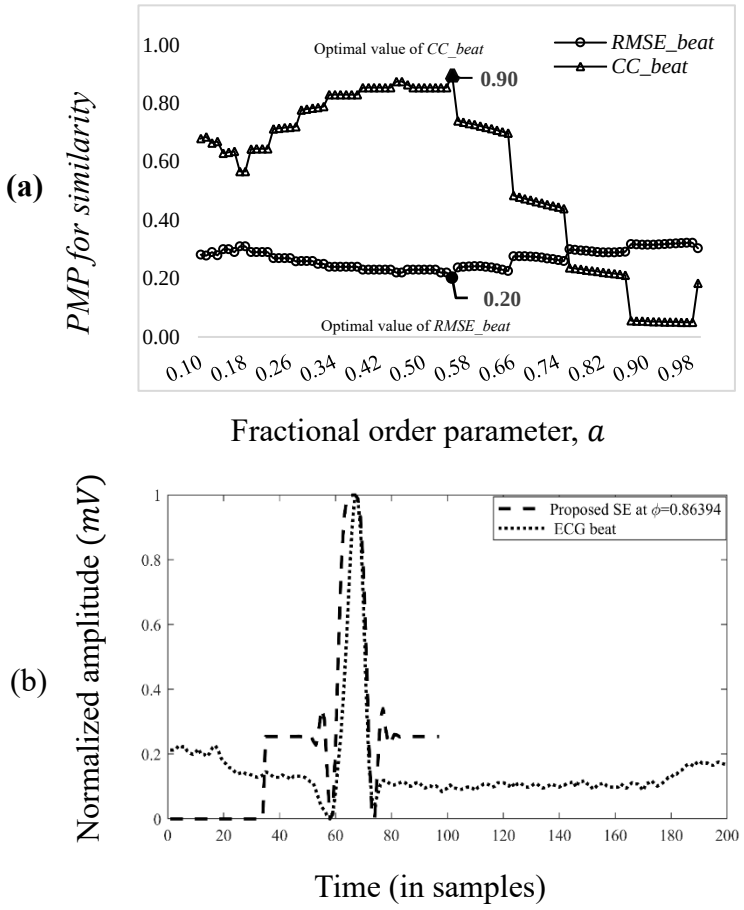

Figure 5.4 Demonstration of *proposed* FrSE adapting to the shape of ECG beat. **(a)** Variation of *PMP for similarity* with changing fractional order parameter a, **(b)** *Proposed* FrSE adapting to the shape at $a_{optimal} = 0.55$ which gives $\varphi_{optimal} = 0.86394$ by relation $\varphi = a\pi/2$.

Stage 4 —**Applying *proposed MO***: In this stage, *proposed FrSE* at $\alpha_{optimal}$ is morphologically applied to ECG beat using *proposed MO* formulated in (5.12). This *proposed MO*, in conjunction with *proposed FrSE* and *flat SE*, not only preserves the distinctive shape of ECG signal but also efficiently eliminates noise.

The primary objective of first MO is to preserve the shape of ECG beat while suppressing beat-like peaks and other spurious peaks of high amplitude. Next, operation described by second MO finally suppresses all the noisy peaks, resulting in a denoised signal. The procedure described in stages 3 and 4 constitutes morphological filtering and these steps are repeated until all signal segments are traversed.

With a sampling rate of 360Hz and the fact that QRS lasts for approximately 100ms (36 samples) [68, 222], *proposed FrSE* with a length of 63 samples is chosen to retain the characteristic shape of ECG beat. Next, for background noise removal, *flat SE* with a length of 5 samples is chosen [13, 85]. These lengths have been chosen in accordance with the length of SE described in Section 2.2.1.

Stage 5 —**Performance Evaluation**: Finally, performance of *proposed* method using *novel FrSE* is assessed using *PMP for evaluation*. The flexibility provided with two degrees of freedom is an additional aspect that distinguishes *proposed* method from conventional methods (having no degree of freedom) employing fixed SE [13, 84, 85, 86, 87, 88, 239, 240]. In addition to employing quantitative analysis using *PMP for evaluation*, the box-plot evaluation method [184] is also utilized to statistically measure the comparison between *proposed* method and state-of-the-art methods for Gaussian and α-stable distribution noise.

5.4 Simulation Results

To evaluate *proposed* $MF_{FrSE\&MO}$ for ECG denoising, 10 ECG records from MIT-BIH Arrhythmia database [196] are used. To demonstrate *proposed* methodology, **Figure 5.5** (for α-stable distribution noise) and **Figure 5.6** (for Gaussian distribution noise) give insight into the output of different stages, i.e., the addition of noise, output of first MO (*closing* followed by *opening* using *proposed* FrSE), and finally the denoised signal (output of second MO: average of *dilation* and *erosion* by employing *flat SE)*.

In further sections, the results of *proposed* methodology are presented from a quantitative and qualitative perspective.

5.4.1 Quantification of Noise Environment

Stage 1 of *proposed* methodology incorporates the α-stable distribution [49] noise model for replicating real-time scenario. To depict the importance of adopted noise analysis model, a visual comparison has been provided by corrupting ECG record 100 of MIT-BIH Arrhythmia Database [196] with α-stable distribution noise as well as Gaussian noise, for illustration purposes in **Figure 5.5 (b)** and **Figure 5.6(b)**, respectively. The important points to consider are:

i. The α-stable noise used here is symmetric α-stable ($S\alpha S$) noise as symmetry parameter β is zero.
ii. For simulation purposes, α-stable distribution noise is generated using the Chambers method [224] in MATLAB software.
iii. As higher order moments do not exist for α-stable distribution (i.e., variance is not defined), so for generating a suitable noise level for α-stable distribution noise, concept of pseudo-SNR described in [250] is employed.

The following distinguishing features are observed when comparing pictorial representations in **Figure 5.5(b)** and **5.6(b)**.

i. Gaussian noise does not alter ECG morphology much, whereas α-stable distribution noise significantly distorts the morphology of ECG.
ii. R-peaks in ECG signal corrupted by Gaussian noise can be identified relatively easily, whereas in ECG corrupted by α-stable distribution noise, identification of R-peaks is a challenging task.

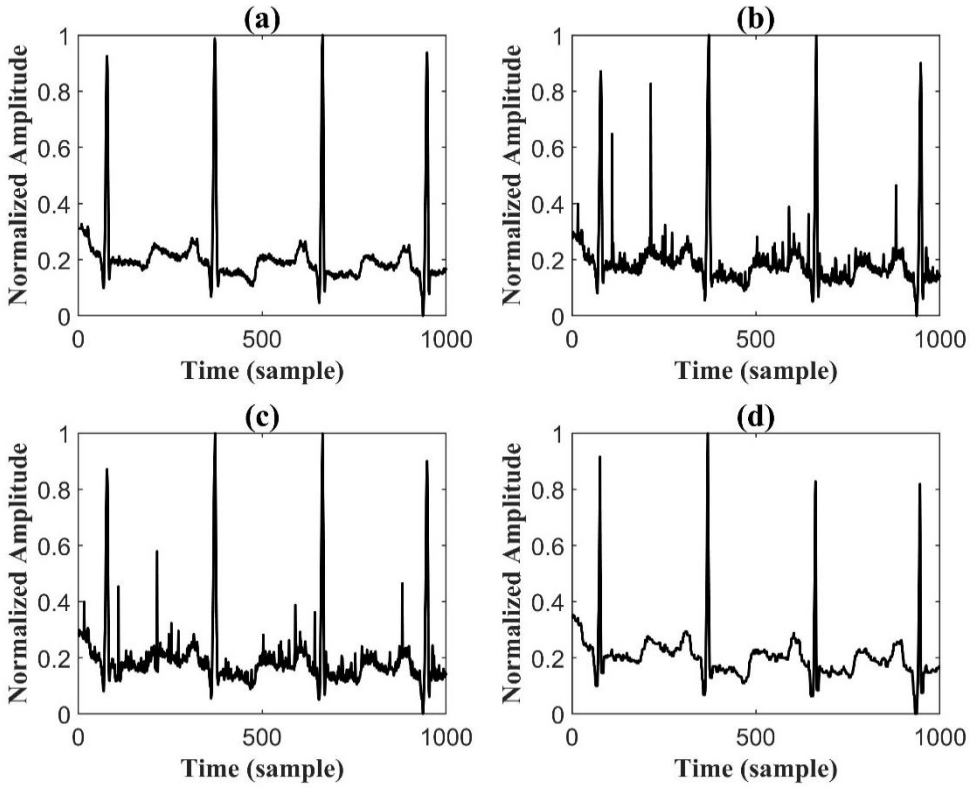

Figure 5.5 Different stages of *proposed* methodology: **(a)** Time domain representation of raw ECG signal (MIT-BIH record 100m), **(b)** Raw ECG signal corrupted with 5dB α-stable distribution noise, **(c)** Output of MO I as per block diagram **(d)** Final denoised signal; Output of MO II as per block diagram.

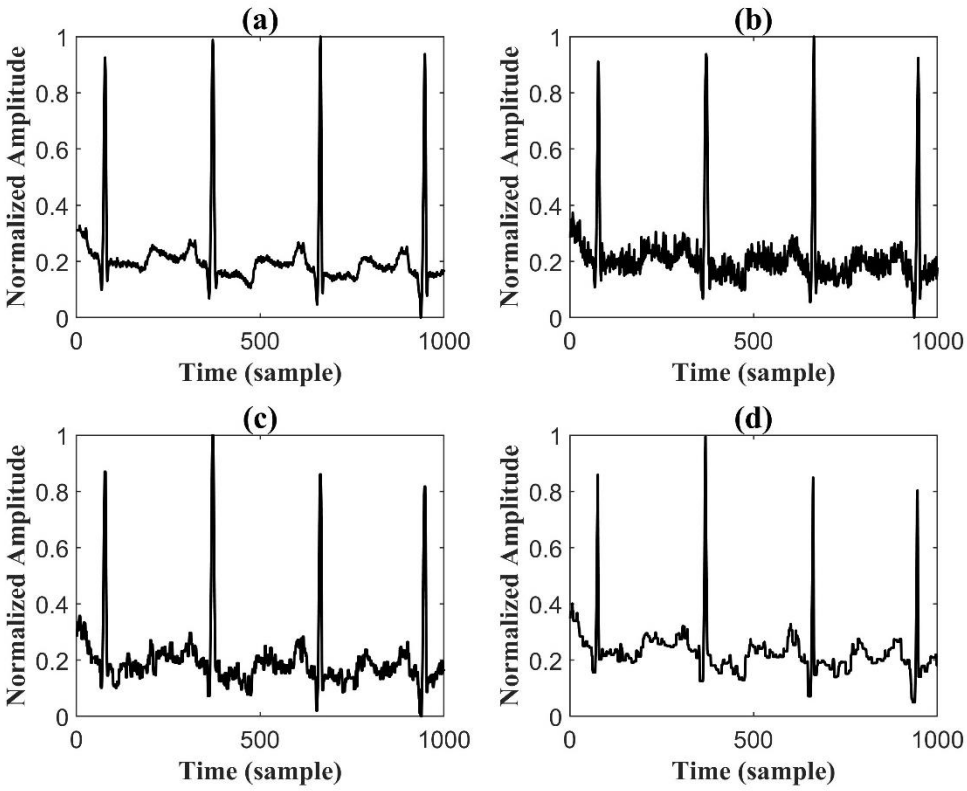

Figure 5.6 Different stages of *proposed* methodology: **(a)** Time domain representation of raw ECG signal (MIT-BIH record 100m), **(b)** Raw ECG signal corrupted with 5dB Gaussian distribution noise, **(c)** Output of MO I as per block diagram, **(d)** Final denoised signal; Output of MO II as per block diagram.

Next, to prove the usefulness of α-stable distribution model over Gaussian distribution model, quantitative analysis is presented in **Figure** 5.7. Here, several input noise levels are utilized to illustrate the extent of deviation/distortion introduced in different noise environments.

By investigating the results in **Figure 5.7 (a)**, it becomes evident that distortion introduced by the addition of α-stable distribution is much higher than Gaussian distribution noise. To provide more clarification, two cases of α-stable distribution noise ($\alpha = 1.2$ and $\alpha = 1.5$) are depicted. It can be deduced that as α value approaches one, impulsiveness increases (as explained in Section 2.3.2), resulting in a higher value of *SDR* and hence, more deterioration in signal quality.

Similarly, from the results recorded for *Max_dev* in **Figure 5.7 (b)**, it can be inferred that the values of *Max_dev* are much larger for α-stable distribution case than Gaussian case. This clearly proves that α-stable distribution model introduces more distortion and hence denoising methods designed considering such noises will perform better in real-time as well.

Furthermore, as established in **Chapter 4**, ECG noises are more closely related to α-stable distribution model. Thus, in the presented work an attempt has been made to model noise using α-stable distribution (of which Gaussian distribution is also included as a special case at $\alpha = 2$) to replicate real environmental conditions better.

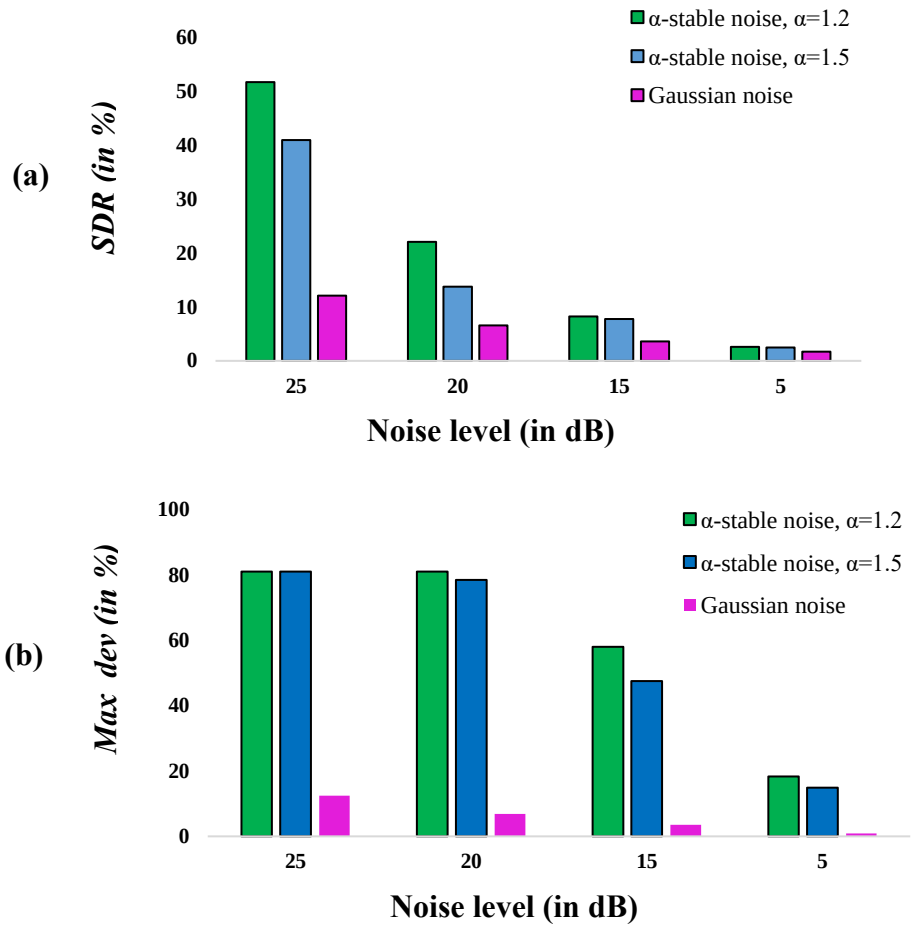

Figure 5.7 Deviation introduced in signal upon adding Gaussian and α-stable noise, **(a)** Signal-to-distortion ratio (*SDR*) introduced after adding noises with different input noise levels, **(b)** Maximum deviation (*Max_dev*) introduced after adding noises with different input noise levels. Here, α-stable noise is generated with $\alpha = 1.2$ and $\alpha = 1.5$.

5.4.2 Role of Adaptive Parameters: Ripple ratio r and FrFT Order Parameter a

The denoising process using *proposed* $MF_{FrSE\&MO}$ has an advantage of having two degrees of freedom (r and a). After beat segmentation is performed in Stage 2, *proposed FrSE* is subsequently employed for each beat by computing $a_{optimal}$, as demonstrated in Stage 3 of *proposed* methodology.

Here, $a_{optimal}$ is responsible for determining best match between the shape of *proposed* FrSE and ECG beat. On the other hand, variable r contributes in minimizing error in reconstruction.

To further demonstrate the dependence of degrees of freedom (r and $a = 2\varphi/\pi$) on performance of denoising method, one segment of ECG record is selected and corrupted with noise following α-stable distribution for purpose of simulation. By doing this, we are able to examine variations in performance of denoising method and demonstrate flexibility of our suggested methodology.

Changing window r level: First, the dependency of changing r level (computed at $a_{optimal}$) on *PMP for evaluation* is illustrated in **Figure 5.8(a)**. By analyzing results, it is evident that as a is optimal, *imp_SNR* and *RMSE* values tend to remain consistent at different r levels. Thus, changing r has less effect on overall denoising performance when a is optimal, i.e., *proposed FrSE* adapts to best possible shape of ECG beat.

Changing fractional order parameter a: Next, to investigate the behavior of changing FrFT order parameter a, **Figure 5.8(b)** represents the variation in *RMSE* values at fixed r levels — 10, 30, 50, 70, and 90. *RMSE* values attained at different r levels signify that, r level at which *RMSE* value is large corresponds to larger *SLL* values. This can be ascertained with the concept stated in Section 5.2.2 that, when used for processing, large SLL level of the window contributes to inaccurate identification of the fiducial points [51].

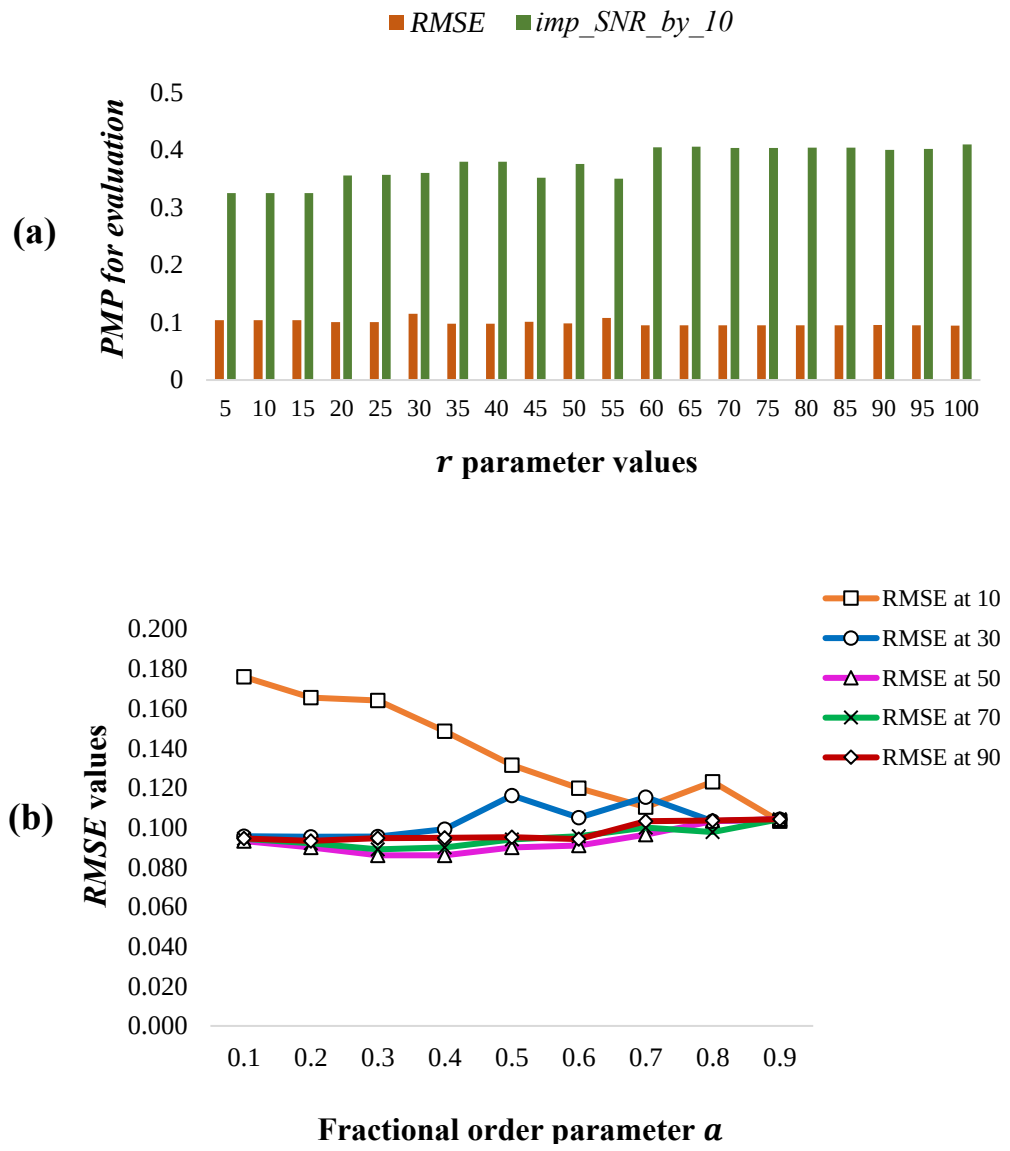

Figure 5.8 Demonstration showing performance evaluation of the *proposed* method varying degrees of freedom; ripple ratio r and FrFT order parameter a, **(a)** Performance evaluation changing r level with a computed at $a_{optimal}$, **(b)** Performance evaluation changing a at different r levels.

Note: To represent *PMP for evaluation* values in same graph, values of obtained *imp_SNR* are divided by 10 in **(a)**.

5.4.3 Performance Evaluation using Real-Time Dataset in Presence of α-Stable Distribution Noise and Gaussian Distribution Noise

To evaluate the performance of *proposed* $MF_{FrSE\&MO}$, 10 ECG records from [196]: 100, 101,102,103,104,105,106,107,108, 109 are selected. The *PMP for evaluation* is computed for these ECG signals (length =21600 samples ~ 1 min) at three noise levels: 5 dB, 10 dB and 15 dB. For experimental purposes and with reference to the explanation presented in Section 5.4.2, denoising is performed by considering $a_{optimal}$ and r =60 dB.

Furthermore for comparison, quantitative analysis is also performed using morphological filtering method given in [13] (herein referred to as MF method 1989) and the method discussed in [85] (herein referred to as MF method 2002) on same records. The results for comparing *proposed* method and aforementioned selected methods are tabulated in **Tables 5.1** and **5.2**.

In **Table 5.1**, performance of the methods is recorded for α-stable distribution case and Gaussian distribution case ($\alpha = 2$) and results are tabulated in **Table 5.2**. Analyzing values of *PMP for evaluation*, it can be ascertained that *proposed* method performed equally well in both α-stable distribution and Gaussian environments in contrast to other two methods, where results are acceptable only for Gaussian noise case. The low values of *RMSE* and high values of *imp_SNR* obtained for both noise distributions prove that the *proposed* method is robust and a suitable contender for practical scenarios.

In order to provide more insights for the results recorded in **Tables 5.1** and **5.2**, the performance of the literature methods: MF method 1989, MF method 2002 and the *proposed* method, are also compared at 10 dB input noise level using box-plot statistical analysis method [184] and results are demonstrated in **Figure** 5.**9**.

Figure 5.9 (a) and **(b)** demonstrate that *proposed* method achieves lowest RMSE for both noise scenarios. This signifies that *proposed* method leads to reduced error in reconstruction and better retention of characteristic information.

Similarly, from **Figure 5.9 (c)** and **(d)**, it is observed that the *imp_SNR* values are much higher for *proposed* method in both noise environments, as compared to other selected literature methods. Also, a point worth mentioning is the lower bound of *imp_SNR* box-plot for *proposed* method is higher than the highest value attained with MF method 2002

and MF method 1989 in both noise environments, which signifies the effectiveness of *proposed* method.

Thus, from overall box-plot analysis it can be depicted that, with two degrees of freedom, *proposed* method has the potential to suppress noise (as inferred from high *imp_SNR* values) and improve reconstruction (as inferred from low *RMSE* values). This clearly highlights that, with *proposed FrSE* used in denoising methodology, *proposed* method has the potential to provide flexible performance in noise environments ranging from Gaussian to impulsive.

Table 5.1 Performance evaluation of *proposed* method with literature based morphological based in presence of α-stable distribution noise

Methods	Input Noise level	PMP for evaluation	ECG records										Average PMP
			100m	101m	102m	103m	104m	105m	106m	107m	108m	109m	
1989 method [13]	5 dB	*RMSE*	0.109	0.104	0.237	0.100	0.126	0.122	0.108	0.150	0.085	0.143	0.13
		imp_SNR (in dB)	5.121	4.290	6.761	7.649	8.863	4.605	6.771	8.267	10.499	7.628	7.05
	10 dB	*RMSE*	0.110	0.104	0.237	0.101	0.126	0.122	0.108	0.150	0.085	0.143	0.13
		imp_SNR (in dB)	5.121	4.269	6.759	7.642	8.850	4.602	6.756	8.263	10.490	7.623	7.04
	15 dB	*RMSE*	0.110	0.104	0.237	0.101	0.130	0.122	0.108	0.150	0.085	0.144	0.13
		imp_SNR (in dB)	5.159	4.236	6.756	7.631	9.596	4.599	6.733	8.257	10.585	7.814	7.14
2002 method [85]	5 dB	*RMSE*	0.099	0.092	0.204	0.090	0.108	0.106	0.096	0.129	0.074	0.124	0.11
		imp_SNR (in dB)	5.700	4.990	7.632	8.289	9.756	5.402	7.437	9.123	11.295	8.469	7.81
	10 dB	*RMSE*	0.099	0.092	0.204	0.090	0.108	0.106	0.096	0.129	0.074	0.124	0.11
		imp_SNR (in dB)	5.696	4.967	7.629	8.279	9.744	5.397	7.421	9.120	11.284	8.463	7.80
	15 dB	*RMSE*	0.100	0.092	0.204	0.090	0.114	0.106	0.096	0.129	0.075	0.125	0.11
		imp_SNR (in dB)	5.721	4.928	7.626	8.261	10.364	5.389	7.395	9.114	11.361	8.624	7.88
Proposed method	5 dB	*RMSE*	0.066	0.051	0.013	0.059	0.049	0.018	0.049	0.011	0.019	0.018	**0.04**
		imp_SNR (in dB)	12.064	12.579	33.186	15.686	20.600	22.183	16.537	32.909	27.109	27.659	**22.05**
	10 dB	*RMSE*	0.066	0.051	0.013	0.060	0.050	0.020	0.049	0.011	0.021	0.019	**0.04**
		imp_SNR (in dB)	12.003	12.433	32.930	15.590	20.434	21.651	16.459	32.617	26.369	27.250	**21.77**
	15 dB	*RMSE*	0.068	0.054	0.014	0.062	0.046	0.024	0.050	0.013	0.026	0.022	**0.04**
		imp_SNR (in dB)	11.908	11.972	32.185	15.291	22.281	20.263	16.243	31.734	24.802	26.441	**21.31**

Bold indicates minimum value of *RMSE* and maximum value of *imp_SNR* (in dB)

Table 5.2 Performance evaluation of *proposed* method with literature based morphological based in presence of Gaussian distribution noise.

Methods	Input Noise level	PMP for evaluation	ECG records										Average PMP
			100m	101m	102m	103m	104m	105m	106m	107m	108m	109m	
1989 method [13]	5 dB	*RMSE*	0.084	0.080	0.182	0.077	0.097	0.094	0.083	0.115	0.065	0.110	0.10
		imp_SNR (in dB)	7.692	6.512	10.260	11.464	13.440	6.990	10.258	12.533	15.896	11.539	10.66
	10 dB	*RMSE*	0.084	0.080	0.182	0.077	0.097	0.094	0.083	0.115	0.065	0.110	0.10
		imp_SNR (in dB)	7.638	6.487	10.269	11.426	13.429	6.999	10.235	12.534	15.874	11.518	10.64
	15 dB	*RMSE*	0.084	0.080	0.182	0.077	0.097	0.094	0.083	0.115	0.065	0.110	0.10
		imp_SNR (in dB)	7.578	6.445	10.285	11.358	13.410	6.999	10.196	12.535	15.859	11.480	10.61
2002 method [85]	5 dB	*RMSE*	0.076	0.071	0.157	0.069	0.083	0.082	0.074	0.099	0.057	0.095	0.09
		imp_SNR (in dB)	8.574	7.573	11.577	12.443	14.780	8.201	11.267	13.830	17.106	12.814	11.82
	10 dB	*RMSE*	0.076	0.071	0.157	0.069	0.083	0.082	0.074	0.099	0.057	0.095	0.09
		imp_SNR (in dB)	8.521	7.548	11.584	12.402	14.762	8.210	11.244	13.830	17.087	12.791	11.80
	15 dB	*RMSE*	0.076	0.071	0.157	0.069	0.084	0.082	0.074	0.099	0.057	0.095	0.09
		imp_SNR (in dB)	8.456	7.504	11.597	12.331	14.732	8.204	11.203	13.830	17.074	12.751	11.77
Proposed method	5 dB	*RMSE*	0.044	0.034	0.008	0.039	0.032	0.012	0.032	0.007	0.012	0.012	**0.02**
		imp_SNR (in dB)	13.357	14.027	36.960	17.365	23.022	24.875	18.406	36.683	30.466	30.879	**24.60**
	10 dB	*RMSE*	0.044	0.034	0.008	0.039	0.032	0.012	0.032	0.007	0.012	0.012	**0.02**
		imp_SNR (in dB)	13.295	14.003	36.914	17.333	23.057	24.834	18.382	36.647	30.379	30.822	**24.57**
	15 dB	*RMSE*	0.044	0.034	0.009	0.039	0.032	0.012	0.032	0.007	0.013	0.012	**0.02**
		imp_SNR (in dB)	13.221	13.954	36.797	17.272	23.105	24.733	18.338	36.551	30.186	30.686	**24.48**

Bold indicates minimum value of *RMSE* and maximum value of *imp_SNR* (in dB)

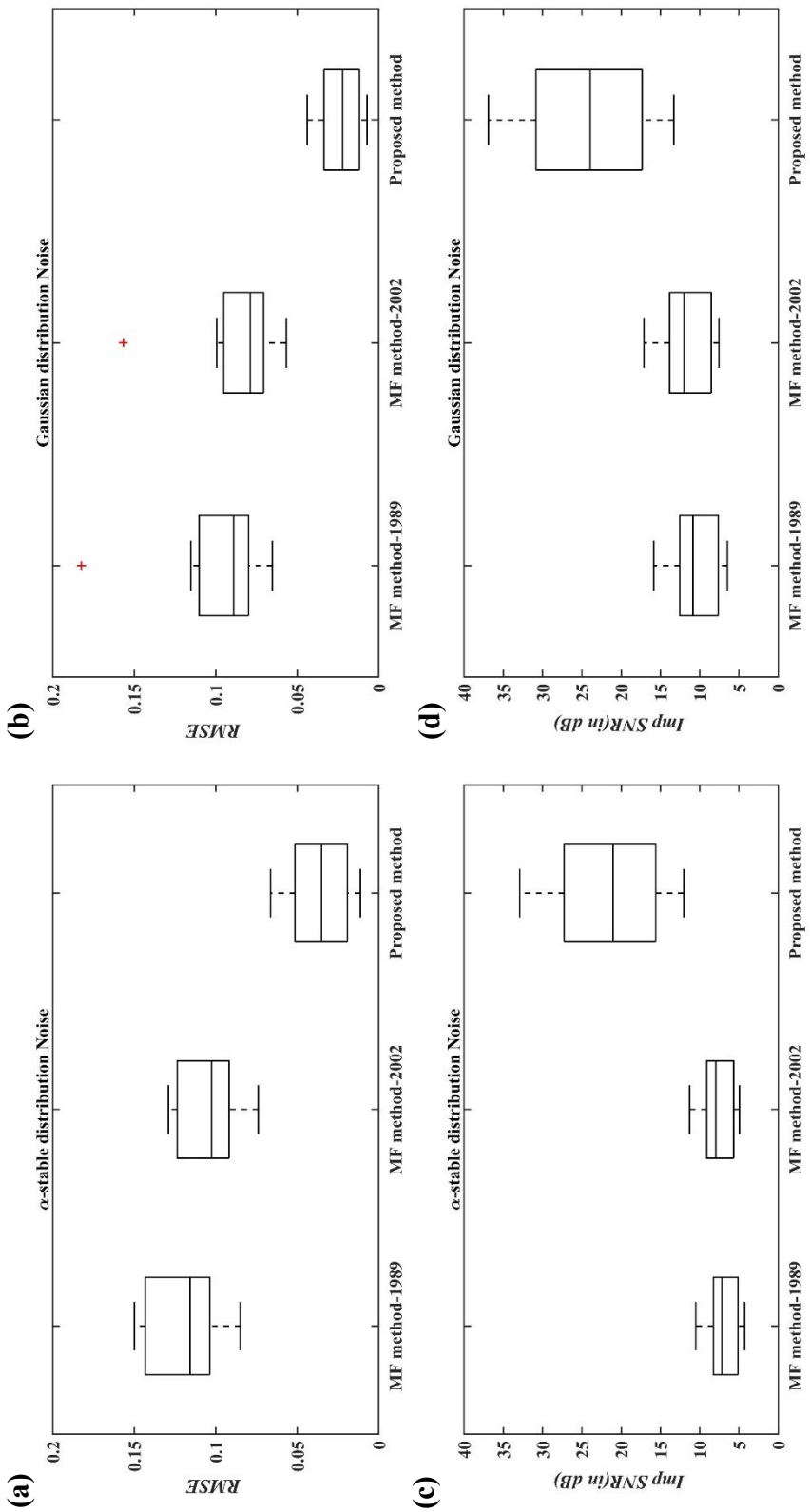

Figure 5.9 Box-plot statistical analysis evaluation for different MF methods and *proposed* method on *RMSE* and *imp_SNR* (in dB) values in different noise environments at 10 dB input noise level. **(a)** RMSE box-plot evaluation in α-stable distribution noise environment, **(b)** RMSE box-plot evaluation in Gaussian distribution noise environment, **(c)** *imp_SNR* (in dB) box-plot evaluation in α-stable distribution noise environment, **(d)** *imp_SNR* (in dB) box-plot evaluation in Gaussian distribution noise environment.

5.4.4 Comparison with State-of-the-Art Methods using Limiting Case of α-Stable Distribution, i.e., Gaussian Distribution

Established state-of-art methods employ the Gaussian noise model to validate the efficacy of their denoising methods. As we have used α-stable distribution noise analysis model in this work, so for fair comparison of the *proposed* $MF_{FrSE\&MO}$ with the well-established methods, the limiting case of α-stable distribution noise model, which corresponds to the Gaussian case (at $\alpha = 2$) is used, and results are shown in **Figures 5.10** and **5.11**.

Firstly, in **Figure 5.10,** the results of the *proposed* method are evaluated at different input SNR levels (-5dB, 0dB, 5dB and 10dB) to provide a fair comparison with the chosen literature methods such as Wavelet [251], EMD [252] and EMD- NLM [253].

Next, in **Figure 5.11**, the *proposed* method is exclusively compared with the morphological-based method [254] (herein, referred to as MF method 2013 [254]) at 10 dB Gaussian distribution noise level. The performance is compared in terms of *imp_SNR* values obtained for two MIT-BIH records: 106 and 228.

Analyzing the graphical depictions in **Figure 5.10**, it can be depicted that the *proposed* method outperforms the established methods in dealing with Gaussian noise by achieving higher *imp_SNR* and *lower RMSE* values. Also, the point worth mentioning is that even at low input SNR levels (corresponding to high noise input level), the *proposed* method consistently performs better than other methods.

Similarly, analyzing the results obtained in **Figure 5.11**, the obtained bar graphs clearly show the superiority of the *proposed* method (illustrated on right-side) in achieving higher *imp_SNR* values compared to the MF method 2013 [254] for the records 106m and 228m.

Therefore, it can be inferred that the *proposed* method has the capability to deliver satisfactory results in the framework of conventional noise analysis models as well.

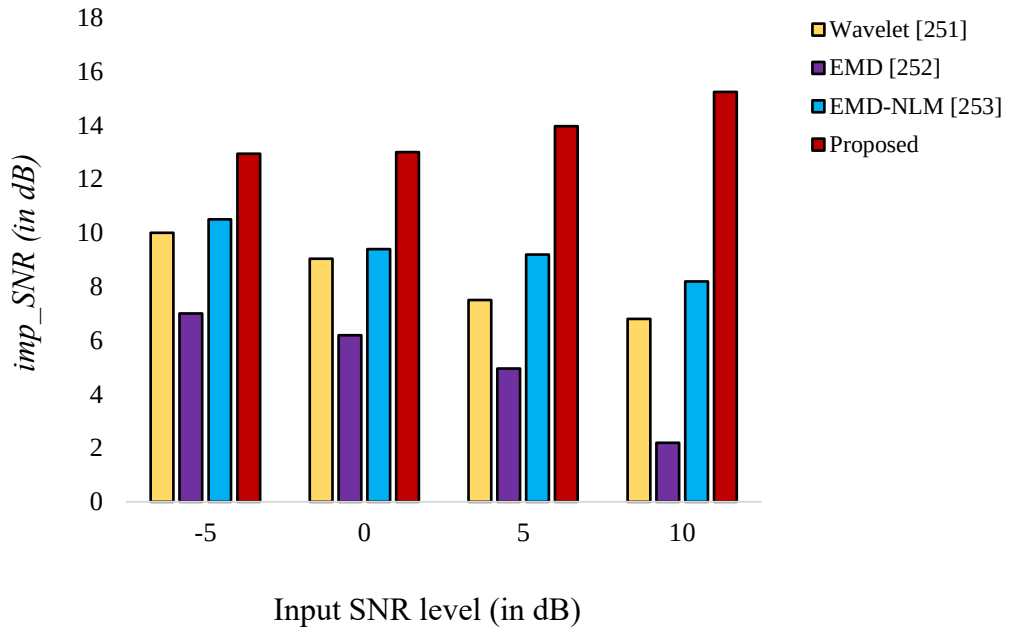

Figure 5.10 Comparison of *proposed* method with literature method when record 100 added with Gaussian noise.

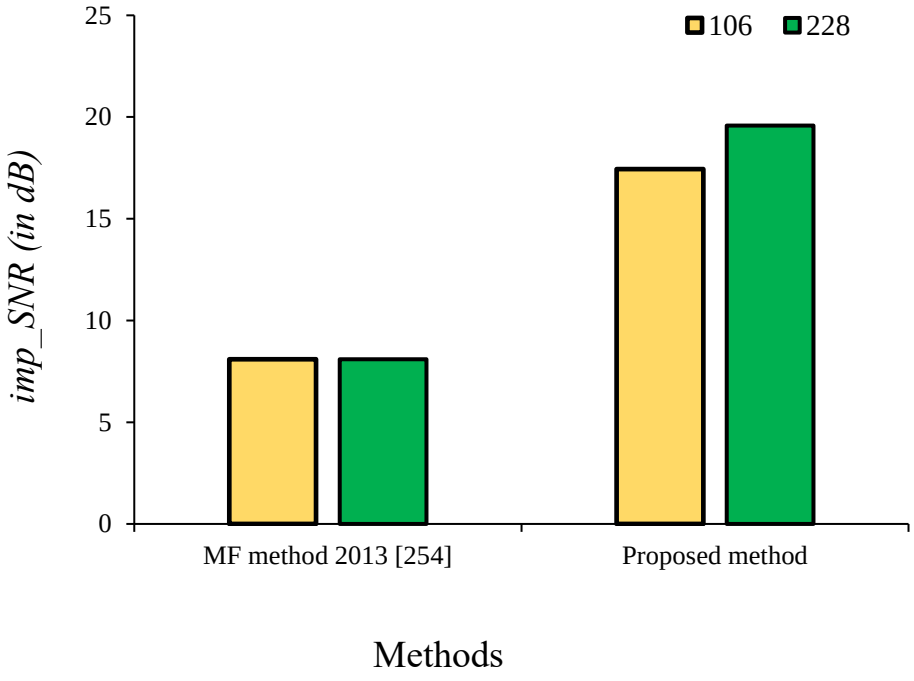

Figure 5.11 Comparison of *proposed* method with MF method 2013 when MIT-BIH records 106 and 228 are corrupted with 10 dB Gaussian distribution noise.

5.4.5 Comparison with State-of-the-Art Methods by Estimating Real-Time Noises with α-Stable Distribution

To evaluate the performance of the *proposed* method in the presence of real-time noises corrupting ECG signals like baseline wander (*bwm*), muscle artifacts (*mam*), electrode motion artifacts (*emm*) and power-line interference (*PLI*), firstly, the nature of noises for *Gaussian* and *non-Gaussian* behavior is investigated. Then, a fair comparison of the *proposed* method with the existing state-of-the-art methods is provided.

A. Investigation of real-time noises: For this, the results for noises available at MIT-BIH Noise Stress Test Database [200, 201] and computed in Chapter 4, section 4.3 are utilized, i.e., the estimate for α-stable distribution noise model parameters $S(\alpha, \beta, \gamma, \zeta)$ is:

- $S(1.64,0.36,47.28,4.04)$ for *bwm*
- $S(1.82,0.67,18.81,0.13)$ for *emm*
- $S(1.54,0.12,18.81,0.13)$ for *mam*

Additionally, expressing *PLI* as a sinusoidal polynomial [58] and applying the Kogon-Williams parameter estimation method, an estimate is obtained as $S(2,0,0.9,0)$. From the estimated values obtained for these noises, the following observations are made:

i. As α value is less than 2, one can ascertain that except for *PLI*, all the other real-time noises corrupting ECG signals have a non-Gaussian nature.
ii. Furthermore, the symmetry parameter β is non-zero, which indicates that the distribution is asymmetric, indicating non-Gaussian nature of noises.

As a result of the aforementioned conclusions, it can be concluded that the α-stable distribution noise analysis model is a better substitute for evaluating the efficacy of denoising techniques.

B. Performance comparison with existing methods: Next, to evaluate the performance of *proposed* $MF_{FrSE\&MO}$ under these real-time noises, MIT-BIH records 100m and 101m are corrupted with *bwm* noise and *PLI,* and comparison is made against well-established state-of-the-art methods Fourier decomposition (FD) [58] and eigenvalue decomposition (EVD) [255] in terms of *imp_SNR* values as depicted in **Figure 5.12 and Table 5.3**. Here, these records are specifically considered, to provide a fair comparison with selected literature methods.

Analyzing the results in **Figure 5.12**, it can be inferred that the *proposed* method outperforms the existing methods in the literature with a higher value of *imp_SNR* at each input SNR level for both noises—*bwm* and *PLI*. Also, on investigating the results tabulated for average performance of these methods from **Table 5.3**, it is evident that value of *imp_SNR* 21.43 dB and 35.53 dB is the maximum for the *proposed* method for *bwm* noise and *PLI* noise, respectively.

This conclude that *proposed* method shows superior performance among literature-based methods.

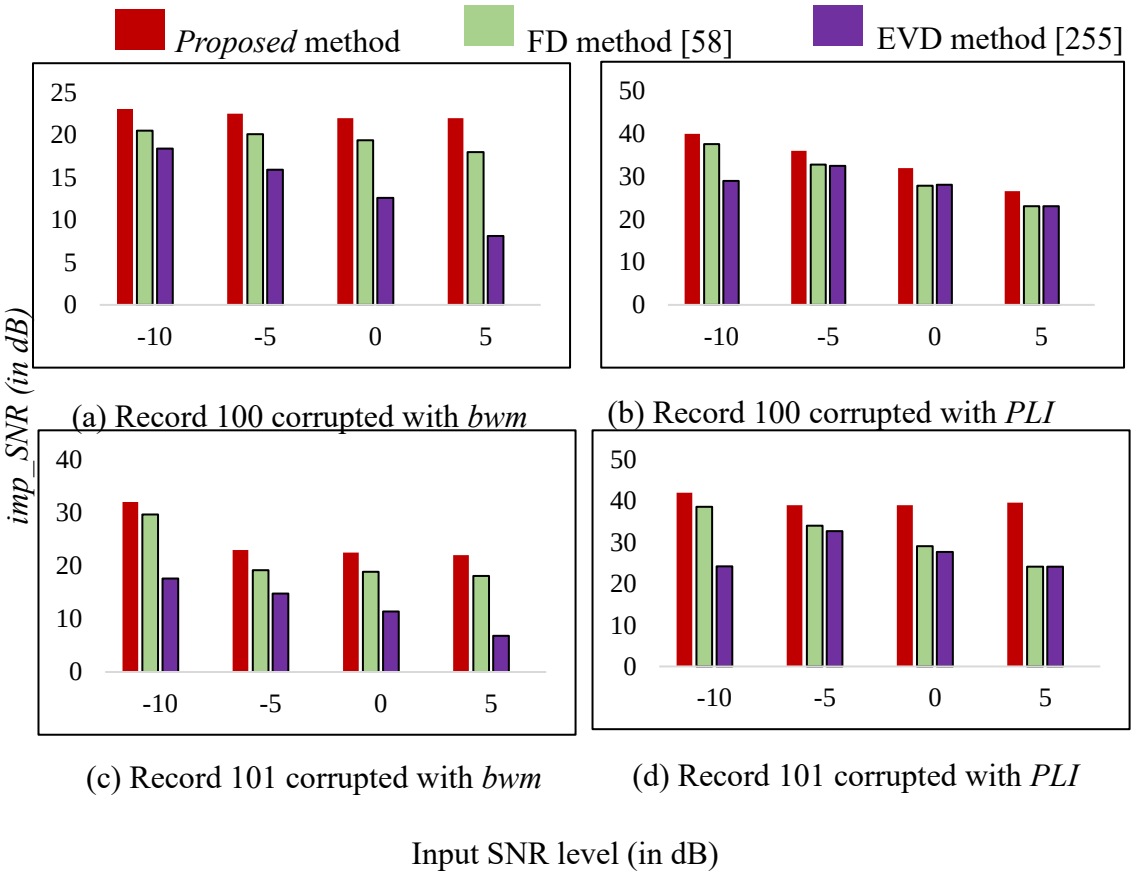

Figure 5.12 Comparison of *proposed* method with literature methods in presence of real-time noises *bwm* and *PLI*

Table 5.3 Average value comparison of literature methods with *proposed* method for *bwm* and *PLI* noise

Input Noise Level (dB)	*imp_SNR (in dB)* Values					
	bwm noise			*PLI noise*		
	Proposed	FD [58]	EVD [255]	*Proposed*	FD [58]	EVD [255]
-10	25.26	25.10	18.00	39.70	38.10	26.60
-5	20.28	19.65	15.35	36.10	33.40	32.60
0	20.00	19.40	12.00	33.80	28.50	27.90
5	20.18	18.05	7.45	32.52	23.60	23.60
Average	**21.43**	20.55	13.20	**35.53**	30.90	27.68

Bold indicates maximum i*mp_SNR* (dB) value

C. **Performance comparison with literature-based morphological filtering method**: To compare the performance of the *proposed* method using morphological based filtering method available in the literature [90] (herein, referred to as MF method 2019), MIT-BIH record 119m is corrupted with *bwm* noise as per the specifications mentioned in [90] to ensure a fair comparison. The comparison is made in terms of *RMSE* values, which is illustrated in **Figure 5.13**. It is evident from the graphical depiction that the *proposed* method has outperformed the state-of-the-art method incorporating MF concept in achieving lower *RMSE* values.

Thus, it proves that the *proposed* method is effective for real-time circumstances and outperforms conventional methods, including morphological [13, 85, 90, 254] and non-morphological methods [58, 251, 252, 253, 255].

5.5 Application of QRS Detection incorporating *Proposed* MF

As proved through a simulation study in previous sections, the primary distinguishing aspects between the *proposed* methodology and the state-of-the-art methods [13, 58, 85, 90, 251, 252, 253, 254, 255] are the use of the *proposed* FrSE, which adapts to shape of the ECG beat, and the incorporation of α-stable distribution noise analysis model. Additionally, the design of FrSE incorporated two degrees of freedom (r and a), which resulted in achieving low *RMSE* values and high *imp_SNR* in a noisy environment by suppressing noise while maintaining flexible beat-adaption for information preservation.

Therefore, to carry forward the benefits obtained using *proposed MF*, this section presents an application of *proposed* MF in QRS complex detection for subsequent stages. Additionally, from the review of rich literature, it has been mentioned in Chapter 2 (Section 2.2) that QRS detection framework is mainly composed of preprocessing followed by decision-making. Therefore, using *proposed MF* of this Chapter and the decision-making methodology *proposed* in Chapter 3, *proposed* block diagram is illustrated in **Figure 5.14.** For QRS complex detection, in the *proposed* scheme illustrated in **Figure 5.14**, firstly, the raw ECG signal is artificially corrupted with α-stable distribution noise model (to replicate the real-time scenario). Then, the corrupted signal is processed using the *proposed* $MF_{FrSE\&MO}$.

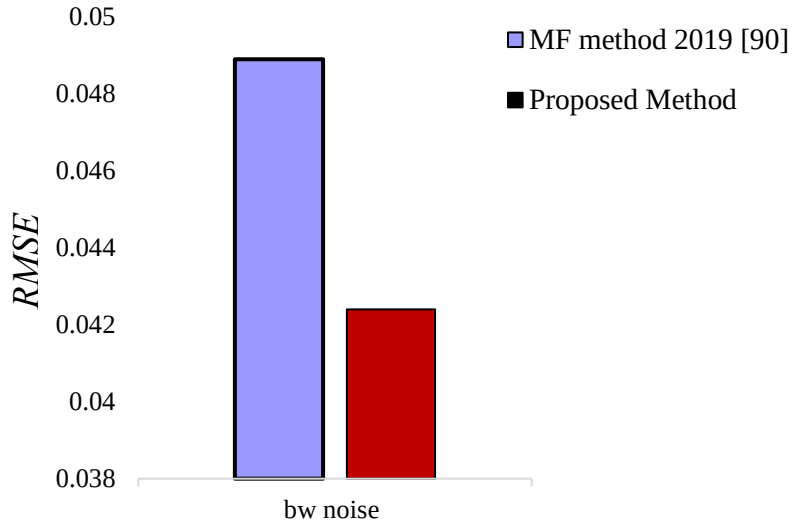

Figure 5.13 Comparison of the *proposed* method with MF method 2019.

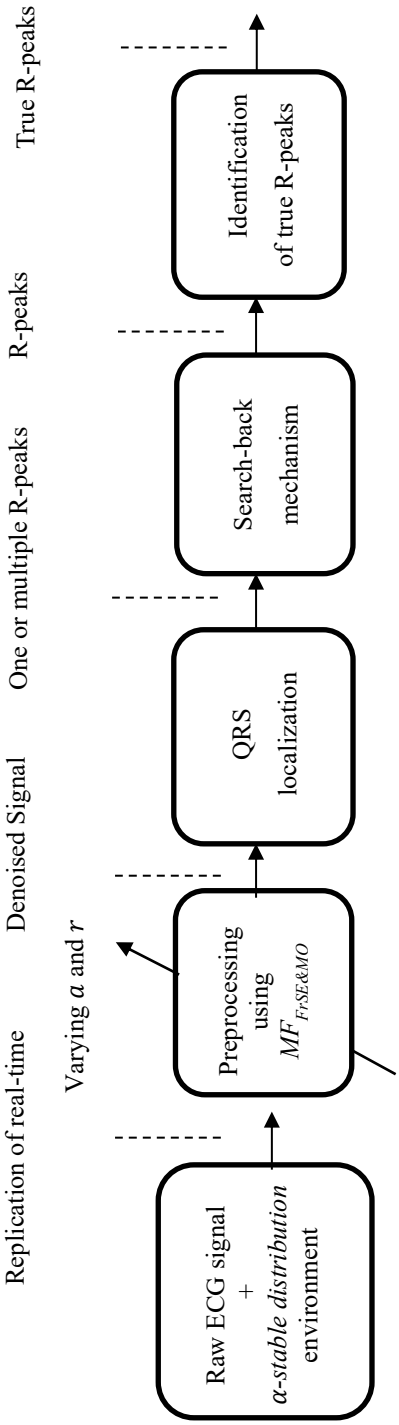

Figure 5.14 Block diagram for QRS complex detection based on *proposed* methodology

Then the morphologically transformed signal is passed through localization stage to accurately identify the occurrence of QRS events. Lastly, a searchback mechanism is applied to reconsider missed R-peaks. This compensates for the minimal error obtained in the time instants computed experimentally using the annotation codes [225] . The last three stages are described in detail in Chapter 3 (Section 3.3).

5.5.1 Performance Metric Parameters

The same performance metric parameters for QRS complex detection are used for performance evaluation. The performance metric parameters are mentioned again for better readability.

$$Sensitivity = \frac{TP}{TP + FN} \tag{5.25}$$

$$Positive\ Predictivity = \frac{TP}{TP + FP} \tag{5.26}$$

$$Error\ Rate = \frac{FN + FP}{Total\ detected\ beats} \tag{5.27}$$

$$Detection\ Accuracy = \frac{TP}{TP + FP + FN} \tag{5.28}$$

where *TP*, *FP*, and *FN* have the usual meaning (for details refer Chapter 3 (Section 3.3.1)).

5.5.2 Simulation Results

To illustrate the *proposed* methodology's effectiveness, the denoised signals from the previous section—100, 101, 102, 103, 104, 105, 106, 107, 108 and 109 are considered. The quantitative analysis is performed considering two scenarios; firstly, real-time scenario is replicated using α-stable distribution noise (as established in Chapter 4 and demonstrated in Section 5.3 as well). Second, the results are obtained using the conventional assumption, i.e., Gaussian environment, by substituting α=2, in the *proposed* methodology. This is undertaken to effectively verify the performance of the *proposed* approach and ensure an equitable comparison with established methodologies. The results for the two scenarios are tabulated in **Table 5.4** and **Table 5.5**, respectively.

Table 5.4 Performance evaluation of *proposed* methodology in α-stable distribution environment

Record No.	Annotated Beats	Detected Beats	TP	FN	FP	Sensitivity	Positive Predictivity	Detection Accuracy	Error Rate
100	2273	2273	2273	0	0	100.00	100.00	100.00	0.00
101	1865	1866	1865	0	1	100.00	99.95	99.95	0.05
102	2187	2187	2187	0	0	100.00	100.00	100.00	0.00
103	2084	2084	2084	0	0	100.00	100.00	100.00	0.00
104	2229	2230	2227	2	3	99.91	99.87	99.78	0.22
105	2572	2572	2569	3	3	99.88	99.88	99.77	0.23
106	2027	2025	2025	2	0	99.90	100.00	99.90	0.10
107	2137	2137	2137	0	0	100.00	100.00	100.00	0.00
108	1763	1763	1761	2	2	99.89	99.89	99.77	0.23
109	2532	2532	2532	0	0	100.00	100.00	100.00	0.00

Table 5.5 Performance evaluation of *proposed* methodology in Gaussian distribution environment

Record No.	Annotated Beats	Detected Beats	TP	FN	FP	Sensitivity	Positive Predictivity	Detection Accuracy	Error Rate
100	2273	2273	2273	0	0	100.00	100.00	100.00	0.00
101	1865	1866	1865	0	1	100.00	99.95	99.95	0.05
102	2187	2187	2187	0	0	100.00	100.00	100.00	0.00
103	2084	2084	2084	0	0	100.00	100.00	100.00	0.00
104	2229	2230	2228	1	2	99.96	99.91	99.87	0.13
105	2572	2572	2570	2	2	99.92	99.92	99.84	0.16
106	2027	2027	2027	0	0	100.00	100.00	100.00	0.00
107	2137	2137	2137	0	0	100.00	100.00	100.00	0.00
108	1763	1765	1763	0	2	100.00	99.89	99.89	0.11
109	2532	2532	2532	0	0	100.00	100.00	100.00	0.00

On analyzing the results obtained in **Tables 5.4** and **5.5**, it is ascertained that QRS complex detection based on the *proposed* methodology that incorporates *proposed* $MF_{FrSE\&MO}$ in the preprocessing stage has the potential to perform as effectively in real-time environment as it does in the Gaussian environment.

Furthermore, for comparative analysis with established morphological-based QRS complex detection methods namely; Zhang [239] (method based on multiscale mathematical morphology), Yazdani [88] (method based on adaptive mathematical morphology), and Chen [256] (combination of mathematical morphology with envelope for QRS complex detection) are selected. These literature methods are designed using the conventional assumption. The results for *FN* (signifying missed detections) and *FP* (signifying false detection) are presented in **Table 5.6**.

From the results tabulated in **Table 5.6**, it can be observed that, for records 100, 102, and 103, all the methods have reported zero missed and false detections, i.e., *FN*=0 and *FP*=0. However, for records 101, 104, 105, 106, 107, 108 and 109, the *proposed* method outperformed the conventional algorithms with the least cases of wrong and false detections (marked in bold values in **Table 5.6**).

Moreover, a graphical depiction of overall wrong detections is illustrated in **Figure 5.15**. The depiction clearly demonstrates that the *proposed* method outperforms established methods in terms of minimizing wrong detections in a conventionally assumed environment. This indicates that despite the design methodology being based on the consideration of utilizing an α-stable distribution environment, the *proposed* method has surpassed established methods in terms of performance. Thus, it substantiates the notion that design methods can effectively operate in a broad spectrum of environments, spanning from the conventionally assumed Gaussian to the practical scenario of impulsive environments.

Table 5.6 Comparative analysis with established morphological based methods under conventional assumption.

Record No.	Zhang [239]		Yazdani [88]		Chen [256]		*Proposed*	
	FN	FP	FN	FP	FN	FP	FN	FP
100	0	0	0	0	0	0	0	0
101	0	1	0	1	0	1	**0**	**1**
102	0	0	0	0	0	0	0	0
103	0	0	0	0	0	0	0	0
104	1	7	1	7	2	7	**1**	**2**
105	19	7	15	22	6	13	**2**	**2**
106	20	21	4	0	0	0	**0**	**0**
107	0	5	1	0	1	0	**0**	**0**
108	2	10	17	3	-	-	**0**	**2**
109	3	3	1	0	-	-	**0**	**0**

Bold indicates the minimum *FN* and *FP* obtained against established methods for records: 101,104, 105, 106,107, 108 and 109.

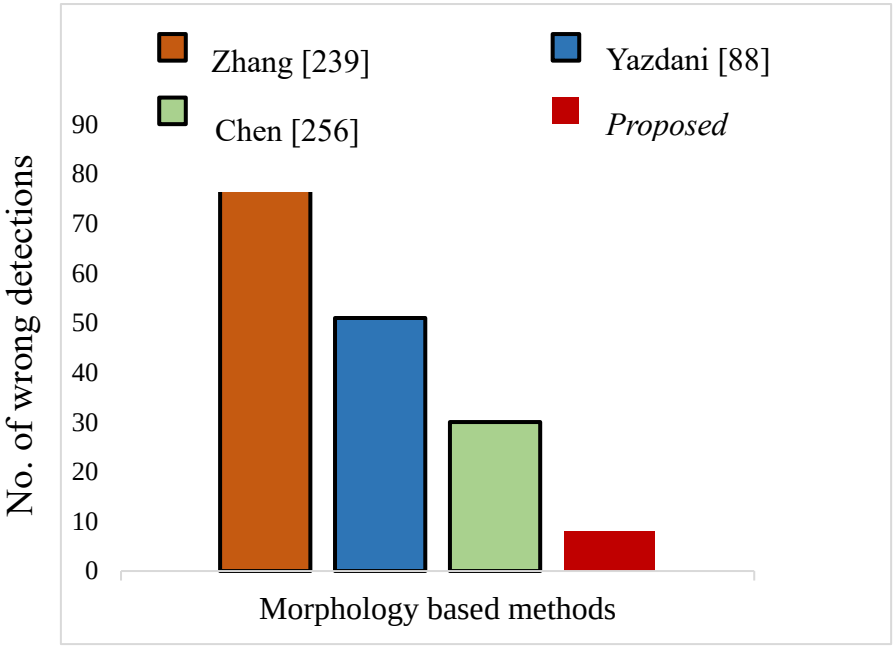

Figure 5.15 Comparison of wrong detections obtained using established methods and *proposed* method.

5.6 Summary

The *proposed* work presents a novel and effective method for processing ECG signals. To begin with, a simple and computationally efficient morphological filtering approach is used. Second, shape-adaptive SE is built using cross-convolution window concept, which takes advantage of varying FrFT order parameter a. Third, cross-convolution windowing method is conceptualized to design SE. More broadly, this new fractional Fourier of cross-convolved window is first-of-its-kind that provides dual benefit of reduced SLL and shape similarity to ECG beat. Finally, α-stable distribution noise model used for testing includes Gaussian distribution as a special case, ensuring that the denoised method can handle a wide range of noise environments with behavior ranging from Gaussian to impulsive. Additionally, filter design based on such model has the ability to enhance performance of further processing stages, as demonstrated by detection of QRS complex in the present work.

Furthermore, the performance of morphological state-of-the-art methods is based on using fixed SE. In contrast, *proposed* method introduces a novel FrSE, which has the flexibility of having two degrees of freedom. Thus, *proposed* FrSE adds an adaptive nature to morphological filtering, a characteristic absent in classical morphological filtering methods. Additionally, experimental results demonstrate that performance of *proposed* denoising method is better than that of other alternative methods that are not based on the concept of morphological filtering.

A significant contribution of *proposed* work demonstrates the importance of using a more generalized noise model: α-stable distribution to improve performance of preprocessing algorithms for biomedical signals. The enhancement obtained in initial stage, using α-stable distribution model, facilitated detection of QRS complex as well.

Lastly, *proposed* work has combined benefits of a time-efficient shape-based filtering method i.e., morphological filtering and the flexibility of variation gained using FrFT order parameter for designing denoising and QRS complex detection algorithm for ECG signals. This results in improved reconstruction and enhanced detection performance and thus outperforms traditional established methods, which have no such flexibilities.

Chapter 6

Introduction of Novel Time-Frequency Tool for α-Stable Distribution Noise Environment

As the research motivation is focused on dealing with *non-stationary* signals in a *non-Gaussian* environment, so after establishing the potential of FrFT kernel-based TF tools for *non-stationary* signals in Chapter 3 and with a successful attempt to prove the existence of *non-Gaussian* α-stable nature in noises in Chapter 4, this chapter focuses on amalgamating the concept of FrFT kernel-based TF tool with non-Gaussian α-stable distribution noise environment.

By introducing a novel tool namely *fractional lower-order fractional Stockwell transform* (FLO-FrST), which provides a satisfactory performance for noise environments ranging from impulsive to Gaussian by integrating the concepts of ST, FrFT and FLOS. The novel introduced tool provides better *robustness* against outliers with an enhanced *resolution* in the TF domain, offering better reconstruction when retrieving processed signal back to the time domain.

6.1 Rise of FLO-TF tools

Over the past few decades, numerous scientific studies and extensive literature have shown the use of time-frequency principles in several engineering disciplines, such as in communication systems for channel estimation and interference mitigation, in biomedical signal processing as an analysis and feature extraction tool, in seismology for detecting transient seismic events, in economics as trend cycle decomposition, machine monitoring for detecting faults and analyzing the vibration signals, to name a few.

However, with extensive research, it has been pointed out that TF tools in general (including both traditional and FrFT-based) emphasize the analysis of real-time signals in the presence of Gaussian noise environment. There has been a surge of research dealing with these signals in non-Gaussian environments. Moreover, literature research has

indicated that the performance of these existing TF tools deteriorates in the presence of impulsive noise. Therefore, to enhance the versatility of TF tools, new definitions using fractional lower-order statistics (FLOS) have been reported in the literature, referred to as fractional lower-order time-frequency (FLO-TF) tools. With the introduction of these tools, a new category of TF tool has been derived based on the α-stable distribution model which encompasses Gaussian model as its special case, as outlined in Section 2.4.2.3.

6.1.1 Need to Design New Tool (FLO-FrST)

FLO-TF tools are gaining popularity and have found extensive applications in areas such as mechanical fault analysis [50, 168, 175] where signal or noise interference tends to show impulsive characteristics.

However, several challenges such as obtaining high resolution and high reconstruction rate remain open problems. Undoubtedly, the newly introduced FLO-TF tools perform better than their TF counterpart and offer more efficiency in impulsive environments. But their performance is still limited by poor resolution, which results in the loss of information when performing reconstruction process. For example, cross terms still arise in FLO-WVD [48, 50], FLO-STFT still faces resolution problems due to window length [175] and the need for choosing proper mother wavelet is still a concern in FLO-CWT [50, 257]. Furthermore, the limitations of existing FLO-TF tools are summarized in **Table 6.1**.

Table 6.1 Summary of various fractional lower order time-frequency distributions (FLO-TFDs)

S.no	Literature	Name	Key Features
1	Long *et al*. (2017) [175]	FLO-STFT	• offers low resolution in TF domain • performance is limited due to fixed length of window function.
2	Griffith *et at.* (1997) [48]	FLO-WVD	• offers high resolution in TF domain. • performance is limited due to cross-terms
3	Gao *et al.* (2012) [257]	FLO-CWT	• offers multi-resolution analysis in TF domain. • performance limited due to absence of phase referenced information.
4	Long *et al.* (2017) [168]	FLO-ST	• offers improved resolution than FLO-STFT and FLO-CWT. • performance lacks resolution ability
5	Long *et al.* (2020) [169]	FLO-LCT	• offers improved resolution than FLO-STFT and FLO-CWT. • performance limited due to smearing.

Therefore, considering the limitations of existing tools, a new variant of FLO-TFD has been put forward to improve the resolution and still provide satisfactory performance in impulsive and Gaussian scenarios. The *proposed* variant of FLO-TFD described in this work is based on hybridizing the concepts of FLOS with fractional Stockwell transform (FrST) [47], which itself is a combination of Stockwell transform (ST) and fractional Fourier transform (FrFT). FrST, a TF tool based on fractional Fourier kernel [258], enhances the time-frequency resolution and the fractional lower-order operator from FLOS is responsible for offering robustness and better reconstruction in impulsive scenarios.

The FLO-FrST, a *proposed* novel tool, integrates the FLO concept within the FrST framework. This tool offers several advantages, including four degrees of freedom namely, the fractional-lower order parameter ρ, two window adjustment factors p and q, and the fractional parameter a. All these factors collectively contribute to the efficacy of FLO-FrST as a technique for attaining superior performance in terms of *resolution*, *reconstruction*, and *robustness*, which will be demonstrated in later sections with an intensive simulation studies.

6.2 Analytical Foundation of *Proposed* FLO-TF

In this section, the mathematical foundation of the *proposed* FLO-FrST is illustrated, along with its inverse formulation. Additionally, a detailed description of the mathematical deduction illustrates the limiting cases of the *proposed* FLO-FrST. Lastly, an algorithm for its computation is also provided for its utility in applications.

6.2.1 *Proposed* Fractional Lower-Order Time-Frequency (FLO-TF) Tool

According to the definition of FLOST and FrST (detailed in Section 2.4), a novel fractional lower order fractional Stockwell transform (FLO-FrST) definition is *proposed*, which is defined as:

$$FLO-FrST_x^a(\tau,u_\varphi)=\int_{-\infty}^{+\infty} x^{<\rho>}(t)g(\tau-t,u_\varphi)K_a(t,u_\varphi)dt \tag{6.1}$$

where description of $x^{<\rho>}(t)$, $g(\tau-t,u_\varphi)$ and $K_a(t,u_\varphi)$ is as follows:

i. $(.)^{<\rho>}$ is the FLO operator [48] defined as

$$x^{<\rho>}(t) = \frac{|x(t)|^{\rho+1}}{x^*(t)};\ 0 \le \rho \le 1. \tag{6.2}$$

ii. $g(\tau - t, u_\varphi)$ is scalable fractional Gaussian window function given by [47]

$$g(t, u_\varphi) = \frac{|u_\varphi \ csc\ \varphi|^p}{\sqrt{2\pi} q} exp\left(\frac{-t^2 (u_\varphi \ csc\ \varphi)^{2p}}{2q^2}\right) \tag{6.3}$$

where p and q are window-adjustment parameters of Gaussian window, u_φ is fractional Fourier frequency with $\varphi = a\pi/2$.

iii. $K_a(t, u_\varphi)$ is kernel of fractional Fourier transform (FrFT), mentioned in Section 2.3.3 and given by [127, 258]

$$K_a(t, u_\varphi) = \begin{cases} \sqrt{\frac{1 - j\ cot\ \varphi}{2\pi}} exp\left[j\left(\frac{t^2 + {u_\varphi}^2}{2}\right) cot\ \varphi - j u_\varphi t\ \ csc\ \varphi\right], & \varphi \neq n\pi \\ \delta(t - u_\varphi) & if\ \varphi = 2n\pi \\ \delta(t + u_\varphi) & if\ \varphi + \pi = 2n\pi \end{cases} \tag{6.4}$$

With the amalgamation of three concepts, the *proposed* tool has four degrees of freedom (ρ, p, q, a) i.e., the fractional-lower order parameter ρ, two window adjustment factors p and q, and fractional parameter a, from FLOS, FrST and FrFT definitions, respectively. Thus, these degrees of freedom make the *proposed* FLO-FrST tool flexible and robust enough to work effectively in *non-stationary* and *non-Gaussian α-stable* environments.

6.2.2 Mathematical Deduction for Limiting Cases of Fractional Lower-Order Fractional Stockwell Transform (FLO-FrST)

As previously mentioned, four degrees of freedom are an advantage of the *proposed* tool. The behavior of established TF tools can be obtained by varying each of these degrees, and this can be determined mathematically as follows:

Substituting values of $a = p = q = 1$, the scalable fractional Gaussian window [47] reduces to Gaussian window, independent of window-adjustment parameters, which is given by

$$g(t, u_\varphi) = \frac{|u_\varphi|}{\sqrt{2\pi}} exp\left(\frac{-t^2 {u_\varphi}^2}{2}\right) \tag{6.5}$$

Additionally, with $a = 1;\ \varphi$ reduces to $\varphi = \pi/2$ and therefore, the FrFT kernel $K_a(t, u_\varphi)$ reduces to the basic Fourier kernel [47, 258] given by

$$K_a(t, u_\varphi) \rightarrow K_1(t, u_{\pi/2}) = exp(-j2\pi u_\varphi t) \tag{6.6}$$

Using the results obtained in (6.5) and (6.6), the mathematical formulation of (6.1) reduces to fractional lower-order Stockwell transform (FLO-ST), which already is an established FLO-TF tool [168].

Furthermore, if the Gaussian window in (6.5) is considered a fixed window independent of frequency, then (6.1) reduces to the case of fractional lower-order Short-time Fourier transform (FLO-STFT) [175].

Now for the degree of freedom represented using ρ, as $\rho \rightarrow 1$

$$x^{<1>}(t) = \frac{|x(t)|^2}{x^*(t)} = x(t) \tag{6.7}$$

This implies the definition of FLO-FrST will get reduced to FrST [47]. Hence, the limiting cases of *proposed* FLO-FrST are FLO-ST, FLO-STFT and FrST, which are obtained by varying a, p and q for FLO-ST and FLO-STFT and ρ, a, p and q for FrST, respectively.

6.2.3 Calculation of Inverse FLO-FrST

In order to establish the invertible property of the suggested tool, a mathematical proof is presented as follows.

Integrating (6.1) with respect to variable τ

$$\int_{-\infty}^{\infty} FLO - FrST_x^a(\tau, u_\varphi)\, d\tau = \int_{-\infty}^{\infty}\int_{-\infty}^{\infty} x^{<\rho>}(t) g(\tau - t, u_\varphi) K_a(t, u_\varphi)\, dt\, d\tau \tag{6.8}$$

Rearranging integral (6.8)

$$\int_{-\infty}^{\infty} FLO - FrST_x^a(\tau, u_\varphi)\, d\tau = \int_{-\infty}^{+\infty} x^{<\rho>}(t)\, K_a(t, u_\varphi) dt \left\{\int_{-\infty}^{\infty} g(\tau - t, u_\varphi)\, d\tau\right\} \tag{6.9}$$

and using property

$$\int_{-\infty}^{\infty} g(\tau - t, u_\varphi)\, d\tau = 1 \tag{6.10}$$

(6.9) reduces to fractional lower-order fractional Fourier transform (FLO-FrFT) of signal $x(t)$ given by:

$$\int_{-\infty}^{\infty} FLO - FrST_x^a(\tau, u_\varphi)\, d\tau = \int_{-\infty}^{+\infty} x^{<\rho>}(t)\, K_a(t, u_\varphi) dt \tag{6.11}$$

The point worth mentioning here is that FLO-FrFT expression obtained in (6.11) is deduced implicitly while proving the invertible property for the *proposed* FLO-FrST. Moreover, with the introduction of FLO-FrFT, the scope of the FrFT tool is expanded to non-Gaussian α-stable distribution framework. Hence enhancing the applicability of FrFT in impulsive environments.

Next, continuing with the proof for invertible property, consider the FrFT of a signal given by:

$$FrFT\{x(t)\} = X(u_\varphi) = \int_{-\infty}^{+\infty} x(t)\, K_a(t, u_\varphi) dt \tag{6.12}$$

Now, let $x^{<\rho>}(t) = \tilde{x}(t)$, then using the definition derived in (6.11) and substituting in (6.12), FrFT of $\tilde{x}(t)$ is given by

$$\tilde{X}(u_\varphi) = \int_{-\infty}^{+\infty} \tilde{x}(t)\, K_a(t, u_\varphi) dt \tag{6.13}$$

Using formulation for inverse FrFT, $\tilde{x}(t)$ can then be represented using

$$\tilde{x}(t) = \int_{-\infty}^{+\infty} \tilde{X}(u)\, K_{-a}(t, u_\varphi) du_\varphi \tag{6.14}$$

Now, with $\tilde{x}(t)$ computed in (6.14), to obtain $x(t)$, consider

$$\begin{aligned} &\tilde{x}(t) = c_t + jd_t, t = 1,2, \cdots L_t, \\ &x(t) = a_t + jb_t, t = 1,2, \cdots L_t \end{aligned} \tag{6.15}$$

where $L_t \in \mathbb{Z}$ representing length of $x(t)$.

Substituting (6.15) in (6.2), we get

$$c_t + jd_t = \frac{\left({a_t}^2 + {b_t}^2\right)^{\frac{\rho+1}{2}}}{a_t - jb_t} \tag{6.16}$$

Simplifying further by comparing real and imaginary parts of complex numbers on both sides, we get

$$x(t) = c_t\left({c_t}^2 + {d_t}^2\right)^{\frac{1-\rho}{2}} + jd_t\left({c_t}^2 + {d_t}^2\right)^{\frac{1-\rho}{2}} \tag{6.17}$$

$$x(t) = Real(\tilde{x})(|\tilde{x}|)^{1-\rho} + Imag(\tilde{x})(|\tilde{x}|)^{1-\rho} \tag{6.18}$$

Hence, it can be concluded that the *proposed* transform FLO-FrST is invertible.

6.2.4 Algorithm for Computing FLO-FrST

For computing FLO-FrST, consider

$$h(t, u_\varphi) = x^{<\rho>}(t) K_a(t, u_\varphi) \tag{6.19}$$

Substituting (6.19) in (6.1)

$$FLO - FrST_x^a(\tau, u_\varphi) = \int_{-\infty}^{+\infty} h(t, u_\varphi) g(\tau - t, u_\varphi) dt \tag{6.20}$$

$$= h(t, u_\varphi) * g(t, u_\varphi) \tag{6.21}$$

where $*$ represents the convolution operator.

Next, we know that FLO-FrFT of $x^{<\rho>}(t)$ and FrFT of scalable fractional Gaussian window can be represented using

$$\tilde{X}(\mu_\varphi) = \int_{-\infty}^{+\infty} x^{<\rho>}(t)\, K_a(t, \mu_\varphi) dt \tag{6.22}$$

$$G(\mu_\varphi) = \int_{-\infty}^{+\infty} g(t, \mu_\varphi)\, K_a(t, \mu_\varphi) dt \tag{6.23}$$

where μ_φ is independent variable representing fractional Fourier frequency with $\varphi = a\pi/2$.

Using inverse of (6.22) and (6.23) in (6.1), we get

$$FLO - FrST_x^a(\tau, u_\varphi) = \int_{-\infty}^{+\infty} \left\{ \left(\int_{-\infty}^{+\infty} \tilde{X}(\mu_\varphi)\, K_{-a}(t, \mu_\varphi) d\mu_\varphi \right) \left(\int_{-\infty}^{+\infty} G(\mu_\varphi)\, K_{-a}(t, \mu_\varphi) d\mu_\varphi \right) K_a(t, u_\varphi) \right\} dt \tag{6.24}$$

Rearranging the integrals in obtained results and using the property of FrFT kernel [127], (6.23) is modified as:

$$FLO - FrST_x^a(\tau, u_\varphi) = \int_{-\infty}^{+\infty} \tilde{X}(\mu_\varphi) \left(\int_{-\infty}^{+\infty} K_a(t, u_\varphi) K_{-a}(t, \mu_\varphi) dt \right) \left(\int_{-\infty}^{+\infty} G(\mu_\varphi)\, K_{-a}(t, \mu_\varphi) d\mu_\varphi \right) d\mu_\varphi \tag{6.25}$$

$$= \int_{-\infty}^{+\infty} \tilde{X}(\mu_\varphi)\, \delta(u_\varphi - \mu_\varphi) d\mu_\varphi \int_{-\infty}^{+\infty} G(\mu_\varphi)\, K_{-a}(t, \mu_\varphi) d\mu_\varphi \tag{6.26}$$

Rearranging integrals and using the concept given in (6.20) and (6.21), expression obtained is given by:

$$FLO - FrST_x^a(\tau, u_\varphi) = \int_{-\infty}^{+\infty} \tilde{X}(\mu_\varphi) * \delta(u_\varphi - \mu_\varphi)\, G(\mu_\varphi)\, K_{-a}(t, \mu_\varphi) d\mu_\varphi \tag{6.27}$$

The result in (6.27) states that FLO-FrST can also be obtained by performing inverse FrFT on the product of FrFT of scalable fractional Gaussian window and shifted version of FLOFrFT of the signal under consideration.

The whole process for computing FLO-FrST is summarized in Algorithm 1.

Algorithm 1: FLO-FrST Computation

1. Calculate FLO-FrFT of the signal using (6.22)
2. Calculate FrFT of Gaussian window using (6.23).
3. Shift the spectra obtained in Step 1.
4. Multiply the results obtained in Step 2 and 3.
5. Calculate inverse FrFT of the product obtained in Step 4.

6.3 Simulation Study

For demonstrating the performance of the *proposed* FLO-FrST tool, this section is composed of various experiments using synthetic signal to verify the effectiveness of the *proposed* tool. It is divided into three parts: In the first part, synthetic signal is described, along with the performance metric measures required for the quantitative assessment of the experiments. Subsequently, in other two parts, the synthetic signal is analyzed and processed using the *proposed* tool and its performance is evaluated in terms of its *robustness*, *resolution*, and *reconstruction* ability.

6.3.1 Prerequisites for Experimental Study for the *Proposed* Tool

- **Experimental Signal**: To demonstrate the performance of the *proposed* tool, synthetic signal $x(n)$ is chosen, which is a linear frequency-modulated signal given by

$$x(n) = x_1(n) + x_2(n) \tag{6.28}$$

with $x_1(n)$ and $x_2(n)$ given by:

$$x_1(n) = e^{-0.004(n-80)^2 - j0.025(n-80)^2 + j1.72(n-80)} \tag{6.29}$$

$$x_2(n) = e^{-0.004(n-180)^2 - j0.025(n-180)^2 + j1.72(n-180)} \tag{6.30}$$

The signal $x(n)$ is subjected to additive interference from undesirable noise $w(n)$, which might be either Gaussian distributed noise or α-stable distributed noise. The resulting noisy signal is denoted as $y(n)$ and this process is described by

$$y(n) = x(n) + w(n) \tag{6.31}$$

For simulation purposes, SNR=10dB is selected for the case of additive white Gaussian noise (AWGN). For the case of α-stable distribution noise, the concept of SNR is invalid [49] and thus, generalized SNR (GSNR) [50, 250] is chosen to be 18dB with $\alpha = 1.1$.

- **Performance Metric Parameters**: Next, for assessing the performance of different experiments, the following quantitative measures are considered:
  a) *For quantification of resolution*, the Jones-Parks (*JP*) measure [37, 259, 260] is chosen, which is defined as:

$$Q_{JP} = \frac{\sum_n \sum_k P_x(n,k)^4}{(\sum_n \sum_k P_x(n,k)^2)^2} \tag{6.32}$$

  where $P_x(n,k)$ is a time-frequency matrix.

  JP measure is a concertation measure used to quantify energy concentration in the spectrogram. The higher value implies high energy concentration in the TF plane with efficient instantaneous frequency representation.

  b) *For quantifying reconstruction*, Root-Mean-Square-Error (*RMSE*) is selected, which is given by:

$$RMSE = \sqrt{\frac{\sum_{n=0}^{N-1}[x(n) - r(n)]^2}{N}} \tag{6.33}$$

  where $x(n)$ is the original signal and $r(n)$ is the reconstructed signal.

  RMSE is used to quantify information content retained in signal post-reconstruction. The lower its value, the better information is preserved.

- **Optimal Parameter Selection:** The *proposed* tool comprises four parameters — ρ, p, q, a —which play a crucial role in deciding the resolution of TF plane and satisfactorily suppressing the impulsive noise. Therefore, to achieve an optimized performance, the following three TF features are used to compute the optimal range for these parameters:
    i. *Renyi entropy* [37, 179, 260] is a widely used concentration measure.
    ii. Image-related feature *perimeter* [37, 179] is computed using the morphometric feature extracted from moments of binary segmented TF under consideration.
    iii. TF statistical features, *standard deviation* and *skewness* [37, 179] are used to describe instantaneous frequency components.

With rigorous simulation on synthetic signal, it has been concluded that the optimal value range for four degrees of freedom conforms to the following ranges:

- For α- stable distribution noise, the value of parameters obtained are:
  $\rho \in (0, 0.45]$, $p \in [0.5, 0.9]$, $q \in [0.25, 0.5]$, and $a \in (0.35, 0.6)$.
- For Gaussian noise, the value of parameters are:
  $\rho \in [0.5, 0.8]$, $p \in [0.5, 0.9]$, $q \in [0.1, 0.6]$, and $a \in (0.1, 0.5)$.

Any combination for (ρ, p, q, a) selected between the ranges as mentioned above will show good performance for the *proposed* FLO-FrST tool.

6.3.2 Experiment 1: Demonstration of Resolution and Robustness Ability

In order to demonstrate the resolution and robustness of the *proposed* tool, this section presents both qualitative and qualitative comparison of the *proposed* FLO-FrST and is compared with established state-of-the-art tools such as ST, FrST and FLO-ST.

A. Qualitative Analysis: To demonstrate the resolution and robustness of the *proposed* tool, a qualitative comparison of the *proposed* FLO-FrST is performed with established state-of-the-art tools such as ST, FrST and FLO-ST. The obtained spectrograms are shown in **Figures 6.1** and **6.2** for Gaussian and α-stable distribution noise, respectively. Furthermore, **Table 6.2** shows values of selected performance metric parameter *JP measure*, computed for all these transforms to quantify the analysis.

By analyzing the illustrations shown in **Figures 6.1** and **6.2**, the following distinguishing features are obtained:

i. Based on observations made from time domain signals, it can be concluded that Gaussian noise has minimal impact on signal morphology. This type of noise is also uniformly added to the signal, as illustrated in **Figure 6.1 (b)**. In contrast, the α-stable distribution noise introduces two prominent peaks and substantially distorts the morphology of signal, as shown in **Figure 6.2 (b)**. Hence, it can be deduced that α-stable distribution noise possesses greater detrimental effects and has the potential to inflict more harm upon the signal.

ii. The spectrograms obtained using ST and FrST can only detect the signal in Gaussian noise, as depicted in **Figure 6.1 (c)** and **Figure 6.1 (d)**. On the other hand, for α-stable distribution case as shown in **Figure 6.2 (c)** and **Figure 6.2 (d)**, the impulses have more energy concentration and thus, signal details are lost, resulting in poor performance of these TF tools.

iii. The spectrogram obtained using FLO-ST (**Figure 6.1 (e))** and **Figure 6.2 (e)**) demonstrates the capability of FLO-ST to identify signal components in both Gaussian and α-stable distribution noise. However, it has performed poorly in terms of resolution in α-stable environment, as depicted in **Figure 6.2 (e**).

iv. On the other hand, it can be deduced from spectrogram analysis of the *proposed* FLO-FrST (as depicted in **Figure 6.1 (f)** and **Figure 6.2(f)**) that it possesses the capability to preserve the signal component while also offering enhanced resolution in both α-stable distribution and Gaussian distribution noise conditions. Hence, it can be inferred that the *proposed* FLO-FrST tool has the capability to provide satisfactory resolution and offers robustness in the presence of diverse noise types, ranging from Gaussian to α-stable.

B. Quantitative Analysis: To evaluate the performance of established tools and the *proposed* tools in terms of quantitative measure, *JP measure* values are recorded in **Table 6.2** for the obtained spectrograms.

On analyzing the obtained values for Gaussian case, it is observed that the obtained *JP measure* value is highest for FLO-FrST, followed by the value obtained for FrST. This indicates superior performance of the *proposed* FLO-FrST against all selected tools. Moreover, the JP measure obtained for FLO-ST is observed to be higher than that of ST. This proves that FLO-TFs, when dealing with limiting case ($\alpha = 2$, corresponding

to Gaussian noise [49]), are able to provide better and satisfactory results when compared with their TF counterparts.

Next, on analyzing **Table 6.2** for α-stable distribution case, *JP measure* values obtained for FLO-ST and FLO-FrST are far better than their TF counterparts, i.e., ST and FrST, respectively. This proves that FLO-TF tools are an excellent choice for non-Gaussian impulsive environment. Furthermore, while comparing values of *JP measure* between FLO-ST and FLO-FrST, it becomes evident that FLO-FrST exhibits superior energy concentration, providing enhanced resolution compared to the existing FLO-ST tool.

Thus, by analyzing simulation results, it can be inferred that *proposed* FLO-FrST cannot only retain signal components in both Gaussian and α-stable distribution environments but is also effective in achieving better resolution in Gaussian as well as α-stable distribution noise environments. This implies that *proposed* FLO-FrST, with its advantage of four degrees of freedom, has the potential to provide enhanced resolution and robustness.

Table 6.2 The values of *JP measure* obtained using different methods under Gaussian noise and α-stable distribution noise.

Methods	Gaussian noise	α-stable distribution noise
ST [163]	9.792	4.809
FrST [47]	18.014	5.729
FLO-ST [168]	12.282	10.604
Proposed	**19.698**	**20.595**

Bold indicates the maximum value

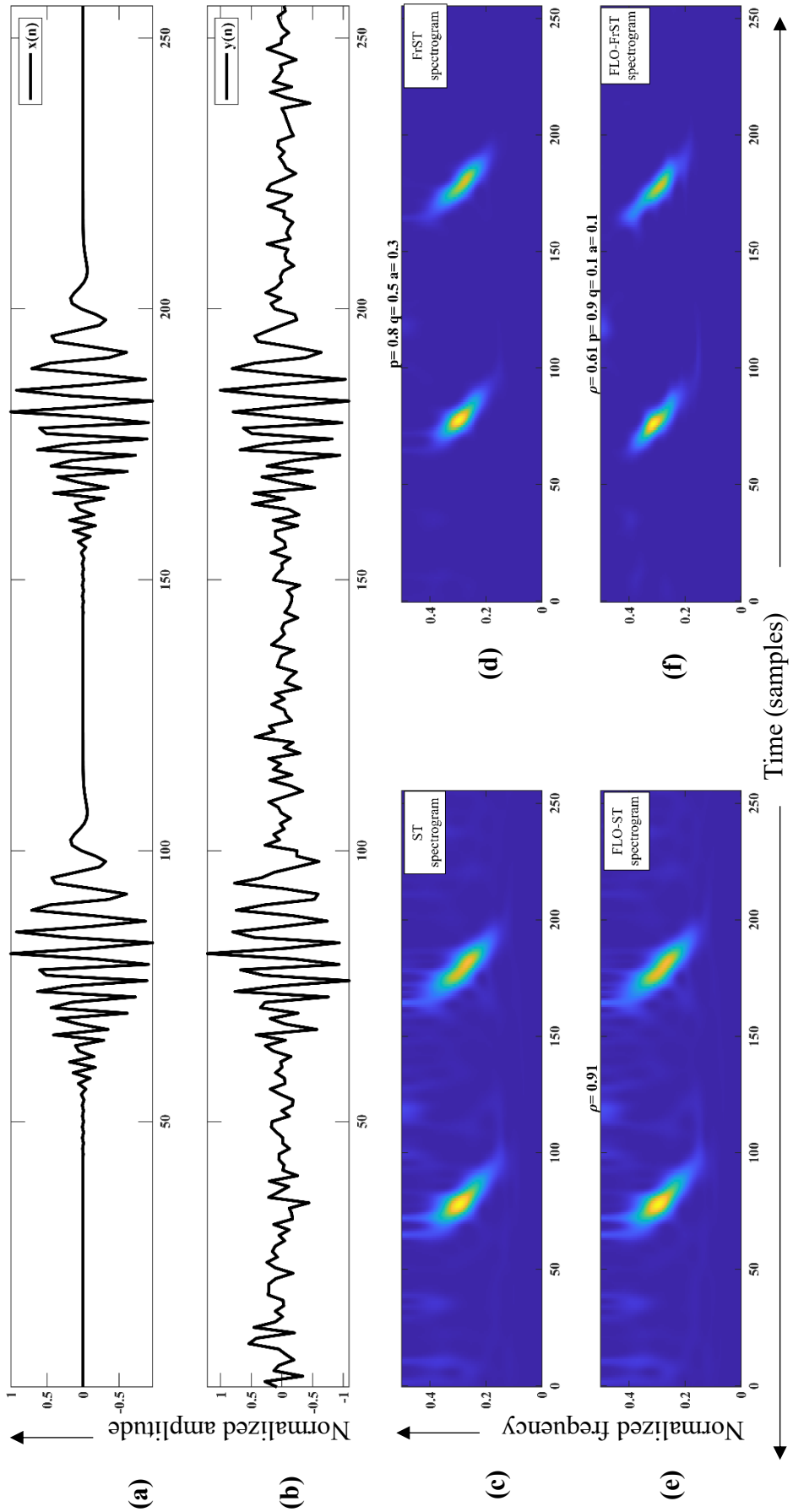

Figure 6.1 **(a)** Time domain representation of synthetic signal $x(n)$, **(b)** Synthetic signal corrupted with additive white Gaussian noise denoted by $y(n)$, **(c)** ST spectrogram of synthetic noisy signal $y(n)$, **(d)** FrST spectrogram of synthetic noisy signal $y(n)$, **(e)** FLO-ST spectrogram of $y(n)$, **(f)** *Proposed* FLO-FrST spectrogram $y(n)$

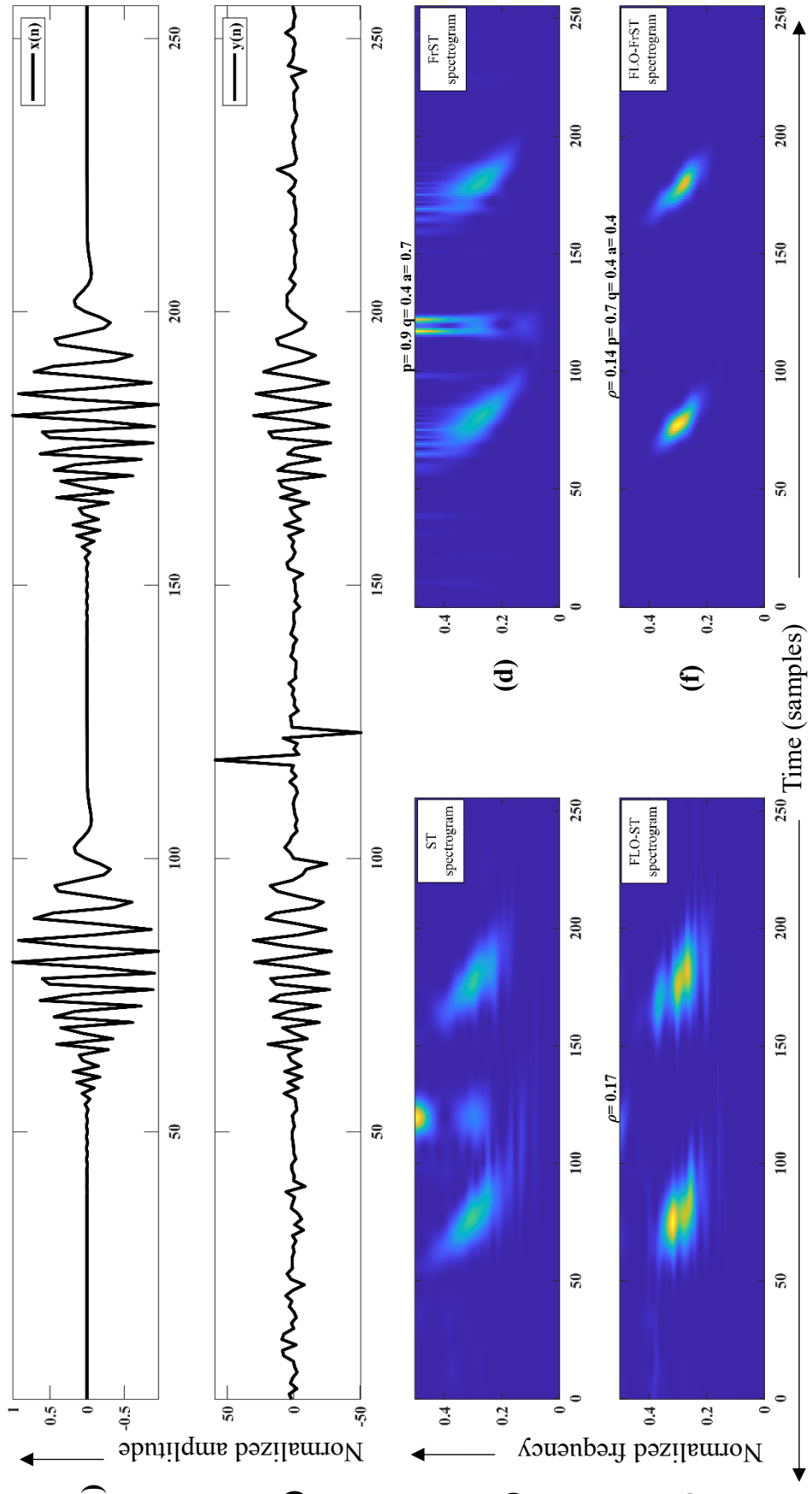

Figure 6.2 (a) Time domain representation of synthetic signal $x(n)$, **(b)** Synthetic signal corrupted with additive white Gaussian noise denoted by $y(n)$, **(c)** ST spectrogram of synthetic noisy signal $y(n)$, **(d)** FrST spectrogram of synthetic noisy signal $y(n)$, **(e)** FLO-ST spectrogram of $y(n)$, **(f)** *Proposed* FLO-FrST spectrogram $y(n)$

6.3.3 Experiment 2: Demonstration of Reconstruction Ability

To demonstrate signal retrieval in time domain, the spectrograms obtained using different methods (ST, FrST, FLO-ST and *proposed* FLO-FrST) are subjected to basic filtering using Algorithm 2. The different spectrograms obtained after applying Algorithm 2 are depicted in **Figure 6.3** (left column) for the Gaussian noise and **Figure 6.4** (left column) for α-stable distribution case. To analyze filtered output in the time domain, the inverse of the respective transform is applied to obtain the reconstructed signal. The results for the same are depicted in **Figure 6.3** (right column) and **Figure 6.4** (right column) for both Gaussian and α-stable distribution cases, respectively.

Additionally, as will be discussed below, qualitative and quantitative analysis are used to compare the effectiveness of these tools:

Algorithm 2: *Proposed* Basic filtering method

1. Apply FLO operator to the signal under consideration using the definition presented in (6.2).
2. Apply the desired TF/FLO-TF transform tool to obtain the matrix $TF(i,j)$.
3. Take a zero matrix $F(i,j)$ of same size as the matrix obtained in Step 2.
4. Obtain matrix $|TF(i,j)|$ and then compute maximum in 3 x 3 regions of $|TF(i,j)|$ and store the corresponding values in a new array mTF.
5. Calculate $th = \frac{mTF_{min}+mTF_{max}}{2}$.
6. If $TF(i,j) \leq th$, mark corresponding location in $F(i,j)$ as zero, i.e., $F(i,j) = 0$; else $TF(i,j) \geq th$, mark corresponding location in $F(i,j)$ as one, i.e., $F(i,j) = 1$;
7. Finally, multiply $TF(i,j)$ x $F(i,j)$ to obtain the filtered output matrix.

A. **Qualitative Analysis:** On comparing the spectrograms, it can be inferred that, for the Gaussian case (depicted in **Figure 6.3 (c)**, **(e)**, **(g)** and **(i)**), all the tools are able to localize the signal components and have shown no effect for Gaussian distributed noise, as it is uniformly spread and therefore only little smearing of frequencies is observed at the edge of localized components.

   On the other hand, on visually inspecting the spectrograms obtained using α-stable distributed noise (shown in **Figure 6.4 (c)**, **(e)**, **(g)** and **(i)**), for ST and FrST case, illustrated in **Figure 6.4 (c)** and **(e)**, the tools are unable to localize the signal components. Energy concentration is more distributed near the impulses, thus depicting the poor performance of conventional TF tools in comparison to FLO-TF tools shown in **Figure 6.4 (g)** and **(i)**.

B. **Quantitative Analysis:** To quantify the performance for reconstruction, performance metric measure *RMSE* is computed for time-domain signals obtained after processing original signal with Algorithm 2. Results for the same are recorded in **Table 6.3**.

Upon investigating the results for Gaussian case, it can be concluded that *RMSE* values for FrST and FLO-FrST are lower than ST and FLO-ST. This implies that FrST and FLO-FrST exhibit superior signal reconstruction capabilities and are more effective in preserving the original signal content than ST and FLO-ST.

In the case of α-stable distributions, *RMSE* value obtained for the TF tools, namely ST and FrST, is significantly greater than the FLO-TFD tools, which implies a large error between original signal and reconstructed signal.

Moreover, while analyzing the performance of FLO-TFD tools, it becomes evident that FLO-FrST has exhibited superior performance compared to FLO-ST, ST and FrST, as indicated by its lowest *RMSE* value. This clearly signifies that the performance of FLO-FrST in terms of reconstruction is much superior to other established tools.

Therefore, it can be inferred that the *proposed* FLO-FrST tool exhibits superiority over existing transforms by providing enhanced robustness and reconstruction capabilities. Additionally, it demonstrates high resolution in both Gaussian and α-stable scenarios, rendering it suitable for processing *non-stationary* signals even in *non-Gaussian* α-stable environments.

Table 6.3 The *RMSE* values obtained for reconstruction experiment using different methods under Gaussian noise and α-stable distribution noise.

Methods	Gaussian noise	α-stable distribution noise
ST [163]	0.337	4.367
FrST [47]	0.328	4.029
FLO-ST [168]	0.330	0.359
Proposed	**0.302**	**0.313**

Bold indicates the maximum value

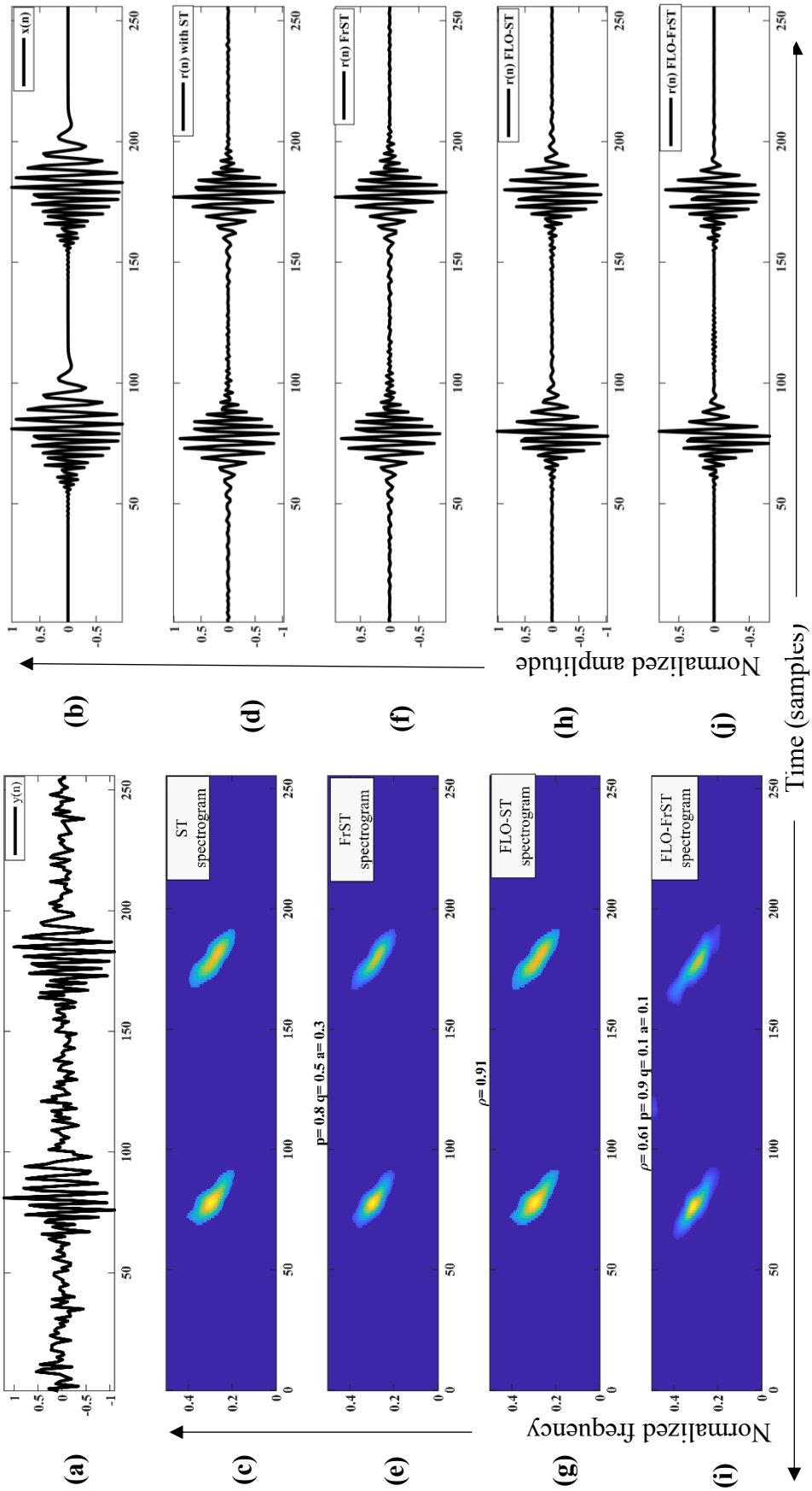

Figure 6.3 (a) Synthetic signal corrupted with additive white Gaussian noise given by $y(n)$, **(b)** Time domain representation original synthetic signal for visual comparison with reconstructed signals using different methods **(c)** ST spectrogram of noisy signal obtained after applying filtering algorithm, **(d)** Reconstructed signal using ST, **(e)** FrST spectrogram of noisy signal obtained after applying filtering algorithm, **(f)** Reconstructed signal using FrST, **(g)** FLO-ST spectrogram of noisy signal obtained after applying filtering algorithm, **(h)** Reconstructed signal using FLO-ST, **(i)** *Proposed* FLO-FrST spectrogram of noisy signal obtained after applying filtering algorithm, **(j)** Reconstructed signal using *proposed* FLO-FrST.

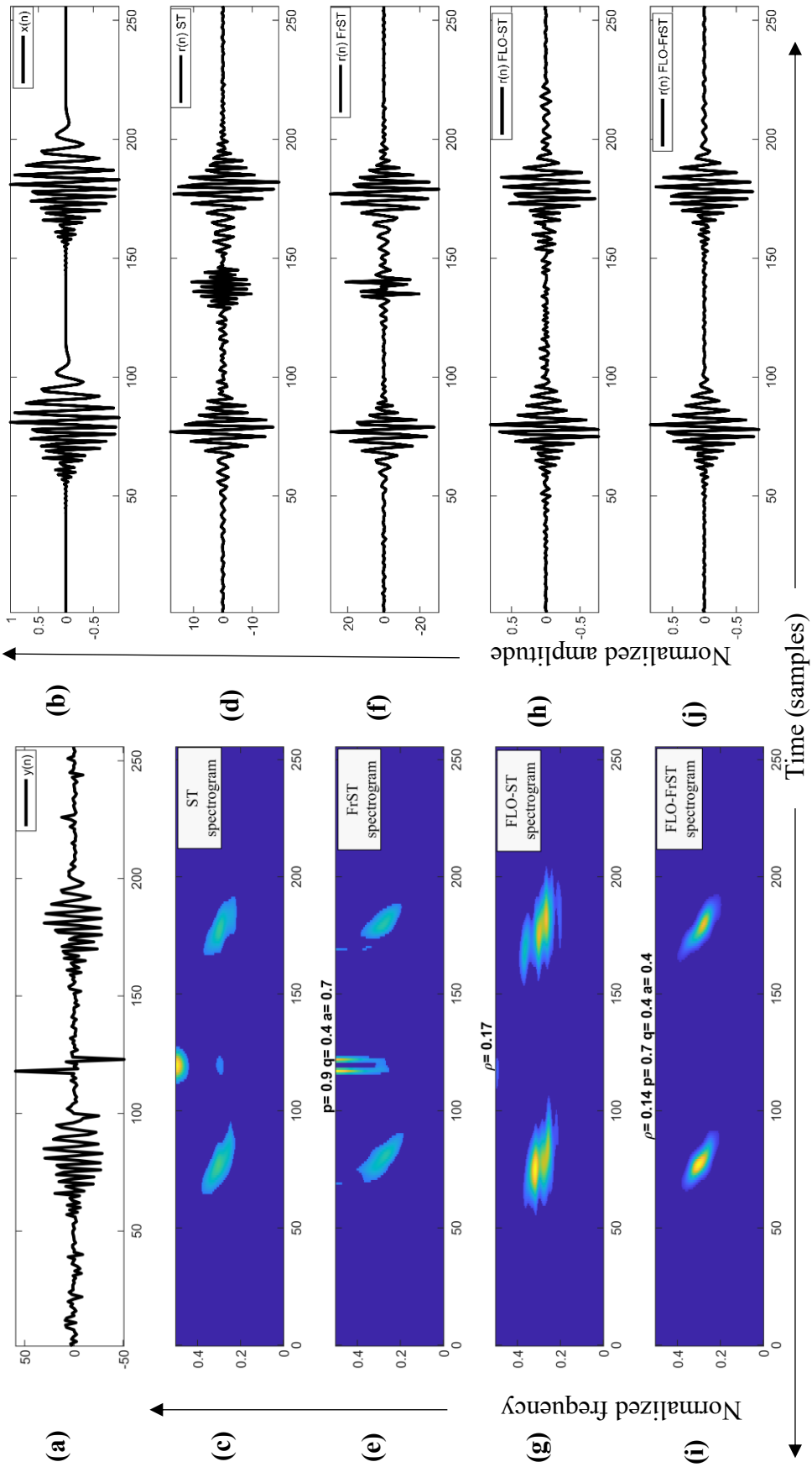

Figure 6.4 (a) Synthetic signal corrupted with additive α-stable distribution noise given by $y(n)$, **(b)** Time domain representation original synthetic signal for visual comparison with reconstructed signals using different methods **(c)** ST spectrogram of noisy signal obtained after applying filtering algorithm, (d) Reconstructed signal using ST, **(e)** FrST spectrogram of noisy signal obtained after applying filtering algorithm, **(f)** Reconstructed signal using FrST, **(g)** FLO-ST spectrogram of noisy signal obtained after applying filtering algorithm, **(h)** Reconstructed signal using FLO-ST, (i) *Proposed* FLO-FrST spectrogram of noisy signal obtained after applying filtering algorithm, **(j)** Reconstructed signal using *proposed* FLO-FrST

6.4 Application of *Proposed* Tool in Seizure Detection based on Transfer Learning

From the viewpoint of signal processing, the concept of FLO-TFDs has never been incorporated into biomedical signal processing domain. With the nature of biomedical signals and interfering noises/artifacts showing impulsive characteristics, such as in electromyogram (EMG) [119] and electroencephalogram (EEG) [117], there is a scope to extend and utilize the FLOS for developing algorithms to process and analyze biomedical signals. With this objective, this section provides insights into exploring the potential of *proposed* FLO-TFD tool in classifying epileptic seizures in EEG signals.

The classification process utilizes deep learning (DL) methodology [261], employing transfer learning and the AlexNet convolutional neural network (CNN) to identify the occurrence of epileptic events: preictal and ictal (seizure) states. The application presented in this section will demonstrate the advantages of using *proposed* FLO-FrST in classification. This demonstration will contribute to establishing the *proposed* FLO-FrST as a potential FLO-TF tool.

Furthermore, to assist in depicting the performance, this section is subdivided into three sections: The first part unfolds the classification process using the *proposed* tool, the second part describes the performance of classification and finally in the third part, comparative analysis is performed with established tools.

6.4.1 *Proposed* Methodology

EEG is a widely employed non-invasive method to understand brain dynamics and nowadays has found extensive applications in many areas, such as computer-aided diagnosis [117, 179] and cognitive science [262, 263]. As EEG signal is impulsive, its processing and analysis must employ statistical models that consider impulsive characteristics. This section of work intends to apply the *proposed* FLO-FrST for processing EEG signals, as the literature has reported that models based on α-stable distribution show superior performance, particularly in the context of handling epileptic activity [117].

Based on the *proposed* tool, the methodology for classification is depicted in **Figure 6.5** and various steps are outlined below:

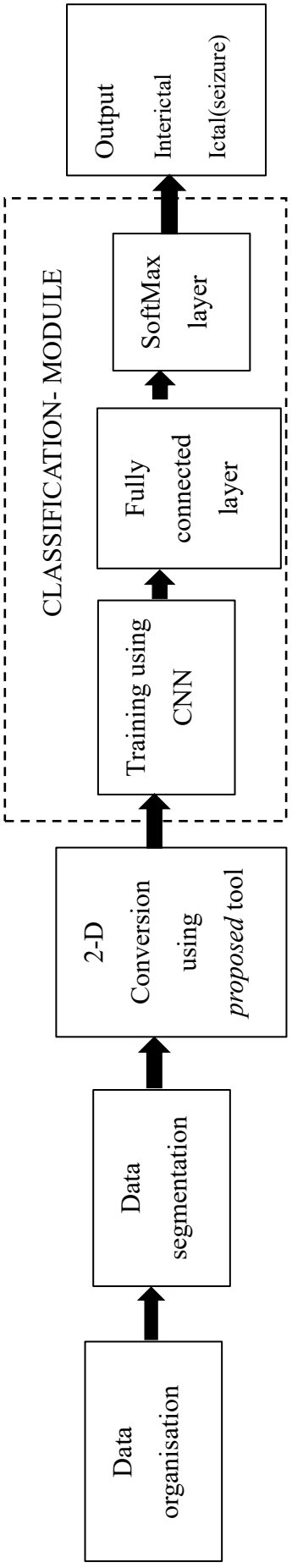

Figure 6.5 Block diagram for EEG epileptic classification using *proposed* FLO-FrST tool

Step 1-Data Organization: The study uses CHB-MIT Scalp EEG Database [208] to evaluate the performance of *proposed* classification method employing *proposed* tool. The description of database is mentioned in Section 2.6.6. Combining EEG data from all channels, there are 198 seizure events [208]. As described before, the primary objective is to detect preictal and seizure states. Therefore, after analyzing the available data, a 10-minute interval ($10 \times 60 \times 256 = 153{,}600$ samples) has been chosen as the preictal segment. The 10-minute interval is chosen to verify the efficacy of *proposed* FLO-FrST-based classification model in differentiating the minute changes occurring just before the seizure from the actual seizure state. For simulation purposes, all 24 records with all channels are considered with their respective seizure and preictal states. The annotation file available with the database [208] is analysed to formulate the dataset required for preictal and seizure(ictal) states.

Step 2-Data segmentation: The EEG preictal data and EEG seizure data are segmented into 1s (256 samples) of non-overlapping segments for analyzing different states of EEG signals.

Step 3-Conversion to 2-D images: The 1s data is further processed using the *proposed* FLO-FrST tool, resulting in a spectrogram, which is then resized to an image with 227 × 227 x 3 dimensions. This resizing is done to utilize the AlexNet CNN-DL model. For simulation study, the optimal value set (ρ, p, q, a) for generating an EEG signal spectrogram using *proposed* FLO-FrST is computed as demonstrated in Section 6.3.1. The values for preictal data are computed to be $(0.01,0.4,0.4,0.3)$ and for seizures are $(0.49,0.4,0.3,0.3)$. This optimal value has been computed by performing a simulation on 12s preictal as well as seizure data.

Step 4-Training: Transfer learning is employed to use the pre-trained model (AlexNet) to facilitate the classification process. The process involves configuring only the last three layers; the fully connected layer, SoftMax layer and Output layer, to classify preictal and seizure outputs. The rest of the layers are transferred from the pre-trained model. In addition, to address the issue of an imbalanced dataset [261], the training phase involves randomly selecting data from larger dataset (in our case, preictal dataset) to ensure that dataset sizes in both categories are equal. For classification process, 10,000 images from each category are used for simulation

purposes. Out of which, 80% of the data is used as a training set and 20% as a testing set, i.e., 8000 images from each category are used for training and 2000 images from each category are used for testing. The configuration parameters were set to following: 'Max Epochs'$= 8$, 'Initial Learning Rate' $= 1$ x 10^{-4}, 'Mini Batch Size' $= 250$ and 'validation frequency' $= 10$, with remaining parameters set to default values.

Step 5- Performance evaluation: To evaluate the performance of classification using the *proposed* FLO-FrST, the following standard performance measures are utilized [264].

$$Sensitivity = \frac{TP}{TP + FN} \tag{6.34}$$

$$Positive\ Predictivity = \frac{TP}{TP + FP} \tag{6.35}$$

$$Error\ Rate = \frac{FN + FP}{TP + FN + FP + TN} \tag{6.36}$$

$$Accuracy = \frac{TP + TN}{TP + FN + FP + TN} \tag{6.37}$$

$$F1 - Score = 2 \times \frac{Recall \times Precision}{Recall + Precision} = \frac{2 \times TP}{2 \times TP + FN + FP} \tag{6.38}$$

$$Matthew's\ Correlation\ Coefficient = \frac{(TP \times TN - FP \times FN)}{\sqrt{(TP + FP) \times (TP + FN) \times (TN + FP) \times (TN + FN)}} \tag{6.39}$$

where *TP*, *FN*, *FP* and *TN* are four labels of confusion matrix, which indicates correct and wrong detection of EEG epileptic state. *TP*: true positive; indicating positive detection, *FN*: false negative; indicating missed detection, *FP*: false positive; indicating false detection, *TN*: true negative; indicating true negative detection.

Sensitivity, also known as "recall," assesses the proportion of true positive cases correctly detected among all actual positive cases. This measure is frequently employed in situations where false negatives or missed detections are a significant concern. A higher value of this parameter corresponds to a lower frequency of missed detections and hence corresponds to better performance of the classificational model

Positive predictivity, also known as "precision" is a measure that evaluates the accuracy of positive predictions. This method is employed in situations where false positives are a matter of greater significance. A higher value indicates a reduced number of false detections, thus corresponding to better classification performance.

Accuracy is used to quantify the correct predictions, with larger value indicating superior performance.

F1-Score evaluates the prediction ability by taking into account the performance of each individual class. Its value falls between 0 and 1, where 1 denotes good model performance.

Matthew's Correlation Coefficient is used to evaluate the effectiveness of prediction over all four areas of a confusion matrix. The value of this coefficient ranges from -1 to +1 with +1 indicating good performance.

6.4.2 Simulation Results

To investigate the performance of classification using *proposed* tool, the output of *Step-4 training progress* generated in MATLAB is shown in **Figure 6.6**. With a mini-batch size of 250 and a dataset of 20,000 classification images (including both categories for simulation), the process was completed in 512 iterations before reaching final convergence. A validation accuracy of 99.1% was attained, accompanied by a loss curve (indicating training loss and validation loss) that converged to zero. This convergence to zero (for both training loss and validation loss) indicates a lesser deviation of predicted probabilities from true ones, thus implying deep learning model is an optimal fit.

To further explain its performance, **Figure 6.7** depicts the confusion matrix obtained for the classification using the *proposed* FLO-FrST method. In this illustration, the green cells (first two diagonal cells) show the number and percentage of correct classifications by the trained network and the red cells indicate incorrect classifications. Of all 4000 images, 1984 are correctly classified as preictal EEGs (which makes up 49.6 % of test data) and 19 are incorrectly classified as preictal EEGs (0.5% of test data). Similarly, 1981 correctly classified as seizure EEGs (which makes up 49.5% of test data) and 16 incorrectly classified as seizure EEGs (0.4 % of test data). Out of total 2003 preictal EEG detections, 99.051% (~ 99.1%) are positive preictal predictions, and out of 1997 seizure EEG detections, 99.19 % (~ 99.2%) are positive seizure predictions. Furthermore, *preictal Sensitivity* corresponds

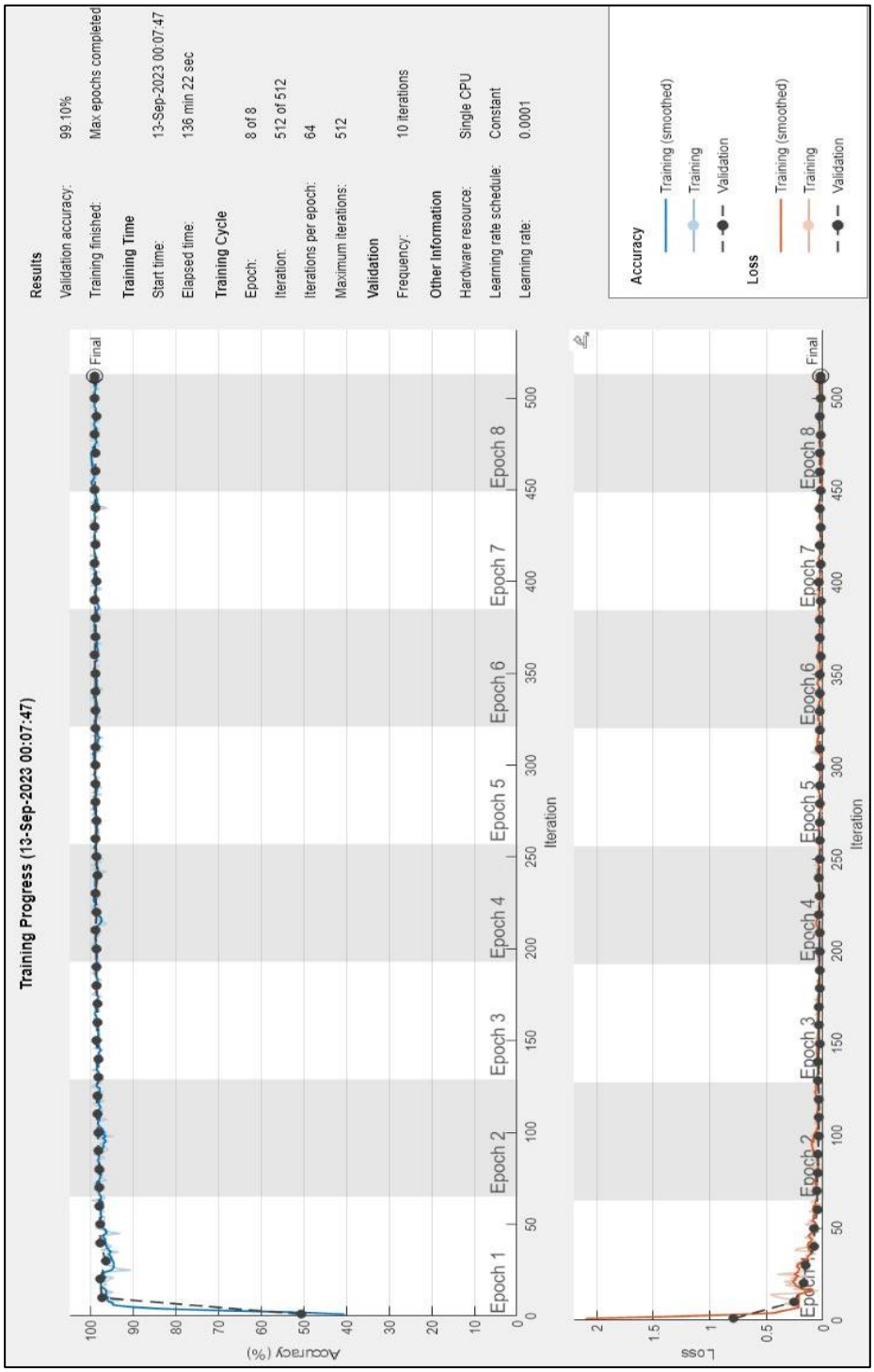

Figure 6.6 Training progress for the classification using *proposed* FLO-FrST method

to 99.2% and *seizure Sensitivity* corresponds to 99.1 %. Thus, overall performance of classification process has contributed to *Accuracy* of 99.1 % (corresponding to total true predictions) and 0.9% is the reported *Error Rate*.

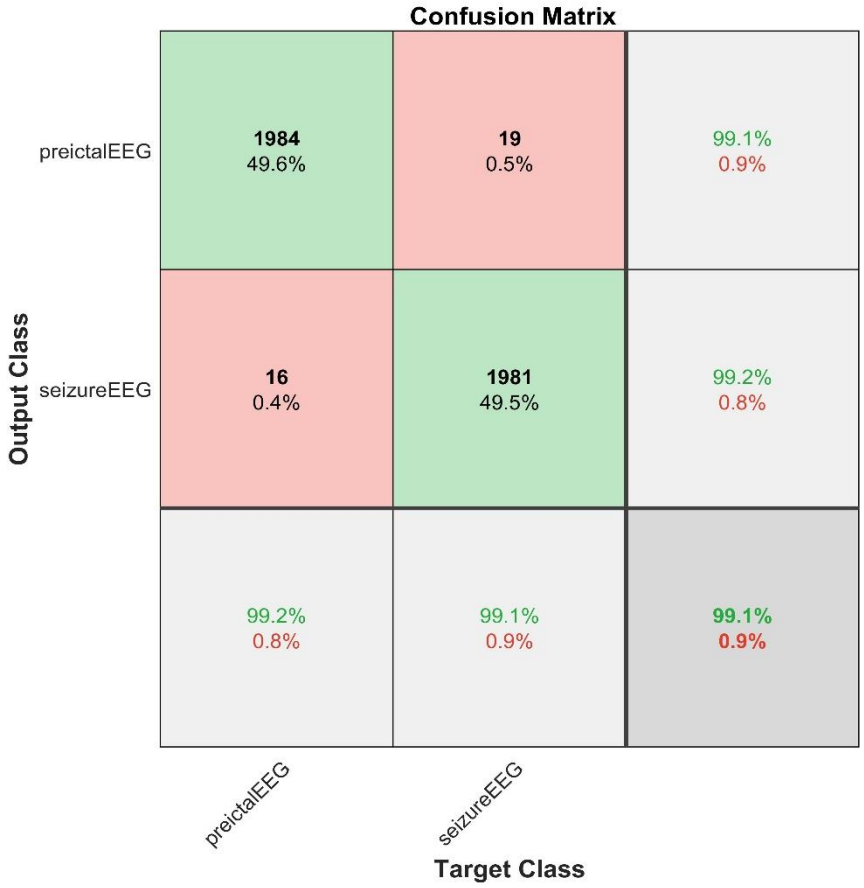

Figure 6.7 Confusion matrix obtained using *proposed* FLO-FrST for preictal and seizure EEGs**.**

6.4.3 Comparative Analysis

To compare the performance of *proposed* method, this section first includes performance validation of *proposed* tool using different transfer learning models: VGG16 and ResNet-50. Finally, a comprehensive evaluation is conducted to compare the *proposed* tool with established methods, employing both qualitative and quantitative analyses.

6.4.3.1 Performance Validation of Classification using Different CNN Models

To illustrate the versatility of *proposed* tool, classification is also performed using different CNN models; VGG16 and ResNet-50, in addition to AlexNet transfer learning model. Keeping same configuration parameters, results over 512 iterations are depicted in **Figure 6.8,** and quantification measures are summarized in **Table 6.4**.

On comparing the training progress shown in **Figure 6.8**, it becomes evident that both VGG16 and ResNet-50 models exhibit validation accuracy of over 98% and the loss curve has converged. Furthermore, **Table 6.4** illustrates the performance parameters obtained for different CNN methods. It can be deduced that the FLO-FrST tool, as indicated by its high values of *Sensitivity*, *Positive Predictivity*, *Accuracy*, *F1-Score*, and *Matthew's Correlation Coefficient*, demonstrates effective performance across several CNN models.

Table 6.4 Performance validation of *proposed* model using different CNN models

EEG Epileptic State	Classification Performance Measures	CNN Models		
		AlexNet	VGG16	ResNet-50
Preictal	*Sensitivity* (%)	99.20	97.25	97.50
	Positive Predictivity (%)	99.05	99.49	99.49
	Accuracy (%)	99.13	98.38	98.50
	F1-Score	0.99	0.98	0.98
	Matthew's Correlation Coefficient	0.98	0.97	0.97
Seizure	*Sensitivity* (%)	99.05	99.50	99.50
	Positive Predictivity (%)	99.20	97.31	97.55
	Accuracy (%)	99.13	98.38	98.50
	F1-Score	0.99	0.98	0.99
	Matthew's Correlation Coefficient	0.98	0.97	0.97

(a)

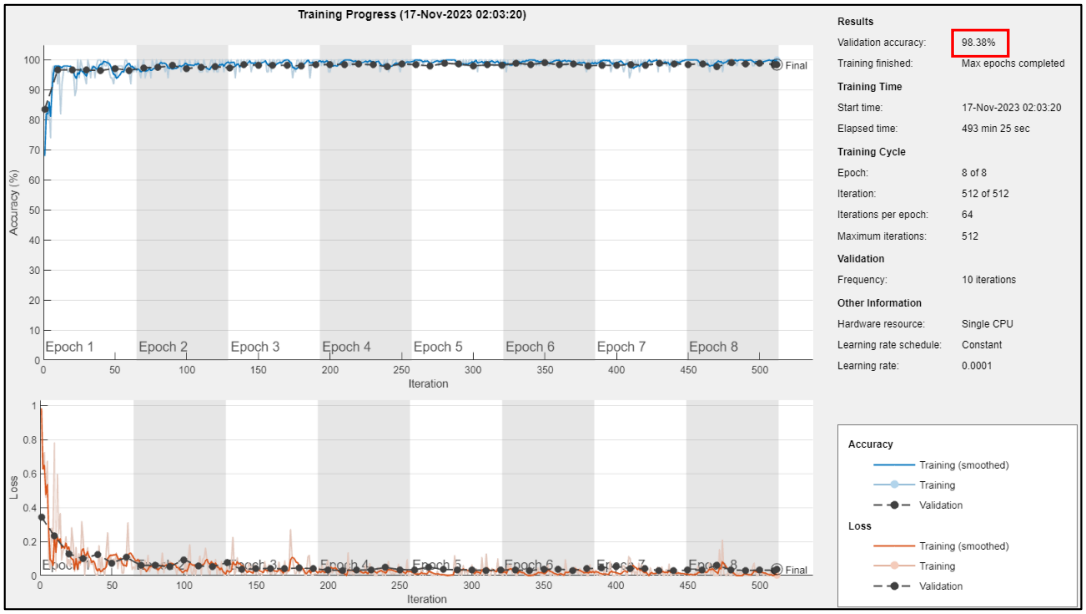

(b)

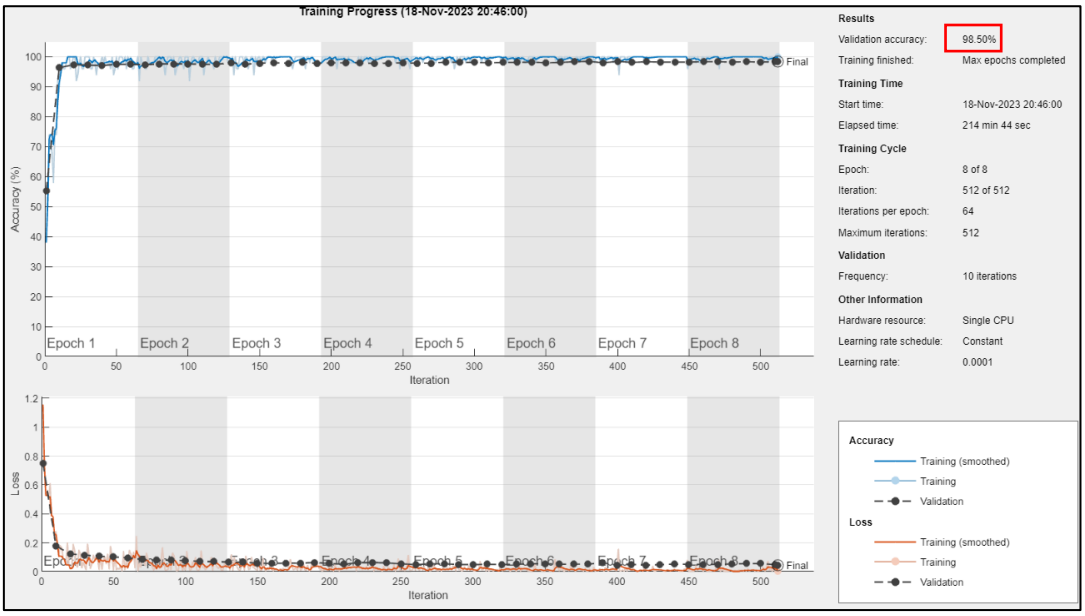

Figure. 6.8 Training progress of different CNN models; (a) VGG16, (b) ResNet-50

6.4.3.2 Qualitative Investigation with Established Tools

To demonstrate the qualitative aspect of using *proposed* FLO-FrST tool for classification (*Step 3-Coversion to 2-D images*), output of spectrograms generated using established methods: ST [163], FrST [47], FLO-ST [168] and *proposed* method, for preictal and seizure segments are illustrated in **Figure 6.9** and **Figure 6.10**, respectively. The colors in the illustrations depict the energy values of signal under consideration: *red*: high energy, *blue*: low energy.

On investigating the results depicted in **Figure 6.9** for preictal EEG, it can be inferred that *proposed* FLO-FrST (**Figure 6.9e)**) is able to distinguish every characteristic feature present in the selected segment, and has offered better time-frequency resolution as compared to ST (**Figure 6.9(b)**), FrST (**Figure 6.9(c)**) and FLO-ST (**Figure 6.9(d)**). This is because with four variable parameters, *proposed* FLO-FrST has the advantage of enhancing flexibility and providing robustness in obtained spectrograms, which is absent in other established methods.

Similarly, on observing the seizure EEG segment in **Figure 6.10**, it can be concluded that *proposed* FLO-FrST (**Figure 6.10(e)**) has the potential to identify the key features of seizure segments even in an impulsive environment due to the presence of FLOS parameter ρ, which on the contrary is absent for ST and FrST as shown in **Figure 6.10(b)** and **Figure 6.10(c)**, respectively. Additionally, with better resolution ability of *proposed* FLO-FrST, the key features of seizure are preserved while also providing a sharp resolution. However, for the FLO-ST case, as shown in **Figure 6.10(d)**, its poor resolution has hindered the distinguishing ability of FLO-ST.

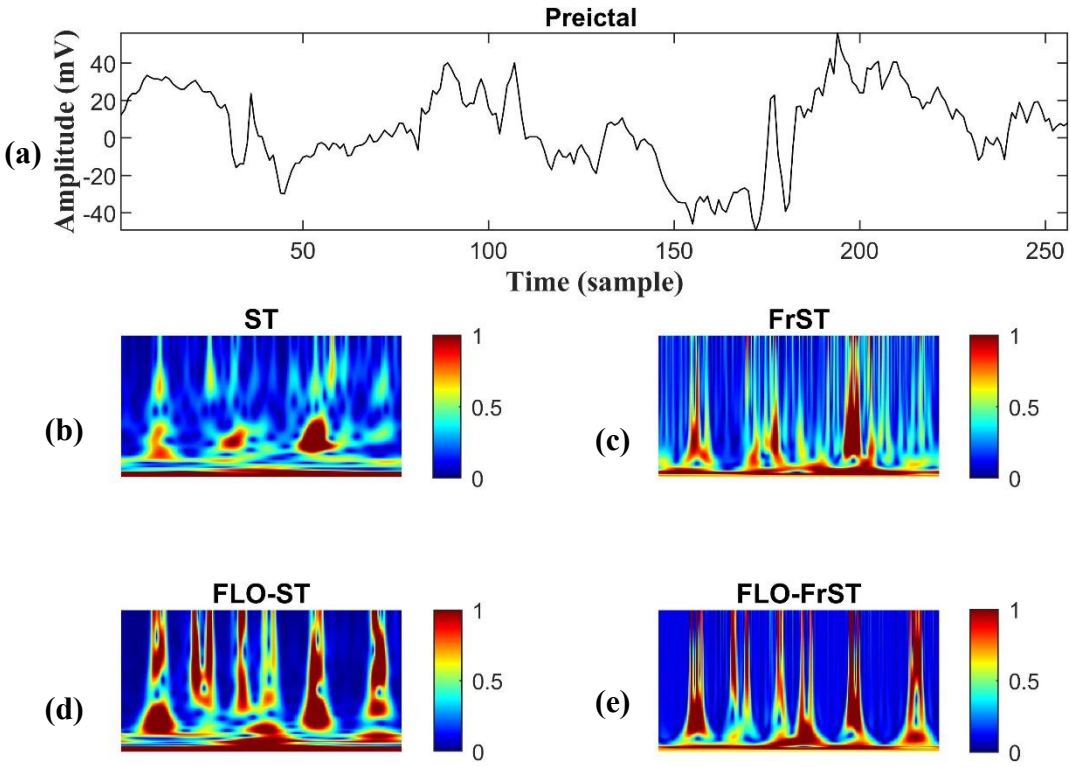

Figure 6.9 (a) Time-domain representation of preictal EEG with duration 256 samples, **(b)** ST spectrogram of preictal EEG, **(c)** FrST spectrogram of preictal EEG, **(d)** FLO-ST spectrogram of preictal EEG, **(e)** Spectrogram obtained using *proposed* FLO-FrST. The colour-bar scale represents the relationship between magnitude and colour.

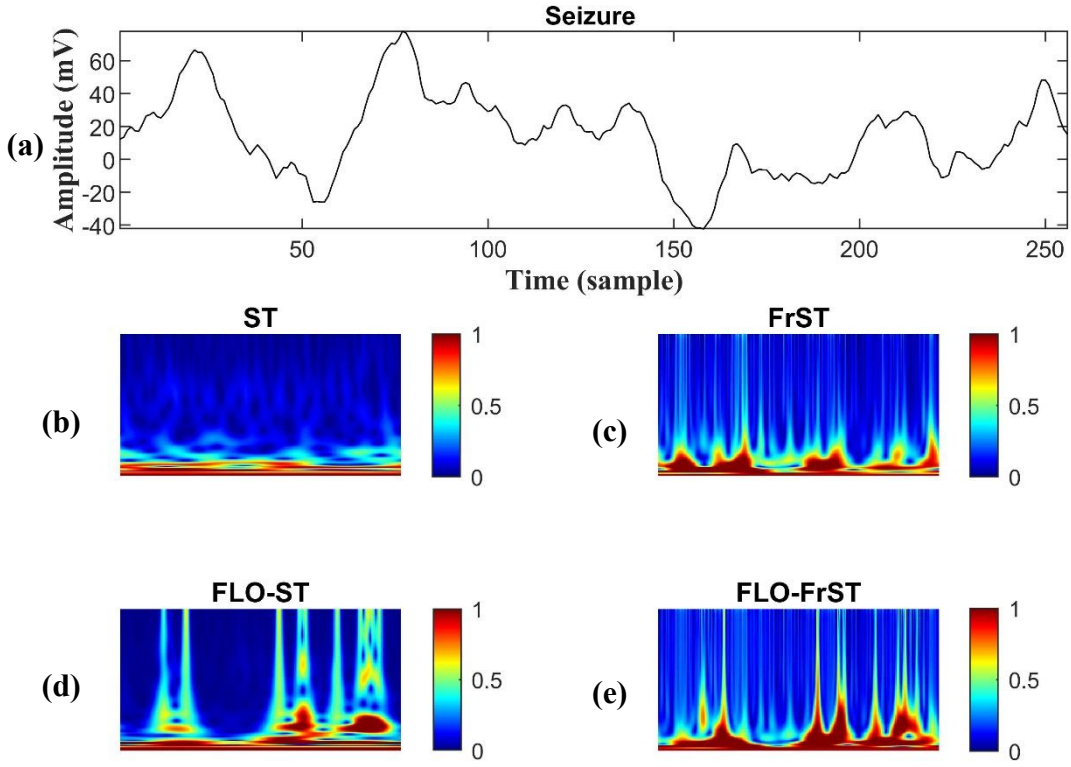

Figure 6.10 (a) Time-domain representation of seizure with duration 256 samples, **(b)** ST spectrogram of seizure EEG, **(c)** FrST spectrogram of seizure EEG, **(d)** FLO-ST spectrogram of seizure EEG, **(e)** Spectrogram obtained using *proposed* FLO-FrST. The colour-bar scale represents the relationship between magnitude and colour.

6.4.3.3 Quantitative Comparison with Established Tools

To validate performance of *proposed* method, the classification model is implemented using ST [22], FrST [6], and FLO-ST [168] tools. The comparison between *proposed* tool-based method and established methods in terms of *Sensitivity*, *Positive Predictivity*, *Accuracy,* and *Error Rate* is tabulated in **Table 6.5**. From the results, we can see that *proposed* method has reported highest *Accuracy* of 99.1 % and the lowest *Error Rate* of 0.9% among other methods, which illustrates superiority of *proposed* method over the established methods.

Furthermore, to analyze values of the *F1-Score* and *Matthew's Correlation Coefficient*, graphical depiction is shown in **Figure 6.11**. On examining bar graphs, it is observed that *proposed* method has the highest value for both *F1-Score* and *Matthew's Correlation Coefficient*, which further emphasizes the superiority of *proposed* method.

Table 6.5 Comparison of classification performance of *proposed* method with ST, FrST and FLO-ST.

	Preictal		Seizure		Overall	
	Sensitivity (%)	Positive Predictivity (%)	Sensitivity (%)	Positive Prediction (%)	Accuracy (%)	Error Rate (%)
ST [163]	82.3	87	87.8	83.2	85.03	14.97
FrST [47]	95.5	91.6	91.2	95.3	93.4	6.6
FLO-ST [168]	96	94.3	94.2	96	95.1	4.9
Proposed	**99.2**	**99.1**	**99.1**	**99.2**	**99.1**	**0.9**

Bold indicates the highest Sensitivity, Positive Predictivity, Accuracy and lowest Error Rate

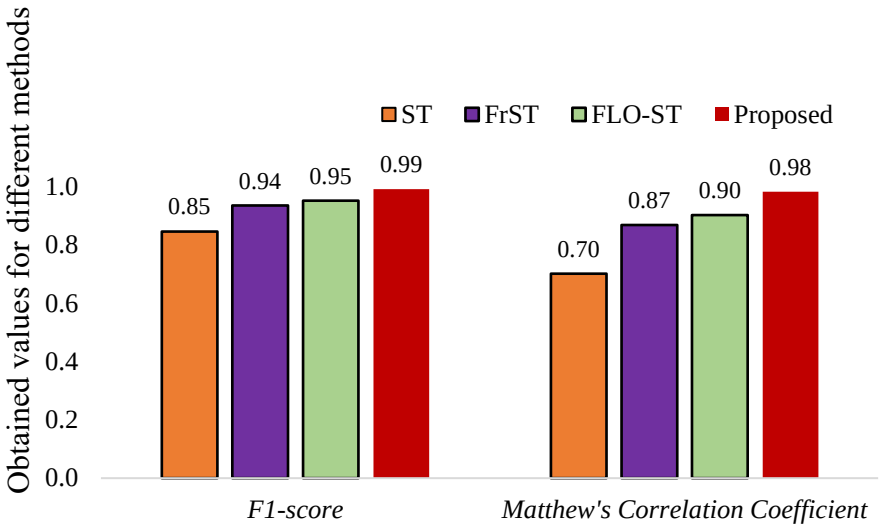

Figure 6.11 Comparison of *F1-Score* and *Matthew's Correlation Coefficient* for *proposed* method with state-of-the-art methods.

6.4.3.4 Performance Comparison with State-of-the-Art Methods

To prove efficacy of *proposed* tool-based classification, comparison with state-of-the-art literature; Khan *et al.* [265], Gao *et al.* [266] and Truong *et al.* [267] for a preictal duration of 10 mins for EEG epileptic classification has been presented in **Table 6.6** As evident from the recorded values, *Sensitivity* for *proposed* method is highest among reported methods, which implies better performance in correctly identifying seizure states.

Hence, with results obtained for classification, one can ascertain that *proposed* FLO-FrST-based classification method has reported high accuracy in differentiating preictal and seizure stages, thus indicating that it can potentially eliminate false alarms in real-time monitoring of epileptic stages.

Table 6.6 Comparison of classification performance of *proposed* method with literature methods

Literature methods	Seizure Sensitivity (%)
Khan et al. [265]	87.8
Gao et al. [266]	95.8
Truong et al. [267]	89.1
Proposed	**99.1**

Bold indicates the highest Sensitivity

6.5 Summary

This chapter puts forward the design of a novel TF that incorporates definitions of existing TF tools namely: Stockwell transform (ST), fractional Fourier transform (FrFT), and integrates them with the concept of fractional lower order statistics (FLOS). The *proposed* tool—fractional lower-order fractional Stockwell transform (FLO-FrST) has four degrees of freedom and ability to offer 3 Rs': *Resolution*, *Reconstruction* and *Robustness*. In a broad sense, *resolution* improves readability, *reconstruction* plays a crucial role in retrieving time domain signals, and the attribute of *robustnes*s is responsible for enhancing performance in adverse noisy conditions.

Furthermore, highlighting factor of designing this tool is while proving its invertibility (Section 6.2.3), fractional lower-order fractional Fourier transform (FLO-FrFT) has also been formulated, which is likewise novel. To the best of our knowledge, no previous studies that combine FrFT with FLOS have been published in the literature.

Apart from rigorous simulation study, which proved the superiority against established tools in both Gaussian as well as non-Gaussian α-stable distribution environments, the application of EEG epileptic classification is also demonstrated. With results obtained for classification, it is inferred that *proposed* FLO-FrST-based methodology has also established itself as an alternative to preprocessing stage as it has eliminated the requirement of preprocessing by suppressing impulsive artifacts, thus making the system model more efficient and robust. Furthermore, versatility of *proposed* tool has been demonstrated by attainment of high accuracy values and other performance metrics while evaluating classification performance utilizing three distinct CNN models, namely AlexNet, VGG16, and ResNet50. Lastly, the *proposed* tool has outperformed most well-established methods and established tools in classifying preictal and ictal states.

Chapter 7

Conclusions and Future Work

Signal processing is an emerging field of study since its inception. With numerous applications in various domains, the focus of research in the field of signal processing has been shifting towards developing solutions for more complex and demanding situations that are *non-stationary* and *non-Gaussian* in nature. The central theme of this thesis revolves around exploring tools for non-stationary signals and in particular, focusing on establishing and developing the methods for non-Gaussian α-stable distribution noise environment. Overall, the contributions of thesis are summarized in this section, followed by futuristic scope that could be achieved using the encapsulated *proposed* methods.

7.1 Conclusion

With the main contribution revolving around the design methods related to non-stationary nature of signals in non-Gaussian α-stable distribution environment and their applications in ECG signal processing and EEG classification, the main highlights of the work are listed below.

- Exploring the potential of fractional Stockwell transform (FrST) in ECG denoising and QRS complex detection.
- Establishment of non-Gaussian nature of ECG noises and proposing an alternative noise model that can handle a wide range of noise behavior ranging from impulsive to Gaussian.
- Proving the degradation of R-peak detection methods and classification performance by incorporating deep learning techniques under Gaussian noise assumption.
- Development of novel structuring element (SE) for morphological filtering based on α-stable distribution noise model and its application in ECG denoising and QRS complex detection.

- Development of novel fractional lower-order fractional Stockwell transform (FLO-FrST) encompassing the 3 R's: resolution, robustness and reconstruction abilities.
- Development of EEG epileptic classification methodology based on *proposed* FLO-FrST, which proved effective in eliminating false alarms by reporting high accuracy in differentiating seizure and preictal stages. Additionally, the *proposed* technique proved itself as an alternative to preprocessing stage by simply providing a high-resolution transformed signal, which has aided in preserving the key features of seizure and preictal stages even in an impulsive environment.

Elaborating on the work focused in this thesis, firstly design methods for ECG processing based on time-frequency (TF) tools are developed considering the non-stationary nature of ECG signals. Fractional Stockwell transformed signals provide greater robustness and time-fractional frequency domain resolution due to the presence of three degrees of freedom namely, fractional order parameter a, window adjustment parameters p and q, which makes it a favorable tool for processing non-stationary ECG signals. This advantage improved performance of the *proposed* denoising technique by achieving superior reconstruction results compared to existing ECG denoising methods. Furthermore, the inclusion of time-fractional frequency support with FrST-based QRS complex detection methodology improved the detection performance by accurately detecting QRS complexes present in the signal. Additionally, the *proposed* methodology accurately identified QRS complex of an unclassifiable beat, eliminating the chances of missed detection, hence enhancing the diagnostic ability of the *proposed* methodology. This broadened the application of FrFT kernel-based TF tools to ECG processing, addressing the initial gap in utilizing these tools for biomedical signal processing.

Additionally, it is common to verify the effectiveness of the *proposed* method for various applications using a standard database and additive white Gaussian noise (AWGN) to simulate real-world conditions. Therefore, while validating the performance of aforementioned *proposed* denoising methodology, it was pointed out that there exists an improvement window for examining the noise analysis model. Hence, further research carried out in thesis incorporated a statistical study to investigate the nature of noises corrupting ECG signals. Various statistical tools were employed to establish that ECG noises do not have Gaussian nature, thus ruling out the assumption of modeling real-time noises with Gaussian distribution. Subsequently, goodness of fit tests and statistical

measures were used to demonstrate that ECG noises are more accurately represented by a non-Gaussian α-stable distribution.

Furthermore, to illustrate the adverse impact of using conventional assumptions i.e., noises follow a Gaussian nature, two post-processing stages, namely R-peak detection and classification based on a deep learning model were chosen. The performance of state-of-the-art methods was evaluated for selected methods individually in conventional noise environment and *proposed* non-Gaussian α-stable distribution environment which as established is a better substitute for replicating real-time noise environment. The results of R-peak detection in the *proposed* noise environment demonstrated poor *Sensitivity*, *Positive Predictivity*, *Detection Accuracy* and increased *Error Rate*, which clearly proved that the performance of well-established methods could deteriorate when real-time noises are encountered. Similarly, deep learning models trained with the assumption of noise following a Gaussian distribution showed poor classification accuracy when tested with ECG signals corrupted using real-time noise, leading to degradation in performance. Hence, it was established using statistical tests and emphasized with performance degradation of post processing stages that there is a need to adopt an alternative noise model that can better replicate real-time noises. With this, the prevailing research gap of theoretical performance and real-time performance of established methods was investigated and a solution based on using non-Gaussian α-stable distribution noise model was *proposed* through extensive simulation study as explained.

After establishing the presence of non-Gaussian α-stable distribution nature in ECG noises, design aspects for ECG processing using morphological filters (MFs) were explored. A detailed literature has been available where the advantages of using MF are outlined in dealing with impulsive noise. However, with intensive research on MFs, it was pointed out that there has been a surge in designing methods for structuring element (SE), which is a key component of MF. Therefore, the next research work of the thesis aimed at designing SE for designing MF-based processing methods for ECG signals. For this, the research area of window functions was referred, as SE in MF design shares characteristics with window functions used for designing finite impulse response filters (FIRs). Thus, a new SE based on cross-convolution of window functions was *proposed*. Also, fractional Fourier transform (FrFT) tool as feature extraction is employed to enhance the filtering and have additional benefit of shape adaption. The advantage of its fractional order parameter a or fractional

rotation parameter φ is utilized with a cross-convolved window, which resulted in better shape adaptability with ECG beats. The performance of the *proposed* SE based on FrFT of cross-convolved window (referred to as fractional structuring element (FrSE)) is then morphologically applied with the *proposed* morphological operation (MO) for denoising ECG signals. The first-of-its kind *proposed* filter (referred to as referred to as $MF_{FrSE\&MO}$) using FrSE and MO and designed with α-stable distribution noise model, proved effective in reducing noise and enhancing reconstruction of ECG signals contaminated with noise. This research work closed the gap of amalgamating the concepts of MF, FrFT and α-stable distribution model in designing solutions for signal processing applications.

Finally, to address the challenges in existing TF tools, a novel fractional lower-order fractional Stockwell (FLO-FrST) based on robust α-stable distribution model is *proposed*, which has the advantage of having robustness against outliers, offers fine resolution in both time and frequency domains and can reconstruct signals back in time domain with less error and can work effectively for noise environments ranging from impulsive to Gaussian. The *proposed* tool outperformed the well-established tools by achieving better resolution, robustness, and reconstruction. Furthermore, its potential as a suitable signal processing tool is demonstrated by its application in electroencephalogram (EEG) epileptic classification. The results have also demonstrated the versatility of FLO-FrST based *proposed* methodology by achieving high accuracy values and other performance metrics when evaluating classification performance using three different CNN models: AlexNet, VGG16 and ResNet-50. With this, the last research gap *proposed* in this thesis is resolved, suggesting the use of fractional lower-order time-frequency (FLO-TF) tools for biomedical signal processing.

7.2 Future Scope

A thorough simulation study pointed out various research gaps, which were achieved using many *proposed* methods and tools. However, signal processing is a limitless domain and there lies opportunities for various research avenues based on the *proposed* work in the thesis as outlined below:

i. The advantages of utilizing FrST parameters namely a, p and q can be extended to feature extraction and classification of ECG signals. Furthermore, there is a

possibility of utilizing time-fractional frequency features for signal processing applications including biomedical domain.

ii. Incorporating α-stable distribution as a noise analysis model can open the possibility of increasing the efficacy of established methodologies for real-time implementation.

iii. The conceptualization of FrFT with a cross-convolved window can open up new possibilities for spectral estimation in signal processing and various other biomedical engineering applications.

iv. There is an opportunity to explore the potential of FLO-FrST tool in ECG processing applications, which can result in an efficient and robust ECG analyzing system as this model is based on a more practical α-stable distribution model.

v. The post-processing techniques employed in TF approaches can be extended by integrating the α-stable distribution model and FLOS.

BIBLIOGRAPHY

[1] J. G. Proakis and D. G. Manolakis, *Digital Signal Processing*, 4th ed. Pearson Education India, 2007.

[2] V. Madisetti, *Digital Signal Processing Handbook*, 2nd ed. CRC Press, 2009.

[3] G. Matheron, *Random Sets and Integral Geometry,*. John Wiley & Sons, 1975.

[4] J. Serra, *Image Analysis and Mathematical Morphology*. Academic Press, 1982.

[5] R. M. Haralick, S. R. Sternberg, and X. Zhuang, "Image Analysis Using Mathematical Morphology," *IEEE Transactions on Pattern Analysis and Machine Intelligence*, vol. PAMI-9, no. 4, pp. 532–550, Jul. 1987.

[6] J. Serra and P. Soille, *Mathematical Morphology and Its Applications to Image Processing*, vol. 2. Dordrecht: Springer Netherlands, 1994.

[7] F. Y. Shih, *Image Processing and Mathematical Morphology*. CRC Press, 2017.

[8] P. Maragos and R. W. Schafer, "Morphological filters--Part I: Their set-theoretic analysis and relations to linear shift-invariant filters," *IEEE Transactions on Acoustics, Speech, and Signal Processing*, vol. 35, no. 8, pp. 1153–1169, 1987.

[9] P. Maragos and R. W. Schafer, "Morphological Filters-Part II: Their Relations to Median, Order-Statistic, and Stack Filters," *IEEE Transactions on Acoustics, Speech, and Signal Processing*, vol. 35, no. 8, pp. 1170–1184, 1987.

[10] P. Maragos and R. W. Schafer, "A unification of linear, median, order-statistics and morphological filters under mathematical morphology," in *ICASSP '85. IEEE International Conference on Acoustics, Speech, and Signal Processing*, Institute of Electrical and Electronics Engineers, 1985, pp. 1329–1332.

[11] S. Nishida, M. Nakamura, A. Ikeda, and H. Shibasaki, "Signal separation of background EEG and spike by using morphological filter," *Medical Engineering & Physics*, vol. 21, no. 9, pp. 601–608, Nov. 1999.

[12] A. F. Al-Bakri, R. Martinek, M. Pelc, J. Zygarlicki, and A. Kawala. Sterniuk, “Implementation of a morphological filter for removing spikes from the epileptic brain signals to improve identification ripples,” *Sensors*, vol. 22, no. 19, p. 7522, Oct. 2022.

[13] C. H. Chu and E. J. Delp, “Impulsive noise suppression and background normalization of electrocardiogram signals using morphological operators,” *IEEE Transactions on Biomedical Engineering*, vol. 36, no. 2, pp. 262–273, 1989.

[14] Q. Li, B. Chen, W. Zhang, and D. Song, “Research on mathematical morphological operators for fault diagnosis of rolling element bearings,” *Measurement*, vol. 203, p. 111964, Nov. 2022.

[15] W. Huang, R. Wang, Y. Zhou, and X. Chen, “Simultaneous coherent and random noise attenuation by morphological filtering with dual-directional structuring element,” *IEEE Geoscience and Remote Sensing Letters*, vol. 14, no. 10, pp. 1720–1724, Oct. 2017.

[16] P. Maragos, “A representation theory for morphological image and signal processing,” *IEEE Transactions on Pattern Analysis and Machine Intelligence*, vol. 11, no. 6, pp. 586–599, Jun. 1989.

[17] J. Goutsias and H. J. A. M. Heijmans, “Nonlinear multiresolution signal decomposition schemes-Part I: Morphological pyramids,” *IEEE Transactions on Image Processing*, vol. 9, no. 11, pp. 1862–1876, 2000.

[18] H. J. A. M. Heijmans and J. Goutsias, “Nonlinear multiresolution signal decomposition schemes-Part II: Morphological wavelets,” *IEEE Transactions on Image Processing*, vol. 9, no. 11, pp. 1897–1913, 2000.

[19] A. Montanari, “Long range dependence in hydrology,” in *Theory and Applications of Long-Range Dependence*, P. Doukhan, G. Oppenheim, and Murad. S. Taqqu, Eds., Boston: Birkhauser, 2003, pp. 461–472.

[20] H. Sheng and Y. Chen, “FARIMA with stable innovations model of Great Salt Lake elevation time series,” *Signal Processing*, vol. 91, no. 3, pp. 553–561, Mar. 2011.

[21] R. Adler, R. Feldman, and M. Taqqu, Eds., *A Practical Guide to Heavy Tails Statistical Techniques and Applications*, 1st ed. Birkhäuser Boston, MA, 1998.

[22] A. A. Stanislavsky, “Probability Interpretation of the Integral of Fractional Order,” *Theoretical and Mathematical Physics*, vol. 138, no. 3, pp. 418–431, Mar. 2004.

[23] F. Mainardi, P. Paradisi, and R. Gorenflo, “Probability distributions generated by fractional diffusion equations,” 2007.

[24] B. Ross, “A brief history and exposition of the fundamental theory of fractional calculus,” 1975, pp. 1–36.

[25] M. D. Ortigueira, *Fractional Calculus for Scientists and Engineers*, vol. 84. Dordrecht: Springer Netherlands, 2011.

[26] H. Sun, Y. Zhang, D. Baleanu, W. Chen, and Y. Chen, “A new collection of real world applications of fractional calculus in science and engineering,” *Communications in Nonlinear Science and Numerical Simulation*, vol. 64, pp. 213–231, Nov. 2018.

[27] H. Sheng, Y. Chen, and T. Qiu, *Fractional Processes and Fractional-Order Signal Processing*. London: Springer London, 2012.

[28] V. Namias, “The Fractional Order Fourier Transform and its Application to Quantum Mechanics,” *IMA Journal of Applied Mathematics*, vol. 25, no. 3, pp. 241–265, 1980.

[29] H. M. Ozaktas, Z. Zalevsky, and M. A. Kutay, *The Fractional Fourier Transform - with Applications in Optics & Signal Processing*, First. New York: John Wiley and Sons, 2001.

[30] G. Samorodnitsky, “Long-Range Dependence as a Phase Transition,” 2016, pp. 285–361.

[31] E. Wigner, “On the Quantum Correction For Thermodynamic Equilibrium,” *Physical Review*, vol. 40, no. 5, pp. 749–759, Jun. 1932.

[32] L. Cohen, *Time-Frequency Analysis*. New Jersey: Prentice Hall, 1995.

[33] Y. Wang, *Time-Frequency Analysis of Seismic Signals*. John Wiley & Sons, 2022.

[34] M. S. Khan, M. Curilem, F. Huenupan, M. F. Khan, and N. B. Yoma, “A Signal Processing Perspective of Monitoring Active Volcanoes [Applications Corner],” *IEEE Signal Processing Magazine*, vol. 36, no. 6, pp. 125–163, Nov. 2019.

[35] Z. Feng, M. Liang, and F. Chu, “Recent advances in time–frequency analysis methods for machinery fault diagnosis: A review with application examples,” *Mechanical Systems and Signal Processing*, vol. 38, no. 1, pp. 165–205, Jul. 2013.

[36] M. Wacker and H. Witte, “Time-frequency techniques in biomedical signal analysis,” *Methods of Information in Medicine*, vol. 52, no. 04, pp. 279–296, Jan. 2013.

[37] B. Boashash, *Time-Frequency Signal Analysis and Processing: A Comprehensive Reference*, Second. London: Academic Press, 2016.

[38] P. Cheng, Z. Chen, Q. Li, Q. Gong, J. Zhu, and Y. Liang, “Atrial Fibrillation Identification With PPG Signals Using a Combination of Time-Frequency Analysis and Deep Learning,” *IEEE Access*, vol. 8, pp. 172692–172706, 2020.

[39] M. Portnoff, “Time-frequency representation of digital signals and systems based on short-time Fourier analysis,” *IEEE Transactions on Acoustics, Speech, and Signal Processing*, vol. 28, no. 1, pp. 55–69, Feb. 1980.

[40] I. Daubechies, “The wavelet transform, time-frequency localization and signal analysis,” *IEEE Transactions on Information Theory*, vol. 36, no. 5, pp. 961–1005, 1990.

[41] T. A. C. M. Claasen and W. F. G. Mecklenbräuker, “The Wigner distribution — A tool for time-frequency signal analysis: Part I: Continuous-time signals,” *Philips Journal of Research*, vol. 35, pp. 217–250, 1980.

[42] T. A. C. M. Claasen and W. F. G. Mecklenbräuker, “The Wigner distribution — A tool for time-frequency signal analysis; Part II: Discrete-time signals,” *Philips Journal of Research*, vol. 35, pp. 276–300, 1980.

[43] T. A. C. M. Claasen and W. F. G. Mecklenbräuker, “The Wigner distribution — A tool for time-frequency signal analysis; Part III: Relations with other time-frequency signal transformations,” *Philips Journal of Research*, vol. 35, pp. 372–389, 1980.

[44] L. B. Almeida, “The fractional Fourier transform and time-frequency representations,” *IEEE Transactions on Signal Processing*, vol. 42, no. 11, pp. 3084–3091, 1994.

[45] R. Tao, Yan. Lei. Li, and Y. Wang, “Short-time fractional Fourier transform and its applications,” *IEEE Transactions on Signal Processing*, vol. 58, no. 5, pp. 2568–2580, May 2010.

[46] D. Mendlovic, Z. Zalevsky, D. Mas, J. García, and C. Ferreira, “Fractional wavelet transform,” *Applied Optics*, vol. 36, no. 20, p. 4801, Jul. 1997.

[47] X. D. Ping and K. Guo, “Fractional S transform — Part 1: Theory,” *Applied Geophysics*, vol. 9, no. 1, pp. 73–79, Mar. 2012.

[48] D. W. Griffith, J. G. Gonzalez, and G. R. Arce, “Robust time-frequency representations for signals in α-stable noise using fractional lower-order statistics,” in *Proceedings of the IEEE Signal Processing Workshop on Higher-Order Statistics*, IEEE Computer Society, pp. 415–419.

[49] C. L. Nikias and M. Shao, *Signal Processing with Alpha-Stable Distributions and Applications*. New York: Wiley-Interscience, 1995.

[50] J. Long, H. Wang, P. Li, and H. Fan, “Applications of fractional lower order time-frequency representation to machine bearing fault diagnosis,” *IEEE/CAA Journal of Automatica Sinica*, vol. 4, no. 4, pp. 734–750, 2017.

[51] R. M. Rangayyan, *Biomedical Signal Analysis: A Case-Study Approach*. John Wiley & Sons, 2015.

[52] L. Sörnmo and P. Laguna, *Bioelectrical Signal Processing in Cardiac and Neurological Applications*. Elsevier, 2005.

[53] N. V Thakor and Y. S. Zhu, “Applications of adaptive filtering to ECG analysis: noise cancellation and arrhythmia detection,” *IEEE Transactions on Biomedical Engineering*, vol. 38, no. 8, pp. 785–794, 1991.

[54] R. W. Schafer, “What Is a Savitzky-Golay Filter? [Lecture Notes],” *IEEE Signal Processing Magazine*, vol. 28, no. 4, pp. 111–117, Jul. 2011.

[55] H. Li, X. Wang, L. Chen, and E. Li, “Denoising and R-peak detection of electrocardiogram signal based on EMD and improved approximate envelope,” *Circuits, Systems, and Signal Processing*, vol. 33, no. 4, 2014.

[56] R. Wang, S. Sun, X. Guo, and D. Yan, “EMD threshold denoising algorithm based on variance estimation,” *Circuits, Systems, and Signal Processing*, vol. 37, no. 12, pp. 5369–5388, Dec. 2018.

[57] P. Singh, S. Shahnawazuddin, and G. Pradhan, “An efficient ECG denoising technique based on non-local means estimation and modified empirical mode decomposition,” *Circuits, Systems, and Signal Processing*, vol. 37, no. 10, 2018.

[58] A. Singhal, P. Singh, B. Fatimah, and R. B. Pachori, “An efficient removal of power-line interference and baseline wander from ECG signals by employing Fourier decomposition technique,” *Biomedical Signal Processing and Control*, vol. 57, p. 101741, 2020.

[59] K. M. Chang, “Arrhythmia ECG noise reduction by ensemble empirical mode decomposition,” *Sensors*, vol. 10, no. 6, pp. 6063–6080, Jun. 2010.

[60] S. Jain, V. Bajaj, and A. Kumar, “Riemann Liouvelle Fractional Integral Based Empirical Mode Decomposition for ECG Denoising,” *IEEE Journal of Biomedical and Health Informatics*, vol. 22, no. 4, pp. 1133–1139, Jul. 2018.

[61] J. Wang, Y. Ye, X. Pan, X. Gao, and C. Zhuang, “Fractional zero-phase filtering based on the Riemann–Liouville integral,” *Signal Processing*, vol. 98, pp. 150–157, May 2014.

[62] J. Wang, Y. Ye, Y. Gao, S. Qian, and X. Gao, “Fractional compound integral with application to ECG signal denoising,” *Circuits, Systems, and Signal Processing*, vol. 34, no. 6, pp. 1915–1930, Jun. 2015.

[63] A. Gupta and S. Kumar, “Design of Atangana–Baleanu–Caputo fractional-order digital filter,” *ISA Transactions*, vol. 112, pp. 74–88, Jun. 2021.

[64] J. Pan and W. J. Tompkins, “A real-time QRS detection algorithm,” *IEEE Transactions on Biomedical Engineering*, vol. BME-32, no. 3, 1985.

[65] N. M. Arzeno, Z. D. Deng, and C. S. Poon, “Analysis of first-derivative based QRS detection algorithms,” *IEEE Transactions on Biomedical Engineering*, vol. 55, no. 2, pp. 478–484, Feb. 2008.

[66] A. Kaur, S. Kumar, A. Agarwal, and R. Agarwal, “An efficient R-peak detection using Riesz fractional-order digital differentiator,” *Circuits, Systems, and Signal Processing*, vol. 39, no. 4, pp. 1965–1987, Apr. 2020.

[67] Y. Ferdi, J. P. Herbeuval, A. Charef, and B. Boucheham, “R wave detection using fractional digital differentiation,” *ITBM-RBM*, vol. 24, no. 5–6, pp. 273–280, Dec. 2003.

[68] A. Kaur, A. Agarwal, R. Agarwal, and S. Kumar, “A novel approach to ECG R-peak detection,” *Arabian Journal for Science and Engineering*, vol. 44, no. 8, pp. 6679–6691, 2019.

[69] A. K. Dohare, V. Kumar, and R. Kumar, “An efficient new method for the detection of QRS in electrocardiogram,” *Computers & Electrical Engineering*, vol. 40, no. 5, pp. 1717–1730, Jul. 2014.

[70] S. Jain, M. K. Ahirwal, A. Kumar, V. Bajaj, and G. K. Singh, “QRS detection using adaptive filters: A comparative study,” *ISA Transactions*, vol. 66, pp. 362–375, Jan. 2017.

[71] L. D. Sharma and R. K. Sunkaria, “A robust QRS detection using novel pre-processing techniques and kurtosis based enhanced efficiency,” *Measurement: Journal of the International Measurement Confederation*, vol. 87, 2016.

[72] Z. Zhang, Q. Yu, Q. Zhang, N. Ning, and J. Li, “A Kalman filtering based adaptive threshold algorithm for QRS complex detection,” *Biomedical Signal Processing and Control*, vol. 58, p. 101827, Apr. 2020.

[73] Z. Zidelmal, A. Amirou, M. Adnane, and A. Belouchrani, “QRS detection based on wavelet coefficients,” *Computer Methods and Programs in Biomedicine*, vol. 107, no. 3, 2012.

[74] Z. Zidelmal, A. Amirou, D. Ould-Abdeslam, A. Moukadem, and A. Dieterlen, “QRS detection using S-transform and Shannon energy,” *Computer Methods and Programs in Biomedicine*, vol. 116, no. 1, pp. 1–9, Aug. 2014.

[75] R. Mabrouki, B. Khaddoumi, and M. Sayadi, “R peak detection in electrocardiogram signal based on a combination between empirical mode decomposition and Hilbert transform,” in *2014 1st International Conference on Advanced Technologies for Signal and Image Processing (ATSIP)*, IEEE, Mar. 2014, pp. 183–187.

[76] J. Lv and J. Yu, “Average combination difference morphological filters for fault feature extraction of bearing,” *Mechanical Systems and Signal Processing*, vol. 100, pp. 827–845, 2018.

[77] Y. Li, M. J. Zuo, Y. Chen, and K. Feng, “An enhanced morphology gradient product filter for bearing fault detection,” *Mechanical Systems and Signal Processing*, vol. 109, pp. 166–184, Sep. 2018.

[78] L. Zhang, J. Xu, J. Yang, D. Yang, and D. Wang, “Multiscale morphology analysis and its application to fault diagnosis,” *Mechanical Systems and Signal Processing*, vol. 22, no. 3, pp. 597–610, Apr. 2008.

[79] Y. Li, X. Liang, and M. J. Zuo, “A new strategy of using a time-varying structure element for mathematical morphological filtering,” *Measurement*, vol. 106, pp. 53–65, Aug. 2017.

[80] M. L. Tian and J. M. Yang, “Optimization of structural element in froth image denoising of coal flotation,” *International Journal of Pattern Recognition and Artificial Intelligence*, vol. 30, no. 04, p. 1654002, May 2016.

[81] V. Ćurić, A. Landström, M. J. Thurley, and C. L. L. Hendriks, “Adaptive mathematical morphology – A survey of the field,” *Pattern Recognition Letters*, vol. 47, pp. 18–28, Oct. 2014.

[82] S. Osman and W. Wang, “A morphological Hilbert-Huang transform technique for bearing fault detection,” *IEEE Transactions on Instrumentation and Measurement*, vol. 65, no. 11, pp. 2646–2656, Nov. 2016.

[83] P. Maragos and R. Schafer, “Morphological filters--Part I: Their set-theoretic analysis and relations to linear shift-invariant filters,” *IEEE Transactions on Acoustics, Speech, and Signal Processing*, vol. 35, no. 8, pp. 1153–1169, Aug. 1987.

[84] P. E. Trahanias, “An approach to QRS complex detection using mathematical morphology,” *IEEE Transactions on Biomedical Engineering*, vol. 40, no. 2, pp. 201–205, 1993.

[85] Y. Sun, K. L. Chan, and S. M. Krishnan, “ECG signal conditioning by morphological filtering,” *Computers in Biology and Medicine*, vol. 32, no. 6, pp. 465–479, Nov. 2002.

[86] Y. Sun, K. L. Chan, and S. M. Krishnan, “Characteristic wave detection in ECG signal using morphological transform,” *BMC Cardiovascular Disorders*, vol. 5, Sep. 2005.

[87] C. J. Deepu, X. Y. Xu, D. L. T. Wong, C. H. Heng, and Y. Lian, “A 2.3 μ W ECG-on-chip for wireless wearable sensors,” *IEEE Transactions on Circuits and Systems II: Express Briefs*, vol. 65, no. 10, pp. 1385–1389, 2018.

[88] S. Yazdani and J. M. Vesin, “Extraction of QRS fiducial points from the ECG using adaptive mathematical morphology,” *Digital Signal Processing*, vol. 56, pp. 100–109, 2016.

[89] K. Friganovic, D. Kukolja, A. Jovic, M. Cifrek, and G. Krstacic, “Optimizing the Detection of Characteristic Waves in ECG Based on Processing Methods Combinations,” *IEEE Access*, vol. 6, pp. 50609–50626, 2018.

[90] X. Wan *et al.*, “Electrocardiogram baseline wander suppression based on the combination of morphological and wavelet transformation based filtering,” *Computational and Mathematical Methods in Medicine*, vol. 2019, pp. 1–7, 2019.

[91] G. Xu, J. Wang, Q. Zhang, S. Zhang, and J. Zhu, “A spike detection method in EEG based on improved morphological filter,” *Computers in Biology and Medicine*, vol. 37, no. 11, pp. 1647–1652, Nov. 2007.

[92] Y. Li, X. Liang, J. Lin, Y. Chen, and J. Liu, “Train axle bearing fault detection using a feature selection scheme based multi-scale morphological filter,” *Mechanical Systems and Signal Processing*, vol. 101, pp. 435–448, Feb. 2018.

[93] L. Meng, J. Xiang, Y. Wang, Y. Jiang, and H. Gao, “A hybrid fault diagnosis method using morphological filter–translation invariant wavelet and improved ensemble empirical mode decomposition,” *Mechanical Systems and Signal Processing*, vol. 50–51, pp. 101–115, Jan. 2015.

[94] X. Zhang, J. Kang, L. Xiao, and J. Zhao, “Alpha stable distribution based morphological filter for bearing and gear fault diagnosis in nuclear power plant,” *Science and Technology of Nuclear Installations*, vol. 2015, pp. 1–15, 2015.

[95] A. Hu and L. Xiang, “An optimal selection method for morphological filter’s parameters and its application in bearing fault diagnosis,” *Journal of Mechanical Science and Technology*, vol. 30, no. 3, pp. 1055–1063, Mar. 2016.

[96] Y. Li, X. Liang, W. Liu, and Y. Wang, “Development of a morphological convolution operator for bearing fault detection,” *Journal of Sound and Vibration*, vol. 421, pp. 220–233, May 2018.

[97] J. Yu, T. Hu, and H. Liu, “A new morphological filter for fault feature extraction of vibration signals,” *IEEE Access*, vol. 7, pp. 53743–53753, 2019.

[98] J. Liang, Y. Zhang, J. H. Zhong, and H. Yang, “A novel multi-segment feature fusion based fault classification approach for rotating machinery,” *Mechanical Systems and Signal Processing*, vol. 122, pp. 19–41, May 2019.

[99] J. K. Patel and C. B. Read, *Handbook of the Normal Distribution*, Second. New York: Marcel Dekker, 1982.

[100] G. L. Squires, *Practical Physics*. Cambridge University Press, 2001.

[101] M. Kateregga, S. Mataramvura, and D. Taylor, “Parameter estimation for stable distributions with application to commodity futures log-returns,” *Cogent Economics and Finance*, vol. 5, no. 1, 2017.

[102] P. Levy, *Calcul des probabilités*. Paris: Gauthier-Villars, 1925.

[103] B. Mandelbrot, “The Pareto-Levy Law and the Distribution of Income,” *International Economic Review*, vol. 1, no. 2, 1960.

[104] B. V. Gnedenko and A. & N. Kolmogorov, *Limit distributions for sums of independent Random Variables*. Creative Media Partners- LLC, 2021.

[105] E. F. Fama and R. Roll, “Some Properties of Symmetric Stable Distributions,” *Journal of the American Statistical Association*, vol. 63, no. 323, 1968.

[106] D. R. Holt and E. L. Crow, “Tables and Graphs of the Stable Probability Density Functions,” *J Res Natl Bur Stand Sect B Math Sci*, vol. 77 B, no. 3–4, 1973.

[107] E. F. Fama and R. Roll, “Parameter estimates for symmetric stable distributions,” *Journal of the American Statistical Association*, vol. 66, no. 334, 1971.

[108] J. H. McCulloch, “Simple consistent estimators of stable distribution parameters,” *Communications in Statistics - Simulation and Computation*, vol. 15, no. 4, 1986.

[109] I. A. Koutrouvelis, “Regression-type estimation of the parameters of stable laws,” *Journal of the American Statistical Association*, vol. 75, no. 372, 1980.

[110] S. M. Kogon and D. B. Williams, “On the characterization of impulsive noise with a-stable distributions using fourier techniques,” in *Conference Record - Asilomar Conference on Signals, Systems and Computers*, 1995.

[111] X. Ma and C. L. Nikias, “Parameter Estimation and Blind Channel Identification in Impulsive Signal Environments,” *IEEE Transactions on Signal Processing*, vol. 43, no. 12, 1995.

[112] J. P. Nolan, “Maximum likelihood estimation of stable parameters,” in *Levy processes: Theory and applications*, 2001.

[113] B. Yue and Z. Peng, “A validation study of α-stable distribution characteristic for seismic data,” *Signal Processing*, vol. 106, pp. 1–9, Jan. 2015.

[114] Y. Chen and J. Chen, “Novel SαS PDF approximations and their applications in wireless signal detection,” *IEEE Transactions on Wireless Communications*, vol. 14, no. 2, pp. 1080–1091, Feb. 2015.

[115] G. Laguna-Sanchez and M. Lopez-Guerrero, “On the use of alpha-stable distributions in noise modeling for PLC,” *IEEE Transactions on Power Delivery*, vol. 30, no. 4, 2015.

[116] H. Sadreazami, M. O. Ahmad, and M. N. S. Swamy, “A study on image denoising in contourlet domain using the alpha-stable family of distributions,” *Signal Processing*, vol. 128, pp. 459–473, Nov. 2016.

[117] Y. Wang, Y. Qi, Y. Wang, Z. Lei, X. Zheng, and G. Pan, “Delving into α-stable distribution in noise suppression for seizure detection from scalp EEG,” *Journal of Neural Engineering*, vol. 13, no. 5, p. 056009, Oct. 2016.

[118] M. L. Talbi and P. Ravier, “Flexible ECG signal modeling and compression using alpha stable functions,” *Medical Engineering & Physics*, vol. 109, p. 103865, Nov. 2022.

[119] T. P. Pander, “A suppression of an impulsive noise in EGG signal processing,” in *Annual International Conference of the IEEE Engineering in Medicine and Biology - Proceedings*, 2004.

[120] H. Hamlili, S. Kameche, and A. Abdelmalek, “A survey on impulsive noise models removal techniques based on adaptive filter in ECG signal,” in *2018 International*

Conference on Electronics, Control, Optimization and Computer Science (ICECOCS), IEEE, Dec. 2018, pp. 1–6.

[121] G. Yu, C. Li, and J. Zhang, "A new statistical modeling and detection method for rolling element bearing faults based on alpha–stable distribution," *Mechanical Systems and Signal Processing*, vol. 41, no. 1–2, pp. 155–175, Dec. 2013.

[122] S. Luan, Y. Gao, J. Zhou, and Z. Zhang, "Automatic modulation classification based on Cauchy-score constellation and lightweight network under impulsive noise," *IEEE Wireless Communications Letters*, vol. 10, no. 11, pp. 2509–2513, Nov. 2021.

[123] H. M. Ozaktas and M. A. Kutay, "The fractional Fourier transform," in *2001 European Control Conference (ECC)*, IEEE, 2001, pp. 1477–1483.

[124] S. Kumar and R. Saxena, "φFrMF : Fractional Fourier matched filter," *Circuits, Systems, and Signal Processing*, vol. 37, no. 1, pp. 49–80, 2018.

[125] S. Kumar, K. Singh, and R. Saxena, "Analysis of Dirichlet and generalized 'Hamming' window functions in the fractional Fourier transform domains," *Signal Processing*, vol. 91, no. 3, pp. 600–606, 2011.

[126] S. Kumar, R. Saxena, and K. Singh, "Fractional Fourier transform and fractional-order calculus-based image edge detection," *Circuits, Systems, and Signal Processing*, vol. 36, no. 4, pp. 1493–1513, 2017.

[127] S. Kumar, R. Saxena, and K. Singh, "Analysis and design of non-recursive digital differentiators in fractional domain for signal processing applications," Thapar University, Patiala, 2014.

[128] S. Das and I. Pan, *Fractional Order Signal Processing*. Berlin, Heidelberg: Springer Berlin Heidelberg, 2012.

[129] H. M. Ozaktas, O. Arikan, M. A. Kutay, and G. Bozdagt, "Digital computation of the fractional Fourier transform," *IEEE Transactions on Signal Processing*, vol. 44, no. 9, pp. 2141–2150, Sep. 1996.

[130] S. C. Pei and J. J. Ding, "Closed-form discrete fractional and affine Fourier transforms," *IEEE Transactions on Signal Processing*, vol. 48, no. 5, pp. 1338–1353, 2000.

[131] M. S. Richman and T. W. Parks, “Understanding discrete rotations,” in *IEEE International Conference on Acoustics, Speech and Signal Processing*, 1997, pp. 2057–2060.

[132] S. C. Pie, C. C. Tseng, and M. H. Yeh, “A new discrete fractional Fourier transform based on constrained eigendecomposition of DFT matrix by Lagrange multiplier method,” *IEEE Transactions on Circuits and Systems II: Analog and Digital Signal Processing*, vol. 46, no. 9, pp. 1240–1245, 1999.

[133] J. R. de Oliveira Neto and J. B. Lima, “Discrete fractional Fourier transforms based on closed-form Hermite–Gaussian-like DFT eigenvectors,” *IEEE Transactions on Signal Processing*, vol. 65, no. 23, pp. 6171–6184, Dec. 2017.

[134] M. Z. Ikram, K. Abed-Meraim, and Y. Hua, “Fast quadratic phase transform for estimating the parameters of multicomponent chirp signals,” *Digital Signal Processing*, vol. 7, no. 2, pp. 127–135, Apr. 1997.

[135] G. Bi, Y. Wei, G. Li, C. Wan, and B. Si, “Radix-2 DIF fast algorithms for polynomial time-frequency transforms,” *IEEE Transactions on Aerospace and Electronic Systems*, vol. 42, no. 4, pp. 1540–1546, Oct. 2006.

[136] X. Deng, Y. Li, D. Fan, and Y. Qiu, “A fast algorithm for fractional Fourier transforms,” *Optics Communications*, vol. 138, no. 4–6, pp. 270–274, Jun. 1997.

[137] G. Cariolaro, T. Erseghe, P. Kraniauskas, and N. Laurenti, “A unified framework for the fractional Fourier transform,” *IEEE Transactions on Signal Processing*, vol. 46, no. 12, pp. 3206–3219, 1998.

[138] B. Santhanam and J. H. McClellan, “The discrete rotational Fourier transform,” *IEEE Transactions on Signal Processing*, vol. 44, no. 4, pp. 994–998, Apr. 1996.

[139] C. C. Shih, “Fractionalization of Fourier transform,” *Optics Communications*, vol. 118, no. 5–6, pp. 495–498, Aug. 1995.

[140] X. Su, R. Tao, and X. Kang, “Analysis and comparison of discrete fractional fourier transforms,” *Signal Processing*, vol. 160, pp. 284–298, Jul. 2019.

[141] H. M. Ozaktas and O. Aytür, “Fractional Fourier domains,” *Signal Processing*, vol. 46, no. 1, pp. 119–124, Sep. 1995.

[142] H. M. Ozaktas, D. Mendlovic, L. Onural, and B. Barshan, “Convolution, filtering, and multiplexing in fractional Fourier domains and their relation to chirp and wavelet transforms,” *Journal of the Optical Society of America A*, vol. 11, no. 2, p. 547, Feb. 1994.

[143] L. P. Castro, L. T. Minh, and N. M. Tuan, “Filter design based on the fractional Fourier transform associated with new convolutions and correlations,” *Mathematical Sciences*, vol. 17, no. 4, pp. 445–454, Dec. 2023.

[144] R. G. Dorsch, A. W. Lohmann, Y. Bitran, D. Mendlovic, and H. M. Ozaktas, “Chirp filtering in the fractional Fourier domain,” *Applied Optics*, vol. 33, no. 32, p. 7599, Nov. 1994.

[145] I. S. Yetik, M. A. Kutay, and H. M. Ozaktas, “Image representation and compression with the fractional Fourier transform,” *Optics Communications*, vol. 197, no. 4–6, pp. 275–278, 2001.

[146] F. J. Yan and B. Z. Li, “Multi-dimensional graph fractional Fourier transform and its application to data compression,” *Digital Signal Processing*, vol. 129, p. 103683, Sep. 2022.

[147] M. Joshi, C. Shakher, and K. Singh, “Fractional Fourier transform based image multiplexing and encryption technique for four-color images using input images as keys,” *Optics Communications*, vol. 283, no. 12, pp. 2496–2505, Jun. 2010.

[148] T. Nagashima *et al.*, “Peak-to-average power ratio reduction of transmission signal of all-optical orthogonal time/frequency domain multiplexing using fractional Fourier transform,” *Optics Communications*, vol. 402, pp. 123–127, Nov. 2017.

[149] D. Mendlovic, H. M. Ozaktas, and A. W. Lohmann, “Fractional correlation,” *Applied Optics*, vol. 34, no. 2, p. 303, Jan. 1995.

[150] E. Garza- Flores and J. Álvarez-Borrego, “Pattern recognition using binary masks based on the fractional Fourier transform,” *Journal of Modern Optics*, vol. 65, no. 14, pp. 1634–1657, Aug. 2018.

[151] B. Barshan and B. Ayrulu, “Fractional Fourier transform pre-processing for neural networks and its application to object recognition,” *Neural Networks*, vol. 15, no. 1, pp. 131–140, Jan. 2002.

[152] R. Desbiens, P. Tremblay, J. Genest, and J. P. Bouchard, “Matrix form for the instrument line shape of Fourier-transform spectrometers yielding a fast integration algorithm to theoretical spectra,” *Applied Optics*, vol. 45, no. 3, p. 546, Jan. 2006.

[153] M. Sayed, M. H. Saad, and H. I. Saleh, “Pulse shape discrimination of LSO and LuYAP scintillators based on Discrete Fractional Fourier Transform,” *Journal of Instrumentation*, vol. 15, no. 06, pp. P06003–P06003, Jun. 2020.

[154] V. Gupta and M. Mittal, “A comparison of ECG signal pre-processing using FrFT, FrWT and IPCA for improved analysis,” *IRBM*, vol. 40, no. 3, pp. 145–156, 2019.

[155] A. J. D. Krupa, S. Dhanalakshmi, N. L. Sanjana, N. Manivannan, R. Kumar, and S. Tripathy, “Fetal heart rate estimation using fractional Fourier transform and wavelet analysis,” *Biocybernetics and Biomedical Engineering*, vol. 41, no. 4, pp. 1533–1547, 2021.

[156] A. Papoulis and S. U. Pillai, *Probablity, Random Variables, and Stochastic Processes*, Fourth. Tata McGraw Hill Education , 2002.

[157] J. A. Wheeler and W. H. Zurek, *Quantum Theory and Measurement*. Princeton University Press, 1983.

[158] D. Gabor, “Theory of communication Part 1: The analysis of information,” *Journal of the Institution of Electrical Engineers - Part III: Radio and Communication Engineering*, vol. 93, no. 26, pp. 429–441, Nov. 1946.

[159] S. Qian and D. Chen, *Joint Time-Frequency Analysis: Methods and Applications*. Prentice Hall PTR, 1996.

[160] R. B. Pachori, *Time-Frequency Analysis Techniques and their Applications*. Boca Raton: CRC Press, 2023.

[161] L. Stanković, *Digital Signal Processing with Selected Topics*. CreateSpace Independent Publishing Platform, 2015.

[162] R. G. Stockwell, L. Mansinha, and R. P. Lowe, “Localization of the complex spectrum: the S transform,” *IEEE Transactions on Signal Processing*, vol. 44, no. 4, pp. 998–1001, Apr. 1996.

[163] R. G. Stockwell, “A basis for efficient representation of the S-transform,” *Digital Signal Processing*, vol. 17, no. 1, pp. 371–393, Jan. 2007.

[164] R. Tao, B. Deng, and Y. Wang, “Research progress of the fractional Fourier transform in signal processing,” *Science in China Series F*, vol. 49, no. 1, pp. 1–25, Jan. 2006.

[165] C. Capus and K. Brown, “Short-time fractional Fourier methods for the time-frequency representation of chirp signals,” *The Journal of the Acoustical Society of America*, vol. 113, no. 6, pp. 3253–3263, Jun. 2003.

[166] M. J. Coates and E. E. Kuruoğlu, “Time–frequency-based detection in impulsive noise environments using α-stable noise models,” *Signal Processing*, vol. 82, no. 12, pp. 1917–1925, Dec. 2002.

[167] M. Djeddi and M. Benidir, “Robust polynomial Wigner-Ville distribution for the analysis of polynomial phase signals in α-stable noise,” in *2004 IEEE International Conference on Acoustics, Speech, and Signal Processing*, IEEE, pp. ii-613–16.

[168] J. Long, H. Wang, D. Zha, P. Li, H. Xie, and L. Mao, “Applications of fractional lower order S transform time frequency filtering algorithm to machine fault diagnosis,” *PLOS ONE*, vol. 12, no. 4, p. e0175202, Apr. 2017.

[169] J. Long, H. Wang, H. Fan, and Z. Lao, “Fractional lower order linear chirplet transform and its application to bearing fault analysis,” *PLOS ONE*, vol. 17, no. 10, p. e0276489, Oct. 2022.

[170] J. Long, H. Wang, H. Fan, and Z. Lao, “Applications of improved linear chirplet time frequency representation to Machine bearing fault analysis,” *Measurement*, vol. 209, p. 112460, Mar. 2023.

[171] J. L. Jiang and D. F. Zha, “Generalized fractional lower-order spectrum of alpha stable distribution process,” in *2008 4th International Conference on Wireless Communications, Networking and Mobile Computing*, IEEE, Oct. 2008, pp. 1–4.

[172] J. Long, H. Wang, P. Li, and H. Xie, “A WHT signal detection-based FLO-TF-UBSS algorithm under impulsive noise environment,” *Circuits, Systems, and Signal Processing*, vol. 37, no. 7, pp. 2997–3022, Jul. 2018.

[173] J. Long, H. Wang, and P. Li, “Applications of fractional lower order frequency spectrum technologies to bearing fault analysis,” *Mathematical Problems in Engineering*, vol. 2019, pp. 1–24, Aug. 2019.

[174] X. Zhu, W. P. Zhu, and B. Champagne, “Spectrum sensing based on fractional lower order moments for cognitive radios in α-stable distributed noise,” *Signal Processing*, vol. 111, pp. 94–105, Jun. 2015.

[175] J. Long, H. Wang, D. Zha, H. Fan, Z. Lao, and H. Wu, “Applications of an improved time-frequency filtering algorithm to signal reconstruction,” *Mathematical Problems in Engineering*, vol. 2017, pp. 1–14, 2017.

[176] A. Papandreou-Suppappola, *Applications in Time-Frequency Signal Processing*. CRC Press, 2018.

[177] F. Auger *et al.*, “Time-frequency reassignment and synchrosqueezing: An overview,” *IEEE Signal Processing Magazine*, vol. 30, no. 6, pp. 32–41, Nov. 2013.

[178] D. Degirmenci, M. Yalcin, M. A. Ozdemir, and A. Akan, “Synchrosqueezing Transform in Biomedical Applications: A mini review,” in *2020 Medical Technologies Congress (TIPTEKNO)*, IEEE, Nov. 2020, pp. 1–5.

[179] B. Boashash and S. Ouelha, “Automatic signal abnormality detection using time-frequency features and machine learning: A newborn EEG seizure case study,” *Knowledge-Based Systems*, vol. 106, pp. 38–50, Aug. 2016.

[180] J. Shi, N. Zhang, and X. Liu, “A novel fractional wavelet transform and its applications,” *Science China Information Sciences*, vol. 55, no. 6, pp. 1270–1279, Jun. 2012.

[181] Y. Chen and Z. Peng, “A novel optimal STFrFT and its application in seismic signal processing,” in *2012 International Conference on Computational Problem-Solving (ICCP)*, IEEE, Oct. 2012, pp. 328–331.

[182] A. Ghasemi and S. Zahediasl, “Normality tests for statistical analysis: A guide for non-statisticians,” *International Journal of Endocrinology and Metabolism*, vol. 10, no. 2, 2012.

[183] H. R. Martin and F. Honarvar, “Application of statistical moments to bearing failure detection,” *Applied Acoustics*, vol. 44, no. 1, 1995.

[184] R. E. Walpole, R. H. Myers, S. L. Myers, and K. Ye, *Probability and Statistics for Engineers and Scientists*, vol. 5. New York: Macmillan, 1993.

[185] G. W. Snedecor and W. G. Cochran, *Statistical Methods*, Eighth. Iowa State University Press, 1989.

[186] G. W. Corder and D. I. Foreman, "Comparing two unrelated samples: the Mann−Whitney U-Test and the Kolmogorov−Smirnov two-sample test," in *Nonparametric Statistics: A Step-by-Step Approach*, Second Edition., 2014, pp. 69–96.

[187] F. Cong, J. Chen, and Y. Pan, "Kolmogorov-Smirnov test for rolling bearing performance degradation assessment and prognosis," *Journal of Vibration and Control*, vol. 17, no. 9, pp. 1337–1347, Aug. 2011.

[188] Y. Dodge, "Kolmogorov–Smirnov Test," in *The Concise Encyclopedia of Statistics*, New York, NY: Springer New York, pp. 283–287.

[189] V. M. Panaretos and Y. Zemel, "Statistical Aspects of Wasserstein Distances," *Annual Review of Statistics and Its Application*, vol. 6, no. 1, pp. 405–431, Mar. 2019.

[190] S. Kolouri, S. R. Park, M. Thorpe, D. Slepcev, and G. K. Rohde, "Optimal mass transport: signal processing and machine-learning applications," *IEEE Signal Processing Magazine*, vol. 34, no. 4, pp. 43–59, Jul. 2017.

[191] G. J. McLachlan and S. Rathnayake, "On the number of components in a Gaussian mixture model," *WIREs Data Mining and Knowledge Discovery*, vol. 4, no. 5, pp. 341–355, Sep. 2014.

[192] S. Nadarajah, "A generalized normal distribution," *Journal of Applied Statistics*, vol. 32, no. 7, pp. 685–694, 2005.

[193] A. Dytso, R. Bustin, H. V. Poor, and S. Shamai, "Analytical properties of generalized Gaussian distributions," *Journal of Statistical Distributions and Applications*, vol. 5, no. 1, p. 6, Dec. 2018.

[194] S. Etemad and M. Amirmazlaghani, "A new multiplicative watermark detector in the contourlet domain using t Location-Scale distribution," *Pattern Recognition*, vol. 77, pp. 99–112, 2018.

[195] G. B. Moody and R. G. Mark, “The impact of the MIT-BIH arrhythmia database.,” *IEEE engineering in medicine and biology magazine : the quarterly magazine of the Engineering in Medicine & Biology Society*, vol. 20, no. 3, pp. 45–50, 2001.

[196] G. Moody and R. Mark, “MIT-BIH Arrhythmia Database.” 2005. [Online]. Available: https://www.physionet.org/content/mitdb/1.0.0/

[197] *Recommended Practice for Testing and Reporting Performance Results of Ventricular Arrhythmia Detection Algorithms (AAMI ECAR-1986)*. Arlington Va: Association for the Advancement of Medical Instrumentation, 1987.

[198] P. de Chazal, M. O’Dwyer, and R. B. Reilly, “Automatic Classification of Heartbeats Using ECG Morphology and Heartbeat Interval Features,” *IEEE Transactions on Biomedical Engineering*, vol. 51, no. 7, pp. 1196–1206, Jul. 2004.

[199] N. D. Gai, “ECG beat classification using machine learning and pre-trained convolutional neural networks,” *arXiv preprint*, Jun. 2022.

[200] G. B. Moody, W. K. Muldrow, and R. G. Mark, “Noise Stress Test for Arrhythmia Detectors,” in *Computers in Cardiology*, 1984.

[201] G. Moody and R. Mark, “MIT-BIH Noise Stress Test Database.” 1999. Accessed: May 29, 2020. [Online]. Available: https://physionet.org/content/nstdb/1.0.0/

[202] A. Taddei *et al.*, “The European ST-T database: standard for evaluating systems for the analysis of ST-T changes in ambulatory electrocardiography,” *European Heart Journal*, vol. 13, no. 9, pp. 1164–1172, Sep. 1992.

[203] A. Taddei *et al.*, “European ST-T Database,” 2009. Accessed: May 27, 2020. [Online]. Available: https://physionet.org/content/edb/1.0.0/

[204] V. Behravan, N. E. Glover, R. Farry, P. Y. Chiang, and M. Shoaib, “Rate-adaptive compressed-sensing and sparsity variance of biomedical signals,” in *2015 IEEE 12th International Conference on Wearable and Implantable Body Sensor Networks, BSN 2015*, 2015.

[205] “Motion Artifact Contaminated ECG Database.” 2015. Accessed: Apr. 06, 2022. [Online]. Available: https://physionet.org/content/macecgdb/1.0.0/

[206] “Examples of Electromyograms Database.” 2009. Accessed: Apr. 06, 2022. [Online]. Available: https://physionet.org/content/emgdb/1.0.0

[207] A. H. Shoeb and J. V. Guttag, “Application of Machine Learning to Epileptic Seizure Onset Detection and Treatment,” PhD Thesis, Massachusetts Institute of Technology, 2009.

[208] “CHB-MIT Scalp EEG Database.” 2010. Accessed: Jun. 08, 2023. [Online]. Available: https://physionet.org/content/chbmit/1.0.0/

[209] M. Alfaouri and K. Daqrouq, “ECG Signal Denoising By Wavelet Transform Thresholding,” *American Journal of Applied Sciences*, vol. 5, no. 3, pp. 276–281, Mar. 2008.

[210] M. K. Das and S. Ari, “Analysis of ECG signal denoising method based on S-transform,” *IRBM*, vol. 34, no. 6, pp. 362–370, Dec. 2013.

[211] B. U. Kohler, C. Hennig, and R. Orglmeister, “The principles of software QRS detection,” *IEEE Engineering in Medicine and Biology Magazine*, vol. 21, no. 1, pp. 42–57, 2002.

[212] M. A. Kabir and C. Shahnaz, “Denoising of ECG signals based on noise reduction algorithms in EMD and wavelet domains,” *Biomedical Signal Processing and Control*, vol. 7, no. 5, pp. 481–489, 2012.

[213] P. S. Hamilton and W. J. Tompkins, “Quantitative Investigation of QRS Detection Rules Using the MIT/BIH Arrhythmia Database,” *IEEE Transactions on Biomedical Engineering*, vol. BME-33, no. 12, 1986.

[214] A. Moukadem, A. Dieterlen, N. Hueber, and C. Brandt, “A robust heart sounds segmentation module based on S-transform,” *Biomedical Signal Processing and Control*, vol. 8, no. 3, pp. 273–281, May 2013.

[215] I. I. Christov, “Real time electrocardiogram QRS detection using combined adaptive threshold,” *BioMedical Engineering OnLine*, vol. 3, no. 1, p. 28, Dec. 2004.

[216] M. S. Manikandan and K. P. Soman, “A novel method for detecting R-peaks in electrocardiogram (ECG) signal,” *Biomedical Signal Processing and Control*, vol. 7, no. 2, pp. 118–128, Mar. 2012.

[217] P. Sabherwal, M. Agrawal, and L. Singh, “Automatic detection of the R Peaks in single-lead ECG signal,” *Circuits, Systems, and Signal Processing*, vol. 36, no. 11, pp. 4637–4652, Nov. 2017.

[218] M. Rakshit, D. Panigrahy, and P. K. Sahu, “An improved method for R-peak detection by using Shannon energy envelope,” *Sādhanā*, vol. 41, no. 5, pp. 469–477, May 2016.

[219] D. Jhanwar, K. K. Sharma, and S. G. Modani, “Generalized fractional S-transform and its application to discriminate environmental background acoustic noise signals,” *Acoustical Physics*, vol. 60, no. 4, pp. 466–473, Jul. 2014.

[220] S. Sahoo, P. Biswal, T. Das, and S. Sabut, “De-noising of ECG Signal and QRS detection using Hilbert transform and adaptive thresholding,” *Procedia Technology*, vol. 25, pp. 68–75, 2016.

[221] Y. Li, X. Tang, Z. Xu, and H. Yan, “A novel approach to phase space reconstruction of single lead ECG for QRS complex detection,” *Biomedical Signal Processing and Control*, vol. 39, pp. 405–415, Jan. 2018.

[222] A. Gacek and W. Pedrycz, *ECG Signal Processing, Classification and Interpretation: A Comprehensive Framework of Computational Intelligence*. Springer Science & Business Media, 2011.

[223] B. Yang, “An Adaptive Filtering Algorithm for Non-Gaussian Signals in Alpha-Stable Distribution,” *Traitement du Signal*, vol. 37, no. 1, pp. 69–75, Feb. 2020.

[224] J. M. Chambers, C. L. Mallows, and B. W. Stuck, “A method for simulating stable random variables,” *Journal of the American Statistical Association*, vol. 71, no. 354, pp. 340–344, 1976.

[225] A. L. Goldberger *et al.*, “Physiobank, physiotoolkit, and physionet,” *Circulation*, vol. 101, no. 23, 2000.

[226] H. Su and H. Zhang, “Distances and kernels based on cumulative distribution functions,” in *Emerging Trends in Image Processing, Computer Vision and Pattern Recognition*, Elsevier, 2015, pp. 551–559.

[227] V. W. Berger and Y. Zhou, “Kolmogorov–Smirnov Test: Overview,” in *Wiley StatsRef: Statistics Reference Online*, Wiley, 2014.

[228] J. A. Cortes, A. Sanz, P. Estopinan, and J. I. Garcia, “On the suitability of the Middleton class A noise model for narrowband PLC,” in *2016 International*

Symposium on Power Line Communications and its Applications (ISPLC), IEEE, Mar. 2016, pp. 58–63.

[229] M. Okada, "A Digital Filter for the QRS Complex Detection," *IEEE Transactions on Biomedical Engineering*, vol. BME-26, no. 12, 1979.

[230] T. Wang, C. Lu, Y. Sun, M. Yang, C. Liu, and C. Ou, "Automatic ECG Classification Using Continuous Wavelet Transform and Convolutional Neural Network," *Entropy*, vol. 23, no. 1, p. 119, Jan. 2021.

[231] M. Rashed-Al-Mahfuz *et al.*, "Deep convolutional neural networks based ECG beats classification to diagnose cardiovascular conditions," *Biomedical Engineering Letters*, vol. 11, no. 2, pp. 147–162, 2021.

[232] A. S. Eltrass, M. B. Tayel, and A. I. Ammar, "A new automated CNN deep learning approach for identification of ECG congestive heart failure and arrhythmia using constant-Q non-stationary Gabor transform," *Biomedical Signal Processing and Control*, vol. 65, p. 102326, Mar. 2021.

[233] S. Singhal and M. Kumar, "A Systematic Review on Artificial Intelligence-Based Techniques for Diagnosis of Cardiovascular Arrhythmia Diseases: Challenges and Opportunities," *Archives of Computational Methods in Engineering*, vol. 30, no. 2, pp. 865–888, Mar. 2023.

[234] W. King, "mathworks / physionet_ECG_data, GitHub, Version 1.0.0.0, 2021." Accessed: Dec. 07, 2023. [Online]. Available: https://github.com/mathworks/physionet_ECG_data

[235] C. Huang *et al.*, "Sample imbalance disease classification model based on association rule feature selection," *Pattern Recognition Letters*, vol. 133, pp. 280–286, May 2020.

[236] W. J. Tompkins, *Biomedical digital signal processing*. Editorial Prentice Hall, 1993.

[237] A. A. Hiasat, M. M. Al-Ibrahim, and K. M. Gharaibeh, "Design and implementation of a new efficient median filtering algorithm," *IEE Proceedings - Vision, Image, and Signal Processing*, vol. 146, no. 5, p. 273, 1999.

[238] P. Singh and G. Pradhan, “A new ECG denoising framework using generative adversarial network,” *IEEE/ACM Transactions on Computational Biology and Bioinformatics*, vol. 18, no. 2, pp. 759–764, 2021.

[239] F. Zhang and Y. Lian, “QRS detection based on multiscale mathematical morphology for wearable ECG devices in body area networks,” *IEEE Transactions on Biomedical Circuits and Systems*, vol. 3, no. 4, pp. 220–228, 2009.

[240] C. F. Zhang and T. W. Bae, “VLSI friendly ECG QRS complex detector for body sensor networks,” *IEEE Journal on Emerging and Selected Topics in Circuits and Systems*, vol. 2, no. 1, pp. 52–59, 2012.

[241] K. M. M. Prabhu, *Window Functions and Their Applications in Signal Processing*. Boca Raton: CRC Press, 2018.

[242] J. Zhang, C. Liang, and Y. Chen, “A new family of windows - Convolution windows and their applications,” *Science in China, Series E: Technological Sciences*, vol. 48, no. 4, pp. 468–481, 2005.

[243] H. Wen, Z. Teng, and S. Guo, “Triangular self-convolution window with desirable sidelobe behaviors for harmonic analysis of power system,” *IEEE Transactions on Instrumentation and Measurement*, vol. 59, no. 3, pp. 543–552, 2010.

[244] F. J. Harris, “On the use of windows for harmonic analysis with the discrete Fourier transform,” *Proceedings of the IEEE*, vol. 66, no. 1, pp. 51–83, 1978.

[245] C. L. Dolph, “A current distribution for broadside arrays which optimizes the relationship between beam width and side-lobe level,” *Proceedings of the IRE*, vol. 34, no. 6, pp. 335–348, 1946.

[246] F. Ykhlef, H. Ykhlef, and A. Aissat, “Influence of Dolph-Chebyshev window on speech enhancement,” in *2012 International Conference on Multimedia Computing and Systems*, IEEE, 2012, pp. 140–143.

[247] J. Chen and S. Itoh, “A wavelet transform-based ECG compression method guaranteeing desired signal quality,” *IEEE Transactions on Biomedical Engineering*, vol. 45, no. 12, pp. 1414–1419, 1998.

[248] E. Merdjanovska and A. Rashkovska, “Comprehensive survey of computational ECG analysis: Databases, methods and applications,” *Expert Systems with Applications*, vol. 203, p. 117206, Oct. 2022.

[249] K. Mourad and B. R. Fethi, “Efficient automatic detection of QRS complexes in ECG signal based on reverse biorthogonal wavelet decomposition and nonlinear filtering,” *Measurement*, vol. 94, pp. 663–670, Dec. 2016.

[250] P. Tsakalides and C. L. Nikias, “Maximum likelihood localization of sources in noise modeled as a stable process,” *IEEE Transactions on Signal Processing*, vol. 43, no. 11, pp. 2700–2713, 1995.

[251] B. N. Singh and A. K. Tiwari, “Optimal selection of wavelet basis function applied to ECG signal denoising,” *Digital Signal Processing*, vol. 16, no. 3, pp. 275–287, May 2006.

[252] M. Blanco-Velasco, B. Weng, and K. E. Barner, “ECG signal denoising and baseline wander correction based on the empirical mode decomposition,” *Computers in Biology and Medicine*, vol. 38, no. 1, pp. 1–13, Jan. 2008.

[253] S. Kumar, D. Panigrahy, and P. K. Sahu, “Denoising of Electrocardiogram (ECG) signal by using empirical mode decomposition (EMD) with non-local mean (NLM) technique,” *Biocybernetics and Biomedical Engineering*, vol. 38, no. 2, pp. 297–312, 2018.

[254] V. Bhateja, R. Verma, R. Mehrotra, and S. Urooj, “A non-linear approach to ECG signal processing using morphological filters,” *International Journal of Measurement Technologies and Instrumentation Engineering*, vol. 3, no. 3, pp. 46–59, 2013.

[255] R. R. Sharma and R. B. Pachori, “Baseline wander and power line interference removal from ECG signals using eigenvalue decomposition,” *Biomedical Signal Processing and Control*, vol. 45, pp. 33–49, Aug. 2018.

[256] Y. Chen and H. Duan, “A QRS Complex Detection Algorithm Based on Mathematical Morphology and Envelope,” in *2005 IEEE Engineering in Medicine and Biology 27th Annual Conference*, IEEE, 2005, pp. 4654–4657.

[257] Y. B. Gao and D. Chen, “Wavelet analysis method of signal in α stable distribution,” *Computer Engineering*, vol. 38, no. 5, pp. 186–188, 2012.

[258] E. Sejdić, I. Djurović, and L. Stanković, “Fractional Fourier transform as a signal processing tool: An overview of recent developments,” *Signal Processing*, vol. 91, no. 6, pp. 1351–1369, Jun. 2011.

[259] I. Orovic, M. Orlandic, S. Stankovic, and Z. Uskokovic, “A Virtual Instrument for Time-Frequency Analysis of Signals With Highly Nonstationary Instantaneous Frequency,” *IEEE Transactions on Instrumentation and Measurement*, vol. 60, no. 3, pp. 791–803, Mar. 2011.

[260] L. Stanković, “A measure of some time–frequency distributions concentration,” *Signal Processing*, vol. 81, no. 3, pp. 621–631, Mar. 2001.

[261] I. Goodfellow, Y. Bengio, and A. Courville, *Deep Learning.* MIT Press, 2016.

[262] L. Liu and G. Z. Liang, “Application of EEG analysis in cognitive science,” *Applied Mechanics and Materials*, vol. 519–520, pp. 816–819, Feb. 2014.

[263] T. Paraschiv, D. Cochior, I. R. Adochiei, R. V. Paraschiv, C. K. Bănică, and F. C. Adochiei, “A study on cognitive and emotional processes carried out through EEG wave processing,” in *2023 13th International Symposium on Advanced Topics in Electrical Engineering (ATEE)*, IEEE, Mar. 2023, pp. 1–6.

[264] B. Boashash and S. Ouelha, “Designing high-resolution time–frequency and time–scale distributions for the analysis and classification of non-stationary signals: a tutorial review with a comparison of features performance,” *Digital Signal Processing*, vol. 77, pp. 120–152, Jun. 2018.

[265] H. Khan, L. Marcuse, M. Fields, K. Swann, and B. Yener, “Focal onset seizure prediction using convolutional networks,” *IEEE Transactions on Biomedical Engineering*, vol. 65, no. 9, pp. 2109–2118, Sep. 2018.

[266] Y. Gao, B. Gao, Q. Chen, J. Liu, and Y. Zhang, “Deep convolutional neural network-based epileptic electroencephalogram (EEG) signal classification,” *Frontiers in Neurology*, vol. 11, May 2020.

[267] N. D. Truong *et al.*, “Convolutional neural networks for seizure prediction using intracranial and scalp electroencephalogram,” *Neural Networks*, vol. 105, pp. 104–111, Sep. 2018.